ISSN 1694-7398
journals.manas.edu.kg

December 2021
Volume 9, Issue 2

MANAS JOURNAL OF ENGINEERING

MJEN

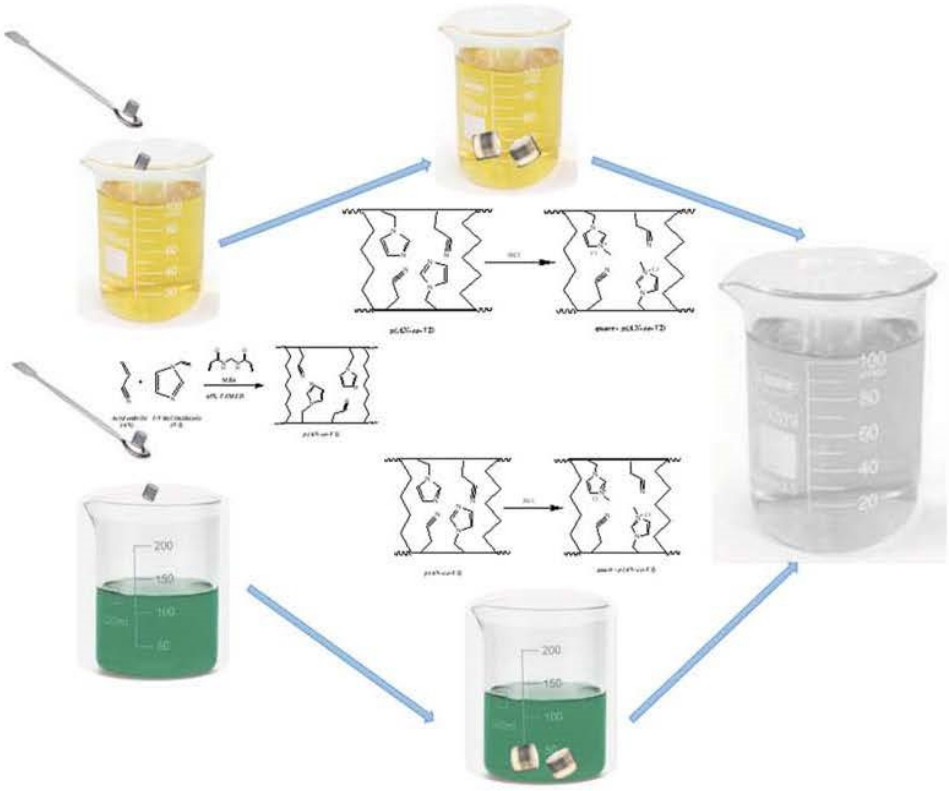

Environmental-Friendly Heavy Metals Treatment with Novel Absorbents

BISHKEK 2021

KYRGYZ TURKISH MANAS UNIVERSITY
MANAS JOURNAL OF ENGINEERING (MJEN)

ISSN: 1694- 7398
Year: 2021
Volume: 9
Issue: 2
http://journals.manas.edu.kg
journals@manas.edu.kg

PUBLICATION PERIOD

Manas Journal of Engineering (MJEN) is published twice year, MJEN is a peer reviewed journal.

CORRESPONDENCE ADDRESS
Kyrgyz Turkish Manas University
Chyngyz Aitmatov Avenue 56 Bishkek, KYRGYZSTAN
URL: http://journals.manas.edu.kg
e-mail: journals@manas.edu.kg
Tel : +996 312 492763- Fax: +996 312 541935

KYRGYZ TURKISH MANAS UNIVERSITY
MANAS JOURNAL OF ENGINEERING (MJEN)

CONTENT

MANAS Journal of Engineering
ISSN 1694-7398 | e-ISSN 1694-7398

Volume 9, Issue 2, (2021) Pages 104-114
https://doi.org/10.51354/mjen.936970

Removal of as(V), Cr(VI) and Cr(III) heavy metal ions from environmental waters using amidoxime and quaternized hydrogels

Duygu Alpaslan*[1,2], Tuba Ersen Dudu[1,2]

[1] Van Yüzüncü Yıl University, Engineering Faculty, Department of Mining Engineering, Campus, Van 65080, Turkey, alpaslanduygu@gmail.com, ORCID: 0000-0002-6007-3397

[2] Van Yüzüncü Yıl University, Institute of Natural and Applied Science, Department of Chemical Engineering,

ABSTRACT

Acrylonitrile (AN) and 1-vinyl imidazole (VI) based hydrogel was prepared in bulk (macro) dimensions via redox polymerization technique. Afterward, this hydrogel was quaternized (positively charged) and exposed to the amidoximation reaction. The prepared hydrogels (quart-p(AN-co-VI), amid-p(AN-co-VI) and p(VI)) characterized using fourier transform infrared spectroscopy (FT-IR) and thermal gravimetric analysis (TGA). Swelling experiments were performed gravimetrically at room temperature in deionized water and different pH solution. Water absorbencies of both amidoximated hydrogels and quaternized hydrogels were founded to be high. Prepared hydrogels were used to remove heavy metal ions such as arsenic(V) (As(V)), Chromium(VI) (Cr(VI)) and Chromium(III) (Cr(III)) from aqueous media. The sorption of As(V), Cr(VI) and Cr(III) metal ions by hydrogels were carried out at different initial metal ion concentrations, different pHs, different times in batch sorption experiments at 25°C. The maximum metal ion sorption capacity by all hydrogels was in the order: As(VI)>Cr(VI)>Cr(III). The maximum sorption capacity for As(VI), Cr(VI) and Cr(III) ions was found to be 598, 303.8 and 4.9 mg g^{-1} for amid-p(AN-co-VI), respectively. As result of, amidoximated hydrogels have more sorption capacity to metal ions than quaternized hydrogels. Three different kinetic models (pseudo first order, pseudo second order and intraparticle diffusion model) were also used to investigate the sorption mechanisms. Furthermore, the Langmuir and Freundlich sorption isotherms were investigated for these metal ions. As a result of, amidoximation and quaternization of AN and VI based hydrogels have been a promising technique to increase the sorption rate and capacity of hydrogels and are thought to provide great advantages in the removal of metal ions from wastewaters. Especially, among the p(AN-co-VI) modification processes, amidoximation reaction was found to give better results than quaternization reaction. Prepared hydrogels were found to be more selective than Cr(III) versus As(V) and Cr(VI).

ARTICLE INFO

Research article

Received: 13.05.2021
Accepted: 21.06.2021

Keywords:
hydrogel,
sorption,
kinetics,
amidoximation,
quaternization

**Corresponding author*

1. Introduction

The hydrogels are polymeric material and they have many properties such as soft, flexible, elastic, wet structure, three-dimensional polymeric networks, indissolubility, permeability, hydrophilic/hydrophobic structure, tunable physical and chemical structure [1-3]. These properties of hydrogels provide ease of use in a lot of fields such as tissue engineering, drug release, environmental and advantageous material design, agriculture, the food industry, biotechnology and cleaning of environmental waters [4-7]. One of the most common applications in which hydrogels are used in these areas is the cleaning of environmental waters. Especially, heavy metal ions are contaminating most of the natural resources and environmental waters. The main origins of these heavy metal ions are cosmetics, fertilizers, paint industries, metal plating, battery manufacturing and chemicals generated from other industrial waste [8,9]. Moreover, many of them are known to be toxic or carcinogenic and are not biodegradable [10]. Therefore, in recent years, for the removal of heavy metals and other hazardous materials have been developed many methods such as chemical precipitation, membrane extraction, coagulation, complexing, solvent extraction, ion change and sorption. These methods are some of the used processes, but each has its own advantages and disadvantages in its applications. Sorption is a remarkable method because of its high

efficiency, ease of handling, energy-saving and availability of different sorbents [11-13].

Many studies in which hydrogels have been used for heavy metal sorption have been widely reported in the literature. The originality of this article is to bring in a new property after the amidoximation and quaternization reactions to the synthesized hydrogel and to increase the sorption capacity of As(V), Cr(VI) and Cr(III) metal ions. For this study, acrylonitrile (AN) and 1-vinyl imidazole (VI) were chosen as monomers. Acrylonitrile-based polymers are widely used in all areas owing to ease of processing, stiffness, abrasion resistance, mechanical properties and chemical resistance [14]. Acrylonitrile is a versatile liquid and has poor hygroscopicity [15]. In addition, the cyano groups in the acrylonitrile structure provide a great advantage for any modification which may alter the chemical and physical properties of the polymer structure [16-17]. The imidazole groups in VI structure have a weak base character and they can be easily protonated in acidic solutions [18-19]. To generate a positive charge, VI structure can be quaternized by the treatment with an aqueous acid solution and exhibit reversible load changes. Therefore, VI based polymers and derivatives have attracted great interest, as they exhibit excellent properties such as easy protonation, ion exchange and complexing behaviors, catalytic, biological and physiological activities and heat resistance [18-20].

In this study, the p(AN-co-VI) hydrogel was synthesized from AN and VI monomers via redox polymerization technique. Afterward, this hydrogel was quaternized (positively charged) (quart-p(AN-co-VI)) and exposed to amidoximation reaction (amid-p(AN-co-VI)). Thus, these hydrogels became an ion exchange material which can be used to remove As(V), Cr(VI) and Cr(III) metal ions from aqueous media. Using Fourier Transform Infrared Spectroscopy (FT-IR) and Thermal Gravimetric Analysis (TGA) methods, the structural characterizations and the thermal stabilities were investigated for p(VI), quart-p(AN-co-VI) and amid-p(AN-co-VI) hydrogels. In the sorption studies, various parameters such as the initial concentration of metals, pH and contact time were investigated. Also, kinetic and isotherm studies were carried out for the sorption of As(V), Cr(VI) and Cr(III) metal ions by the quart-p(AN-co-VI), amid-p(AN-co-VI) and p(VI) hydrogels.

2. Materials and methods

2.1 Materials

1-vinyl imidazole (VI, 99%), acrylonitrile (AN, 99%) and hydrochloric acid (HCl, 37.5%) were purchased from Sigma–Aldrich, N, N'-methylene bisacrylamide (MBA, 99%) was purchased from Sigma, ammoniumpersulfate (APS, 98%) and sodium hydroxide (NaOH) were purchased from Aldrich, N, N, N', N'-tetramethylethylenediamine (TEMED) was purchased from Across, hydroxylamine hydrochloride (NH_2OH•HCl), potassium dichromate ($K_2Cr_2O_7$) and chromium (III) chloride hexahydrate ($CrCl_3.6H_2O$) were purchased from Merck, arsenate heptahydrate ($Na_2HAsO_4.7H_2O$) was purchased from Fluka Analytical. All reagents were of analytical grade or highest purity available and used without further purification. The deionized water (DI water) was obtained from 18.2 MΩ.cm (Millipore Direct-Q3 UV). The pH measurements were carried out with a Sartorius Documenter pH meter. Atomic absorption spectroscopy (AAS, Thermo scientific ice 3000 series) was used to quantify the of As(V), Cr(VI) and Cr(III) metal ions during sorption studies. The instruments were calibrated by using 1000 mg L^{-1} standard As(V), Cr(III) and Cr(VI) solution (Merck) by sequential dilutions.

2.2 Synthesis of p(AN-co-VI) hydrogel

AN and VI monomers were used to synthesis hydrogel via redox polymerization technique as shown in Figure 1a. Briefly, 2 mol% of MBA was dissolved in AN monomer and mixed (at 2500 rpm) thoroughly for one minute. Then to the AN monomer even amount (1:1 mole ratio) of the VI monomer was added to the mixture and mixed well for one minute. After then, 5 µL TEMED was added to the mixture and the initiator solution APS (1 mol% of total monomer) in 100 µL water was added to the reaction mixture. The reaction mixture was mixed carefully for approximately one minute and transferred into plastic straws with 5 mm diameter and allowed to polymerize and crosslink to complete the reaction at room temperature for approximately four hours. Then, the hydrogel was removed from the polymerization medium, cut into 6 mm long cylinders and cleaned by placing in DI water. After the cleaning procedure, the hydrogel was dried in an oven at 40°C to a constant weight and kept in sealed containers for further studies [21, 22].

2.3 Amidoximation reaction and quaternization of p(AN-co-VI) based hydrogel

To generate a positive charge, VI shell was quaternized by treating hydrogel with 0.5 M hydrochloric acid solution as a quaternization agent (Figure 1b). The quaternized p(AN-co-VI) hydrogels were washed with DI water to remove acid residues and these hydrogels were named as quart-p(AN-co-VI) hydrogels. Finally, these hydrogels were dried in an oven at 40°C to a constant weight.

Amidoximation reaction was used to convert hydrophobic nitrile groups into hydrophilic amidoxime groups of the AN structure as illustrated in Figure 1c. The three-fold excess amount of 10 wt% NH_2OH.HCI (based on nitrile groups) neutralized by a 1:1 mol ratio of NaOH was prepared and reacted with the polymeric amid-p(AN-co-VI) hydrogels under constant stirring at 150 rpm for 24 h at room temperature. The amidoximated hydrogels were washed with a copious amount of DI water and were dried in an oven at 40°C to a constant weight.

2.4 Fourier-transform infrared spectroscopy analysis (FTIR)

Functional groups of hydrogels were analyzed by FTIR spectroscopy (Perkin Elmer, model Perkin Elmer Spectrum 100 instrument, USA) in the range of 4000–650 cm^{-1}. The hydrogel beads were ground to obtain powder and then placed on the diamond sample surface of the machine. The number of scans used was at a resolution of 4 cm^{-1}.

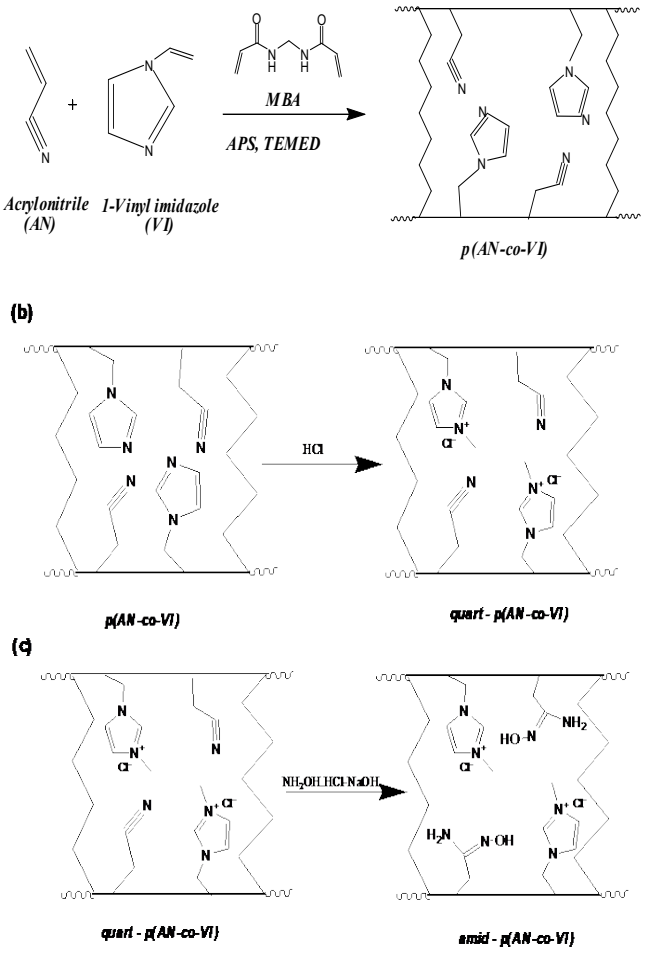

Figure 1. *(a) The chemical structure of the synthesized p(AN-co-VI) hydrogel, (b) schematic presentation of the quaternization reaction mechanism on the p(AN-co-VI) hydrogel and (c) schematic presentation of the amidoximation reaction mechanism on the p(AN-co-VI) hydrogel.*

2.5 Thermal gravimetric analysis (TGA)

To evaluate the thermal stability of the hydrogels, TGA analyses were performed on Thermo Gravimetric Analyzer (SII TG/DTA 6300 model, France) using between 4 and 6 mg of the hydrogel. The analysis was performed at a heating rate of 10 °C min^{-1} under a nitrogen atmosphere and ramped up to 1000 °C. As a result of the analysis, a graph of mass loss versus temperature was obtained.

2.6 Measurement of swelling in distilled water and buffer solutions

Equilibrium swelling experiments were performed in distilled water and buffer solutions at room temperature to examine the swelling ratios of quart-p(AN-co-VI), amid-p(AN-co-VI) and p(VI) hydrogels. Swelling ratios (SR) measurements for hydrogels were performed out in triplicate (%) calculated as;

$$SR\% = \left(\frac{(M_t - M_0)}{M_0}\right) * 100 \quad (1)$$

where M_0 and M_t are the hydrogel mass (g) at beginning and at the time t, respectively. After time t, the hydrogels were removed from the DI water and blotted gently with blotting paper and weighed. All the experiments were carried out in triplicate and the average values were used with their standard deviations [23, 24]. Swelling ratio was also studied as a function of pH between 2 and 12 by adjusting the pH of the solutions with 0.1 M HCl and 0.1 M NaOH. Again, hydrogels were kept for 24 h in acidic and basic solutions to determine the effect of medium pH on the swelling ratios.

2.7 Sorption Studies

All batch sorption experiments of As(V), Cr(VI) and Cr(III) metal ions were accomplished at 25°C for 24 h. To achieve the complete mixing of the media, the mixture was stirred at 250 rpm. In order to improve the performance of sorption conditions, metal ion concentration, media pH and time were optimized. The effect of metal ion concentration on the sorption performance was investigated ranging from 1 to 5000 mg L^{-1} for each metal ion species, at 1 g L^{-1} hydrogel concentration. The influence of pH on the sorption of metal ions was examined over the pH range of 3–9 and the pH was adjusted by using 0.1 M NaOH and 0.1 M HCl solutions. The effect of sorption time on the sorption capacity was investigated until reaching equilibrium at 10 mg L^{-1} metal ion concentration, 0.25 g L^{-1} hydrogel concentration. To determine the equilibrium concentrations of the metal ions, samples were withdrawn from the solution medium at certain time intervals and diluted with distilled water. Metal ion concentration measurements were carried out by Atomic Absorption Spectrophotometer (AAS). The equilibrium (q_e (mg g^{-1})) amounts of sorption metal ions per unit mass of the hydrogels were calculated by the following equation [25, 26];

$$q_e = \frac{(C_o - C_e) * V}{M} \quad (2)$$

Where C_o and C_e are the initial and equilibrium metal ion concentrations (mg L^{-1}) respectively; V is the volume of metal ion solution (L); M is the mass (g) of the hydrogels used.

The sorption percentages of metal ions were calculated by the following equation [25, 26];

$$\text{Sorption\%} = \frac{(C_o - C_e)}{C_o} * 100 \quad (3)$$

Sorption capacities of metal ions have been evaluated from the Langmuir (Eq. 4) and Freundlich (Eq. 5) sorption isotherms by applying below equations [27, 28];

$$\frac{C_e}{q_e} = \left(\frac{C_e}{q_{max}}\right) + \left(\frac{1}{q_{max} * K_L}\right) \quad (4)$$

$$\log q_e = \log K_f + \left(\frac{1}{n}\right) \log C_e \quad (5)$$

Where q_e is the amount of sorbed metal ion at equilibrium (mg g^{-1}), q_{max} is the maximum sorption capacity of metal ions (mg g^{-1}) and K_L is the Langmuir sorption equilibrium constant (L mg^{-1}). The Langmuir constants, q_{max} and K_L, were determined from the slope and intercept of the linear plot of specific sorption's (C_e/q_e) against the equilibrium concentrations (C_e) for As(V), Cr(VI) and Cr(III) metal ions. K_f and n are the physical Freundlich constants and were determined from the slope and intercept of the linear plot of log q_e versus log C_e.

Experimental data generated from As(V), Cr(VI) and Cr(III) sorption tests using the hydrogels were evaluated by pseudo first kinetic, second order kinetic and intraparticle diffusion model to understand the mechanisms and dynamics of the sorption process [29-31]. Equation 6 and 7 represent the change of sorption capacity with time for first and second pseudo kinetics.

$$\frac{dq_t}{dt} = k_{p1}\,(q_e - q_t) \quad (6)$$

Where q_t(mg g^{-1}) is the sorption capacities at time t (min), k_{p1} (min^{-1}) is the pseudo first order rate constant for the kinetic model. Pseudo second order rate kinetic is expressed as;

$$\frac{dq_t}{dt} = k_{p2}(q_e - q_t)^2 \quad (7)$$

k_{p2} (min^{-1}) is the pseudo second order rate constant for the kinetic model.

The intraparticle diffusion model can be presented as [32];

$$q_t = R_{id}\sqrt{t} + C \quad (8)$$

Where C is the intercept and R_{id} *is* the rate constant of intraparticle diffusion (mg g^{-1} $h^{-1/2}$).

3. Results and discussion

3.1 Fourier-transform infrared spectroscopy analysis (FTIR)

FTIR spectra of prepared hydrogels with their characteristic peaks were shown in Figure 2a. p(VI) hydrogel shown peaks at 3105 and 1496 cm^{-1} which assigned to C-H and C-N stretching vibration in vinyl group and crosslinker, respectively, while the peaks at 3122 cm^{-1} correspond to stretching of N-H bond. The peaks observed at approximately 1649 and 1226 cm^{-1} correspond to the vibration bands C=N and C-N, respectively. The characteristic nitrile stretching band ($C \equiv N$) of the pure AN occurs at about 2243 cm^{-1}. However, as shown in Figure 2a, this band was lost after the amidoximation reaction. In addition, in p (AN-co-VI) hydrogel, occurred both positive charges and the new $–NH_2$ and –OH functional groups after quaternization and amidoximation. This formation was evidenced by the increase in the width of the N-H and –OH band observed from 3724 cm^{-1} to 2600 cm^{-1}, as observed in the FT-IR spectrum of quart-p (AN-co-VI) hydrogel. In this spectrum was also clearly shown which the peaks at 1656 cm^{-1}, 1631 cm^{-1}, 1648 cm^{-1} belong to the C=O stretching vibrations for all hydrogels. Furthermore, it was determined that the C-N peak observed at about 1226 cm^{-1} and 1497 cm^{-1} decreased after the quaternization and amidoximation.

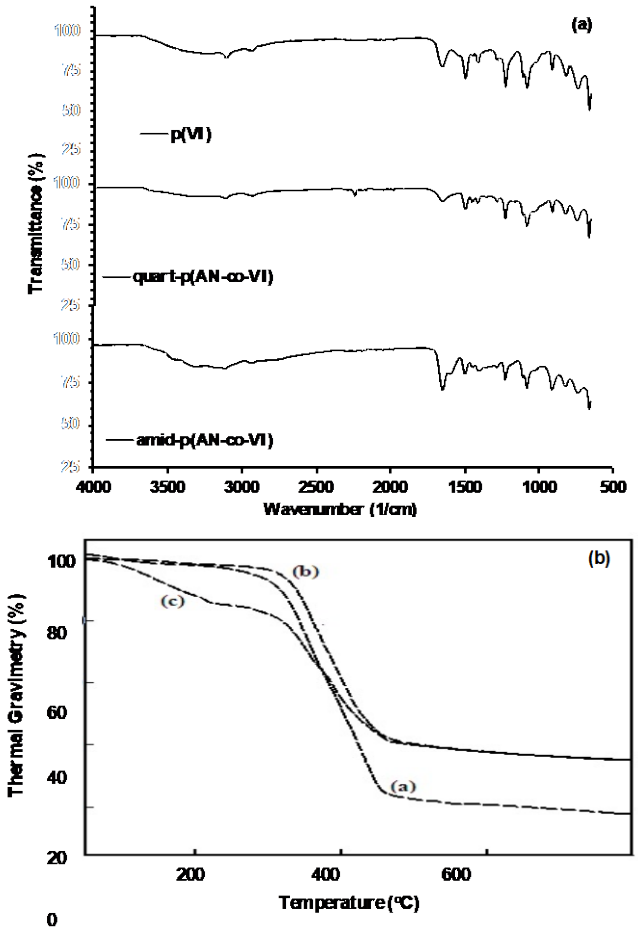

Figure 2. *(a) FT-IR spectra of (a) p(VI), (b) quart-p(AN-co-VI) and (c) amid-p(AN-co-VI) (1:1) hydrogels and (b) the Thermo*

Gravimetric analysis of (a) p(VI), (b) quart-p(AN-co-VI) and (c) amid-p(AN-co-VI) (1:1) hydrogels.

3.2 Thermal gravimetric analysis (TGA)

TGA/DSC analyzer was used to examine the thermal degradation behavior of p(VI), quart-p(AN-co-VI) and amid-p(AN-co-VI) hydrogels and results were presented in Figure 2b. As can be seen, mass loss of p(VI) hydrogel was nearly 78% when heated up to 542°C under argon atmosphere. And at the same time quart-p(AN-co-VI) and amid-p(AN-co-VI) hydrogels showed similar degradation temperatures with 62% and 58% mass loss, respectively. Hence, it can be said that quaternization and amidoximation reactions contributed almost 38-42% weight more degradation to the p(AN-co-VI) based hydrogel. Another prominent feature was that amid-p(AN-co-VI) hydrogel had three degradation step: the first stage was at 200°C with 11% mass loss, the second stage was in the temperature range of 200-282°C with 5% mass loss and the third step was in the temperature range of 282-525°C with 42% mass loss. The p(VI) and quart-p(AN-co-VI) hydrogels had the same thermal behavior and had two different degradation steps. The first step for p(VI) was starting at about 50 to almost 258°C with a 5% mass loss, and the other was between 258 and 542°C with 73% mass loss. The first mass loss for quart-p(AN-co-VI) was 8% in the temperature range of 50-302°C. The second step was observed in the range of 302-550°C and mass loss reached 54%. According to the data obtained, it was determined that p(AN-co-VI) hydrogel has a good resistance against increasing temperature.

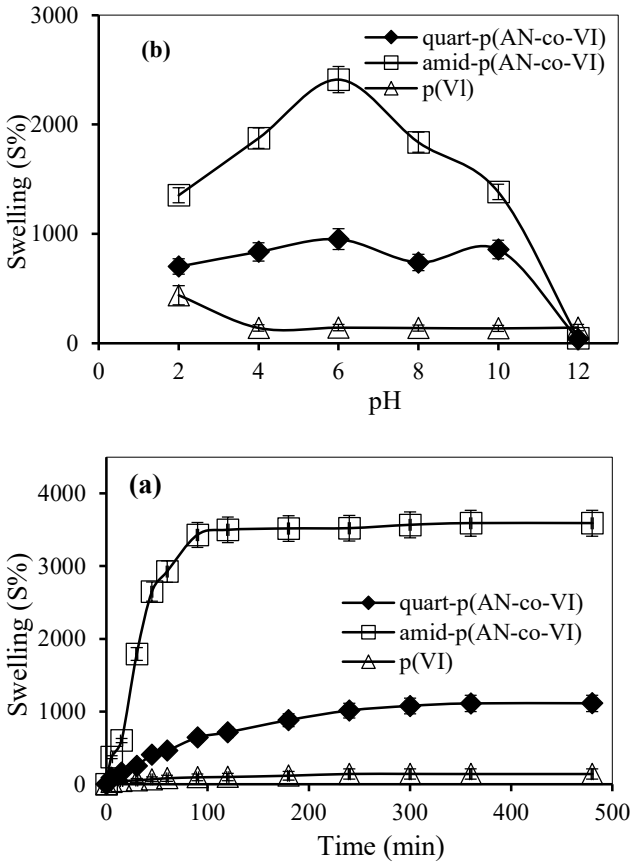

Figure 3. *(a) Percent swelling degree of the p(VI), quart-p(AN-co-VI) and amid-p(AN-co-VI) hydrogels with time in DI water and (b) Percent swelling degree of the p(VI), quart-p(AN-co-VI) and amid-p(AN-co-VI) hydrogels as a function of pH (pH is adjusted by the addition of 0.1 M HCl, 0.1 M NaOH).*

3.3 Measurement of swelling in distilled water and buffer solutions

The equilibrium swelling ratios (SR) of hydrogels (p(VI), quart-p(AN-co-VI) and amid-p(AN-co-VI)) were indicated in Figure 3a. The swelling rates of the hydrogels in DI water increased with increasing time and then slowed down. Figure 3a showed that the value of S% of p(VI) was 141%. On the contrary of p(VI) hydrogel, the values S% of quart-p(AN-co-VI) and amid-p(AN-co-VI) hydrogels were 1113% and 3590%, respectively. Results demonstrated that of S% values of p(AN-co-VI) based hydrogels were increased after quaternization and amidoximation reactions. Since VI is both a hydrophilic monomer and nitrogen in the imidazole structure can produce positive charges after quaternization reaction and it may cause an increase in swelling of the hydrogel. Even if AN is a hydrophobic monomer, the hydrophobic nitrile groups in the AN structure can be converted to hydrophilic amidoxime groups after the amidoximation reaction and thus the degree of swelling of the hydrogel can be increased [33]. Therefore, in this study, we aimed to increase the equilibrium swelling capacities of

hydrogels by quaternization and amidoximation reactions and to use them in heavy metal sorption.

Figure 3b indicated the pH-dependent changes in the equilibrium swelling ratio for p(VI), quart-p(AN-co-VI) and amid-p(AN-co-VI) hydrogels at room temperature in buffer solution from 2 to 12. Maximum swelling values for p(VI), quart-p(AN-co-VI) and amid-p(AN-co-VI) were obtained as 439% at pH 2, 950% at pH 6 and 2411% at pH 6, respectively. After quaternization and amidoximation reactions, the breakdown of hydrogen bonds at different pHs and the electrostatic repulsion between the polymer networks increases and then more water intake to the hydrogels is achieved [34].

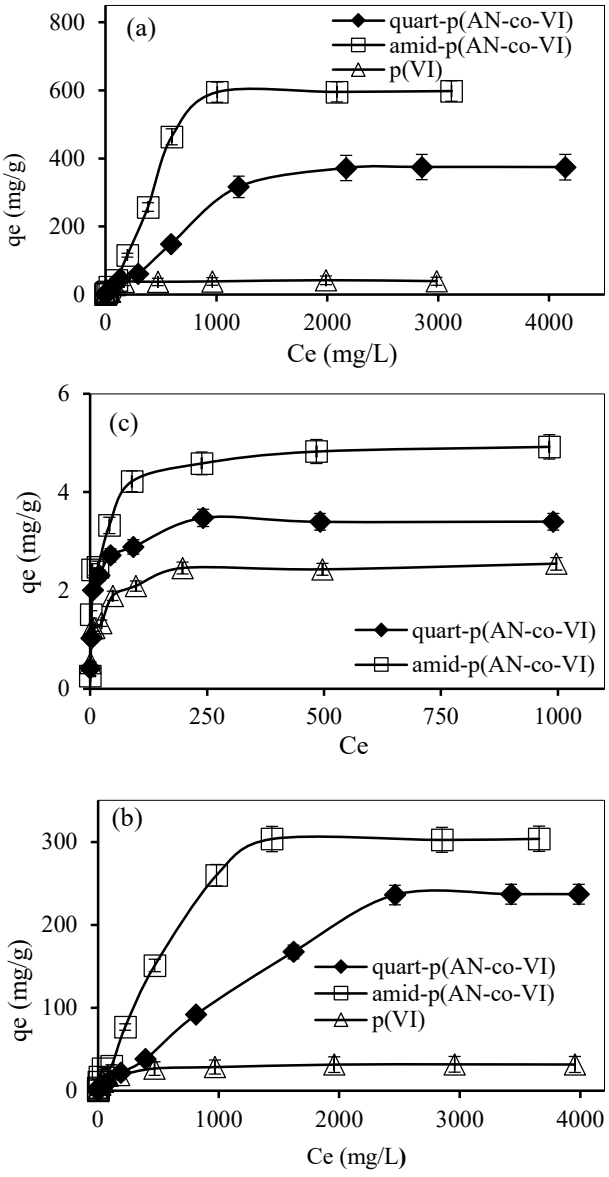

Figure 4. *The q_e vs C_e graphs of p(VI), quart-p(AN-co-VI) and amid-p(AN-co-VI) hydrogels* ***(a)*** *at different As(V) concentrations, (b) at different Cr(VI) concentrations and (c) at different Cr(III) concentrations, respectively [Heavy metal concentration: 1-5000 mg L^{-1} (50 mL), sorbent dosage: 1 g L^{-1}, time: 24 h].*

3.4 Equilibrium sorption studies

Single, quaternized and amidoximated hydrogels were used for the removal of some heavy metal ions such as As(V), Cr(III) and Cr(VI). The heavy metal ion concentrations were varied from 1 mg L^{-1} to 5000 mg L^{-1} while media temperature (°C), pH, contact time (hours) and hydrogel dosage (g L^{-1}) were set as 25, 6, 24 and 1, respectively. As shown in Figure 4(a-c), the sorption capacities to three heavy metal ions of three hydrogels gradually increased with the rise of initial concentration and then reached to maximum equilibrium sorption capacity. It was shown that the order of metal ions up taken by hydrogels was As(V)>Cr(VI)>Cr(III), while the removal capacity of the hydrogels followed the order amid-p(AN-co-VI)>quart-p(AN-co-VI)>p(VI). It were clearly seen that As(V) and Cr(VI) was considerably removed by quaternized and amidoximated hydrogels and but these hydrogels cannot removal Cr(III) ions. This data proved that positive charges in the imidazole structure were formed by the quaternization reaction and then the hydrophobic nitrile groups in the copolymer structure by the amidoximation reaction turned into hydrophilic amidoxime groups [17, 18, 33]. In addition, after the quaternization and amidoximation reactions, it was seen that the diffusion and electrostatic attraction forces increased between the functional groups and the metal ions.

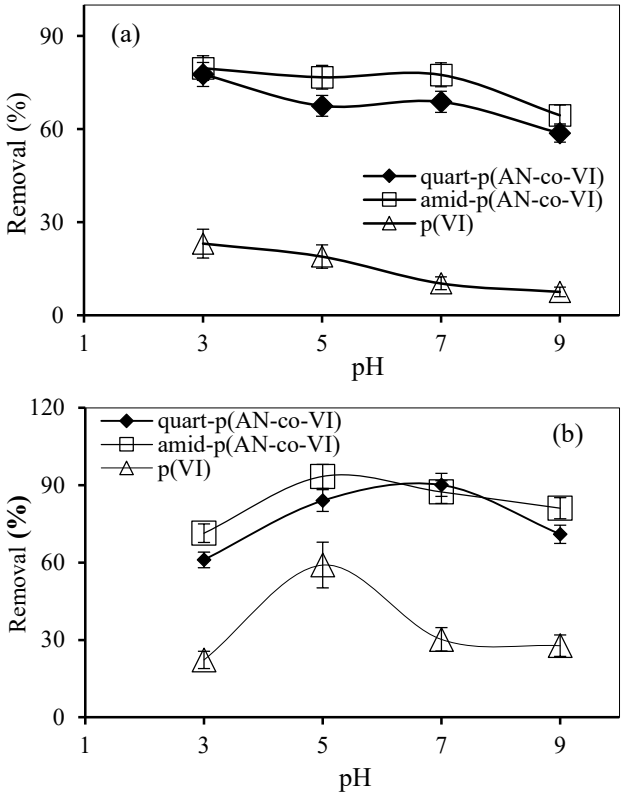

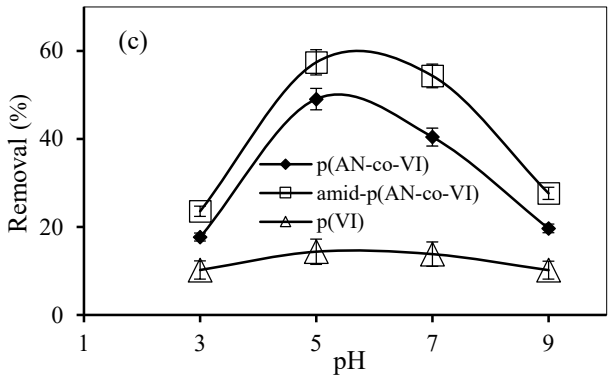

Figure 5. *Sorption of* ***(a)*** *As(V),* ***(b)*** *Cr(VI) and* ***(c)*** *Cr(III) into p(VI), quart-p(AN-co-VI) and amid-p(AN-co-VI) hydrogels as a function of solution pH [Heavy metal concentration: 10 mg L^{-1} (50 mL), sorbent dosage: 1 g L^{-1}, time: 24 h].*

The sorption amounts of p(VI), quart-p(AN-co-VI) and amid-p(AN-co-VI) hydrogels towards As(V), Cr(VI) and Cr(III) ions were measured at pHs ranging from 3 to 9 with the initial metal concentration of 10 mg L^{-1} for 24 h at room temperature and were shown in Figure 5. As illustrated in Figure 5(a-c), the highest sorption capability were observed for the amid-p(AN-co-VI) hydrogels and were determined to be 79.7% at pH 3 for As(V), 93.4% at pH 5 for Cr(VI) and 57.4% at pH 5 for Cr(III). This case may originate from that As(V) (AsO_4^{3-}, $HAsO_4^{2-}$, $H_2AsO_4^-$ and H_3AsO_4), Cr(VI) ($Cr_2O_7^{2-}$, $HCrO_4^-$, CrO_4^{2-}) and Cr(III) (Cr^{3+}, $Cr(OH)^{2+}$, $Cr(OH)_2^+$) ions have different oxidation steps at different pHs [35-37]. The results showed the sorption of As(V) and Cr(VI) species by synthesized hydrogels was dominant.

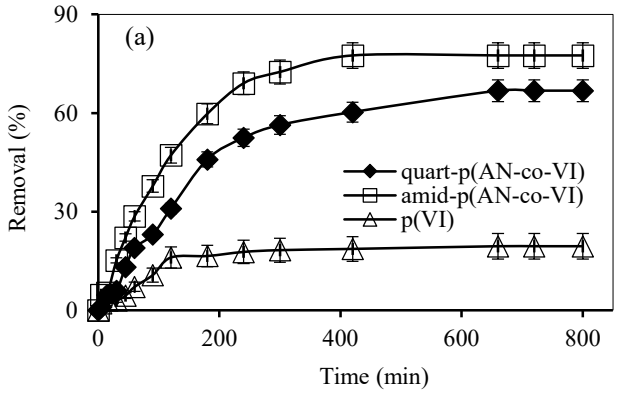

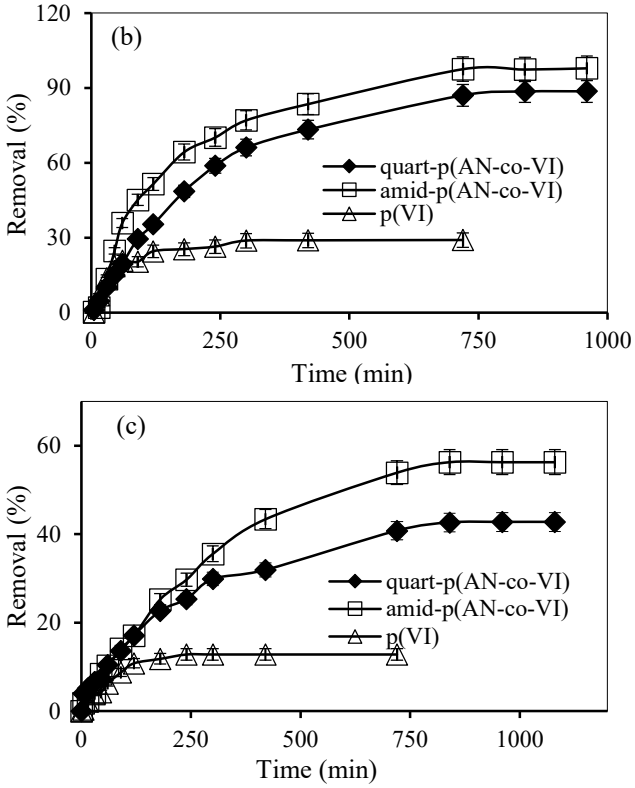

Figure 6. *The effect of contact time on (a) As(V) sorption, (b) Cr(VI) sorption and (c) Cr(III) sorption by p(VI), quart-p(AN-co-VI) and amid-p(AN-co-VI) hydrogels [Heavy metal concentration: 10 mg L^{-1} (50 mL), sorbent dosage: 0.25 g L^{-1}].*

Using 10 mg L^{-1} of the metal ion solutions and 1 g L^{-1} sorbent dosage, Figure 6(a-c) was shown typical results of As (V), Cr (VI) and Cr (III) sorption amounts against sorption times. For all three metal ions, it was observed that sorption equilibria were reached very quickly and lasted between 3 and 5 hours. The initial fast sorption may be due to the reaction between the metal pores with the macroscopic pore and the hydrogel outer sites. Subsequent deceleration may be due to the micropores of the crosslinked hydrogel. As shown in Figure 6(a-c), the uptake percentage of As(V), Cr(VI) and Cr(III) ions by amidoximated hydrogels was 77% in 420 min, 98% in Cr(VI) and 56% in 840 min, respectively.

3.5 Sorption isotherm studies

Langmuir and Freundlich sorption isotherms were used to evaluate the sorption behavior and were the isotherm parameters were summarized in Table 1. Based on the correlation coefficient, the sorption behavior of hydrogels was shown that was generally better fitted to the Freundlich isotherm. The Freundlich isotherm model describes the surface energies in different types of sorption sites and the Langmuir isotherm model describes monolayer sorption at the sorption site. According to experimental data, sorption of As(V), Cr(VI) and Cr(III) heavy metals were more related to multilayer sorption than monolayer sorption. Even though the

sorption capacity of the As(V) and Cr(VI) ions of amid-p(AN-co-VI) hydrogel were enhanced by modifying of p(AN-co-VI) hydrogel, there was not a significant increase in the sorption capacity of Cr(III) ion. The maximum amount of As(V), Cr(VI) and Cr(III) metal ions sorbed by amid-p(AN-co-VI) hydrogel were founded to be 833.3, 344.8 and 4.82 mg g^{-1}, respectively. The values of the Freundlich calculated sorption intensity, n>1, indicated that was favorable of sorption of all the metal ions by p(VI), quart-p(AN-co-VI) and amid-p(AN-co-VI) hydrogels [27, 28].

3.6 Sorption reaction models

To determine the reaction kinetics of the sorption, we investigated three different reaction models such as first order, pseudo second order and intraparticle diffusion using equations numbered 6, 7, 8. In Table 2 was shown that the correlation coefficients of the pseudo second order kinetic model obtained for p(VI) hydrogel were above 0.97 and that the sorption of three metal ions was generally followed the pseudo second order. In addition, the q_e values calculated from the pseudo second order were determined to be in agreement with the experimental q_e values. Table 2 and Table 3 showed that the sorption of quart-p(AN-co-VI) and amid-p(AN-co-VI) hydrogels generally followed first order kinetics and the calculated q_e values were in agreement with the experimental q_e values. It was concluded that intraparticle diffusion was the rate-limiting step and it was observed that the intra-particle diffusion model was effective on the sorption of heavy metal ions by synthesized hydrogels. Firstly, it can be assumed that the diffusion took place in the film and boundary layer around the hydrogel and then there was intraparticle diffusion into the macro and micropores of the hydrogels.

Table 1. *Langmuir and Freundlich isotherm data for sorption of As(V), Cr(VI) and Cr(III) by p(VI), quart-p(AN-co-VI) and amid-p(AN-co-VI) hydrogels*

Sorbents	Ions	Langmuir isotherm constants			Freundlich isotherm constants		
		K_L (L mg^{-1})	q_m (mg g^{-1})	R^2	K_f	n	R^2
p(VI)	As(V)	$2.15x10^{-2}$	40	0.9958	2.13	2.26	0.8310
quart-p(AN-co-VI)		$1.23x10^{-3}$	400	0.9046	1.39	1.43	0.9824
amid-p(AN-co-VI)		$1.02x10^{-3}$	833.3	0.7704	1.67	1.28	0.9733
p(VI)	Cr(VI)	$2.76x10^{-3}$	25.3	0.5831	1.52	2.33	0.9020
quart-p(AN-co-VI)		$7.34x10^{-4}$	312.5	0.5476	5.82	2.05	0.9299
amid-p(AN-co-VI)		$2.73x10^{-3}$	344.8	0.8654	2.54	2.02	0.9187
p(VI)	Cr(III)	$1.14x10^{-2}$	2.57	0.9796	0.82	5.95	0.8651
quart-p(AN-co-VI)		$1.21x10^{-2}$	2.33	0.8798	1.38	7.36	0.7535
amid-p(AN-co-VI)		$5.29x10^{-3}$	4.82	0.8780	1.16	4.42	0.8916

Table 2. *Kinetic constants for sorption of As(V), Cr(VI), and Cr (III) by p (VI), quart-p(AN-co-VI) and amid-p(AN-co-VI) hydrogels*

Sorbents	Ions	Pseudo first order		Pseudo second order		Intraparticle diffusion	
		K_{p1} (min^{-1})	R^2	K_{p2} (g mg^{-1} min^{-1})	R^2	R_{id} (mg g^{-1} $min^{-1/2}$)	R^2
p(VI)	As(V)	$1.08x10^{-2}$	0.9494	$1.62x10^{-3}$	0.9741	0.1912	0.7361
quart-p(AN-co-VI)		$5.99x10^{-3}$	0.9888	$3.71x10^{-4}$	0.9054	0.2781	0.9215
amid-p(AN-co-VI)		$9.44x10^{-3}$	0.9935	$7.8x10^{-4}$	0.9749	0.3550	0.8570
p(VI)	Cr(VI)	$1.27x10^{-2}$	0.9443	$2.64x10^{-2}$	0.9991	0.0616	0.7733
quart-p(AN-co-VI)		$5.3x10^{-3}$	0.9805	$3.23x10^{-4}$	0.8901	0.3085	0.9545
amid-p(AN-co-VI)		$6.7x10^{-3}$	0.9590	$3.31x10^{-4}$	0.6946	0.2213	0.9067
p(VI)	Cr(III)	$1.47x10^{-2}$	0.9842	$1.04x10^{-2}$	0.9820	0.0334	0.9108
quart-p(AN-co-VI)		$5.8x10^{-3}$	0.8966	$1.01x10^{-3}$	0.9792	0.1381	0.9726
amid-p(AN-co-VI)		$4.1x10^{-3}$	0.9797	$3.38x10^{-4}$	0.9608	0.2026	0.9888

Table 3. *The sorption capacity of sorption of As(V), Cr(VI), and Cr(III) by the p(VI), quart-p(AN-co-VI) and amid-p(AN-co-VI) hydrogels.*

Sorbents	Ions		Pseudo first order	Pseudo second order
		$q_{e,exp}$ (mg g^{-1})	$q_{e,cal}$ (mg g^{-1})	$q_{e,cal}$ (mg g^{-1})
p(VI)	As(V)	5.12	5.34	5.95
quart-p(AN-co-VI)		5.83	5.98	8.64
amid-p(AN-co-VI)		8.07	8.61	9.77
p(VI)	Cr(VI)	3.68	2.3	1.79
quart-p(AN-co-VI)		7.83	8.59	10.6
amid-p(AN-co-VI)		6.94	7.77	9.77
p(VI)	Cr(III)	1.17	1.28	1.3
quart-p(AN-co-VI)		3.95	4.68	4.75
amid-p(AN-co-VI)		4.98	5.44	7.19

4. Conclusions

This article, it was aimed to remove heavy metal wastes such as As(V), Cr(VI) and Cr(III) which pollute the ecosystem and damage the living species. To remove these metal ions, p(VI-co-AN) based hydrogels were synthesized and their sorption properties were investigated. To change the synthesized p (VI-co-AN) hydrogel surface, it was subjected to quaternization (positively charged) and amidoximation reactions and it has been found that the hydrogel's both swelling and sorption capacity enhanced with modification. According to swelling data, the values S% of p(VI), quart-p(AN-co-VI) and amid-p(AN-co-VI) hydrogels were 141%, 1113% and 3590%, respectively. Results indicated that S% values of p(AN-co-VI) based hydrogels were raised after quaternization and amidoximation reactions. The removal of As(V), Cr(VI) and Cr(III) metal ions from aqueous solution by quart-p(AN-co-VI) and amid-p(AN-co-VI) hydrogels was found to be effective. However, the removal of As(V) and Cr(VI) by quart-p(AN-co-VI) and amid-p(AN-co-VI) hydrogels was determined to be greater than the Cr(III) removal. The maximum amount of As(V), Cr(VI) and Cr(III) sorption onto the amid-p(VI-AN) were calculated to be 598, 303.8 and 4.9 mg g^{-1}, respectively. When the isotherm models were examined, the sorption behavior of hydrogels was shown that was generally better fitted to the Freundlich isotherm. The reaction kinetics of the sorption were determined using first order, pseudo second order and intraparticle diffusion models. In addition, q_e values calculated with experimental q_e values were found to be compatible. Based on these results, we believe that p(VI-co-AN) based hydrogels can be used as an effective sorbent for the removal of heavy metal residues that threaten the ecosystem and the living.

Funding

This work is supported by the Van Yuzuncu Yıl University BAP with grant # FBA-2018-7084.

References

[1]. Üzüm Ö.B., Kundakci S., Karadağ E., "Uranyl Ion Uptake from Aqueous Solutions by Chemically Cross-linked Polyelectrolyte CAMA Hydrogels", Polymer-Plastics Technology and Engineering, 46, (2007), 775–780.

[2]. Kara A., Uzun L., Beşirli N., Denizli A., "Poly(ethylene glycol dimethacrylate-n-vinyl imidazole) beads for heavy metal removal", Journal of Hazardous Materials, 106, (2004), 93–99

[3]. El-Hag Ali A., Shawky H.A., Abd El Rehim H.A., Hegazy E.A., "Synthesis and characterization of PVP/AAc copolymer hydrogel and its applications in the removal of heavy metals from aqueous solution", European Polymer Journal, 39, (2003), 2337–2344.

[4]. Crini G., "Recent developments in polysaccharide-based materials used as adsorbents in wastewater treatment", Prog. Polym. Sci., 30, (2005), 38–70

[5]. Sahiner N., Ozay O., Aktas N., Blake D.A., John V.T., "Arsenic (V) removal with modifiable bulk and nano p(4-vinylpyridine)-based hydrogels: The effect of hydrogel sizes and quarternization agents", Desalination, 279, (2011), 344–352

[6]. Liu Y., Cao X., Hua R., Wang Y., Liu Y., Pang C., Wang Y., "Selective adsorption of uranyl ion on-

imprinted chitosan/PVA cross-linked hydrogel", Hydrometallurgy, 104, (2010), 150–155.

[7]. Chai Q., Jiao Y., Yu X., Hydrogels for Biomedical Applications: Their Characteristics and the Mechanisms behind Them, Gels, 3, (2017), 6-10.

[8]. Bansod B.K., Kumar T., Thakur R., Rana S., Singh I., A review on various electrochemical techniques for heavy metal ions detection with different sensing platforms, Biosensors and Bioelectronics, 94, (2017), 443-455.

[9]. Pakdel P.M., Peighambardoust S.J., "Review on recent progress in chitosan-based hydrogels for wastewater treatment application", Carbohydrate Polymers, 201, (2018), 264-279.

[10]. Rıfi E.H., Rastegar F., Brunette J.P.," Uptake of cesium, strontium and europium by a poly(sodium acrylate-acrylic acid) hydrogel", Talanta , 42(6), (1995), 811–816.

[11]. Manju G.N., Krishnan K.A., Vinod V.B., Anirudhan T.S., An investigation into the sorption of heavy metal from wastewaters by polyacrylamide-grafted iron(III) oxide, Journal of Hazardous Materials, 91, (2002), 221–238.

[12]. Charerntanyarak L., "Heavy metals removal by chemical coagulation and precipitation", Water Sci Technol, 39, (1999), 135–138.

[13]. Chen Q., Zhu L., Zhao C., Zheng J., "Hydrogels for Removal of Heavy Metals from Aqueous Solution", Environmental Analytical Toxicology, 2, (2012), 2161-0525

[14]. Liu X., Chen H., Wang C., Qu R., Ji C., Sun C., Zhang Y., "Synthesis of porous acrylonitrile/methyl acrylate copolymer beads by suspended emulsion polymerization and their adsorption properties after amidoximation", Journal of Hazardous Materials, 175, (2010), 1014–1021.

[15]. Nie F.Q., Xu Z.K., Ye P., Wu J., Seta P., "Acrylonitrile-based copolymer membranes containing reactive groups: effects of surface-immobilized poly(ethylene glycol)s on anti-fouling properties and blood compatibility", Polymer, 45, (2004), 399–407.

[16]. Liu X., Chen H., Wang C., Qu R., Ji C., Sun C., Zhang Y., "Synthesis of porous acrylonitrile/methyl acrylate copolymer beads by suspended emulsion polymerization and their adsorption properties after amidoximation", Journal of Hazardous Materials, 175, (2010), 1014–1021.

[17]. Das S., Pandey A.K., Athawale A.A., Manchanda V.K., "Exchanges of uranium(VI) species in amidoxime-functionalized sorbents", J. Phys. Chem. B., 113, (2009), 6328–6335.

[18]. Genc F., Uzun C., Guven O., "Quaternized poly(1-vinylimidazole) hydrogel for anion adsorption", Polym Bull, 73, (2016), 179-190.

[19]. Erdem B., "Synthesis and Characterization Studies of a Series of N-Vinyl Imidazole-Based Hydrogel", Anadolu University Journal of Science and Technology A- Applied Sciences and Engineering, 17(5), (2016), 974 – 983.

[20]. Erdem M., Dikişler Ö., Erdem B., "Removal of Orange II from Aqueous Solutions Using N-Vinyl Imidazole-based Hydrogels as Adsorbents", Chemical Engineering Communications, 203,(2016), 1403–1412.

[21]. Ersen Dudu T., Sahiner M., Alpaslan D., Demirci S., Aktas N., "Removal of As (V), Cr (III) and Cr (VI) from aqueous environments by poly (acrylonitril-co-acrylamidopropyl-trimethyl ammonium chloride)-based hydrogels", Journal of Environmental Management, 161, (2015), 243-251

[22]. Ersen Dudu T., Alpaslan D., Uzun Y., Aktas N., "Utilization of hydrogel-fungus composites as absorbents for removal of textile dyes from aqueous media", Int. J. Environ. Res., 11, (2017), 557-568.

[23]. Chang C., Zhang L., Zhou J., Zhang L., Kennedy J.F., "Structure and properties of hydrogels prepared from cellulose in NaOH/urea aqueous solutions", Carbohydrate Polymers, 82(1), (2010), 122–127.

[24]. Tang H., Chen H., Duan B., Lu A., Zhang L., "Swelling behaviors of superabsorbent chitin/ carboxymethylcellulose hydrogels," Journal of Materials Science, 49(5), (2014), 2235–2242.

[25]. Cardenas G., Orlando P., Edelio T.," Synthesis and applications of chitosan mercaptanes as heavy metal retention agent", International Journal of Biological Macromolecules 28, (2001), 167–174

[26]. Wu N., Li Z., "Synthesis and characterization of poly(HEA/MALA) hydrogel and its application in

removal of heavy metal ions from water", Chemical Engineering Journal, 215, (2013), 894–902.

[27]. Langmuir I., "The adsorption of gases on plane surfaces of glass, mica and platinum", Journal of the American Chemical Society, 40(9), (1918), 1361-1403.

[28]. Freundlich H.M.F., "Uber die adsorption in losungen", Zeitschrift für Physikalische Chemie, 57, (1906), 385–470.

[29]. Lagergren S., "Zur theorie der sogenannten adsorption geloester stoffe", Kungliga Svenska Vetenskapsa, Handlingar, 24, (1898), 1–39.

[30]. Blanchard G., Maunaye M., Martin G., "Removal of heavy metals from waters by means of natural zeolites", Water Research, 18, (1984), 1501–1507

[31]. Toor M., Jin B., "Adsorption characteristics, isotherm, kinetics, and diffusion of modified natural bentonite for removing diazo dye", Chemical Engineering Journal, 187, (2012), 79–88

[32]. Weber W.J., Morris J.C., "Kinetics of adsorption on carbon from solutions", J. Sanit. Eng. Div. Am. Soc. Civ. Eng., 89, (1963), 31–60.

[33]. Alpaslan D., Aktas N., Yilmaz S., Sahiner N., Guven O., "The Preparation of p(acrylonitrile-co-acrylamide) hydrogels for uranyl ion recovery from aqueous environments", Hacettepe J. Biol. Chem., 42(1), (2014), 89–97.

[34]. Gupta N.V., Shivakumar H.G., "Investigation of Swelling Behavior and Mechanical Properties of a pH-Sensitive Superporous Hydrogel Composite", Iranian Journal of Pharmaceutical Research, 11(2), (2012), 481-493.

[35]. Makris K.C.S.D., Datta R., "Evaluating a drinking-water waste by-product as a novel sorbent for arsenic", Chemosphere, 64 (5), (2016), 730-741

[36]. Kim Y.S., Kim D.H., Yang J.S., Baek K., "Adsorption Characteristics of As(III) and As(V) on Alum Sludge from Water Purification Facilities", Separation Science and Technology, 47, (2012), 2211–2217.

[37]. Deng S., Bai R., "Removal of trivalent and hexavalent chromium with aminated polyacrylonitrile fibers: performance and mechanisms", Water Research, 38, (2004), 2423-2431.

MANAS Journal of Engineering
ISSN 1694-7398 | e-ISSN 1694-7398

Volume 9, Issue 2, (2021) Pages 115-121
https://doi.org/10.51354/mjen.934839

Study of the activity of a novel green catalyst used in the production of hydrogen from methanolysis of sodium borohydride

Tülin Avcı Hansu

Siirt University, Department of Chemical Engineering, Siirt, Turkey, tulin.hansu@siirt.edu.tr, ORCID: 0000-0001-5441-4696

ABSTRACT

Biomass is an important energy source because it is easily accessible, contributes to the protection of the environment, and can be easily used in industry. Biomass resources can be classified as plants, vegetable and animal wastes, urban and industrial wastes. Highly active catalysts can be prepared by physical and chemical activation methods. Here, *Microcystis aeruginosa* was used as a biomass source and a metal-free catalyst was synthesized. The production conditions were determined by burning the microsistis modified with 3M H_3PO_4 at different temperatures (100, 200, 300 and 400 ^oC) and at different times (30, 45, 60 and 90 minutes). Parameters such as NaBH4 amount, catalyst amount and temperature of the synthesized MA-H_3PO_4 catalyst that affect methanolization were investigated. In the kinetic calculations, the reaction order was found as n 0.18, activation energy 19.014 kj / mol and initial rate 4998.7 ml $H_2 min^{-1} g_{cat}^{-1}$. The reusability of the MA-H_3PO_4 catalyst was tested 5 times and its stability determined.

ARTICLE INFO

Research article

Received: 8.05.2021
Accepted: 16.10.2021

Keywords:
metal-free catalyst,
microcystis aeruginosa,
methanolysis,
$NaBH_4$

**Corresponding author*

1 Introduction

The need for energy used in every field in the world is increasing day by day. The limited reserves of fossil fuels used to meet energy needs in the world have increased the tendency towards alternative energy sources [1]. In addition, fossil fuels are not economically, ecologically and environmentally sustainable. This is an additional disadvantage of these fuels being limited [2]. Carbon dioxide (CO_2) and carbon monoxide (CO) emissions from the use of fossil fuels are among the main causes of global warming. Carbon dioxide emitted from many combustion sources, especially fossil fuels, provides a significant increase in greenhouse gas emissions [3,5]. In order to reduce these negative effects, it is important to find a sustainable, renewable and environmentally friendly energy source. [2]. Hydrogen, one of the alternative clean energy sources, has attracted the attention of researchers for the last decade [6]. The importance of reliability and lightness in the storage of hydrogen is highlighted by the storage of hydrogen in the hydride structure. In addition to being stable and safe $NaBH_4$, in the long term it can be used easily in the dry and moisture free short term in aqueous form, making it ahead of other hydride compounds. The sodium boron hydride compound among the hydrides is used in studies because it contains more unit volume of hydrogen atoms than the others. Sodium borohydride, which contains 10,60% hydrogen in its structure, is a good hydrogen storage [7]. There are many studies in the literature to produce hydrogen from sodium borohydride [8, 12]. In addition, fuel cell issues have also been studied in the literature, apart from hydrogen production from sodium boron hydride [13, 18]

By methanolysis of $NaBH_4$ at room temperature, only a small percentage of the amount of H_2 expected to be obtained in theory can be obtained. However, the rate of methanolysis is increased by using a catalyst. For this reason, the reactions must be carried out in the presence of catalyst in order to quickly obtain all of the hydrogen in sodium borohydride. A catalyst must be developed for selective and efficient methanolysis. Catalyst development and utilization in the methanolysis of $NaBH_4$ is necessary to overcome the heat transfer limitations for this powerful endothermic hydrolysis reaction [4, 5, 20]. Researchers have drawn attention to the synthesis of cheaper catalysts by applying different methods such as the combination of support materials and 2–3 non-noble metals in hydrogen production [23, 26].

Half of the hydrogen gas produced according to the reaction given in Equation (1) is obtained from sodium borohydride and the other half from methanol. Methanolysis reaction is preferred in the production of hydrogen from sodium

borohydride. Because methanolysis occurs faster than hydrolysis reaction [20,21].

$$NaBH_4 + 4CH_3OH \rightarrow NaB(OCH_3)_4 + 4H_2 \quad (1)$$

In this study, it was aimed to investigate the methanolysis performance of sodium borohydride in the presence of a sustainable and environmentally friendly metal-free catalyst. In addition, this study proposes that the use of organic materials that are abundant in nature, such as *Microcystis aeruginosa*, can be used directly as catalyst materials without the addition of any precious metals (Pt and Ru) and support materials to produce a highly efficient catalyst. Microalgae are preferred because of their simple development, use of CO_2 gas released into the atmosphere as a nutrient and have a faster growth rate than plants [22]. *Microcystis aeruginosa* strain was used as microalgae in this paper.

2. Meterial and methods

The *Microcystis aeruginosa* was collected as described in the literature and dried for experiments [20]. Catalyst synthesis from the *Microcystis aeruginosa* was carried out in two steps. In the first step, the *Microcystis* strain was treated with 3M H_3PO_4 acid. Chemical activation was achieved by keeping the sample treated with acid for 1 day at 80 ºC. Then, the sample was washed with distilled water and dried, and the second activation process was performed. The second stage activation process was carried out using the carbonization method. The sample treated with acid was burned in an ash furnace at different temperatures (100, 200, 300 and 400 ºC) and at different times (30, 45, 60 and 90 min) and carbonization process was carried out. The resulting catalyst was named MA-H_3PO_4.The hydrogen gas released during the methanolysis reaction was read from a measure by setting a water trap. The volume of hydrogen released over time was recorded. The production scheme of the catalyst and the setup used in the experiment are given in Figure 1 (a, b). After determining the optimum combustion time and temperature, parameters affecting methanolysis were investigated.

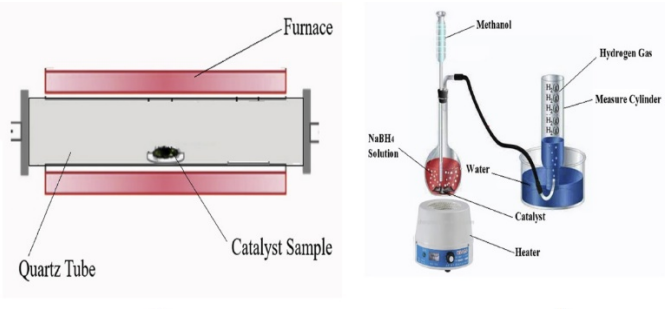

Figure 1. *a) Furnace system scheme for catalyst preparation, b)hydrogen gas measurement scheme [4,14]*

3. Results

3.4. Burning Temperature Effect

In order to examine the effect of burning temperature on methanolysis reaction, methanolysis reaction was carried out by adding 100 mg MA-H_3PO_4 catalyst, which was burned at different temperatures for 45 minutes, to the solution medium consisting of 2.5% $NaBH_4$ and 10 ml of methanol at 30 ºC. The time-dependent hydrogen production graph of the burning temperature is given in Figure 2. As seen in the figure, while the combustion temperature was increased from 100 ºC to 400 ºC, the burning time was set as 45 minutes. The modified MA-H_3PO_4 catalyst, which was burned at 300 ° C for 45 minutes, completed the methanolysis reaction in the shortest time.

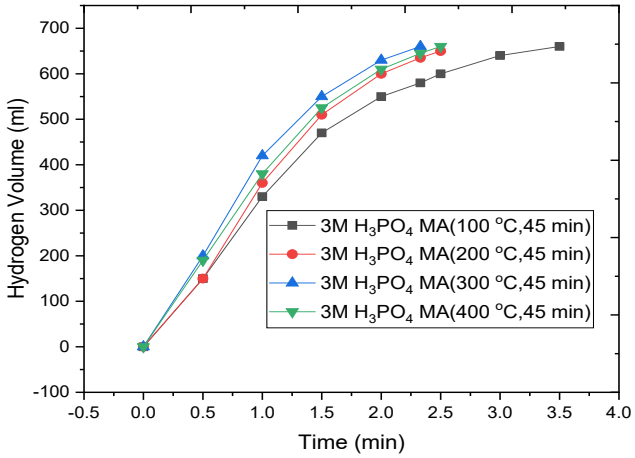

Figure 2. *Time dependent hydrogen production graph of burning temperature (30 ºC, 2.5% $NaBH_4$, 10 ml methanol and 0.1 g catalyst)*

3.5. Burning Time Effect

After determining the burning temperature, the effect of burning time on methanolysis reaction was investigated. The methanolysis reactions of the modified MA-H_3PO_4 catalyst fired at 300 ° C for different times under the same conditions (2.5% $NaBH_4$, 10 ml methanol, 0.1 g catalyst, 30 ºC) are given in Figure 3. Figure 3 shows the time dependent hydrogen production graph in the presence of MA-H_3PO_4 catalyst. As can be seen in the figure, the methanolysis reaction was completed in the shortest time in the presence of the catalyst with a burning time of 45 minutes.

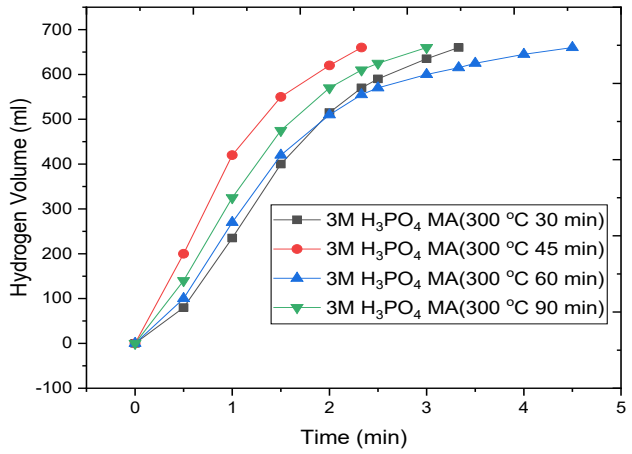

Figure 3. *Time dependent hydrogen production graph of burning time (30 °C, 2.5% $NaBH_4$, 10 ml methanol and 0.1 g catalyst)*

3.6. Catalyst Amount Effect

Experiments were carried out to examine the effect of the amount of catalyst on the methanolysis reaction. The methanolysis reaction was carried out at 30 ° C in the presence of % 2.5 $NaBH_4$, 10 ml methanol and different amounts of MA-H_3PO_4 catalyst. Figure 4 shows the time dependent hydrogen production graph in the presence of MA-H_3PO_4 catalyst. As can be seen in the figure,as the amount of catalyst increases, the completion time of the methanolysis reaction decreases. While the catalyst amount is 0.05 g, the methanolysis reaction is completed in 3.75 minutes, when the amount is increased to 0.25 g, the methanolysis reaction is completed in 1.5 minutes.

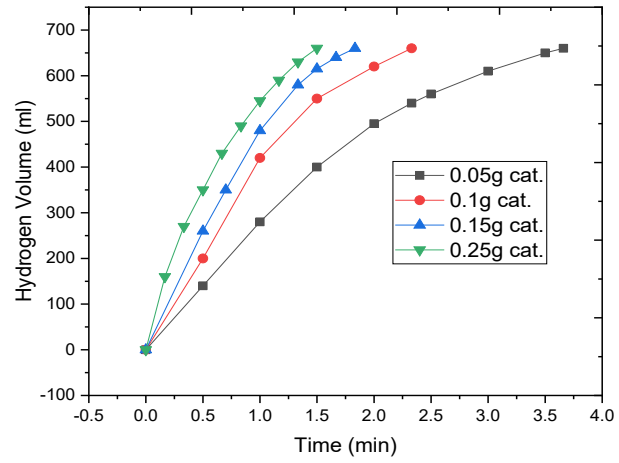

Figure 4. *Hydrogen production graph with time of catalyst amount effect (30 °C, %2.5 $NaBH_4$ and 10 ml methanol)*

3.7. $NaBH_4$ Concentration Effect

In order to examine the effect of the amount of $NaBH_4$ on the hydrogen production rate, experiments were carried out at 30 °C, in the presence of 10 ml of methanol, 0.1 g of MA-H_3PO_4 catalyst and different concentrations of $NaBH_4$ (1%,2.5%, 5% and 7.5% by weight). Figure 5 shows the time dependent hydrogen production graph in the presence of MA-H_3PO_4 catalyst. As the amount of $NaBH_4$ increases in the methanolysis reaction environment, the hydrogen production rate is expected to increase. As seen in the figure, as the amount of $NaBH_4$ increases, the rate of hydrogen production increases. Consequently, the completion time of the reaction without methanol increases.

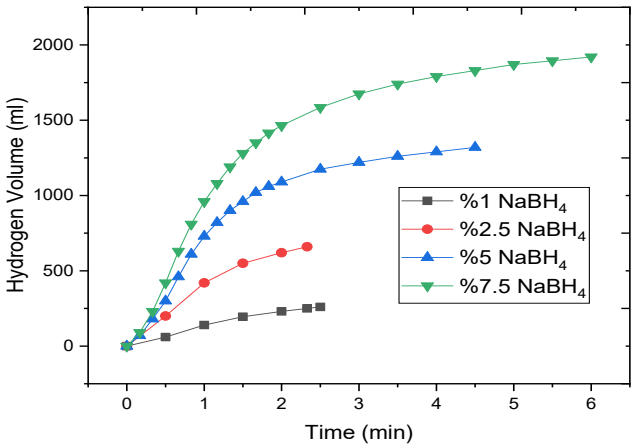

Figure 5. *Hydrogen production graph with time of $NaBH_4$ amount effect (30 °C, 0.1 g catalyst and 10 ml methanol)*

3.8. Temperature Effect

Experiments were carried out in the presence of 2.5% $NaBH_4$, 10 ml methanol and 0.1 g MA-H_3PO_4 catalyst at different temperatures (30-60 °C) to investigate the effect of temperature on the methanolysis reaction. Figure 6 shows the time dependent hydrogen production graph in the presence of MA-H_3PO_4 catalyst. As seen in the figure, as the temperature increases, the reaction completion time decreases. Because as the temperature increases, the number of collisions between molecules increases and the kinetic energy of the molecules also increases. Consequently, the reaction rate increases and the reaction completion time decreases. As seen in the figure, when the temperature is increased from 30 °C to 60 °C, the completion time of the methanolysis reaction decreases from 2.5 minutes to 1.3 minutes.

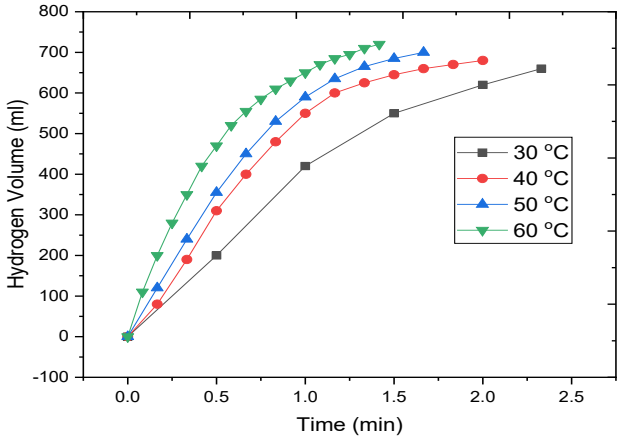

Figure 6. *Hydrogen production graph with time of temperature effect (2.5 % $NaBH_4$, 0.1 g catalyst and 10 ml methanol)*

3.9. Finding the constant k at different temperature values

Considering that the hydrolysis reactions occurring at different temperature values in order to determine the reaction rate constant (k) take place at the nth degree;

$$-r_A=k*C_A^n \quad (2)$$

$$dC_A/dt=-r_A \quad (3)$$

Equation 1 and Equation 2 are combined If $t_0 = 0$, $t_1 = t$ and C_{A0} are integrated in C_A boundary conditions, the following equation is obtained.

$$(1/n-1)*(1/C_A^{n-1})=k*t+(1/n-1)*(1/C_{A0}^{n-1}) \quad (4)$$

The term graph on the left side of Equation 4 against time is plotted and the value k is calculated from the slope of the obtained line. These graphs are drawn for each temperature at which the hydrolysis reaction takes place. With the trial and error method [8, 9], the reaction order was determined by taking the value that gives the highest regression coefficient n. Calculated reaction rate constant values of hydrolysis reaction at different temperatures are given in Table 1.The reaction order was found as n = 0.18 by trial and error method.

3.10. Calculation of activation energy;

Arhenius equation;

$$k=A*e^{-E/RT} \quad (5)$$

If ln of both sides of equation 5 is taken, equation 6 is obtained:

$$lnk=lnA-E/RT \quad (6)$$

The values calculated at different temperatures with the help of Equation 6 are given in Table 1. If the lnk versus 1 / T graph is drawn using the values given in the calculated table 1, the slope gives the activation energy and the graph in Figure 7 is obtained. The E / R value is found from the slope of this graph.

Table 1. *Calculated k values at different temperatures*

T (°C)	k	1/T	Lnk
30	0.43731	0.0033	-0.82711
40	0.5349	0.003195	-0.62568
50	0.6598	0.003096	-0.41582
60	0.8699	0.003003	-0.13938

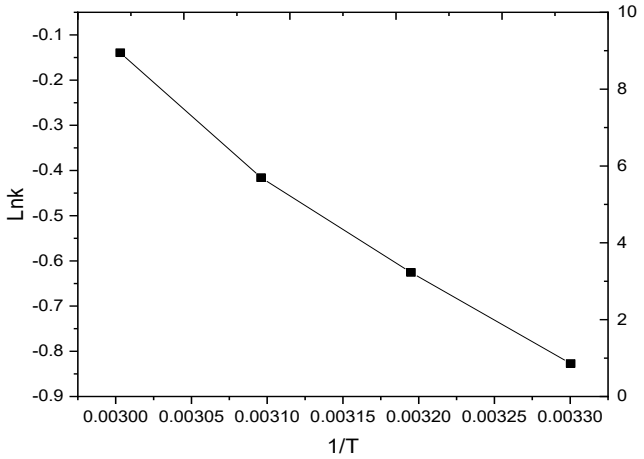

Figure 7. *Lnk- 1 / T Arrhenius plot of MA-H_3PO_4 catalyst*

In the calculations made, the activation energy of the MA-H_3PO_4 catalyst was calculated as 19,014 kj / mol. In optimum conditions, the initial rate of the MA-H_3PO_4 catalyst was calculated as 4998.1 ml H_2 $min^{-1}g_{cat}^{-1}$.

3.11. Reusability of MA-H_3PO_4 Catalyst in Methanolysis Reaction

Reusability experiments were performed in the presence of 30 °C, 10 ml methanol, 2.5% $NaBH_4$ solution and 0.1 g MA-H_3PO_4 catalyst. In Figure 8 obtained as a result of the experiments, a time dependent hydrogen production graph is given. As seen in the figure, when the catalyst is used repeatedly, the completion time of the methanolysis reaction increases.The reason for this behavior is thought to be due to the fact that NaBO2 formed in the environment during methanolysis was not completely cleaned and blocked active surfaces. [27]. It is also due to the reduced amount of catalyst when the catalyst is washed for reuse. Despite all these negativities, when MA-H_3PO_4 was used even for the 5th time, methanolysis reaction completed its conversion 100%. This shows the stability of the catalyst.

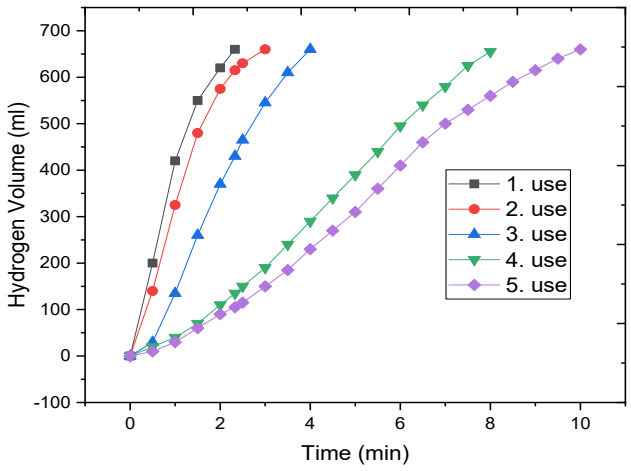

Figure 8. *Reusability graph of MA-H_3PO_4 catalys*

4. Conclussions

Hydrogen energy, which can be an alternative to fossil fuels and environmentally friendly energy solutions, is shown among the most suitable renewable energy sources. This work aims to produce a stable and environmentally friendly catalyst to be used in hydrogen production. *Microcystis aeruginosa* strain was used as a biomass source. After the microcystic was modified with acid, it was transformed into a catalyst using the carbonization method. In experiments, it has been found that optimum conditions for carbonization are 300 ºC and 45 minutes. Parameters affecting methanolysis were examined. In the kinetic calculations, the reaction order was found as 0.18, the activation energy as 19.014 kj / mol and the initial rate as 4998.7 ml H_2 min^{-1} g_{cat}^{-1}. The reusability was tested 5 times to determine the stability of the catalyst. Although MA-H_3PO_4 was used 5 times, it continued its catalytic activity. In Table 2, activation energies and initial speeds of some organic wastes or biomass-based and metal contaning catalysts in the literature are given. As seen in the table, MA-H_3PO_4 catalyst showed better activity than metal-containing catalysts.

Table 2. *Comparison of activation energies and initial rate of catalysts in the literature*

Catalyst	İnitial Rate (ml $H_2min^{-1}g_{cat}^{-1}$)	Activation Energy (kj/mol)	Reference
DSCG-CH_3COOH	3171.4	25.23	[5]
PC-PEI^+	4040	23.82	[28]
Co-Fe-B (Water)	1300	31	[29]
CVMS-H_3PO_4—CuB	6500	23.79	[30]
Co–P/CNTs-Ni foam	2430	49.94	[31]
Co/Al_2O_3	4400	21.9	[32]
MA-H_3PO_4	**4998.7**	**19.014**	**This study**

In conclusion, using biomass-based catalyst for hydrogen production from sodium borohydride is important for the environment and sustainable energy. In addition, the production of catalysts from biomass is both environmentally friendly and economical. Microsystis microalgae was used as a biomass source in this study. An environmentally friendly catalyst has been developed using microalgae. The catalyst obtained as a result of the activation processes showed higher catalytic activity than many catalysts in the literature.

References

[1]. Milano J., Ong H.C., Masjuki H.H., Chong W.T., Lam M.K., Loh P.K., Vellayan V., "Microalgae biofuels as an alternative to fossil fuel for power generation", Renewable and Sustainable Energy Reviews, 58, (2016), 180-197.

[2]. Suganya T., Varman M., Masjuki H.H., Renganathan, S., "Macroalgae and microalgae as a potential source for commercial applications along with biofuels production: a biorefinery approach", Renewable and Sustainable Energy Reviews, 55, (2016), 909-941.

[3]. Hosseini S. E., Wahid, M.A., "Hydrogen production from renewable and sustainable energy resources: promising green energy carrier for clean development", Renewable and Sustainable Energy Reviews, 57, (2016), 850-866.

[4]. Kaya M., "Evaluating organic waste sources (spent coffee ground) as metal-free catalyst for hydrogen generation by the methanolysis of sodium borohydride", International Journal of Hydrogen Energy, 45(23), (2020), 12743-12754.

[5]. Kaya M., "Production of metal-free catalyst from defatted spent coffee ground for hydrogen generation by sodium borohyride methanolysis", International journal of hydrogen energy, 45(23), (2020), 12731-12742.

[6]. Mustafa K.A.Y.A., Bekirogullari, M., "Investigation of hydrogen production from sodium borohydride methanolysis in the presence of Al2O3/spirulina platensis supported Co catalyst", Avrupa Bilim ve Teknoloji Dergisi, (16), (2019), 69-76.

[7]. Bilici M.S.U. "Energy Carrier Hydrogen", Hydrogen Carrier Sodium Borohydride, Mining Bulletin, (67), (2004).

[8]. Hansu T.A., Sahin O., Caglar A., Kivrak H.," A remarkable Mo doped Ru catalyst for hydrogen generation from sodium borohydride: the effect of Mo addition and estimation of kinetic parameters",

Reaction Kinetics, Mechanisms and Catalysis, 131(2), (2020), 661-676.

[9]. Avci Hansu T., Sahin O., Çağlar A., Demir Kivrak, H.," Untangling the cobalt promotion role for ruthenium in sodium borohydride dehydrogenation with multiwalled carbon nanotube-supported binary ruthenium cobalt catalyst", International Journal of Energy Research, 45(4), (2021), 6054-6066.

[10]. Hansu F., "The effect of dielectric barrier discharge cold plasmas on the electrochemical activity of Co–Cr–B based catalysts", Journal of the Energy Institute, 88(3), (2015), 266-274.

[11]. Kivrak H. D., Caglar A., Hansu T. A., Şahin, Ö." Carbon nanotube supported direct borohydride fuel cell anode catalysts: the effect of catalyst loading", MANAS Journal of Engineering, 8(1), (2020), 1-10.

[12]. Akdemir M., Avci Hansu T., Caglar A., Kaya M., Demir Kivrak, H.," Ruthenium modified defatted spent coffee catalysts for supercapacitor and methanolysis application", Energy Storage, e243, (2021).

[13]. Hansu T. A., Caglar A., Sahin O., Kivrak, H., "Hydrolysis and electrooxidation of sodium borohydride on novel CNT supported CoBi fuel cell catalyst", Materials Chemistry and Physics, 239, (2020), 122031.

[14]. Braesch G., Bonnefont A., Martin V., Savinova E. R., Chatenet M., "Borohydride oxidation reaction mechanisms and poisoning effects on Au, Pt and Pd bulk electrodes: From model (low) to direct borohydride fuel cell operating (high) concentrations", Electrochimica Acta, 273, (2018), 483-494.

[15]. Braesch G., Wang Z., Sankarasubramanian S., Oshchepkov A. G., Bonnefont A., Savinova E. R., ... & Chatenet, M., "A high performance direct borohydride fuel cell using bipolar interfaces and noble metal-free Ni-based anodes", Journal of Materials Chemistry A, 8(39), (2020),20543-20552.

[16]. Caglar A., Ulas B., Cogenli M.S., Yurtcan A.B., Kivrak, H., "Synthesis and characterization of Co, Zn, Mn, V modified Pd formic acid fuel cell anode catalysts", Journal of Electroanalytical Chemistry, 850, (2019), 113402.

[17]. Ulas B., Caglar A., Kivrak H.," Determination of optimum Pd: Ni ratio for Pd x Ni 100-x/CNT s formic acid electrooxidation catalysts synthesized via sodium borohydride reduction method", International Journal of Energy Research, 43(8), (2019), 3436-3445.

[18]. Ulas B., Alpaslan D., Yilmaz Y., Dudu T. E., Er O. F., Kivrak, H., "Disentangling the enhanced catalytic activity on Ga modified Ru surfaces for sodium borohydride electrooxidation.",Surfaces and Interfaces, 23, (2021), 100999.

[19]. Biniwale R. B., Rayalu S., Devotta S., Ichikawa, M.," Chemical hydrides: a solution to high capacity hydrogen storage and supply", International Journal of Hydrogen Energy, 33(1), (2008), 360-365.

[20]. Duman F., Atelge M.R., Kaya M., Atabani A. E., Kumar G., Sahin U., Unalan S., "A novel Microcystis aeruginosa supported manganese catalyst for hydrogen generation through methanolysis of sodium borohydride", International Journal of Hydrogen Energy, 45(23), (2020), 12755-12765.

[21]. Inal I.I.G., Akdemir M., Kaya M., "Microcystis aeruginosa supported-Mn catalyst as a new promising supercapacitor electrode: A dual functional material", International Journal of Hydrogen Energy, 46(21), (2021), 21534-21541.

[22]. Rangabhashiyam S., Behera B., Aly N., Balasubramanian, P.,"Biodiesel from microalgae as a promising strategy for renewable bioenergy production-A review", Journal of Environment & Biotechnology Research, 6(4), (2017), 260-269.

[23]. Ahlström-Silversand A F., Odenbrand C.U.I., "Modelling catalytic combustion of carbon monoxide and hydrocarbons over catalytically active wire meshes", Chemical Engineering Journal, 73(3), (1999), 205-216.

[24]. Brack P., Dann S E., Wijayantha K. U.," Heterogeneous and homogenous catalysts for hydrogen generation by hydrolysis of aqueous sodium borohydride (NaBH4) solutions", Energy Science & Engineering, 3(3), (2015), 174-188.

[25]. Sahiner,N., Demirci S.," Natural microgranular cellulose as alternative catalyst to metal nanoparticles for H2 production from NaBH4 methanolysis.",Applied Catalysis B: Environmental, 202, (2017), 199-206.

[26]. Mustafa K.A.Y.A., BekiroğullarI, M., "Tarımsal Atıktan Elde Edilen Aktif Karbon Destekli Co-B Katalizörü Varlığında Sodyum Borhidrürün

Metanolizi", Türkiye Tarımsal Araştırmalar Dergisi, 6(1), (2019), 80-86.

[27]. Kaya M., Ceyhan A.A., Şahin Ö.," Effects of different temperatures and additives on the metastable zone width precipitation kinetics of NaBO 2", Russian Journal of Physical Chemistry A, 88(3), (2014), 402-408.

[28]. Demirci S., Yildiz M., Inger E., Sahiner N.,"Porous carbon particles as metal-free superior catalyst for hydrogen release from methanolysis of sodium borohydride", Renewable Energy, 147, (2020), 69-76.

[29]. Wang A., Yin H., Lu H., Xue J., Ren M., Jiang T.," Effect of organic Modifiers on the structure of nickel nanoparticles and catalytic activity in the hydrogenation of p -nitrophenol to p –Aminophenol,Langmuir", 25, (2009), 12736-12741

[30]. Bekirogullari M.," Catalytic activities of non-noble metal catalysts (CuB, FeB, and NiB) with C. Vulgaris microalgal strain support modified by using phosphoric acid for hydrogen generation from sodium borohydride methanolysis", International Journal of Hydrogen Energy, 44(29), (2019), 14981-14991.

[31]. Wang F., Zhang Y., Luo Y., Wang Y., Zhu H.," Preparation of dandelion-like Co–Mo–P/CNTs-Ni foam catalyst and its performance in hydrogen production by alcoholysis of sodium borohydride", International Journal of Hydrogen Energy, 45(55), (2020), 30443-30454.

[32]. Xu D., Zhao L., Dai P., Ji S.," Hydrogen generation from methanolysis of sodium borohydride over Co/Al2O3 catalyst", Journal of natural gas chemistry, 21(5), (2012), 488-494.

MANAS Journal of Engineering
ISSN 1694-7398 | e-ISSN 1694-7398

Volume 9, Issue 2, (2021) Pages 122-128
https://doi.org/10.51354/mjen.928670

Environmental pollution size of the Bishkek Solid Waste Landfill and treatment of generated leachate wastewater

Venera Edilbek Kyzy*[1], Nurzat Şaykiyeva[1], Kubat Kemelov[1], Mustafa Dolaz[1,2], Mehmet Kobya[1,3]

[1] Kyrgyz-Turkish Manas University, Department of Environmental Engineering, Bishkek, Kyrgyzstan, venera127992@gmail.com, ORCID: 0000-0002-9345-3660, nurzat.saykiyeva@manas.edu.kg, ORCID: 0000-0000-1905-0086

[2] Kahramanmaraş Sütcü İmam University, Department of Environmental Engineering, 46040, Kahramanmaraş-Turkey

[3] Gebze Technical University, Department of Environmental Engineering, 41400, Gebze-Turkey

ABSTRACT

The disposal of municipal solid wastes (MSW) is one of the important issues today. The MSW is generally disposed of in a landfill. The disintegration of wastes in landfill generates the wastewater known as leachate and it became one of the budding environmental impacts. The landfill leachate seeps into natural ponds next to the Bishkek (Kyrgyzstan) landfill. The MSWs are dumped with an irregular landfill in Bishkek, and it has been observed that this situation creates many environmental pollution problems (air pollution due to the combustion of wastes and generated biogas, due to leakage of leachate from the landfill) around the landfill. The leachate in the ponds is not treated and leaks into the environment. In this study, the potential of the coagulation-flocculation(CF) and electrooxidation (EO) processes was investigated for the treatment of leachate from the sanitary landfill located in Bishkek-Kyrgyzstan. The initial COD (1400 ± 50 mg/L), TOC (540 ± 15 mg/L), and ammonia nitrogen (315 ± 10 mg/L) from landfill leachate were treated by the CF process as 33, 23, and 14% at pH 6.5 with alum dosage of 5 g/L, and 40, 29 and 10.1% at pH 8.5 with ferric chloride dosage of 5 g/L, respectively.

Removal efficiencies at applied currents of 1.0, 3.0, and 5.0 A with an EO reactor using boron-doped diamond (BDD) plate anode and stainless steel (SS) plate cathode were 67.20, 88.30, and 97.90% for COD, 60.10, 85.38, and 95.53% for TOC, and 48.9, 94.6 and 99.8% for ammonia nitrogen, respectively. As a result, it was seen that Bishkek's irregular solid waste landfilling leachate, which causes environmental pollution, was effectively treated with the EO process. By establishing a regular landfill, Bishkek municipal solid wastes must be disposed of in the landfill and treated of the leachate.

ARTICLE INFO

Research article

Received: 27.04.2021
Accepted: 14.06.2021

Keywords:
Solid waste landfill,
landfill leachate treatment,
coagulation,
electrooxidation

**Corresponding author*

1. Introduction

The amount of municipal solid waste (MSW) generated due to rapid urbanization and growing populations has increased even more today. According to the reports of the World Bank, it is estimated that about 2.2 billion tons of solid waste will be generated in 2025 and the management cost of these wastes will be $375.5 billion [1]. The amount of waste generated per person per day averages worldwide is 0.74 kg but ranges widely, from 0.11 to 4.54 kg. The quantity and the composition of the MSW are critical for the determination of the appropriate handling and management of these wastes. Among the different MSW management approaches, disposal of in landfills is still the most used and accepted method worldwide because of its low cost and relatively low maintenance requirements [2].

The interaction of waste with water that percolates through the landfill produces highly polluted wastewater termed as landfill leachate. During the decomposition process of wastes in landfills, one ton of waste is estimated to generate 0.20 m^3 of landfill leachate [3]. With the increasing age of a landfill, the characteristics of the leachate vary from one site to another. Various factors that affect the composition of the leachate include the type and composition of the MSW landfilled, the stage of the MSW decomposition, climate, seasonal variation, hydrology of the site, and conditions

within the landfill such as its design and operation, pH, and moisture content. As landfill age increases, the biodegradable fraction of organic pollutants in leachate decreases due to anaerobic decomposition occurring in a landfill site. The old landfill leachate (> 10 years old) normally contains pH >7.5, high quantity of ammonia (>400 mg/L), moderately high strength of COD (<4000 mg/L), low BOD (80 mg/L), and a low BOD_5/COD ratio of less than 0.10. Unlike the old landfill leachate, young landfill leachate (< 5 years old) is typically characterized by pH <6.5, high BOD_5 (4000–13,000 mg/L) COD (30,000–60,000 mg/L), ammonia (<400 mg/L) concentrations and high ratio of BOD_5/COD (0.4–0.7) [4]. After all, the BOD_5/COD ratio of old leachate also decreases as the amount of carboxylic acid reduces and the amount of recalcitrant organic molecules increases. Due to the high levels of ammonia, heavy metals, and different organic compounds, landfill leachate can result in serious pollution for the environment [2].

To reduce a negative impact on the environment, a combination of physical, chemical, and biological methods is used for the efficient treatment of landfill leachate [5]. The coagulation-flocculation process is generally applied to reduce the pollution load of the leachate. The young leachates are effectively treated by biological treatment methods (aerobic, anaerobic, and anoxic). Membrane biological reactors (MBRs), with nitrification/denitrification steps, followed by membrane technologies, are commonly used to treat sanitary landfill leachates [6]. The desired discharge standards are met in the treatment of the leachate by membrane processes (nanofiltration and reverse osmosis) that follow the biological treatment of the leachate. However, most of the recalcitrant substances in leachate are difficult to degrade during the biological process. These recalcitrant substances can be removed with the membrane processes, but since membrane processes are a physical process, the leachate membrane concentrate typically represents 10-30% of the volume of the leachate influent [7]. Advanced oxidation processes (AOPs) are commonly used for the removal of the membrane concentrates and nonbiodegradable and/or toxic substances from especially old leachate. The AOPs are characterized by the highly reactive hydroxyl radicals (•OH) presence, which is suitable for a rapid and indiscriminate reaction with an organic compound inducing its almost total mineralization [8]. One of the AOPs is electro-oxidation (EO). Due to its effectiveness and ease in operation, the EO process has recently received significant attention for the treatment of wastewaters such as landfill leachate. This process has shown its efficacy for the destruction of refractory pollutants [9].

In this study, first, the environmental problems of the urban landfill of Bishkek (Kyrgyzstan) were investigated. Then, the treatability of the leachate that emanated from the existing landfill and formed natural ponds by the CF and EO processes was examined. COD, TOC, and ammonia nitrogen removal efficiencies at different coagulant dosages for CF and applied currents for EO processes were determined.

2. Material and methods

2.1. The Bishkek solid waste landfill area

Bishkek is the capital and largest city of Kyrgyzstan (Kyrgyz Republic). This city (coordinates of 42°52′29″N and 74°36′44″E) is situated at an altitude of about 800 meters, just off the northern fringe of the Kyrgyz Ala-Too Range, an extension of the Tian-Shan mountain range. These mountains rise to a height of 4,895 meters. The city covers an area of ~200 km^2. The annual average precipitation is around 440 mm. Average daily high temperatures range from 3 °C in January to about 31 °C during July (around −10°C in winter). The official population of Bishkek in 2020 is approximately 1,053,915 people and the population growth rate is approximately 2.3% (above the national average of 2.1%). However, many inhabitants (~400,000 person) live in Bishkek unofficial.

All municipal waste is delivered to the only operational dumpsite in Bishkek – the Bishkek Solid Waste Landfill (BSWL). The BSWL has located 12 km to the north of the city center and 300-600 m east of the Ala-Archa reservoir. The site is situated within city limits nearing the Alamedin district of the Chui region. The dumpsite is located on a 36-hectare area to the North of the City with favorable geological and hydrogeological conditions for landfill. However, it is estimated that over the years its dimensions have expanded up to 48 ha. The city landfill site has been operating since 1976, and today the population of Bishkek is about 1.4 million (400,000 inhabitants). Today, over 1010 tons of solid waste is collected daily in Bishkek, and the country has accumulated more than 100 million tons of waste, which is placed in the BSWL. According to these results, the amount of solid waste per capita ranges from 0.74-1.00 kg.

In 2013, the Kyrgyz government and the European Bank for Reconstruction and Development signed a loan agreement to finance the project “Improvement of Solid Waste Management System in Bishkek”. The solid waste to be disposed of is 220,000 tons. The new solid disposal (the northern edge from the old BSWL is ~500 m); the maximum length of the site north to south of 715 m and the maximum width east to west of 366 m; the landfill site consists of three cells of 27,600 m^2, 31,200 m^2 and 30,200 m^2; thick of protective geotextile layer (high-density polyethylene) of 2 mm, the thickness of artificial geological clay barrier (measured after compaction) of the bottom layer and slopes in each cell of 0.50 m, a drainage layer (washed gravel of fraction 16/32 mm) to be placed on the protective geotextile) will be located next to the old city landfill, which after the construction is completed will be closed and reclaimed.

Figure 1. *General views from the Bishkek Solid Waste Landfill (November 2021).*

2.2. Characteristics of landfill leachate

Leachate samples in this study were supplied from the BSWL which islanded on 233 ha area at Bishkek (Kyrgyzstan) and this landfill is still operated. The landfill is composed of different cells and the leachate leaking from the landfill cells is collected in the natural lagoons near the landfilling. This landfill area leachate is not treated. The leachate sample leaking from the old landfill cells was used in this study. The collected landfill leachate was stored in a 4 °C refrigerator to keep the wastewater characteristics unchanged. The characteristics of the Bishkek landfill leachate (BLL) used of this study were as follows: pH 8.1 ± 0.2, conductivity 14.3 ± 0.5 mS/cm, chemical oxygen demand (COD)= 1400 ± 50 mg/L, biological oxygen demand (BOD_5)= 20 ± 2 mg/L, total organic carbon (TOC)= 540 ± 15 mg/L, and ammonia nitrogen (NH_3-N)= 315 ± 10 mg/L (Table 1).

Table 1. *The characteristics of landfill leachate*

Parameter	Value
pH	8.1 ± 0.2
conductivity	14.3 ± 0.5 mS/cm
chemical oxygen demand (COD)	1400 ± 50 mg/L
biological oxygen demand (BOD_5)	20 ± 2 mg/L
total organic carbon (TOC)	540 ± 15 mg/L
ammonia nitrogen (NH_3-N)	315 ± 10 mg/L.

2.3. Experimental set-up and procedures

Coagulation-flocculation (CF) experiments were conducted using a conventional jar test apparatus in a 250 mL beaker with a working volume of 100 mL. Ferric chloride ($FeCl_3.6H_2O$) and alum ($Al_2(SO_4)_3.18H_2O$) can both be used as coagulants to treat leachate. The initial pH of leachate in the beaker was adjusted to 6.50 for alum and 8.50 for ferric chloride by adding a 0.1-2 M H_2SO_4 or a NaOH solution. The pH values were selected based on the best performance of the coagulants and obtained optimum pH results from coagulation of raw landfill leachate in the literature, in order to reduce

operating costs by pH adjustment. The desired coagulant doses (0.10, 0.20, 0.40, and 0.50 g/L) were added to the beaker, and the sample was then agitated under a rapid mixing (200 rpm) for 2 min followed by a slow stirring (30 rpm) for 30 min. During the rapid mixing stage, the pH was maintained at the initial value by adding NaOH. After a 60 min long settling, the supernatant was taken from the beaker for filtration (with Whatman membrane filter of pore diameter of 0.45 µm), and then the filtrate was used for chemical analysis. After analysis of samples, the COD, TOC, and NH_3-N removal percentages were calculated. Bulk solution after coagulation-flocculation was filtered membrane filters to determine the amount of sludge (dried for 24 hours in an oven at 105 ºC).

The electro-oxidation (EO) experiments were conducted in batch mode, without stirring, and using 1000 mL of landfill leachate. A boron-doped diamond (BDD) plate on niobium anode and a stainless-steel plate cathode (20 × 6 cm) with the same dimension, both with an area of 120 cm^2, were used. The electrodes were arranged parallel to each other at a distance of 1.60 cm. The applied current intensities evaluated were 1.0 A (41.67 A/m^2), 3.0 A (125 A/m^2), and 5.0 A (208.33 A/m^2), at room temperature (22±3 ºC) and without the addition of a background electrolyte. A volume of V = 1000 mL of landfill leachate in the batch EO reactor was treated in each experiment. During the experiments, leachate samples were periodically collected from the EO reactor and filtered by a 0.45 µm microspore membrane filter before analyses. The leachate in the reactor was well mixed by a magnetic stirrer (Daigger model), and a direct current (dc) power supply (GW Instek, GPD-4303S Bench PSU model, 0-3 A, 0-30 V) was used to conduct the experiments under constant current conditions. Adjustments to the pH were made by the addition of concentrated H_2SO_4 or NaOH solutions. Each experiment was performed at least twice, and the results presented in this work are the average values.

2.4. Chemicals and analytical methods

COD, BOD, TOC, and NH_3-N in raw and treated landfill leachate samples were measured according to the Standard Methods [10]. The COD of the leachate samples was determined using the titrimetric open reflux method described by the Standard Methods. TOC was determined by a TOC analyzer (Shimadzu, TOC-L model, Japan). BOD was determined for cultivating 5 days at a constant temperature of 20 ºC using an OXITOP® system. The nitrate, nitrite, sulfate, and chloride concentrations were measured using the HACH spectrophotometer (DR 2000 model). Conductivity was measured with a conductive meter (YSI, 30 models) and pH was measured with a pH meter (Thermo Scientific, Eutech pH 150). All the experiments were carried out at room temperature (20 ± 1 ºC). All chemicals used were of analytical grade.

3. Result and discussion

3.1. Environmental pollution size of the BSWL

Waste sorting is carried out by informal players at various stages of the supply chain, from the waste collection points to the dumpsite. There is no formal sorting of waste taking place in the city. About 1.5 million m^3 of municipal solid waste is generated in the city annually, about 220 thousand tons of waste per year. Waste pickers within the town take some valuable materials from the waste at collection points, but the waste in collection trucks was analyzed and still contains 28% of valuable recyclables (composition of the municipal wastes; 49% organics, 1% textiles, 8% plastics, 1% metals, 8% glass, 10% paper or cardboard, and 22% other).

There are major environmental and social problems associated with the dumpsite. The solid wastes are dumped with an irregular landfill in Bishkek. Recyclable wastes (such as plastic and metal wastes) from the wastes brought to the landfill area by garbage trucks are sorted irregularly by people living near this area. The municipal waste is unloaded over a large area, providing easy access by waste pickers. Because it's not surrounded by any fences, currently informal waste picking and sorting take place at the BSWL and a number of informal settlements are located within its sanitary protection zone. Also, the dumped wastes are not compacted or covered by layers of soil, giving easy access to the waste by rats, birds, insects, and dogs for food, breeding, and living in the waste. In some parts of the landfill area, it is seen that the spilled waste is burning, and smoke is generated because of burning. There is also an air pollution problem in the region due to the storage of irregular solid wastes and the burning of biogas in some places in the solid waste landfill area and these combustion emissions are inhaled by residents in the region. Therefore, there are methane emissions, a major greenhouse gas, across the landfill area. Some light garbage is scattered all over the district near the landfill area, and in the summertime, the stench spreads right up to the shore. There is no fence or other perimeter around the dumpsite enabling access to the waste by dogs and people. Polluted water (landfill leachate) from the site collects in the clay pit to the north of the site and in the pond to the east of the site with a risk of contaminating the Ala-Archa river and groundwater. The large artificial reservoir (it is a surface area of 5.1 km^2 and an annual capacity of 39 million m^3) of the Ala-Archa river is located ~250 m (new landfill of 300 m) to the south of the BSWL landfill location.

Informal settlements have been built near the landfill area. About 900 people a year are involved in collecting recyclables on the dumpsite with up to 200 people them working there on a typical day. Their activities make it difficult to close any area of the BSWL. There are single-story houses near the landfill with infrastructure problems and people built without permission. Although no health problems are stated regarding the residents of the waste landfill, many houses do not have

drinking and utility water, the site is considered to be responsible for poor health by the residents to the west and southeast of the site. The access road of the dumpsite is not maintained and is dilapidated. This leads to additional noise, vehicle emissions, dust, and mud from vehicles. Part of the old waste deposits and the main leachate pond is located within the protection zone of a gas pipeline to the East of the site, and these problems have to be resolved during the recultivation of the dumpsite.

3.2. Treatment studies with CF process of BLL

Coagulation-flocculation (CF) is a simple process used to treat landfill leachate [11]. This process has been widely used in the pre-or post-treatment of landfill leachate to enhance the biodegradability of leachate or to remove organic matters (especially refractory organics) to reduce the pollution load of wastewater [12]. In the coagulation-flocculation process, when an inorganic coagulant such as alum and ferric chloride is added to water containing a colloidal suspension, the cationic metal ion (Al^{3+}, Fe^{3+}) from the coagulant neutralizes the negatively charged electric double layer of the colloid. The hydrolyzed coagulant species come into contact with impurities, forming destabilized particles during the fast mixing step. The collision of these destabilized particles (an essentially physical step) then forms larger particles or flocks, which can be removed by means of sedimentation, flotation, or rapid filtration. The main parameters employed to evaluate the efficiency of this process are pH and coagulant dosage. To study the efficiency of the CF process for the removal of COD, TOC, and NH_3-N, two types of coagulants were tested; aluminum sulfate (alum) and ferric chloride, and in addition to coagulant type and dosage effects were also assessed. The effect of alum and ferric chloride dose on CF efficiency was shown in Figure 2.

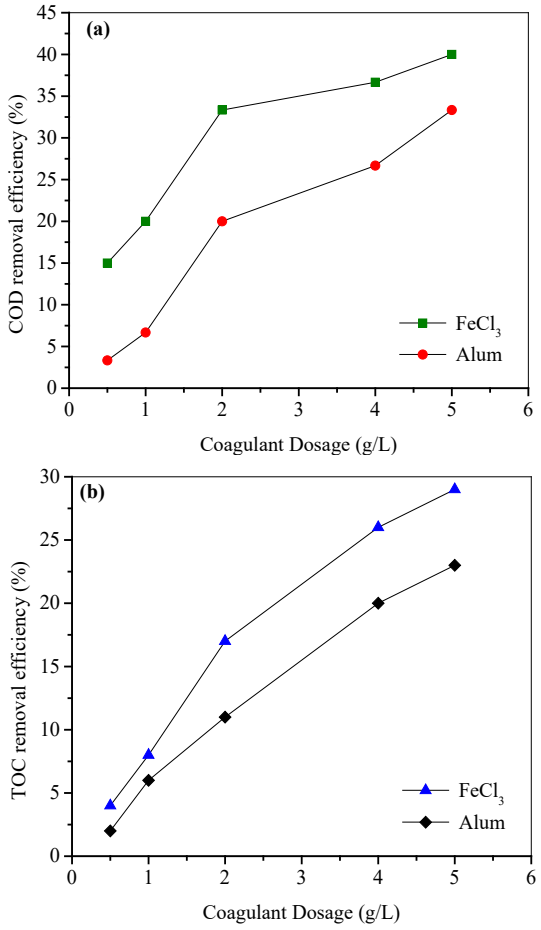

Figure 2. *Removal efficiencies at different dosages of coagulant for alum and $FeCl_3$, (a) COD, and (b) TOC.*

The COD and TOC removals increased to 15% (1020 mg/L) to 40% (720 mg/L) and 4% (1152 mg/L) and %29 (880 mg/L) for ferric chloride at pH 8.5, and 3.3% (1160 mg/L) to 33.3% (800 mg/L), and 2% (1176 mg/L) and 23% (925 mg/L) and for alum at pH 6.5, respectively, when coagulant dose increased from 500 to 5000 mg/L (Figure 2). At coagulant dose of 500, 1000, 2000, 4000 and 5000 mg/L, ammonia nitrogen removal was 4.1, 8.4, 10.4, 12 and 14% for alum and 2.3, 4.5, 7.3, 8.2, and 10.1% for $FeCl_3$, respectively. Considering these results, COD, TOC, and NH_3-N removal efficiencies were low in the treatment of stabilized leachate with CF process, and higher removal efficiency for the elimination of the organic compounds and ammonia nitrogen was obtained with iron chloride than alum. Iron and aluminum hydroxides flocks in the CF process would be formed and the complex formation between the hydroxides and the organic compounds enhanced the removal efficiency. A few organic substances in the landfill leachate, like some special humic and fulvic substances, could not be effectively removed by the coagulation process. Therefore, it is seen that COD and TOC removal efficiencies for both coagulants are low. The removal mechanisms of organic compounds in the leachate in the CF process could be charge adsorption–neutralization and

complexation followed by precipitation. Other researchers have also reported similar results regarding treatment by the CF process of landfill leachate [11, 13, 14]. Amount of produced sludge (after dried at 105 ºC, 24 hour) at coagulant dose of 500, 1000, 2000, 4000 and 5000 mg/L was 1.42, 2.38, 2.26 and 2.75 g/L for alum and 1.49, 2.12, 2.53 and 3.96 g/L for $FeCl_3$, respectively. It was observed that the treatment efficiency of landfill leachate was not very high. In addition, a large amount of treatment sludge arises in this process. This is the disadvantage of the CF process. The concentration of humic substances is high in stabilized leachates. Therefore, it is very difficult to treat such wastewater with the CF process. Ultimately, it is necessary to treat the stabilized leachate by an oxidation process such as EO. In addition, there is no treatment sludge problem in this process.

3.3. Treatment studies on electro-oxidation of BLL

In recent years, the electro-oxidation (EO) process has been successfully applied to the degradation of toxic and nonbiodegradable organic pollutants for wastewaters [15]. Compared with conventional processes, EO has attractive advantages such as high oxidation efficiency, amenability to automation, little or no need for the addition of chemicals, and no secondary pollution, etc. In addition, the boron-doped diamond (BDD) film electrode used in the EO process has received great attention in wastewater treatment for its wide potential window, high anodic stability, and almost complete mineralization of organic matters [16]. Besides, the EO process has been successfully applied for landfill leachate treatment [17]. At BDD anodes, organics oxidation is thought to take place mainly by mediated hydroxyl radical oxidation, whereas ammonia removal occurs through indirect oxidation by means of electro-generated active chlorine.

In this study, the treatment of leachate by the EO process was carried out by using BDD anode and SS cathode electrodes. COD and TOC removals at different applied currents depending on the EO time are shown in Figure 3. The COD concentration of landfill leachate was 1400 ± 50 mg/L, residual COD concentrations were reduced as 460 mg/L (67.2%), 164 mg/L (88.3%), and 30 mg/L (97.9%) for applied currents of 1.0, 3.0, and 5.0 A at the end of 260 min EO time, respectively (Figure 3a). At currents of 1.0, 3.0, and 5.0 A and the end of 260 min EO time, the TOC concentration decreased from 536.6 mg/L to 214.4, 78.9, and 24.1 mg/L, respectively (Figure 3b). In other words, TOC removal was found to be 60.3, 85.4, and 95.5% at 1.0, 3.0 and 5.0 A applied currents. Ammonia nitrogen removal efficiency at 1.0, 3.0, and 5.0 A was 48.9, 94.6, and 99.8%, respectively. Considering the results obtained, it shows that the EO process is a very effective process in the oxidation of leachate. BDD anodes show that very effective in both ammonium-nitrogen removal and TOC removal. In the EO process, there is the oxidation of organic substances to CO_2, H_2O, and simpler organic substances, and nitrogen gas oxidation of ammonium nitrogen.

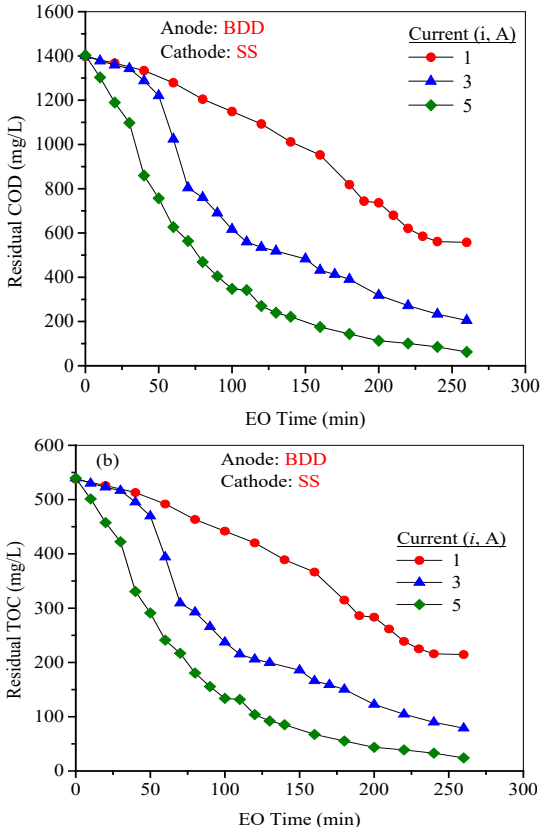

Figure 3. *Removal efficiencies at different applied current from the BLL: (a) COD, (b) TOC.*

4. Conclusion

It was observed that the irregular solid waste field in Kyrgyzstan Bishkek caused some environmental pollution and problems. Air pollution is the biggest problem as a result of the burning of wastes together with the gases from the solid waste landfill. In addition, the proximity of settlements indicates that many health and hygienic problems will arise in the future. It is seen that the water resources very close to the solid waste landfill area and the groundwater in the area will be affected. It is obvious that solid waste leakage waters leak and form small ponds in the region, causing environmental pollution. The treatability of the leachate by coagulation-flocculation (CF) and EO processes has been investigated. COD, TOC, and ammonia-nitrogen from landfill leachate with the CF process were removed 40, 29, and 10.1% at pH 8.5 with $FeCl_3$ dosage of 5 g/L, respectively. It was observed that the CF process was not very effective in Bishkek landfill leachate treatment. COD, TOC, and ammonium-nitrogen by EO process using BDD anodes were removed as 97.90, 95.5, and 99.8% at the applied current of 5 A, respectively. As a result, it was seen that Bishkek's irregular solid waste landfilling leachate, which causes environmental pollution, was effectively treated with the EO process. By establishing a regular landfill, Bishkek municipal solid wastes must be disposed of in the landfill and treated of the leachate.

Acknowledgments

This study was published from the thesis of the graduate student Venera Edilbek Kyzy. The authors thank the Kyrgyz-Turkish Manas University and the Municipality of Bishkek

References

[1]. Iskander S.Md., Zhao R., Pathak A., Gupta A., Pruden A., Novak J.T., He Z., "A review of landfill leachate induced ultraviolet quenching substances: Sources, characteristics, and treatment", Water Research, 145 (2018) 297-311.

[2]. Renou S., Givaudan J., Poulain S., Dirassouyan F., Moulin P., "Landfill leachate treatment: review and opportunity", J. Hazard. Mater. 150 (2008) 468–493.

[3]. Kurniawan T. A., Waihung Lo., Chana G., Mika E. T. Sillanpaa., "Biological processes for treatment of landfill leachate", Journal of Environmental Monitoring, 2010, 12, 2032–2047.

[4]. Foo K.Y., Hameed B.H., "An overview of landfill leachate treatment via activated carbon adsorption process", Journal of Hazardous Materials 171 (2009) 54–60.

[5]. Gao J., Oloibiri V., Chys M., Audenaert W., Decostere B., He Y., Langenhove H.V., Demeestere K., Hulle S.W.H.V., "The present status of landfill leachate treatment and its development trend from a technological point of view", Rev Environ Sci Biotechnology, 14 (2015) 93–122.

[6]. Ahmed F.N., Lan C.Q., "Treatment of landfill leachate using membrane bioreactors: A review", Desalination, 287, (2012), 41-54.

[7]. Zhang Q.Q., Tian B.H., Zhang X., Ghulam A., Fang C.R., He R., "Investigation on characteristics of leachate and concentrated leachate in three landfill leachate treatment plants", Waste Management, 33 (2013) 2277–2286.

[8]. Gautam P., Kumar S., Lokhandwala S., "Advanced oxidation processes for treatment of leachate fromhazardous waste landfill: A critical review", Journal of Cleaner Production, 237 (2019) 117639.

[9]. Mandal P., Dubey B.K., Gupta A.K., "Review on landfill leachate treatment by electrochemical oxidation: Drawbacks, challenges and future scope", Waste Management, 69 (2017) 250-273.

[10]. APHA (2005) Standard Methods for the Examination of Water and Wastewater. 21st Edition, American Public Health Association/American Water Works Association/Water Environment Federation, Washington DC.

[11]. Fleck E., Gewehr A.G., Cybis L.F.A., Gehling G.R., Juliano V.B., "Evaluation of the treatability of municipal waste landfill leachate in a SBR and by coagulation-flocculation on a bench scale", Brazilian Journal of Chemical Engineering, 33 (2016) 851-861.

[12]. Long Y., Xu J., Shen D., Du Y., Feng H., "Effective removal of contaminants in landfill leachate membrane concentrates by coagulation", Chemosphere, 167 (2017) 512-519.

[13]. Orescanin V., Ruk D., Kollar R., Mikelic I.L.,Nad K., Mikulic N., "A combined treatment of landfill leachate using calciumoxide, ferric chloride and clinoptilolite", J. Environ. Sci. Health A, 46 (2011) 323-328.

[14]. Maranon E., CastrillonL., Fernandez-Nava Y., Fernandez-Mendez A., Fernandez-Sanchez, A., "Coagulation–flocculation as a pretreatment process ata landfill leachate nitrification–denitrification plant", J. Hazard. Mater., 156 (2008) 538-544.

[15]. Garcia-Segura S., Ocon J.D., Chong M.N., "Electrochemical oxidation remediation of realwastewater effluents-A review", Process Safety and Environmental Protection, 113 (2018) 48-67.

[16]. Anglada A., Urtiaga A., Ortiz I., Mantzavinos D., Diamadopoulos E., "Boron-doped diamond anodic treatment of landfill leachate:Evaluation of operating variables and formation of oxidationby-products", Water Research, 45 (2011) 828-838.

[17]. FernandesA., PachecoM.J., CiríacoL., LopesA., "Review on the electrochemical processes for the treatment of sanitarylandfill leachates: Present and future", Applied Catalysis B, 176 (2015) 183-200.

MANAS Journal of Engineering
ISSN 1694-7398 | e-ISSN 1694-7398

Volume 9, Issue 2, (2021) Pages 129-135
https://doi.org/10.51354/mjen.918635

Toxicity of polyvinyl alcohols in medicinal chemistry

Orkun Dalyan[*1], Ömer Faruk Öztürk[2], Mehmet Pişkin[*3]

[1]Çanakkale Onsekiz Mart University, School of Graduate Studies, Department of Occupational Health and Safety, Çanakkale, Turkey, orkundalyan@outlook.com, ORCID: 0000-0003-4791-9084

[2]Çanakkale Onsekiz Mart University, Faculty of Arts and Sciences, Department of Chemical, Çanakkale, Turkey, ofozturk@comu.edu.tr, ORCID: 0000-0002-9244-6805

[3]Çanakkale Onsekiz Mart University, Vocational School of Technical Sciences, Department of Food Processing, Çanakkale, Turkey, mehmetpiskin@comu.edu.tr, ORCID: 0000-0002-4572-4905

ABSTRACT

Polyvinyl alcohol (Chemical Abstracts Service No: 9002-89-5), biodegradable, biocompatible, water-soluble, odorless, tasteless, transparent, white to creamy granular or powder appearance, and is a synthetic hydroxy polymer used in a broad variety of industrial, trading, medicinal and food implementations. The aim of this review is to back the safety of polyvinyl alcohol qua a coating agent for medicinal chemistry and dietary addition products, considering the current knowledge of polyvinyl alcohol. All available information on polyvinyl alcohol obtained from a comprehensive scientific literature review was seriously evaluated. Orally directed polyvinyl alcohol is comparatively harmless. The safety of polyvinyl alcohol when directed orally is based on: (a) Acute oral toxicity LD50 rates are in the range of 14.7–20 g/kg, very low, (b) is very poorly absorbed from the digestive system, (c) does not accumulate in the body, (d) the highest levels of polyvinyl alcohol with no observed adverse effects when directed orally in male and female rats, 5000 mg / kg body weight / day in a 90-day diet survey as the highest dose tested and 5000 mg / kg body weight / day was found in two generation reproductive studies.

ARTICLE INFO

Review article

Received: 17.04.2021
Accepted: 17.05.2021

Keywords:
polyvinyl alcohol,
toxicity,
medicinal chemistry,
dietary supplement,
coating material

**Corresponding author*

1 Introduction

Polyvinyl alcohol (PVOH) is an odorless, tasteless, transparent, biodegradable, biocompatible, water-soluble hydroxy synthetic polymer with a white to creamy granule or powder appearance [1]. With its high tensile strength, heat and chemical resistance, water solubility and flexibility properties, PVOH has been used in a broad variety of industrial, trading, medicinal and food implementations, including resins, varnishes, surgical threads and food contact implementations since the early 1930s. It is obtained by partial and complete hydrolysis of polyvinyl acetate. It is not toxic or carcinogenic. It shows stability in different temperature and pH ranges. Its resolution occurs at 80 ºC. It has the formula (C2H4O)x. Its density is 1.19-1.31 g / cm³ and its melting temperature is 230 ° C. [2,3].

The physical properties of PVOH depend on the process of preparedness from the hydrolysis or local hydrolysis of polyvinyl acetate (Figure 1). PVOH is usually divided into two groups, locally hydrolyzed (A) and completely hydrolyzed (B).

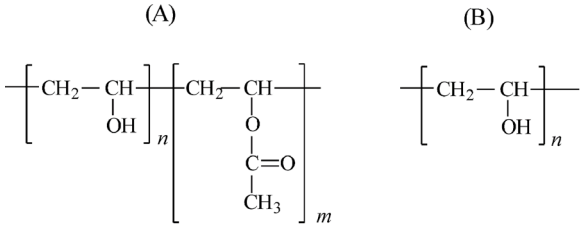

Changing the extent of the first vinyl acetate polymer and the grade of hydrolysis under alkaline or acidic conditions constitutes PVOH products of different molecular weights (20,000-400,000), solvability, elasticity, tensile force and stickiness. To characterize PVOH, various properties are determined like pH, viscosity, drying deprivation, melting point, refractive index, heavy metals and ruins in combustion. These characteristics change depending on the molecular weight and% hydrolysis for the degree of PVOH.

PVOH is involved in the Pharmaceutical Excipients Handbook. Identifications for pharmaceutical usage are supplied in Japanese Pharmaceutical Excipients, United States of America Pharmacopoeia / National Formulary and European Pharmacopoeia. Pharmaceutical grade PVOH must be produced under CGMP standards. Pharmaceutical grades further need lower impurities and residual solvent grades than industrial grades.

In the US, most of PVOH is used as a sizing and finishing agent in the textile industry. PVOH can further be included into a water-solvable cloth in the output of degradable preventive clothing, laundry bags for hospitals, diapers, sponges, sheets, coatings, and further physiological hygiene products.

PVOH is further broadly used in the output of paper products. Like with textiles, PVOH is applied as a sizing and coating agent. It ensures rigidity to these materials and becomes useful in tube wrapping, cardboard sealing and cardboard lamination. PVOH is used in paint and common household white glue. It is also used as a thickening agent in gypsum-based cements such as those used for ceramic tiles. PVOH is comparatively insolvable in organic solvents and its solvability in aqueous solutions can be adapted to its required implementation [4].

The US Food and Drug Administration (US FDA) allows PVOH to be used as an indirect food contribution in food contact products (Table 1).

Table 1. *PVOH approved food contact uses (US FDA)*

Section	Title
175.300	Resin and polymeric coatings
175.320	Resinous and polymeric coatings for polyolefin films
175.380	4-4′- Xylene-formaldehyde resins thickened with isopropylidene diphenol epichlorohydrin epoxy resins
175.390	Zinc-silicon dioxide matrix coatings
176.170	Paper and cardboard components that come into contact with aqueous and fatty foods
176.180	Paper and cardboard components in contact with dry food
177.1200	Selofan
177.1210	Sealed lids for food containers
177.1400	Hydroxyethyl cellulose film insoluble in water
177.2260	Resin-bonded filters
177.2800	Textile and textile fibers
178.3910	Surface lubricants used in the manufacture of metallic products
181.30	Substances used in the manufacture of paper and cardboard products used in food packaging

According to Federal Regulation 21 CFR 73.1 (b) (2), PVOH is confirmed as a diluent in color contribution mixtures to color shell eggs and further under Federal Regulation 21 CFR 349.12, PVOH is confirmed as an ophthalmic sedative of 0.1-4.0%.

PVOH is approved for use in the packaging of meat products by the Meat Inspection Division of the United States Department of Agriculture, and for use in the packaging of poultry products by the United States Department of Agriculture's Poultry Division. PVOH has been approved for use in a variety of medicinal implementations, involving the preparation of gels that dry quickly when applied to the skin, as well as prompt and sustained release tablet formulations. Cross-linked PVOH microspheres are further used for the controlled release of oral drugs. Ophthalmic solutions, like synthetic tears, may include PVOH as they ensure good dispersion and coating properties (2). PVOH is involved in the FDA Inactive Ingredients Guidelines for ophthalmic preparations and oral tablets. As an industrial and trading product, PVOH is rated for its solvability and biodegradability, which conduces to its truly low environmental effect. Various microorganisms ubiquitous in synthetic and natural environments like septic systems, garbage dumps, compost and soil that can degrade PVOH through enzymatic processes have been identified [4]. A compound of oxidase and hydrolase enzyme activities reduces PVOH to acetic acid, but not only the percentage of hydrolysis but its solvability impact the biodegradation grade of PVOH. There are further potential food uses for PVOH that are now being evaluated, involving uses in candy products and high humidity food products. The aim of this review is to back this crucial assessment of current knowledge on PVOH and the safety of PVOH as a coating agent for pharmaceutical and dietary supplement products.

2. Biological Data

Absorption, distribution and excretion of PVOH (mol. Weight <50,0001) was worked in male and female Fischer 344 rats [5]. Over 98% of a sole oral dose of 0.01mg / kg 14C-labeled PVOH directed to three male rats was saved in the feces within 48 hours of implementation. Less than 0.2% of the total dose was detected in urine. No radioactivity from PVOH was detected as expired 14CO2 or volatiles. There was no detectable tissue collecting. These data show that very little PVOH is absorbed from the gastrointestinal tract. To further evaluate the possible bio collecting, 0.1 mg / kg body weight / day of 14C-labeled PVOH was directed to three additional mice by gavage for 10 consecutive days. Similar consequences were found in the first study, almost all radioactivity saved 0.2% of the total dose in feces, urine and 0.05% of the total dose detected in major tissues (blood liver, kidneys, skin, muscle, and adiposis) [5].

3. Toxicity Studies

3.1. Acute toxicity

The consequences of the acute toxicity works are summarized in Table 2. These data suggest that orally directed PVOH would fall in the "comparatively harmless" category of the fewest concern [6].

Table 2. *PVA between acute oral LD 50*

Species	LD50 (mg / kg)	Reference
Rat	> 20.000 *	Zaitsev et al., 1986 [7]
Rat	21.500	Clydesdale, 1997 [8]
Mouse	147.000	Zaitsev et al., 1986 [7]
Mouse	> 4000 *	Burford and Chappel, 1968 [9]
Dog	20.000	Clydesdale, 1997 [8]

* The highest dose administered.

3.2. Dermal toxicity

Short-Term: Pure PVOH (1.0 ml / kg for 1000 mg / kg dose) was implemented to the shaved skin of 20 albino rats (10 of each breed) 5 days a week for 5 weeks and every day once a day (27 in total). Daily observations were made. Blood samples were taken after 16 hours of fasting. Animals were autopsied. No differences in body weights, and visual view were seen between cured and control animals. Mean hematocrit and red blood cell worth were notably under for cured men comparison to controls ($p < .05$). No change was found to be associated with PVOH treatment at autopsy [10].

Sub-Chronic: Ten female albino rats were cured 5 times per week for 13 weeks with a peelable face mask involving 13% PVOH. The test material was implemented to the shaved back skin. Because of the growing skin irritation and worries about the survival of the animals, a face mask was applied. It was erased after a 15-minute exposure in the 3rd week. Subsequently, the test standard was followed again. Skin irritation is balanced. After blood samples were taken at 6 and 13 weeks, hematological and serum chemistry parameters were measured. An autopsy was done. No important toxic impacts were found to be associated with the test material [11].

3.3. Parenteral toxicity

Short-Term: In a study by Hueper [12], 12 albino rats (70-88 g) obtained 20 injections (1 ml) of 5% PVOH solution over a period of 4 weeks. One of the 6 rats died during dosing, the remaining five mice were killed for autopsy after 2 weeks. The pathological changes of the animals killed 2 weeks after dosing were more violent. There was a significant quantity of PVOH at the injection site, consequence in necrosis and granulomatous purulent tissue. Very few of the applied PVOH was determined in lymph nodes. PVOH aggregates were concentrated in the glomeruli of the kidneys. PVOH was found to remain dispersed in the lumen of blood vessels of various organs and occlude the lumen by forming globules. Vascular occlusion was particularly seen in the lungs of some rats. Enlarged endothelial cells with foamy cytoplasm were seen in the occluded capillaries. Histiocytes in a variety of tissues involved PVOH in granular form. Of the parenchymal cells, those containing PVOH were the ganglion cells of the brain, renal tubular epithelium, and adrenal cortical cells. The spleens were darker red in color, moderate enlarged and hard. A grow in the number and swelling of Kupffer cells was observed in the liver of all rats. Other organs were quite normal but had little foam cell groups. Hueper (12) further applied 5% PVOH solution to three male rabbits at 10-15-25 doses for 5 days. Resulting were likewise those observed in rats, with the exclusion that the most violent and broad lesions were detected in the lungs, spleen, and testes following intravenous implementation, whereas the hypodermic route resulted in marked replaces in the kidneys, liver, and spleen.

Hall and Hall [13] conducted a hypertension work with female Houston-Cheek rats weighing 65-75g. He gave 1 ml of 5% PVOH solution in physiological saline daily for 28 days four groups of seven animals. While the test material was directed hypodermically to groups 1 and 2, it was directed intraperitoneally to groups 3 and 4. The PVOH used in the study had a mean molecular weight of 133,000. After the 28th day of dosing, treatment groups 2 and 4 were given an injection of 0.1 mg d-aldosterone-21 acetate twice daily in sesame oil for 7 successive days. Other groups were given vehicle injections only. Non-PVOH dosed control groups (5 and 6) received hormones in vehicle or were left uncured. Sufficient feed and water were ensured; systolic blood pressures were obtained regularly and besides before and after aldosterone implementation. Four animals died during the 28-day interval after the PVOH dose and before aldosterone or vehicle cure. The mean blood pressure of each group was: (1) 208, (2) 204, (3) 252, (4) 225, (5) 137, and (6) 141 mm Hg. Three animals further died after the week of aldosterone cure; One of these three animals in group 4 developed acute peripheral edema and ascites. Other animals were killed, organs were weighed, and tissues were analyzed microscopically. All rats in surviving groups 1 and 3 treated with PVOH and vehicle injections alone developed hypertension. Although the oppression increased from 208 to 213 mm Hg in group 1 animals, it stayed the same in group 3 animals. Except for PVOH implementation, a decrease in blood pressure was observed in rats treated with hormone only. Blood pressure in the animals in group 2 reduced from 204 to 187 mm Hg and in the animals in group 4 from 225 to 208 mm Hg. Blood pressures were comparatively unmodified between 141 and 136 mm Hg in group 5 and 137 to 128 mm Hg in group 6. In checks, aldosterone cure lonely did not induce or compound hypertension. At autopsy, the heart, liver, spleen, and kidneys of the PVOH-treated rats were importantly heavier than the other organs. Further, the heart

and kidneys were importantly heavier in rats treated intraperitoneally compared to those treated hypodermic. Adrenal glands were littler in animals treated with aldosterone. After all, the adrenal glands were importantly lesser in the PVOH groups than in the untreated controls. Remarkable histopathological changes involved dilated hepatic sinusoids in rats cured with PVOH, plentiful multinucleated huge cells in the livers of those cured intraperitoneally, large numbers of PVOH accrued in the spleen and kidneys and involved intense macrophage and huge cell proliferation. Hypertrophy, inflammatory changes and necrosis were present in the splenic arteries in rats with hypertension. Polyarteritis nodosa was detected in the pancreas of 5 of 13 rats given subcutaneous PVOH. In the hearts of rats treated intraperitoneally, foam cell transformation of the arterial site or foam cells was detected. Peritubular sclerosis and blown and ischemic glomeruli and thickened capillaries were observed in the kidneys of a few rats. He stated that no lesions could be particularly ascribed to aldosterone cure.

Riviere et al. [14] used pureblood Beagle dogs to define whether PVOH-induced toxicosis could give qua a model for glomerulonephritis. A silastic cannula was surgically implanted in the right outer jugular vein of four dogs. Three dog were dedicated daily injections owing to the cannula of 20 ml solutions including 47 mg PVOH/ml; the fourth dog was injected with saline. The PVOH used had a molecular weight of 125,000 and was 88% hydrolyzed. Blood samples were contained routine for the definition of blood urea nitrogen (BUN) and packed cell volume (PCV) rates. Urine samples were taken fortnightly. At the end of intervention, blood and urine samples were acquired for full analysis and autopsy was done. After 1 week of intervention, a reduce in PCV was watched. At the end of the study, the rates fell by 64% of the original rate. No changes in BUN were detected. A rise in the certain gravity of urine was detected; nevertheless, the rise lonely could not define the proteinuria which consisted by the end of the study. Body weight, feed consumption, and gastrointestinal task stayed normal. The study was finished after 3 weeks of dosing owing to low grade central nervous system (CNS) depression as specified by mutual depression of the extensor postural thrust, hopping, front limb placing, and rear limb righting reflexes. After the work cured animals had reduced total serum protein, sodium, potassium, and phosphorus concentrations. Hematologic analysis observed monocities, immature neutrophilia, marked polymorphonuclear leukocyte toxicity, reduced PCV, reduced hemoglobin, and reduced erythrocyte counts, slight anisocytosis, and many huge platelets. No gross lesions were detected. Light microscopic inspection observed diffuse vacuolation of the red pulp cells in the spleen and formation of foam cells in the glomeruli. No changes in the brain were detected. In electron micrographs, a granular sediment was present on the luminal surface of most endothelial cells. Mesangial cells and, to a less degree, endothelial and epithelial cells had cytoplasmic vacuolation. Because anemia and CNS depression happened before development of important renal injury, the analysts refused the usefulness of PVOH induced glomerulonephritis in the dog as a model for working glomerular disorders.

Hall and Hall [13] done a work using female Holtzman rats and three solutions of PVOH of diverse molecular weight to define the effect of the grade of polymerization. Groups of 12 rats taken daily hypodermic injections of 1 ml of 5% PVOH dissolved in physiological saline. The degrees of PVOH used had molecular weights of 37,000 (low), 133,000 (medium), or 185,000 (high). The fourth group became the control group and taken just vehicle. The animals were given feed and distilled water to drink as much as. It was measured hebdomadal blood pressures and everyday liquid intake of animals. Systolic pressures larger than 150 mm Hg were think hypertensive. So that it was investigated tissues and organs, these animals were killed after 29 days. PVOH was not determined in any of organs and tissues. Nonetheless it was determined that one third of the animals of cure group rise of blood pressure. The high molecular weight PVOH collected in a number of organs and tissues and reasoned puffing and multiplication of endothelial and epithelial cells of the renal glomeruli. One of the two the animals in the loud molecular weight cured group improved slight hypertension and some organs grown. The intermediate polymer was the just 1 out of 3 tested that made polydipsia. In the consequence nephrotic syndrome, ascites and oedema were come with by strong hypertension, evidenced renal harm with violent glomerulonephritis, and widespread cardiovascular lesions. Animals of this cured group finished on the mean more of the salt dispersion than them of the alternative groups. The analysts think about that molecular dimension rather than chemical structure effected the toxic effects and lesion development.

Carver et al. [15] recorded everyday hypodermic (1 ml) doses of 5% watery PVOH of mid molecular weight (133,000) directed for 21 days to male Sprague-Dawley rats resulted in a benign glomerulopathy with collecting of the macromolecule in the glomerular mesangium. These rats afterwards had an early temporal dose related sensibility to gentamicin nephrotoxicity. After all, after 12 days of daily dosing with gentamicin, no variation was discovered in the response of PVOH-cured rats as compared to non-cured controls.

Sub-Chronic: Burgener, Gutierrez, and Logsdon [16] used injections of PVOH spalls in male crossbred dogs to develop a model of hepatic cirrhosis. Portal hypertension and hepatic fibrosis were induced using PVOH in size from between 100-400 microns then the spalls were suspended using in 0.9% NaCl dispersion. To protect portal hypertension in 20 cm of water, injections of 0.1 to 0.9 g of PVOH once a week or two weeks were required. Sole doses to be given daily and per dog

were detected by portal vein pressure. The total dose requirements differentiated between dogs. It was from 0.8 g implementation over 22 months in the Four fraction to 4.8 g implementation over 6 months in the 14 fractions.

3.4. Short-term vaginal toxicity

A PVOH sponge was put into the vagina of each of three New Zealand white adult female rabbits weighing 4-5 kg and kept for 10 days [17]. After the animals were killed and the vaginas of each were investigated with light and electron microscopy. No differences were detected with light microscopy in the vaginal tissue as compared to samples from other controls. Microvilli electron microscopy and cell boundaries showed minimal irritation. A 30-day intravaginal PVOH study in B6C3F1 mice was done by the National Toxicology Program (NTP) [18]. Two groups of 50 female mice were cured with 25% PVOH implementations for 30 days (intravaginally daily). Animals of one group were kept for a few minutes following each implementation and only one control animal was treated with vehicle. As well as no deaths during dosing, no effects on body weight or total weight rise were found. Only some animals had vaginal irritation and expansion of the uterine horns.

3.5. Dermal irritation

Patches involving 0.3 ml of 10% PVOH in distilled water of unspecified molecular weight were implemented to groups of four female albino rabbits (Kb1: JW). The substance was implementation to the cut off back for 24-hours of contact. One group's skin was eroded. Skin affects were scored with respect to the Draize scoring system at the time of darn removal and 72 hours after removal. The Primary Irritation Index (PII) was 0.2 (maximum score 8.0). Erythema was noted at the 24-hour seen in three of four rabbits with eroded skin. No reaction was detected during the 72-hour observation [19]. No dermal irritation was observed in nine rabbits sustained once to undiluted PVOH in an occlusive darn. Watching were made at 2 and 24 hours after opening of wrapping. In another study on 6 rabbits following the alike method, irritation was minimum. In the 2-hour observation, it was stated that five animals had 1 point (maximum score 8). The reactions of three of the five animals continued at 1 point at 24-hour observation [20].

3.6. Dermal sensitization

A group of five Hartley albino pigs was used in a modified maximization test of 10% PVOH in fractionated water [21]. On the first day of induction, Freund's Complete Adjuvant (FCA) emulsified in distilled water, 10% PVOH in distilled water and 10% PVOH emulsified with FCA were injected intradermally into the nape. One week later, 10% sodium lauryl sulfate (SLS) in petrolatum was implemented to the region. One day following SLS cure, 0.2 ml of PVOH was implemented under a 48-hour occlusive darn. The control group of four animals was cured with distilled water following the same process. After 3 weeks following the first induction; 0.1 ml PVOH was implemented under an occlusive darn to the flank. Reactions were monitored 24 and 48 hours after implementation, but no reaction was seen.

3.7. Ocular irritation / toxicity

Knight and Link [22] researched diverse substances to find a proper coating for intraocular lenses (IOLS) made of polymethylmethacrylate (PMMA) in order to decrease corneal endothelial cell deprivation. To measure research, freshly cut rabbit corneas were contacted to the coating substance and then exposed to endothelial cell staining. On a scale of 0-4, with 0 being no damage and 4 being extensive damage (>50%); the uncured PMMA lens scored mean of 2.5 after static touch and mean of 3.6 after dynamic touch, and the PVOH cured cornea pointed mean of 0.7 after static touch and mean of 0.8 after dynamic touch. These analysts further notified three in vivo toxicity analysis for PVOH. In the first analysis, five times the quantity of PVOH as would a lens was injected into the front chamber of one sphere in each of 12 rabbits. Saline solution was injected into the other sphere as a control. Intraocular pressure (IOP), slot-lamp inspections and entire-eye microscopic works were applied routinely for 6 months. No important difference was observed between control and experimental eyes. In the second analysis, radioactive PVOH was injected into the front chamber of the eyes of 21 rabbits. In the tissue samples received, almost half of the directed dose was excreted in the urine within 48 hours by the kidneys after clearing the sphere within 45 minutes. PVOH was not determined in any organ, involving the sphere. In the third analysis, 20 IOLs (10 coated, 10 uncoated) were injected one-sidedly in 20 cats. A sham operation was applied on the toward eye. Endothelial cell calculates, IOP quantity's, pachymetry and slot lamp examinations were made for 6 weeks postoperatively. A decrease in endothelial cell deprivation was detected in gloves implanted with a coated lens. No other differences were observed between check and cured spheres [22]. Even an only drop of undiluted PVOH into the conjunctival bag of six rabbits did not reason irritation. After operation, eyes were not washed and marked using the Draize standard (maximum score 110). Similar conclusions were stated in another study [23] that a peel-off mask including 13.0% PVOH did not reason ocular irritation in six rabbits.

3.8. Reproduction toxicity

PVOH was implemented in the diet to male and female Sprague Dawley rats (26 / sex / group) at doses of 0, 2000, 3500 and 5000 mg / kg body weight / day for two generations. The work design rated the gonadal function, estrus cycle, mating behavior, conception, pregnancy, birth, breastfeeding, weaning and growth and development of F1 and F2 offspring. Parent rats were cured 70 days before mating, until sacrificed for the periods of mating, pregnancy and lactation. Clinical

observations, body weights and feed consumption were registered always. Dietary concentrations were arranged for each gender to reach the intended levels of mg / kg / day of PVOH on a weekly basis, except during pregnancy and lactation. Puppies were continuously weighed and weaned at 21 days before selection for the next generation. Shapeless faeces were recorded predominantly at levels of 3500 and 5000 mg / kg body weight / day in P0 and F1 parent animals. This finding was ascribed to high levels of PVOH that was fed and then excreted in the faeces. Slight reduces in mean body weights of P0 men were registered in 2000 and 5000 mg / kg / day. Feed consumptions rise primarily at cured levels of 3500 and 5000 mg / kg / day in both generations but did not rise in either lactation period. These rises were usually detected in a dose-dependent manner (g / kg / day) as a consequence of consuming large quantities of PVA to maintain the calorie intake required for normal growth. PVOH had no effect on P0 or F1 male or female reproductive performance or offspring survival, growth, organ weights, and macroscopic or microscopic watching. Dietary concentrations of PVOH 2000, 3500, and 5000 mg / kg / day for male and female rats did not reason any adverse toxicological or reproductive effects in parent animals (P0 and F1) or F1 and F2 offspring. The NOAEL for this work was 5000 mg / kg, the highest dose tested [24].

4. Results and discussion

All usable knowledge on polyvinyl alcohol from a comprehensive scientific literature review was critically evaluated. Oral polyvinyl alcohol is comparatively innocuous. The safety of polyvinyl alcohol is based on:

(a) The acute oral toxicity of polyvinyl alcohol is very low and the mean lethal dose rates are in the range of 15-20 g / kg;
(b) orally implemented polyvinyl alcohol is very weakly absorbed from the digestive system;
(c) when implemented orally polyvinyl alcohol does not accumulate in the body;
(d) polyvinyl alcohol is not mutagenic or clastogenic; and
(e) The highest levels of polyvinyl alcohol directed orally in male and female rats were 5000 mg / kg body weight / day and 5000 mg / kg body weight / day in two generations of reproductive work, the highest dose tested in the 90-day dietary work. Orally directed polyvinyl alcohol is safe and appropriate for it choose to use qua a coating for dietary addition and pharmaceutical product tablets and capsules. Polyvinyl alcohol can be used in high moisture foods to maintain the overall satisfactory taste, texture and quality of the foods. Confectionery products may further include polyvinyl alcohol to maintain the integrity of moisture sensitive ingredients. It is used as a moisture barrier film for food addition tablets and for dry food containing inclusions that must be maintained from moisture absorption, or food containing inclusions.

Acknowledgments

This study was supported by the Office of Scientific Research Projects Coordination at Çanakkale Onsekiz Mart University. Project number: FHD-2021-3364.

References

[1]. Köysüren NH., Köysüren Ö., "Preparation of Polyvinyl Alcohol Composite Nanofibers and Solid-Phase Photocatalytic Degradation Polyvinyl Alcohol", Journal of The Faculty of Engineering and Architecture of Gazi University, 33, (2018), 1411-1418.

[2]. Wade A., Handbook of Pharmaceutical Excipients, Weller PJ, Ed. American Pharmaceutical Association, Washington DC. 1994.

[3]. Rowe RC., Sheskey PJ., Handbook of Pharmaceutical Excipients. Owen SC, Ed. Pharmaceutical Press and American Pharmacists Association, Washington DC. 2006.

[4]. Isolyser Company, 1998. Isolyser Company, Inc. 4320 International Boulevard, NW, Norcross, GA.

[5]. Sanders JM., Matthews HB., "Vaginal Absorption of Polyvinyl Alcohol in Fischer 334 rats", Human and Experimental al Toxicology, 9. (1990), 71 – 77.

[6]. Hodge HC., Sterner JH., "Tabulation of Toxicity Classes", American Industrial Hygiene Association Quarterly, 10, (1949), 93-96.

[7]. Zaitsev NA., Skachkova IN., Sechenov IM., "Substantiation of Hygienic Standards for some Polymeric Compounds in Water with the Use of Gradual Standardization", Gig Sanit, 10, (1986), 75-76.

[8]. Clydesdale FM., Food Additives: Toxicology, Regulation and Properties. CRC Press, Boca Raton, FL. 1997.

[9]. Burford, RG, Chappel C, 1968. Range-Finding Acute Toxicity Studies of Polyvinyl Alcohol, Phthalic Acid and Cellulose Acetate Phthalate in the Mouse. Bio-Research Laboratories, Ltd., Point Claire, Quebec. For: Merck, Sharpe and Dohme Research Laboratories, West Point, Penn./Charles E. Frosst & Company, Montrél, Unpublished study.

[10]. CTFA. 1975. Six-week subacute dermal toxicity study in rats: Polyvinyl Alcohol. Unpublished data submitted by the CTFA, June 20, 1995. (8 pages).

[11]. CTFA. 1977. Safety evaluation of peel-off mask: containing 13% Polyvinyl Alcohol. Thirteen-week subchronic dermal toxicity study in rats. Unpublished data submitted by the CTFA, June 20, 1995. (9 pages).

[12]. Hueper WC., "Organic Lesions Produced by Polyvinyl Alcohol in Rats and Rabbits", Archives of Pathology, 28, (1939), 510–531.

[13]. Hall CH., Hall O., "Polyvinyl Alcohol Nephrosis: Relationship of Degree of Polymerization to Pathophysiologic Effects", Proceedings of the Society for Experimental Biology Medicine, 112, (1963), 86-91.

[14]. Riviere JE., Coppoc GL., Carlton WW., Hinsman EJ., "Polyvinyl Alcohol Toxicosis as a model of Glomerulonephritis in Beagle Dogs", American Journal of Veterinary Research, 41, (1980), 502 – 505.

[15]. Carver MP., Monteiro-Riviere NA., Brown TT., Riviere JE., "Dose-Response Studies of Gentamicin Nephrotoxicity in Rats with Experimental Renal Dysfunction. II. Polyvinyl Alcohol Glomerulopathy", Toxicology and Applied Pharmacology, 80, (1985), 264 – 273.

[16]. Burgener FA., Gutierrez OH., Logsdon GA., "Angiographic, hemodynamic, and histologic evaluation of portal hypertension and periportal fibrosis induced in the dog by intraportal polyvinyl alcohol injections", Radiology, 143, (1982), 379 – 385.

[17]. Chvapil M., Chvapil TA., Owen JA., Kantor M., Ulreich JB., Eskelson C., "Reaction of vaginal tissue of rabbits to inserted sponges made of various materials", Journal of Biomedical Materials Research, 13, (1979), 1–13.

[18]. National Toxicology Program (NTP). 1992. 30-Day intravaginal study of PVOH in B 16C3F mice. Study No. 688066. Research Triangle Park, NC: NTP.

[19]. Shiseido Research Center. 1978. Primary skin irritation: Polyvinyl Alcohol. Unpublished data submitted by the CTFA, July 17, 1995. (3 pages).

[20]. Cosmetic, Toiletry, and Fragrance Association (CTFA). 1974. Primary skin irritation: Polyvinyl Alcohol. Test # 06-183. Unpublished data submitted by the CTFA, June 20, 1995. (1 page).

[21]. Shiseido Research Center. 1977. Contact allergenicity: Polyvinyl Alcohol. Unpublished data submitted by the CTFA, July 17, 1995. (3 pages).

[22]. Knight PM., Link WJ., "Surface Modification of Intraocular Lenses to Reduce Corneal Endothelial Damage", American Intra-Ocular Implant Society Journal, 5, (1979), 123 – 130.

[23]. CTFA. 1980. Eye irritation: Polyvinyl Alcohol. Test # 47-093. Unpublished data submitted by the CTFA, June 20, 1995. (1 page).

[24]. Colorcon. 2001. Polyvinyl Alcohol (PVA): Study of the Effects of PVA on Fertility, Early Embryonic Development to Weaning, and the Growth and Development when Directed in the Diet to Rats.

MANAS Journal of Engineering
ISSN 1694-7398 | e-ISSN 1694-7398

Volume 9, Issue 2, (2021) Pages 136-141
https://doi.org/10.51354/mjen.910090

Study on antimony cake as a technogenic raw material for the production of antimony oxides

Zarlyk Maimekov [1], Zhyldyz Tunguchbekova [2], Kubat Kemelov*[1], Uran Maimekov[3], Damira Sambaeva[2]

[1]Kyrgyz-Turkish Manas University, Engineering Faculty, Department of Environmental Engineering, Bishkek, Kyrgyz Republic, kubat.kemelov@manas.edu.kg, ORCID:0000-0001-7375-6325

[2]Kyrgyz State University of Geology, Mining and Natural Resources Development, Bishkek, Kyrgyz Republic

[3]Moscow Institute of Physics and Technology, Dolgoprudny, Russia

ABSTRACT

In the process of hydrometallurgical and pyrometallurgical production of antimony at the Kadamzhai antimony plant of the Kyrgyz Republic, large-tonnage waste was generated: tailing sand, matte, slag, off-balance ore, cakes, furnace fragments, and electrolytes in salt warehouses. The waste cake is poorly studied; accordingly, the elemental and phase compositions of antimony cake have not been established. In this regard, it was noted that antimony in the cake occurs in the form of calcium antimonate and antimony hydroxide. The content of antimony in the mine tailings cakes is from 3.53 to 4.4%, with a high content of iron (27.5%) and sodium (8.86%). Based on the established elemental and phase compositions, a chemical matrix of antimony cake was compiled. The equilibrium compositions were calculated and the concentration distribution of the main elements of the cake (Fe, Na, Si, Sb) and their compounds in the gas phase was found depending on the temperature of the destruction of the solid phase. It was found that condensed antimony oxides are formed in the range of 1098 - 1348 K. Taking into account the range of temperatures for decomposition of the solid phase, a two-stage smelting of antimony cake is proposed (melting and cupellation). The conversion of antimony cake sulfides from the gas phase into a solution was carried out based on a study of the system: antimony sulfide- manganese (IV) dioxide- sulfuric acid - sodium chloride. The pH value and the redox potential (Eh) of the solution were calculated. It is noted that the sulfur compounds of antimony from the cake are converted to antimony oxychloride with the formation of antimony (III) oxide in an alkaline medium. The use of sodium chloride as a chlorinating agent of antimony sulfur compounds does not lead to the formation of toxic phosgene and hydrogen sulfide; in the solid phase, elemental sulfur is released, which is important for minimizing the technogenic load of pollutants on the environment.

ARTICLE INFO

Research article

Received: 6.04.2021
Accepted: 21.06.2021

Keywords:
Kadamzhai antimony,
antimony cake,
modeling,
complex system,
waste,
environment

**Corresponding author*

1 Introduction

Antimony cake is an insoluble solid obtained in the process of extracting valuable components from ore. Currently, considerable attention is paid to the environmental problems of the chemistry and technology of antimony and its compounds [1-17]; environmental pollution with antimony wastes [1, 13, 16]; behavior of antimony in swampy groundwater [2]; antimony waste and dust emissions during smelting process [3, 14, 17]; environmental risks [4] and removal of antimony in water by electrocoagulation [5]; accumulation and transformation of antimony in the environment [5]; removal of antimony (III) by adsorption using carbon nanotubes and bimetallic oxide polymer anion exchange resin, adsorption of Sb (V) on the surface of binitite and ferrihydrite; geochemistry of antimony mobility and transport [6-9, 11].

It is noted that the cakes of the tailing dump are multicomponent and occur in the form of a technogenic formation. Environmental problems of industrial waste, including the production of antimony, are very important [10]. In particular, the assessment of pollution in the area of antimony mining, prevention of the process of waterlogging of spent electrolytes and their seepage into groundwater, reduction of the destruction of antimony by plants and soil of systematic scientific and practical research. In this study, to predict the processes of chemical transformation of the solid

phase and the formation of antimony oxide (III), the physicochemical principles of the destruction of waste antimony cake in a gas-liquid oxidizing medium were considered based on experimental analyzes of antimony cake examples of the Kadamzhai antimony plant (KAP).

2. Material and methods

The main elemental composition of the antimony cake, formed in the KAP, was determined by an atomic absorption spectrometer AAnalyst 800 (Perkin Elmer, USA). An ICP OES Optima 7000 optical emission spectrometer with inductively coupled plasma was used to detect small impurities of individual elements. The processing of the diffraction pattern and the calculation of interplanar distances were carried out using the EVA software. Sample decoding and the search for phases were performed with "Search / Match" program using the PDF-2 powder diffractometric database (Fig. 1) [18]. The study of the process of oxidation and destruction of antimony cake in oxygen at different temperatures was carried out by the method of thermodynamic modeling of the system at maximum entropy using the "Terra" program [19]. Methodical calculation algorithm equilibrium of formation of gaseous, condensed substances, electrically neutral and ionized components, pure phases, and their solutions. The equilibrium of the studied system was achieved at the maximum entropy relative to the thermodynamic degrees of freedom (M, T, P). Specific volume (V) and internal energy (U) are related to the concentration of components in the filter cake, as well as temperature and pressure. The pressure value and the temperature limits of the decomposition of the solid phase were given. The elemental composition of the cake was experimentally determined per 1 kg of the carrier (mol/kg).

It is noted that antimony cake consists of complex independent components. The destruction of the cake in the gas phase proceeds with the formation of individual low molecular weight components, atomic and ionic particles. Therefore, the phase transition of the components was taken as a chemical reaction, and the number of independent reactions was equal to the number of components. In this case, the reactions were chosen as independent reactions, in which the distribution of the concentrations of individual independent elements (Fe, O, Si, S, Na, Ca, Sb, H, Al, Mg) was taken into account. The physicochemical and thermodynamic parameters of the system antimony cake - oxygen were calculated at P = 0.1 MPa, T = 298-3098 K (with a step of 200 K). The calculation of entropy from the values of ΔS, ΔH, Cp, T, made it possible to determine the changes in the Gibbs energy ($\Delta G_T = \Delta H_T - T\Delta S_T$), and the transition from ΔGT to the equilibrium constant (K) was carried out according to the formula ΔG = -RTlnK [19].

3. Results and discussion

In the scope of this study, the elemental and phase compositions of the KAP antimony cake were examined (Table 1, Figure 1). As the results showed, the content of antimony in the mine tailings cakes ranged from 3.53 to 4.42%. Besides, high levels of iron (27.5%) and sodium (8.86%) were detected.

The phase composition of antimony cake, obtained by semi-quantitative X-ray phase analysis, showed (Fig. 1) that the main minerals are hematite - cristobalite (Fe_2O_3 SiO_2), pyrites (FeS_2), magnetite (Fe_3O_4), hexasodium iron tetrasulfate $Na_6Fe(SO_4)_4$, pyrrhotite ($Fe_{1.05}S_{0.95}$), calcium antimonate $CaNaSb_2O_6(OH)$-calcium oxide CaO, antimony hydroxide $SbSb_2O_6(OH)$, sodium aluminate ($NaAlO_2$), periclase (MgO); the composition of the gas phase is 100% oxygen.

Table 1. *Elemental composition of antimony cake of the KAP (in ppm) according to the atomic absorption spectrometer*

Sample cake	Concentration, ppm	Sample cake	Concentration, ppm
As	10256.5	**Mo**	0.9
Cd	29	**Ni**	94
Cr	84	**Pb**	8292.5
Cu	893.5	**Zn**	3294.5
Hg	4.5	**Sb**	44221

Antimony in antimony cake occurs in the form of calcium antimonate $CaNaSb_2O_6(OH)$ and antimony hydroxide $SbSb_2O_6(OH)$. Based on the experimentally found elemental and phase compositions of antimony cake (Table 1 and Fig. 1), the chemical matrix of the antimony cake was compiled (in %): $Fe_2O_3SiO_2$ (25.5) - FeS_2 (21.2) - Fe_3O_4 (12.4) - $Na_6Fe(SO_4)_4$ (12.1) - $Fe_{1.05}S_{0.95}$ (11) - $CaNaSb_2O_6OH$ (8.2) , CaO (1.67) - $SbSb_2O_6OH$ (5.4) - $NaAlO_2$ (2.65) - MgO (0.13). Taking into account the chemical matrix of antimony cake, thermodynamic modeling of the process of destruction of antimony cake in an oxygen medium was carried out, and temperature ranges of the formation and chemical transformation of antimony-containing components and particles in the gas phase were revealed.

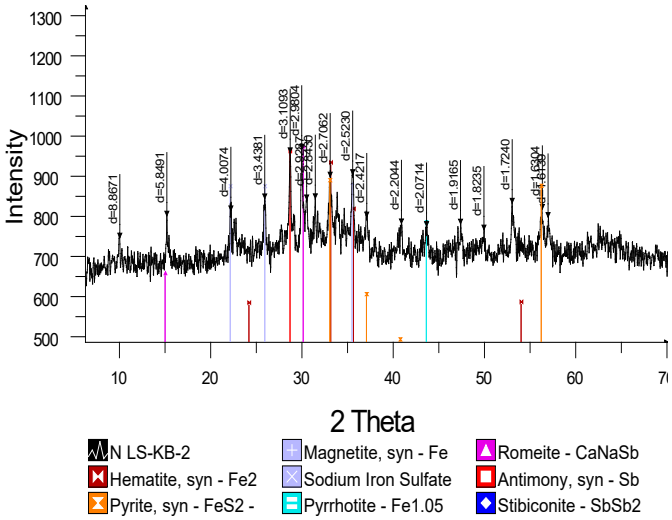

Figure 1. *Diffractogram of the KAP antimony cake*

The calculated partial pressure of oxygen in the antimony cake - oxygen system was 0.084 MPa at 298K; 0.084 MPa at 848K; 0.084 MPa at 1448K; 0.078 MPa at 2298K and 0.060 MPa at 3048K, that is, in the range of 298-1448K, P_{O2} was equal to 0.084 MPa; molar concentration of oxygen in the gas phase at various temperatures was as follows: 10.88 mol/kg at 298K; 10.88 mol/kg at 848K; 10.88 mol/kg at 1448K, i.e in the temperature range of 298-1448K C_{O2} is 10.88 mol/kg, and P_{O2} is 0.084 MPa (constant), which reflects the conditions of existence of the studied system. Thus, further calculations were carried out at a pressure of 0.1 MPa. It should be noted here that the temperature range from 298 to 3100 K (Fig. 2) in the computational experiments was selected based on the temperature of combustion, decomposition, and melting of the main components of the antimony cake. Also, the formation of active particles and ions in the gas phase (Fe, Tm=1812 K; Na, Tm =371 K; Sb, Tm =904 K; Si, Tm =1688 K; Ca, Tm =1115 K; Al, Tm =933 K; Mg, Tm =923K, Tm is a melting temperature) were taken into consideration.

During the high-temperature decomposition of the antimony cake in the gas phase, the following components were formed: Sb, SbO, SbH, Sb_4O_6, Sb_2O4 (c), Sb_2O_5 (c), Sb_2, Sb_3, Sb_4, Sb-, SbO_2-, SbS, SbO_2 (Table 2).

Table 2. *Equilibrium compositions and concentrations of Sb-containing components and cake particles at various temperatures of the destruction of the solid phase*

C, mol/kg	T, K			
	1648	**2048**	**2348**	**2698**
Sb	$4\cdot10^{-7}$	$1\cdot10^{-3}$	$1\cdot10^{-2}$	$3.1\cdot10^{-2}$
Sb_2	$6\cdot10^{-11}$	$5\cdot10^{-6}$	$5\cdot10^{-1}$	$6\cdot10^{-5}$
Sb_3	-	$1\cdot10^{-9}$	$2\cdot10^{-8}$	$2\cdot10^{-8}$
Sb_4		$1\cdot10^{-12}$ (2098K) – $1\cdot10^{-12}$ (2648K)		
Sb^-	-	$3\cdot10^{-10}$	$5\cdot10^{-8}$	$6\cdot10^{-7}$
SbO_2^-	$6\cdot10^{-10}$	$2\cdot10^{-6}$	$2\cdot10^{-5}$	$1\cdot10^{-5}$
SbO	$6\cdot10^{-4}$	$1.4\cdot10^{-1}$	$3.5\cdot10^{-1}$	$3.2\cdot10^{-1}$
SbH	$6\cdot10^{-9}$	$8\cdot10^{-5}$	$1\cdot10^{-3}$	$1.1\cdot10^{-2}$
SbS	-	$1\cdot10^{-8}$	$7\cdot10^{-7}$	$9\cdot10^{-6}$
SbO_2	$5\cdot10^{-7}$	$9\cdot10^{-5}$	$2\cdot10^{-4}$	$2\cdot10^{-4}$
Sb_4O_6	$9\cdot10^{-2}$	$5.6\cdot10^{-2}$	$2\cdot10^{-5}$	$6\cdot10^{-10}$
Sb_2O_4(c)		$1.82\cdot10^{-1}$ (1098K) – $3.64\cdot10^{-2}$ (1348K)		
Sb_2O_5(c)		$1.82\cdot10^{-1}$ (1048K)		

Figure 2 shows the equilibrium compositions and concentrations of the main antimony-containing components, including the condensed phases of Sb_2O_4 (c), Sb_2O_5 (c) during the decomposition of antimony cake. Here, the concentration of the condensed phase was in the range of 10-2 mol/kg. and for low molecular weight particles and ions, such as Sb_2, Sb_3, Sb_4, Sb-, SbO_2-, the concentration ranged from 10^{-12} to 10^{-4} mol/kg (Table 2).

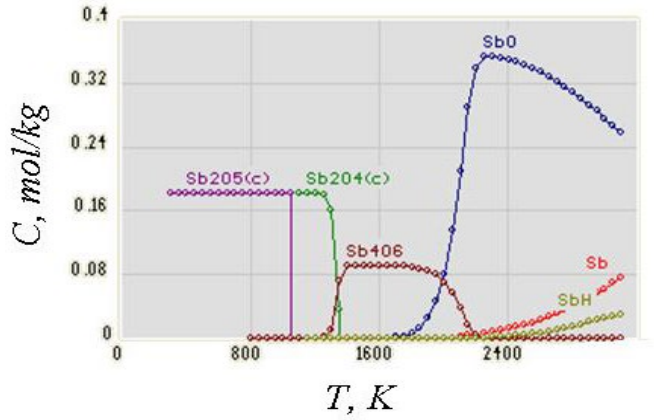

Figure 2. *Concentrations of Sb containing components and particles in the gas phase depending on the decomposition temperature of the cake*

The experimental results show that some condensed substances like Sb_2O_4(c), Sb_2O_5(c) can be formed at a temperature of 1048 K (Table 2), and particles (Sb, Sb_2, Sb_3, Sb_4) and ions (Sb^-, SbO_2^-) are formed at high temperatures up to 3000 K (Fig. 2, Table 2). Table 2 shows the maximum temperature that needs to be reached in the process of Sb-cake destruction equals 1812 K. Thus, the chemical transformation of antimony-containing condensed substances proceeds at1348 K. As mentioned above, the formation of atomic-molecular (Sb, Sb_2, Sb_3, Sb_4) and ionic particles (Sb^-, SbO_2^-) in the gas phase were detected at higher temperatures (Fig. 2).

Table 2 shows only negative ions of antimony, while the results of decomposition of the antimony cake at high temperatures showed the formation of negative and positive ions (mol/kg), for example, at 2698 K: $O^- = 0{,}25\cdot10^{-4}$, $O_2^- = 0{,}23\cdot10^{-4}$, $H^- = 0{,}73\cdot10^{-8}$, $OH^- = 0{,}55\cdot10^{-5}$, $HO_2^- = 0{,}18\cdot10^{-7}$, $S^- = 0{,}14\cdot10^{-6}$, $S_2^- = 0{,}74\cdot10^{-10}$, $SO^- = 0{,}12\cdot10^{-5}$, $SO_2^- = 0{,}12\cdot10^{-3}$, $SH^- = 0{,}17\cdot10^{-8}$, $Sb^- = 0{,}56\cdot10^{-6}$, $SbO_2^- = 0{,}15\cdot10^{-4}$, $Al^+ = 0{,}12\cdot10^{-11}$, $AlO^- = 0{,}40\cdot10^{-5}$, $AlO_2^- = 0{,}53\cdot10^{-5}$, $Fe^+ = 0{,}52\cdot10^{-9}$, $Mg^+ = 0{,}46\cdot10^{-10}$, $Ca^+ = 0{,}31\cdot10^{-10}$, $CaO^+ = 0{,}65\cdot10^{-10}$, $CaOH^+ = 0{,}37\cdot10^{-9}$, $Na^+ = 0{,}76\cdot10^{-3}$, $Na_2O^+ = 0{,}9\cdot10^{-7}$.

It was found that during the destruction of the antimony cake of the KAP condensed antimony oxides are formed in the range of 1098-1348 K (Table 2). Based on the range of formation and transformation of the condensed phase, a two-stage smelting of antimony cake was proposed. A sample of antimony cake was placed into a ball mill. Then, the crushed sample was subjected to batching (70% glut / PbO / +20% soda + 10% borax) in the cake - the ratio of the mixture was set 1: 3. The mixture was mixed with flour (1-3 g) and silver nitrate (0.2 ml). Flour was used to stabilize an acidic medium (borax is used in an alkaline medium); lead oxide was used to produce a lead alloy (crude lead), and silver nitrate was used to absorb noble metals from the cake. The resulting mixture was mixed until a homogeneous mixture was obtained. This mixture was loaded into fireclay crucibles. In the furnace, the mixture started melting at the temperature of 1328-1473 K (45-50 min.). At the initial stage of smelting (30 min), the sample melted at a temperature of 1203-1303K.

At the initial stage of melting (30 min) at a temperature of 1203-1303 K, the sample melted with the formation of a lead melt and the release of gaseous products (sulfide sublimation). Within 20 minutes, drops of liquid lead melt completely covered the antimony cake. After 50 minutes, the multi-component melt was poured into cast-iron molds and the latter cooled in the air (10-15 minutes). In primary smelting, many metals and their impurities, including precious ones, are absorbed by the lead-silver collector. Thus, a lead alloy was formed - crude lead, which was covered with quartz slag. This quartz slag was cleaned off from the surface of the lead alloy with a hammer. At the second stage of melting (cupellation), the furnace was heated to a temperature of 1253 K. For this, the crude lead was preheated (1173 K) for 10-15 minutes (the melting point of lead is 600 K). During the cupelling process, the white finely porous surface of the crucible turns yellow due to the sorption of some alkaline, alkaline-earth, and other metals in the cake, including lead (at temperatures below 800 K). At the bottom of some crucibles, an alloy of antimony with metal impurities (Ag) remained, which melt above 800 K (melting temperatures of antimony are equal to 904 K). The silver-antimony glance glares brightly when the last particles of lead are removed from its surface. It means the end of the cupellation process of the lead alloy. To transfer the sulfide sublimate of antimony cake to the solution, the following system was studied: antimony sulfide – manganese dioxide (IV) – sulfuric acid – sodium chloride within the temperature ranged from 288 K to 358 K and pressure of $P=10^5$ Pa with the minimal Gibbs energy based on the program “Selector” [20].

The values of pH and Eh of solution in a wide temperature ranges (288 K, pH=2.05, Eh=1.14 V; 298 K, pH=1.96, Eh=1.15 V; 318 K, pH=2.02, Eh=1.13 V; 338 K, pH=2.14, Eh=1.12 V; 358 K, pH=2.3, Eh=1.1 V) were calculated. The pH of the solution ranged between 1.96 and 2.3; the ionic strength was equal to 10, the oxidizing medium was greater than zero (Eh> 0). It was noticed that antimony compounds (sublimates of sulfur of the type: SbS, Sb2S3) from the cake pass into antimony (III) chloride according to the following reaction [14]:

$$Sb_2S_3+3MnO_2+6H_2SO_4+12NaCl=2SbCl_3+3MnCl_2+6Na_2SO_4+3S\downarrow+6H_2O.$$

Antimony trioxide can be obtained by hydrolysis of antimony chloride followed by dehydration of the resulting methantimonic acid.

$$2SbCl_3 + 3Na_2CO_3 + H_2O = 2HSbO_2 + 3CO_2 + 6NaCl$$
$$2HSbO_2 = Sb_2O_3 + H_2O.$$

A solution of antimony trichloride in a mixture of HCl and water was slowly poured into a boiling solution of Na_2CO_3 $10H_2O$. The mixture was boiled until CO_2 is completely removed, then the liquid was carefully decanted. The precipitate was sucked off, washed with hot water until the complete absence of chlorine ions in the washings, and dried at 150 °C until constant weight (80% yield). Antimony pentoxide was obtained through the interaction of Sb_2O_3 and oxygen.

The results of the research showed that the pH value of the working solution at 298 K was equal to 1.96, and Eh = 1.15 V, which means that the medium was acidic. When sodium chloride was used, hydrogen chloride was formed as a chlorinating agent during the intramolecular chemical transformation of the starting components. No toxic phosgene and hydrogen sulfide were formed in the reaction medium; elemental sulfur was deposited, which plays a vital role in minimizing technogenic loads of pollutants on the environment.

4. Conclusions

In antimony cake, antimony occurs in the form of calcium antimonate and antimony hydroxide. Taking into account the temperature of the formation of condensed antimony oxides (1098-1348K), in the study, a two-stage smelting of antimony cake was performed (smelting and cupellation). Acid sublimates of antimony cake were placed in a mixture of manganese dioxide (IV), sulfuric acid, and sodium chloride solute to gradually obtain antimony chloride (III) and antimony chloroxide (SbOCl). Emission of antimony oxide (III) was observed during the interaction of antimony oxychloride with ammonium hydroxide. The use of sodium chloride as a chlorinating agent eliminated the possibility of the formation of toxic phosgene and hydrogen sulfide in the reaction medium.

References

[1]. He M.C., Wang X.Q., Wu F.C., Fu Z.Y., “Antimony pollution in China”, Science of the Total Environment, 421-422, (2012), 41-50.

[2]. Wan X.M., Tandy S., Hockmann K., Schulin R., “Changes in Sb speciation with waterlogging of shooting range soils and impacts on plant uptake”, Environmental Pollution, 172, (2013), 53-60.

[3]. Xuejun G., Kunpeng W., Mengchang H., Ziwei L., Hailin Y., Sisi L., “Antimony smelting process generating solid wastes and dust: Characterization and leaching behaviors”, Journal of Environmental Sciences, 26, (2014), 1549-1556.

[4]. Wilson S. C., Lockwood P. V., Ashley P. M., Tighe M., “The chemistry and behavior of antimony in the soil environment with comparisons to arsenic: A critical review”, Environmental Pollution, 158, (2010), 1169-1181.

[5]. Yang H., He M., Wang X., “Concentration and speciation of antimony and arsenic in soil profiles around the world’s largest antimony metallurgical area in China”, Environmental Geochemistry and Health, 37(1), (2014), 21-33.

[6]. Zhu J., Wu F., Pan X., Guo J., “Removal of Antimony from Antimony Mine Flotation Wastewater by Electrocoagulation With Aluminum Electrodes”, Journal of Environmental Sciences, 23. (7), (2011), 1066-1071.

[7]. Miao Y., Han F., Pan B., Niu Y., Nie G., Lv L., “Antimony (V) removal from water by hydrated ferric oxides supported by calcite sand and polymeric anion exchanger”, Environmental Sciences, 26, (2014), 307-314.

[8]. Li X., Dou X., Li J., “Antimony(V) removal from water by iron-zirconium bimetal oxide: Performance and mechanism”, Journal of Environmental Sciences, 24(7), (2012),1197-1203.

[9]. Qi P.F., Pichler T., “Sequential and simultaneous adsorption of Sb (III) and Sb(V) on ferrihydrite: Implications for oxidation and competition”, Chemosphere, 145, (2016), 55-60.

[10]. Indika H., Meththika V., Jochen B., “Antimony as a global dilemma: Geochemistry, mobility, fate and transport”, Environmental Pollution, 223, (2017), 545-559.

[11]. Wang H.W., Li X.Y., Li W.H., Sun Y.L., “Effects of pH and complexing agents on Sb(V) adsorption onto binessite and ferrihydrite surface”, Environmental Science, 38, (2017),180-187.

[12]. Bolshakov L.A., Salimzhanova E.V., Yuryev A.I., “Studies on the possibility of reducing the content of non-ferrous metals in mine tailings ferrous cakes”, Ore and metals, 6, (2013), 65 - 68.

[13]. Maymekov Z.K., Sambaeva D.A., Shabdanova E.A., “Ecological aspects of antimony production and some ways to minimize the formation of man-made waste in them”, KNAU Bulletin, 2 (29), (2013), 227-228.

[14]. Solozhenkin P.M., Zinchenko Z.A., "Enrichment of antimony ores", Nauka, 1985, 180

[15]. Ochurool A.P., Shoeva T.N., The study of the composition and properties of the cake, Collected Works of Tuva State University, 2015, 198-199.

[16]. Kozhonov A.K., Nogayeva K.A., Molmakova M.S., "Review and classification of industrial wastes from ore deposits of the Kyrgyz Republic", News KSTU. I.Razzakov, 3(39), (2016), 259 - 263.

[17]. Akimenko D.O., Pashkevich M.A., "Estimates of the influence of the cake mine tailings on the components of the environment and the possibility of its full processing, as a technogenic deposit of CJSC ZSU", Mountain science and technology, 8, (2011) 3-8.

[18]. Knyazev A.V., Suleymanov E.V., Fundamentals of X-ray phase analysis. Study guide. Nizhny Novgorod, 2005, 23

[19]. Trusov B.G., Badrak S.A., Turov V.P., Baryshevskaya I.I., "Automated system of thermodynamic data and calculations of equilibrium states", Mathematical methods of chemical thermodynamics, (1982), 213-219.

[20]. Karpov I.K., Chudnenko K.V., Kulik D.A., Bychinskii V.A., "The convex programming minimization of five thermodynamic potential other than Gibbs energy in geochemical modeling", Amer. J. Sci, 302, (2002), 281-311.

MANAS Journal of Engineering
ISSN 1694-7398 | e-ISSN 1694-7398

Volume 9, Issue 2, (2021) Pages 142-152
https://doi.org/10.51354/mjen.980286

Boric acid versus boron trioxide as catalysts for green energy source H_2 production from sodium borohydride methanolysis

Sahin Demirci[1], Betul Ari[1], Sultan B. Sengel[2], Erk Inger[3], Nurettin Sahiner*[1,2,4]

[1] Department of Chemistry, Faculty of Sciences & Arts, and Nanoscience and Technology Research and Application Center (NANORAC), Canakkale Onsekiz Mart University Terzioglu Campus, Canakkale, 17100, Turkey, sahiner71@gmail.com, ORCID: 0000-0003-0120-530X

[2] Canakkale Onsekiz Mart University, Faculty of Sciences and Arts, Chemistry Department, 17100-Canakkale, Turkey

[3] Atilim University, Airframe and Powerplant Maintenance Department, Incek, Ankara, 06839, Turkey

[4] Department of Chemical & Biomedical Engineering, and Materials Science and Engineering Program, University of South Florida, Tampa, FL 33620, USA.

ABSTRACT

Here, boric acid (H_3BO_3) and its dewatered form, boron trioxide (B_2O_3) were tested as catalysts for hydrogen (H_2) evolution in the methanolysis of sodium borohydride ($NaBH_4$) in methanol. Parameters such as catalyst types and their amounts, $NaBH_4$ concentration, and the reaction temperature affecting the hydrogen generation rate (HGR) were studied. It has been found that H_3BO_3 and B_2O_3 catalyzed methanolysis reaction of $NaBH_4$ follow up first-order kinetics relative to the concentration of $NaBH_4$. Furthermore, the conversion and activity of these catalysts were examined to determine their performance in ten consecutive use. Interestingly, H_3BO_3 and B_2O_3 have demonstrated superior catalytic performances in methanolysis of $NaBH_4$ comparing to the studies published in literature with the activation energy of respectively 22.08 kJ.mol^{-1}, and 23.30 kJ.mol^{-1} in H_2 production. The HGR was calculated as 6481 mL.min^{-1}.g^{-1} and 5163 mL.min^{-1}.g^{-1} for H_3BO_3 and B_2O_3 catalyst, respectively for 50 mg catalyst at 298 K. These results are comparably better than most metal nanoparticle catalysts used for H_2 production in addition to the naturally occurring boron-based environmentally friendliness of these materials.

ARTICLE INFO

Research article

Received: 8.09.2021
Accepted: 28.10.2021

Keywords:
boric acid,
boron oxide,
catalyst,
hydrogen production,
$NaBH_4$ methanolysis,
natural catalyst

*Corresponding author

1. Introduction

The energy need with the industrial development is on the rise. The environmental anxieties from fossil fuel consumption along with the pursue of cleaner and high energy density materials help to pave the roads for fast hydrogen (H_2) production systems from various new sources [1-4]. H_2 energy systems have vital importance as substitutes for fossil-based fuels due to their many superior characteristics. H_2 fueling the sun is the most abundant element in the universe and can be stored in different physical forms with their complications. For instance, H_2 storage and delivery in gas and/or in liquid forms is not easy as it requires huge volume and compressing problems [5-9]. In that respect, chemical hydrides such as sodium borohydride ($NaBH_4$) is one of the most commonly employed benign hydrides as the best known and the most studied H_2 storage material. Having a relatively high gravimetric hydrogen content of nearly 10.8% and the suitability for hydrolysis and methanolysis reactions make $NaBH_4$ a pretty attractive substrate for H_2 generation applications. The reaction of $NaBH_4$ with water and methanol can be described as follows:

$$NaBH_4 + 2H_2O \rightarrow NaBO_2 + 4H_2 \uparrow + heat\ (-300\ kJ.mol^{-1}) \quad (1)$$

$$NaBH_4 + 4CH_3OH \rightarrow NaB(OCH_3)_4 + 4H_2 \uparrow \quad (2)$$

From the reactions in Eq (1) and Eq (2) of $NaBH_4$, methanol has some advantages over water: a) the kinetic reaction realizes faster in methanol, b) methanol offer higher catalytic activities than water at lower temperatures (subzero temperatures) owing to the low melting point of methanol (-97.6°C), c) by comparison of by-products e.g., $NaBO_2$ versus $NaB(OCH_3)_4$, there is a lesser problem in the methanolysis reactions and easy/possible to reconversion to the reactant. The use of an appropriate catalyst system plays a significant role in accelerating and/or controlling H_2 generations from

hydrolysis and methanolysis reactions [10-13]. Many different types of catalyst such as metal catalyst [14-20], polymeric particles and materials [21-23], polymeric ionic liquids [24, 25], and composite catalyst [26-28] as well as acid catalyst [29-31] for $NaBH_4$ hydrolysis and methanolysis were reported. Methanolysis reaction of $NaBH_4$ is well-known for acid catalysis, directly or indirectly e.g., increasing proton numbers in the reaction media affect the H_2 generation rate positively [31, 32]. Here, boron chemicals such as boric acid and boron oxide were employed the methanolysis of $NaBH_4$ as catalysts, and their catalytic activities were determined and compared.

Boric acid (H_3BO_3) is considered as an environmentally friendly reagent used in boron oxide or boron trioxide (B_2O_3) preparation. Dewatering of boric acid starts at around 80 °C, and the first reaction is completed at around 130 °C. Reactions slow down at around 450 °C [33, 34].

$$H_3BO_3 \leftrightarrow HBO_2 + H_2O \quad (T < 130\,°C) \quad (3)$$

$$HBO_2 \rightarrow 1/2\,B_2O_3 + 1/2\,H_2O \quad (T > 130\,°C) \quad (4)$$

In the last decade, boric acid chemistry has shown rapid development [35]. Boric acid is a weak inorganic acid and is widely used as an effective catalyst in organic synthesis. Boric acid attracts attention and is preferred because it is perfectly soluble in water, commercially available, chemically stable, low cost, non-toxic, recyclable, light, selective and environmentally friendly [35]. In addition, its dissolution in water and alcohols makes it possible to use it as a homogeneous catalyst in different reactions, e.g., in the reaction of H_2 production from $NaBH_4$. In this study, a new catalytic pathway is presented to produce clean and sustainable energy source H_2 from the methanolysis of $NaBH_4$ using H_3BO_3 and B_2O_3 as direct catalysts. These boron-containing catalysts are environmentally benign and have been used as a green catalyst in the methanolysis of $NaBH_4$.

Although there is a report in literature in the methanolysis of $NaBH_4$ in the presence of H_3BO_3 at high concentration of H_3BO_3 (at least 0.2 M) [36], in this study, the utilization of H_3BO_3 (at low concentration, approximately 0.04 M) and B_2O_3 as catalysts in the methanolysis of $NaBH_4$ for the first time in literature is reported. In this paper, B_2O_3 was produced in a furnace via the dewatering process of H_3BO_3 at 500 °C for its potential to be used in H_2 generation as a catalyst in the methanolysis of $NaBH_4$. H_3BO_3 and B_2O_3 catalysts were characterized via Fourier Transform Infrared Radiation (FT-IR) spectroscopy and thermogravimetric analysis (TGA). The effect of various parameters on the methanolysis reaction of $NaBH_4$ was investigated to determine reaction order. Moreover, the influence of type and amounts of catalysts, the concentration of $NaBH_4$ as well as the temperature of the reaction from 268 K to 308 K on HGR of catalysts was testified. Additionally, the reuse performance of the catalysts was investigated by employing the same catalysts in ten consecutive runs in the same reaction taking into consideration of the change in their activity and conversion%.

2. Experimental

2.1. Materials

Boric acid (H_3BO_3, ≥99.5% Sigma-Aldrich, CAS number: 10043-35-3) as the catalyst and B_2O_3 precursor, methanol (≥99.9%, Carlo Erba, CAS number: 67-56-1) as a solvent, sodium borohydride ($NaBH_4$, ≥96 %, Merck, CAS number: 16940-66-2) as H_2 source were used without further treatment.

2.2. Instrumentation

Fourier transform infrared radiation (FT-IR, NICOLET iS10, Thermo Fisher Scientific) spectra of H_3BO_3 and B_2O_3 were recorded by collecting data using ATR technique in the range of 4000-650 cm^{-1} with 4 cm^{-1} resolving power. Thermal decomposition characters of H_3BO_3 and B_2O_3 were analyzed via thermo gravimetric analysis (TGA, SII TG/DTA 6300 model) under continuous N_2 purging with the rate of 100 $mL.min^{-1}$ min gas flow and the rate of 10°$C.min^{-1}$ temperature increase. For the TG analysis, approximately 4 mg of the samples were placed in ceramic TGA crucibles and the analysis was run between 50-900°C temperature ranges.

2.3. Preparation of boron trioxide catalyst

B_2O_3 was prepared by dewatering process using a furnace (Protherm, ASP series) with a temperature controller unit. Briefly, a certain amount of H_3BO_3 was weighed and transferred to the porcelain crucible and put in the furnace. The temperature program was set up as in 10 min reach the 500 °C from room temperature and the sample was kept at 500 °C temperature for 30 min. Then, the sample was cooled to room temperature and transferred to a mortar for fine grinding. Finally, the B_2O_3 was kept in a sealed bag for further use.

2.4. Determination of the catalytic activity of H_3BO_3 and B_2O_3 as catalysts in methanolysis of $NaBH_4$

The activity of H_3BO_3 and B_2O_3 as catalysts in the $NaBH_4$ methanolysis reaction was designated by recording the displacement of water volume in the course of H_2 evolution. For the experimental part, 50 mg catalyst was placed into 20 mL methanol solution containing 125 mM $NaBH_4$ in a 50 mL round-bottomed flask under continuous stirring at 1000 rpm and H_2 evolution was tracked via attached gas burette to the flask. Determination of activation parameters (E_a, $\Delta H^{\#}$, $\Delta S^{\#}$) and HGR by using H_3BO_3 and B_2O_3 catalysts was also realized by continuously measuring the released H_2 gas. Some reaction parameters on HGR in methanolysis reaction of $NaBH_4$ were assessed i.e., the catalyst type (H_3BO_3 and

B_2O_3), catalyst amount (12.5-100 mg), initial concentration of $NaBH_4$ (62.5-500 mM), and the reaction temperature (268-308 K).

2.5. Reusability of boron-based catalysts

The reuse of H_3BO_3 and B_2O_3 catalysts was tested by measuring the conversion and catalytic activity% of the catalysts after each successive use. For this objective, the same catalyst was used repeatedly in the same reaction medium by just consecutive addition of $NaBH_4$ after each H_2 elution was ended, and these cycles was continued up to ten times usage. All the reuse studies were conducted at 298 K, under 1000 rpm stirring by using 50 mg catalyst, and 20 mL 125 mM $NaBH_4$ solution in methanol. Stoichiometric ratio was used to calculate conversion%, and activity% using HGR (r_{80}) accepting the first use as 100%.

3. Results and discussion

3.1. Preparation and characterization of catalyst

Here, H_3BO_3 and B_2O_3 were exploited as a catalyst in H_2 generation reaction due to their environmentally benign and boron-containing nature. The FT-IR spectra of H_3BO_3 and B_2O_3 were given in Fig. 1. The characteristic at 3185 cm^{-1} belong to O-H bands and the bands at 1400 and 1190 cm^{-1} were assigned to symmetric stretching vibrations of B-O. The spectral peaks at 804 cm^{-1} were designated to stretching frequency of B-O-B for boron oxide. Thermal degradation patterns of H_3BO_3 and B_2O_3 were elucidated by TGA and the corresponding TG thermograms are demonstrated in Fig. 1 (b). In the thermogram, B_2O_3 seems to have better thermal stability than H_3BO_3 as anticipated from Eq (3) and (4).

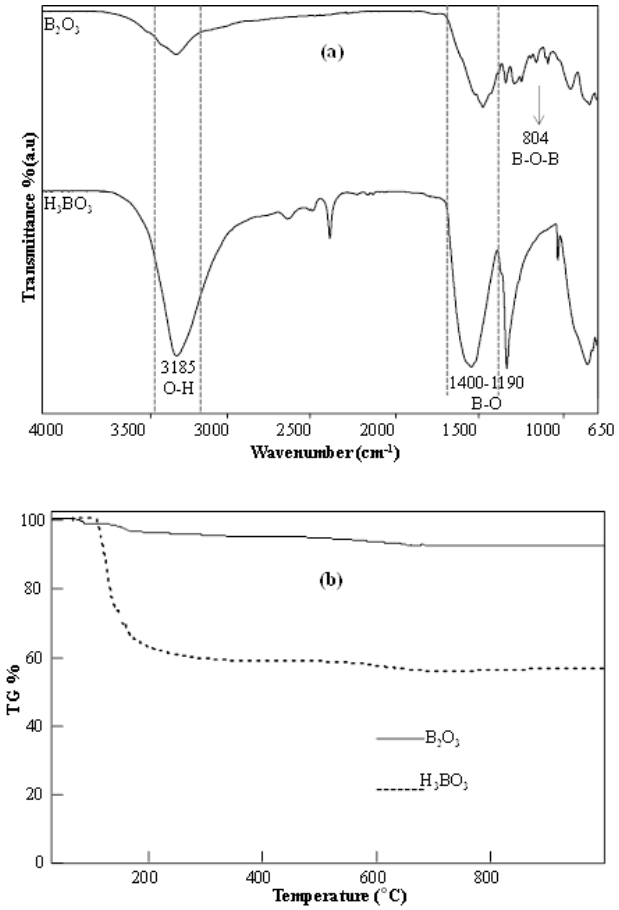

Figure 1. *The comparison of (a) FT-IR spectra of H_3BO_3 and B_2O_3, and (b) their thermal degradation curves.*

In the thermograms, the initial major decomposition temperature of H_3BO_3 was revealed from its DTG plot and determined to be around 126 °C due to removal of bounded water and upon heating up to 900°C 56% residual composition was observed with respect to the initial weight of the sample. The B_2O_3 catalyst exhibited a smoother gradual decomposition pattern and 93% of its weight was remained after heating up to 900°C.

3.2. Catalytic performance of H_3BO_3 and B_2O_3 catalysts

The rates of hydrogen generation in methanolysis of $NaBH_4$ under catalytic activities of H_3BO_3 and B_2O_3 were calculated from the constructed H_2 production plots. Rates of $NaBH_4$ methanolysis reactions were determined at the half points of conversion (r_{50}) from the H_2 generation curves recorded as a function of time ($mL.min^{-1}.g^{-1}$).

3.3. The impact of the used catalyst type on methanolysis of $NaBH_4$

It is very well-known that the methanolysis of $NaBH_4$ is an acid-catalyzed reaction and therefore elevating the number of protons in the H_2 generation medium is anticipated to

have positive effects on HGR. Here, H_3BO_3 and B_2O_3 were used as acid catalysts and their catalytic performances were compared under the reaction conditions of 50 mg catalyst, and 125 mM $NaBH_4$ in 20 mL methanol at 298 K and 1000 rpm stirring.

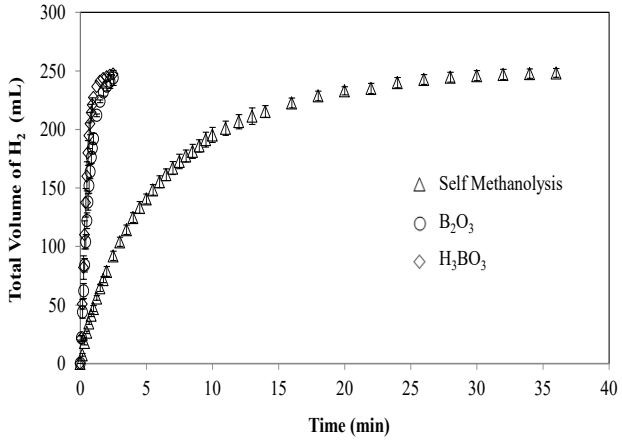

Figure 2. *Hydrogen volume vs time plots H_3BO_3 and B_2O_3 catalysts and self-methanolysis used in $NaBH_4$ methanolysis, [without catalyst or 50 mg catalyst, 125 mM $NaBH_4$ solution in 20 mL methanol, at 298 K, 1000 rpm].*

Self methanolysis was realized as a control to comprehend the catalytic activity under the same conditions with the absence of catalyst, and 100% conversions were achieved in all reactions with and without the addition of catalysts with and the same amount of H_2, ~250 mL were produced. As expected, different reaction rates were observed in self methanolysis of $NaBH_4$ and in the H_3BO_3 and B_2O_3 catalysis as plotted in Fig. 2. The HGRs H_3BO_3 and B_2O_3 were calculated as 6481, 5163 $mL.min^{-1}.g^{-1}$, respectively. So, H_3BO_3 has higher activity than B_2O_3 and it can be assumed that both catalysts possess great catalytic activity.

The suggested reaction mechanism in H_2 generation from H_3BO_3 catalyzed methanolysis of $NaBH_4$ is demonstrated in Supporting Fig. S1. A similar reaction mechanism can be considered with the exception of proton abstraction for the initial reaction of B_2O_3 as was proposed for H_3BO_3 catalyzed H_2 production.

3.3. The effect of H_3BO_3 amount as a catalyst in $NaBH_4$ methanolysis

The activity and amount catalysts are of paramount importance for scale up H_2 generation applications in terms of financial concerns, therefore, five different amounts of catalyst, 12.5, 25, 50, 75, and 100 mg of H_3BO_3 were chosen and the other parameters were held constant in $NaBH_4$ methanolysis reactions. It was demonstrated in Fig. 3(a) that, the total volume of generated H_2 is independent of the amount of catalyst. The kinetic rates of performed reactions were calculated based on the half points in the conversion (r_{50}) of $NaBH_4$ from the graphs constructed as the volume of H_2 production versus time. In other words, from the H_2 production curve with time, the curves up to 125 mL H_2 production with time are considered. For the catalytic activity that is the rate of hydrogen generation per gram catalyst, HGR is constructed by calculating the reaction rates from the slope released H_2 versus time graphs for different weights (gram) of used catalysts. Besides, the figure inset in Fig. 3(a) demonstrates that increasing the amount of H_3BO_3 from 12.5 mg to 100 mg proportionally increased the rate of the methanolysis reaction from 152 $mL.min^{-1}$to 424 $mL.min^{-1}$, and the catalytic activity (HGR) of the H_3BO_3 catalyst was calculated to reduce to 4243 from 12145 $mL.min^{-1}.g^{-1}$. As shown in the inset, the rate of H_2 release reaction versus the amount of used catalyst was constructed, and the value of 2623 $mL.min^{-1}$ was obtained from the slope of the plot. This result states the dependence of catalyst weight on the rate of H_2 release reaction in the weight range of 12.5 mg and 100 mg catalyst that results in an HGR value of 2623 $mL.min^{-1}$ weight average H_2 production rate.

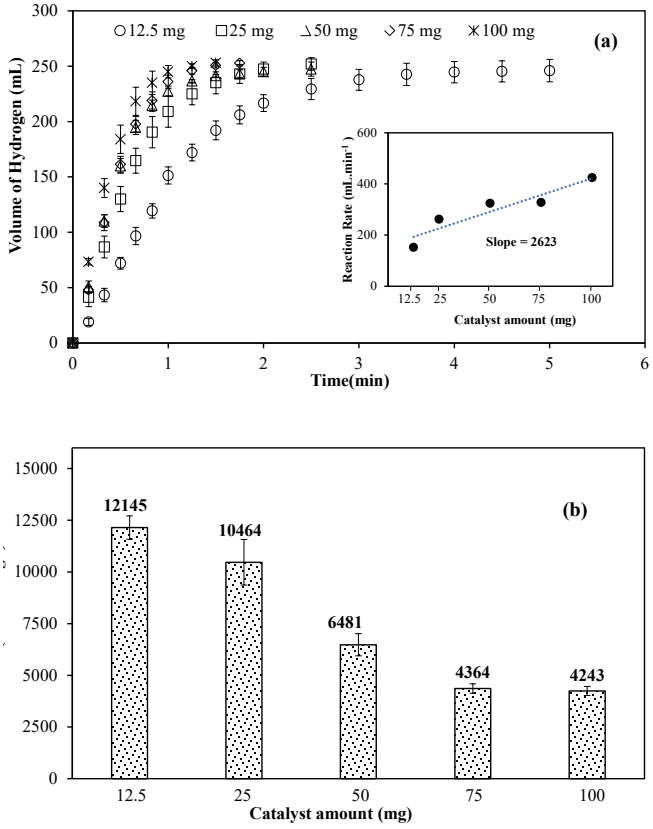

Figure 3. *Effect of H_3BO_3 catalyst amount on the methanolysis of $NaBH_4$, (a) H_2 production volume as a function of time, and reaction rate versus catalyst amount in the inset figure and, (b) the effect of catalyst amount on HGR. [catalyst: 12.5-100 mg H_3BO_3; 125 mM $NaBH_4$ solution in 20 mL methanol, at 298 K 1000 rpm].*

As can be readily understood from Fig. 3(b) that regardless of the amount of H_3BO_3 catalyst, the same volume of H_2 was produced, increasing weight of the catalyst from 12.5 mg to 100 mg shortens the H_2 production time, HGR which was respectively decreased from 12145 to 4243 $mL.min^{-1}.g^{-1}$,

Moreover, ln(rate) vs ln(catalyst concentration) graph was plotted to evaluate the impact of the amount of H_3BO_3 catalyst on reaction order which in turn shows an almost linear relationship with the slope of 0.44 that is less than 1.

The same experiments were carried out for B_2O_3 and corresponding graphs were given in Fig. 4. Again, the same amount of H_2 was produced in the course of H_2 generation and only the time got shortened to produce the same amounts of H_2 upon increasing the weight of catalyst from 12.5 mg to 100 mg. On the other hand, the rate of the reaction was increased from 161 mL.min^{-1} to 305 mL.min^{-1} for B_2O_3 catalyst, and the HGR value of 1569 mL.min^{-1} weight average H_2 production rate was calculated from the slope of the plot given in the inset figure as the rate of the reaction with respect to the mass of the catalyst (Fig. 4(a)).

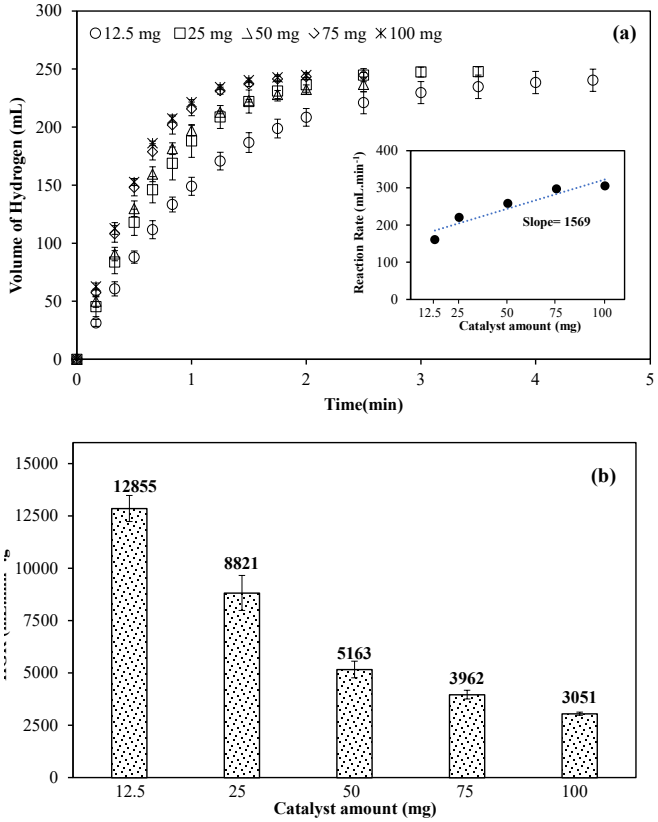

Figure 4. *The impact of B_2O_3 catalyst amounts on methanolysis of $NaBH_4$, (a) H_2 production volume as a function of time, and reaction rate versus catalyst amount was given in the inset figure and, (b) the effect of catalyst amount on HGR. [catalyst: 12.5-100 mg B_2O_3; 125 mM $NaBH_4$ solution in 20 mL methanol, at 298 K 1000 rpm].*

As shown in Fig. 4(b), weights of the used B_2O_3 catalyst were increased from 12.5 mg to 100 mg and a corresponding decrease in HGR values were observed respectively from 12855 mL.min^{-1}.g^{-1} to 3051 mL.min^{-1}.g^{-1}. The impact of B_2O_3 catalyst weight on reaction order was also evaluated from the slope of ln(rate) vs ln(catalyst concentration) plot and the slope of 0.29 with a straight line was obtained which was also less than 1. Customarily, the amount of catalyst in literature is chosen as 50 mg for these types of reactions [21]. Here 50 mg of the catalyst was therefore used for comparative purposes with those of the formerly reported catalyst systems.

3.4. The impact of used $NaBH_4$ concentration

The change in HGR with respect to altered $NaBH_4$ concentrations was investigated by using five $NaBH_4$ concentrations such as 62.5, 125, 250, 375, 500 mM of $NaBH_4$, and only the $NaBH_4$ concentration was changed by keeping other parameters constant as in the following: weight of B_2O_3 catalyst, 50 mg; a volume of methanol, 20 mL; temperature of the reaction, 298 K; rate of stirring, 1000 rpm. The H_2 production plot given in Fig. 5(a) was generated as a function of time under different $NaBH_4$ concentrations and demonstrates that volume of H_2 production proportionally increases with the increased concentration of $NaBH_4$. Similarly, in Fig. 5(b), HGR was evidenced to show a linear increase with increased $NaBH_4$ concentration. The slope of ln(reaction rate) versus ln($NaBH_4$ concentration) plot was calculated to be 1.10, hence indicating the reaction follows first-order kinetics according to $NaBH_4$ concentration.

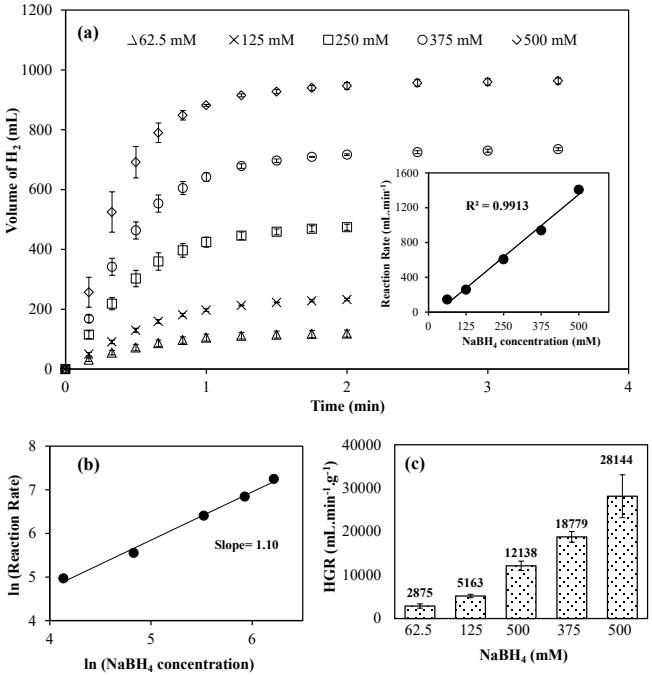

Figure 5. *The impact of $NaBH_4$ concentration on the B_2O_3 catalyzed methanolysis of $NaBH_4$, (a) H_2 production volume as function of time, and reaction rate versus amount of $NaBH_4$ was given in the inset, (b) ln(reaction rate) vs ln($NaBH_4$ concentration), and (c) effect of $NaBH_4$ concentration on HGR [catalyst: 50 mg B_2O_3; 20 mL 62.5-500 mM $NaBH_4$ at 298 K, 1000 rpm].*

As shown in Fig. 5(c), by increasing the concentration of $NaBH_4$ from 62.5 mM to 500 mM, HGR increases from 2875 mL.min^{-1}.g^{-1} to 28144 mL.min^{-1}.g^{-1}. This particular increase

might be mainly due to the inadequacy of the initial $NaBH_4$/catalyst ratio to reach the dynamic saturation point of the used catalyst with the present hydride.

3.5. The impact of temperature

The impact of temperature on H_3BO_3 and B_2O_3 catalyzed methanolysis of $NaBH_4$ has been investigated at five different temperatures (268, 278, 288, 298, 308). Using 50 mg H_3BO_3 catalyst at different reaction temperatures in $NaBH_4$ methanolysis, volumes of produced H_2 were graphed against increasing temperature and presented in Fig. 6(a).

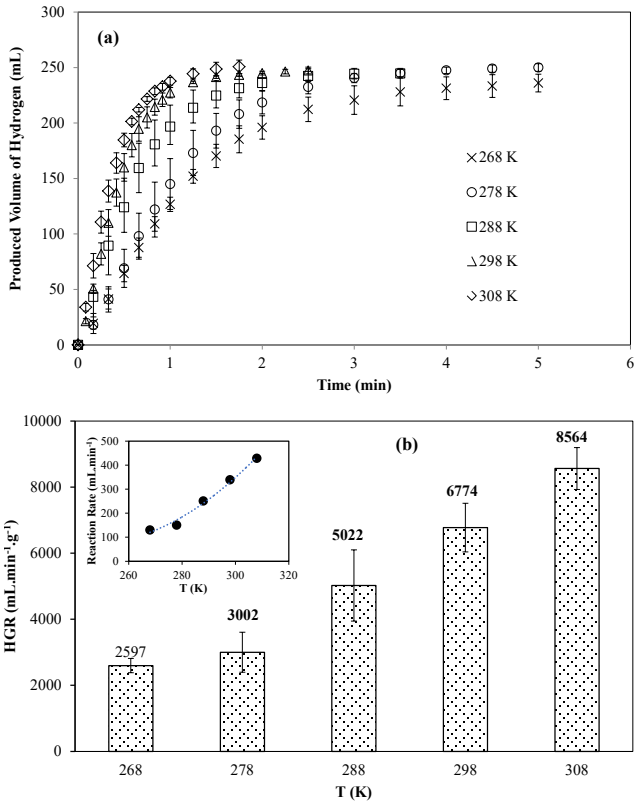

Figure 6. *The impact of temperature on H_3BO_3 catalyzed methanolysis of $NaBH_4$, (a) H_2 production volume as a function of time, and (b) effect of temperature on HGR and, inset figure is the reaction rate versus temperature [catalyst: 50 mg H_3BO_3; 125 mM $NaBH_4$ solution in 20 mL methanol, temperature range 268-308 K, 1000 rpm].*

All of the methanolysis reactions performed at different temperatures produced an average volume of 250 mL H_2. Based on the presented graph in Fig. 6(b), HGR of the H_3BO_3 was increased from 2597 $mL.min^{-1}.g^{-1}$ to 8564 $mL.min^{-1}.g^{-1}$ as the temperature of the reaction was raised from 268 K to 308 K. The reaction rate is given in the inset of Fig. 6(b) clearly illustrates that almost an exponential increase was occurred from 130 $mL.min^{-1}$ to 428 $mL.min^{-1}$ upon increasing the temperature of the reaction from 268 K to 308 K. The HGR value of 2597 $mL.min^{-1}.g^{-1}$ even at -5 °C offers great advantages for these systems.

The catalytic performance of B_2O_3 was also examined at the range of 268 K-308 K and the rate of H_2 generation in response to changing temperatures was demonstrated in Fig. 7(a).

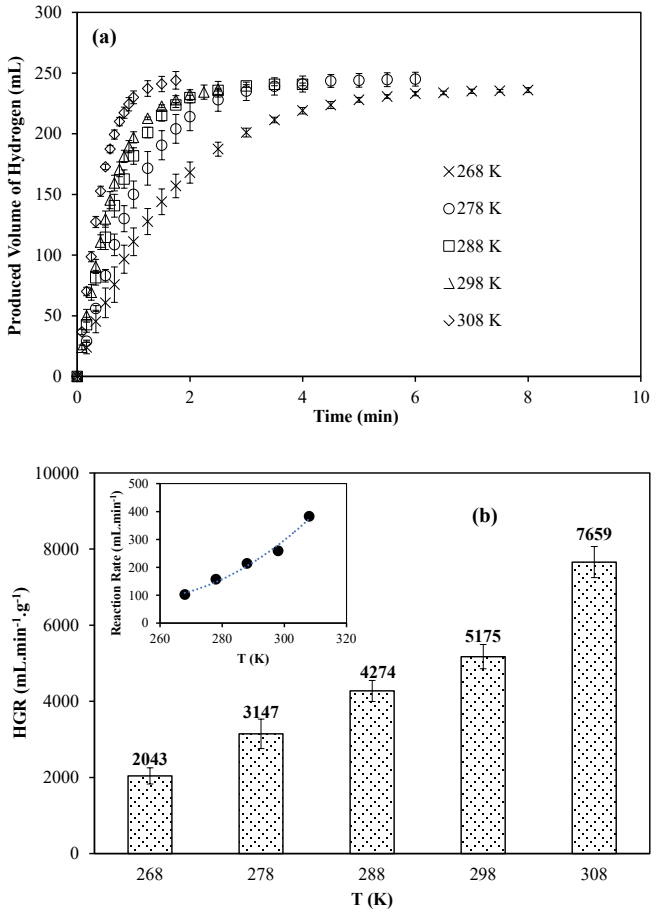

Figure 7. *The impact of temperature on methanolysis of $NaBH_4$, (a) H_2 production volume as a function of time, and (b) effect of temperature on HGR and, inset figure is the reaction rate versus temperature [catalyst: 50 mg B_2O_3; 125 mM $NaBH_4$ solution in 20 mL methanol, temperature range 268-308 K, 1000 rpm].*

Again, 250 mL of average H_2 volume was recorded for all reactions of $NaBH_4$ conducted at varying temperatures. The HGR graph of the B_2O_3 catalyzed methanolysis reaction was depicted in Fig. 7(b) as can be noticed wherefrom the HGR has experienced an increase from 2043 $mL.min^{-1}.g^{-1}$ to 7659 $mL.min^{-1}.g^{-1}$ upon raising temperature of the reaction from 268 K to 308 K. and the figure given in the inset of Fig. 7(b) apparently reveals an increment in the rate of H_2 evolution from 102 $mL.min^{-1}$ to 383 $mL.min^{-1}$ after boosting the temperature from 268 K to 308 K. Therefore, even natural B_2O_3 can be used as a benign catalyst to generate H_2 from chemical hydrides offer unprecedented alternatives to the existent metal nanoparticle, polymeric IL, and IL molecule-based catalyst.

The parameters of activation energy Ea, enthalpy ΔH, and entropy ΔS were determined for H_3BO_3 and B_2O_3 catalyzed methanolysis of $NaBH_4$, and the rate constants between 268 - 308 K reaction temperature range, graphs of ln(k) vs T^{-1} plots and ln(k.T^{-1}) vs (1.T^{-1}) were plotted based on well-established Arrhenius (Eq. (5)) and Eyring (Eq. (6)) equations, respectively.

$$lnk = ln\,A - \left(\frac{Ea}{RT}\right) \quad (5)$$

$$ln\left(\frac{k}{T}\right) = ln\left(\frac{k_B}{h}\right) + \frac{\Delta S^{\#}}{R} - \frac{\Delta H^{\#}}{R}\left(\frac{1}{T}\right) \quad (6)$$

Where, k is the rate constant, E_a is the activation energy, R is the gas constant (8.314 $J.K^{-1}.mol^{-1}$), T is temperature, k_B is Boltzmann constant (1.381 x 10^{-23} $J.K^{-1}$), h is Planck constant (6.626 x 10^{-34} J.s), $\Delta S^{\#}$ is the entropy of activation, and $\Delta H^{\#}$ is the activation enthalpy.

The results show very well fitness with the Arrhenius and Eyring equations and respective plots for H_3BO_3 and B_2O_3 catalysts were respectively shown in Supporting Fig. S2 (a) and Supporting Fig. S2 (b), and used to calculate activation parameters. The comparison of activation energies was given in Supporting Fig. S2 (c). The activation parameters for H_3BO_3 and B_2O_3 catalyzed $NaBH_4$ methanolysis and rate constants were summarized in Table 1.

Table 1. *The rate constants calculated at different temperatures, and activation parameters for H_3BO_3 and B_2O_3 catalyzed $NaBH_4$ methanolysis.*

Catalyst	T (K)	k (min^{-1})	E_a ($kJ.mol^{-1}$)	$\Delta H^{\#}$ ($kJ.mol^{-1}$)	$\Delta S^{\#}$ ($J.mol^{-1}.K^{-1}$)
H_3BO_3	268	0.8422	22.08	19.70	-171.93
	278	1.2281			
	288	1.7401			
	298	2.3297			
	308	3.0068			
B_2O_3	268	0.5863	23.30	20.91	-169.54
	278	1.1273			
	288	1.3931			
	298	1.6765			
	308	2.5924			

Reaction conditions: 50 mg catalyst; 125 mM $NaBH_4$ solution in 20 mL methanol at 298 K, 1000 rpm.

The E_a, $\Delta H^{\#}$, $\Delta S^{\#}$ were designated as 22.08 $kJ.mol^{-1}$, 19.70 $kJ.mol^{-1}$ and -171.93 $J.mol^{-1}.K^{-1}$, respectively for H_3BO_3 and as 23.30 $kJ.mol^{-1}$, 20.91 $kJ.mol^{-1}$and -169.64 $J.mol^{-1}.K^{-1}$, for B_2O_3 catalyzed methanolysis reactions, respectively. Interestingly, both boron-based catalysts demonstrated one of the best ones or the lowest E_a amongst the different catalysts used for the same purpose of H_2 generation from methanolysis of $NaBH_4$ as presented in Table 2. As can be seen wherefrom the E_a values of 22.08 and 23.30 $kJ.mol^{-1}$ for H_3BO_3 and B_2O_3 catalysts calculated in the range of 268-308 K is considerably lower than those of the previously reported metal-based catalyst, polymeric nanoparticles, etc. as compared in Table 2. As a result, H_3BO_3 and B_2O_3 catalysts may have great potential for an environmentally benign H_2 generation system with the capability of working even relatively lower temperature e.g., subzero temperatures from the methanolysis of $NaBH_4$ for real industrial applications.

Table 2. *The comparison of activation energies of some of the different catalysts used in literature in catalytic hydrolysis and methanolysis reactions of hydrides for H_2 generation.*

Catalyst	Temperature (K)	Activation energy ($kJ.mol^{-1}$)	HGR ($mL.g^{-1}.min^{-1}$)	References
Co-TiO_2 (methanolysis)	273-298	20.4	-	[8]
1 M Phosphoric acid (KBH_4 ethanolysis)	303-333	2.98	6423	[12]
Cu/Co catalyst (hydrolysis)	293-333	42.66	-	[14]
Ni_2P-sol-gel (methanolysis)	273-313	24.9	3700	[15]
Ni_2-P-TPR (methanolysis)		44.5	7140	
$CoCI_2$ (methanolysis)	253-323	25-29	-	[16]
Ru/Al_2O_3 (hydrolysis)	273-308	14.8	204.3	[17]
Ru–Co/C (methanolysis)	298-333	36.83	9360	[18]
Co-P/CNTs-Ni foam (methanolysis)	298-313	49.94	2430	[19]
Fe-B NPs (methanolysis)	293-323	7.02	5487	[20]

Cell-EPC-DETA-HCl (methanolysis)	263- 313	30.80	2015	[21]
P(MTMA) (methanolysis)	258-318	24.10	4838±126	[23]
SSA (hydrolysis)	298-343	17	3900	[29]
H_3BO_3 (hydrolysis)	293-313	20.31	-	[30]
Hydrochloric acid (semi-methanolysis)	293-323	5.84	4875	[31]
Acetic acid (semi-methanolysis)		2.81	3960	
Self methanolysis	273-313	62.99	-	[37]
H_3BO_3 (methanolysis)	268-308	22.08	6481	This study
B_2O_3 (methanolysis)		23.30	5163	

As presented in Table 2, systems catalyzed by H_3BO_3 and B_2O_3 exhibit better catalytic performance than most of the methanolysis reactions reported in the literature [14, 16, 18, 19, 21, 23].

3.6. Reuse of H_3BO_3 and B_2O_3 catalyst

The reuse of a catalyst and its performance is the foremost important parameters for the industrial success of any catalyst system. To determine the reusability, the H_3BO_3 and B_2O_3 catalysts were used repetitively in the same setting by calculating the conversation and catalytic activities and comparing their values after each use. The conversion is calculated based on stoichiometry of the reaction in accord with Eq (2), and activity is calculated presuming the initial catalytic activity as 100% for the first use by considering its reaction rate as base taking its' ratio to each consecutive use. The conversion and activity % of H_3BO_3 and B_2O_3 as a catalyst for H_2 generation from methanolysis reaction is illustrated in Fig. 8 (a) and (b), respectively.

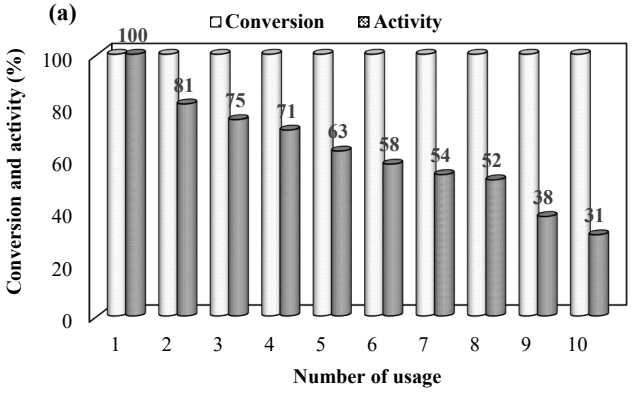

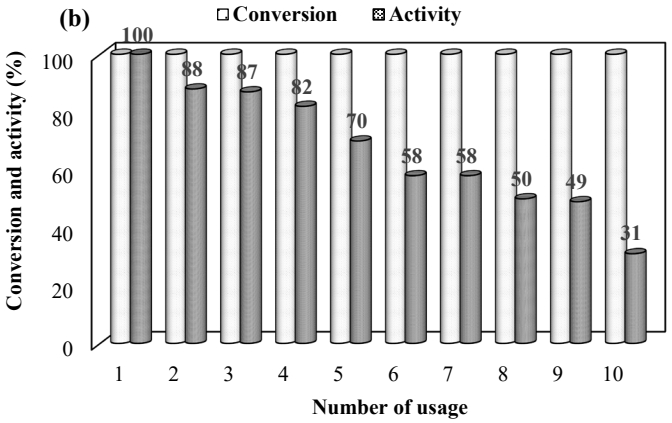

Figure 8. *The reuse of (a) H_3BO_3 and (b) B_2O_3 catalyst in methanolysis of $NaBH_4$ in terms of conversion and % catalytic activity [catalyst: 50 mg; 125 mM $NaBH_4$ solution in 20 mL methanol at 298 K, 1000 rpm].*

Regardless of catalysts types, both of the catalysts provided 100 % conversion up to 10 successive runs. The catalytic activity on the other hand reduced after each for both of the catalysts. For example, 100 % catalytic activity of H_3BO_3 catalyst decreased to 81% at 2nd use and continued to decrease to 31% at 10th use. The same reduction trend is also seen for the B_2O_3 catalyst as the 100% catalytic activity is decreased to 88% at 2nd use and continues to decrease afterward reaching 31% at 10th use as shown in Fig. 8b. Although the reduction in catalytic activity% of B_2O_3 catalyst is not as sharp as H_3BO_3 catalyst, both catalysts can keep over 50% activity up to 8th cycles. Therefore, both of these catalysts can be safely used as green catalysts for the generation of green energy carrier, H_2 generation from hydride methanolysis reactions.

4. Conclusions

In conclusion, the utilization of boron containing environmentally benign catalysts such as H_3BO_3 (~ 0.04 M) and B_2O_3 in the methanolysis of $NaBH_4$ were reported for the first time in this study. The H_3BO_3 and B_2O_3 as catalysts afforded relatively low Ea values, 22.08 kJ.mol^{-1}, and 23.30

kJ.mol^{-1}, respectively in methanolysis of $NaBH_4$ in comparison to the conventional catalysts reported for the same reaction as given in Table 2. These values are better than most of the reported noble metal-based catalysts in the literature make these boron-based natural catalysts better suited of feasible than most of those reported expensive and toxic ones e.g., metal nanoparticle-based catalysts and/or IL-based catalysts employed in methanolysis of $NaBH_4$ for H_2 generation. Besides, these environmentally friendly boron based catalysts also provided higher hydrogen generation rates (HGR) e.g., 6481 mL.min^{-1}.g^{-1} and 5163 mL.min^{-1}.g^{-1} in comparison to the many metal nanoparticle based catalysts reported in the literature. Furthermore, the reusability studies revealed that both H_3BO_3 and B_2O_3 catalysts can be used up to 8 repeated reuse cycles at 298 K, retaining 50% of their catalytic activity by providing 100% substrate ($NaBH_4$) conversion for every single use. Consequentially, the acid-based catalysts reported here with laborless, cost-effective preparation and environmentally benign natures bestow outstanding candidacy for the displacement of mostly toxic and/or costly counterparts used in industrial and environmental implementations.

References

[1]. Stern A.G., "A new sustainable hydrogen clean energy paradigm", International Journal of Hydrogen Energy, 43, (2018), 4244 – 4255.

[2]. Gustafsson Ö., Kruså M., Zencak Z., Sheesley R.J., Granat L., Engström E., Praveen P.S., Rao P.S.P., Leck C., Rodhe H., "Brown clouds over South Asia: biomass or fossil fuel combustion?", Science, 323, (2009), 495 – 498.

[3]. Baykara S.Z., "Hydrogen: A brief overview on its sources, production and environmental impact", International Journal of Hydrogen Energy 43, (2018), 10605 – 10614.

[4]. Cui L., Cao X., Sun X., Yang W., Liu J., "A bunch-like copper oxide nanowire array as an efficient, durable, and economical catalyst for the methanolysis of ammonia borane", ChemCatChem, 10, (2018), 710 – 715.

[5]. Arzac G.M., Fernández A., "Hydrogen production through sodium borohydride ethanolysis", International Journal of Hydrogen Energy, 40, (2015), 5326 – 5332.

[6]. Kalidindi S.B., Nethaji M., Jagirdar B.R., "Dehydrogenation of ammonia borane in fluoro alcohols", International Journal of Hydrogen Energy, 35, (2010), 10819 – 10825.

[7]. Kojima Y., Kawai Y., Nakanishi H., Matsumoto S., "Compressed hydrogen generation using chemical hydride", Journal of Power Sources, 135, (2004), 36 – 41.

[8]. Hannauer J., Demirci U.B., Pastor G., Geantet C., Herrmann J.M., Mielea P., "Hydrogen release through catalyzed methanolysis of solid sodium borohydride", Energy & Environmental Science, 3, (2010), 1796 – 1803.

[9]. Lin K.A., Chang H., "Efficient hydrogen production from NaBH4 hydrolysis catalyzed by a magnetic cobalt/carbon composite derived from a zeolitic imidazolate framework", Chemical Engineering Journal, 296, (2016), 243 – 251.

[10]. Lo C.F., Karan K., Davis B.R., "Kinetic studies of reaction between sodium borohydride and methanol, water, and their mixtures" Industrial & Engineering Chemistry Research, 46, (2007), 5478 – 5484.

[11]. Inger E., Sunol A.K., Sahiner N., "Catalytic activity of metal-free amine-modified dextran microgels in hydrogen release through methanolysis of NaBH4", International Journal of Energy Research, 7, (2020), 5990 – 6001.

[12]. Saka C., Balbay A., "Fast and effective hydrogen production from ethanolysis and hydrolysis reactions of potassium borohydride using phosphoric acid", International Journal of Hydrogen Energy, 43, (2018), 19976 – 19983.

[13]. Chozhavendhan S., Singh M.V.P., Fransila B., Kumar R.P., Devi G.K., "A review on influencing parameters of biodiesel production and purification processes", Current Research in Green and Sustainable Chemistry, 1-2, (2020), 1 – 6.

[14]. Saka C., Şahin Ö., Demir H., Karabulut A., Sarikaya A., "Hydrogen generation from sodium borohydride hydrolysis with a Cu-Co-based catalyst: A kinetic study", Energy Source, 37, (2015), 956 – 964.

[15]. Yan K., Li Y., Zhang X., Yang X., Zhang N., Zheng J., Chen B., Smith K.J., "Effect of preparation method on Ni2P/SiO2 catalytic activity for NaBH4 methanolysis and phenol hydrodeoxygenation", International Journal of Hydrogen Energy, 40, (2015), 16137 – 16146.

[16]. Lo C.F., Karan K., Davis B.R., "Kinetic assessment of catalysts for the methanolysis of sodium borohydride for hydrogen generation", Industrial & Engineering Chemistry Research, 48, (2009), 5177 – 5184.

[17]. Su C., Lu M., Wang S., Huang Y., "Ruthenium immobilized on Al2O3 pellets as a catalyst for hydrogen generation from hydrolysis and methanolysis of sodium borohydride", RSC Advances, 2, (2012), 2073 – 2079.

[18]. Wang F., Wang Y., Zhang Y., Luo Y., Zhu H., "Highly dispersed RuCo bimetallic nanoparticles supported on carbon black: enhanced catalytic activity for hydrogen generation from NaBH4 methanolysis", Journal of Materials Science, 53, (2018), 6831 – 6841.

[19]. Wang F., Zhang Y., Wang Y., Luo Y., Chen Y., Zhu H., "Co-P nanoparticles supported on dandelion-like CNTs-Ni foam composite carrier as a novel catalyst for hydrogen generation from NaBH4 methanolysis" International Journal of Hydrogen Energy, 43, (2018), 8805 – 8814.

[20]. Ocon J.D., Tuan T.N., Yi Y., Leon R.L., Lee J.K., Lee J., "Ultrafast and stable hydrogen generation from sodium borohydride in methanol and water over Fe-B nanoparticles", Journal of Power Sources, 243, (2013), 444 – 450.

[21]. Sahiner N., Demirci S., "Natural microgranular cellulose as alternative catalyst to metal nanoparticles for H2 production from NaBH4 methanolysis", Applied Catalysis B: Environmental, 202, (2017), 199 – 206.

[22]. Pham D.D., Cho J., "Low-energy catalytic methanolysis of poly(ethyleneterephthalate)", Green Chemistry, 23, (2021), 511 – 525.

[23]. Ozturk O.F., Demirci S., Sengel S.B., Sahiner N., "Highly regenerable ionic liquid microgels as inherently metal-free green catalyst for H2 generation". Polymers for Advanced Technologies, 29, (2017), 1426 – 1434.

[24]. Chinnappan A., Puguan J.M.C., Chung W.J., Kim H. "Hydrogen generation from the hydrolysis of sodium borohydride using chemically modified multiwalled carbon nanotubes with pyridinium based ionic liquid and decorated with highly dispersed Mn nanoparticles". Journal of Power Sources, 293, (2015), 429 – 436.

[25]. Tamboli A.H., Chaugule A.A., Kim H., "Highly selective and multifunctional chitosan/ionic liquids for conversion of CO2 and methanol to dimethyl carbonates at mild reaction conditions", Fuel, 166 (2016), 495 – 501.

[26]. Wei L., Dong X.L., Yang Y.M., Shi Q.Y., Lu Y.H., Liu H.Y., Yu Y.N., Zhang M.H., Qi M., Wang Q.," Co−O−P composite nanocatalysts for hydrogen generation from the hydrolysis of alkaline sodium borohydride solution", International Journal of Hydrogen Energy, 45, (2020), 10745 – 10753.

[27]. Gnanakumar E.S., Chandran N., Kozhevnikov I.V., Atienza A., Fernandez E.V.R., Escibano A., Shiju N.R., "Highly efficient nickel-niobia composite catalysts for hydrogenation of CO2 to methane", Chemical Engineering Science, 194, (2019), 2 – 9.

[28]. Khan S.B., "Metal nanoparticles containing chitosan wrapped cellulose nanocomposites for catalytic hydrogen production and reduction of environmental pollutants", Carbohydrate Polymers, 242, (2020), 116286.

[29]. Manna J., Roy B., Sharma P., "Efficient hydrogen generation from sodium borohydride hydrolysis using silica sulfuric acid catalyst", Journal of Power Sources, 275, (2015), 727 – 733.

[30]. Balbay A., Şahin Ö., Saka C., "Effect of acid addition on hydrogen production from potassium borohydride hydrolysis", Energy Sources Part A, 39, (2017), 1383 – 1389.

[31]. Balbay A., Saka C., "The effect of the concentration of hydrochloric acid and acetic acid aqueous solution for fast hydrogen production from methanol solution of NaBH4", International Journal of Hydrogen Energy, 43, (2018), 14265 – 14272.

[32]. Brack P., Dann S.E., Wijayantha K.G.U., "Heterogenous and homogenous catalysts for hydrogen generation by hydrolysis of aqueous sodium borohydride (NaBH4)", Energy Science& Engineering, 3, (2015), 174 – 188.

[33]. Wang N., Zhao L., Zhang C., Li L., "Water states and thermal processability of boric acid modified poly(vinyl alcohol)", Journal of Applied Polymer Science, 133, (2016), 43246.

[34]. Balcı S., Sezgi N.A., Eren E., "Boron oxide production kinetics using boric acid as raw material", Industrial &

Engineering Chemistry Research, 51, (2012), 11091 – 11096.

[35]. Nath J., Chaudhuri M.K., "Boric acid catalyzed bromination of a variety of organic substrates: an eco-friendly and practical protocol", Green Chemistry Letters and Reviews, 1, (2008), 223 – 230.

[36]. Saka C., Balbay A., "Influence of process parameters on enhanced hydrogen evolution from alcoholysis of sodium borohydride with a boric acid catalyst", International Journal of Hydrogen Energy, 45, (2020), 16193 – 16200.

[37]. Xu D., Zhao L., Dai P., Ji S., "Hydrogen generation from methanolysis of sodium borohydride over Co/Al2O3 catalyst", Journal of Natural Gas Chemistry, 21, (2012), 488 – 494.

MANAS Journal of Engineering
ISSN 1694-7398 | e-ISSN 1694-7398

Volume 9, Issue 2, (2021) Pages 153-159
https://doi.org/10.51354/mjen.953547

A cleaner application on hydrogen sulfide

Merve Aksu, Mehmet Hakan Morcali*

Gaziantep University, Naci Topcuoglu Vocational High School, Gaziantep, Turkey, merveaks1996@gmail.com, ORCID: 0000-0003-1212-8060, hakanmorcali@gmail.com, ORCID: 0000-0002-5021-4459.

ABSTRACT

With the increasing industrial production, there was a significant number of toxic and harmful hydrogen sulfide (H_2S) gas generated. Due to the industrial activities, converting H_2S gas from the waste of industrial process is environmentally attractive. This paper focuses on the conversion of H_2S to elemental sulfur (S°) and other sulfur species (i.e., sulfite ion (SO_3^{2-}); sulfate ion (SO_4^{2-}) using Fenton reagent. The effects of some reaction parameters such as Fe^{2+} ion concentration, amount of hydrogen peroxide (H_2O_2), reaction time, initial H_2S concentration and, liquid-gas ratio on H_2S conversion percentage were explored thoroughly. The results revealed that the increase of the Fe^{2+} ion concentration and H_2O_2 quantity could promote the conversion of H_2S. Besides, the comparable results were recorded for each reaction parameter. An apparent positive effect was observed with increasing the amount of H_2O_2 on H_2S conversion. However, the conversion percentage was decreased while increased in the initial concentration of the H_2S in the Fenton reactor. It was well accepted that the main conversion pathway of H_2S was hydroxyl radical (•OH). Additionally, the oxidative reaction of H_2O_2 on H_2S is thought another removal pathway. The expected products are sulphuric acid and S°.

ARTICLE INFO

Research article

Received: 16.06.2021
Accepted: 15.10.2021

Keywords:
conversion,
hydrogen sulfide,
fenton reagent,
hydroxyl radical (•OH)

**Corresponding author*

1. Introduction

Hydrogen sulfide (H_2S) is highly toxic, poisonous, corrosive, and, flammable. It is also with the characteristic foul odor of rotten eggs. H_2S commonly occurs in oil-gas production, volcanic gases, natural gas, coal/biomass gasification, leaching of sulfide-based ores, wastewater treatment, etc [1-3]. Acid rain, also called acid deposition, can easily occur in the polluted air when H_2S is oxidized to sulfur dioxide (SO_2) [2]. Besides, it affects nearly everything. Nowadays, various industrial companies have focused on eliminating H_2S due to the implementation of more strict environmental rules by the governments and also having bad odorous and occurring corrosive conditions in the production areas. However, most of them do not have still a plan regarding the H_2S removal process. Until recently, various technologies have been investigated for removing H_2S [1,2,4,5]. H_2S removal technologies can be collected in two main groups. These are physicochemical methods and biotechnological methods. The physicochemical method generally contains ozonation, photo/catalytic/chemical oxidation, photo-decomposition, several absorption techniques, etc. [1,3,6,9]. The biotechnological method primarily comprises biochemical processes such as thiobacillus sp., thermothrix azorensis, and thiothrix nivea, thioalkalispira microaerophila, cholorobium limicola [10-13]. In these processes, the conversion of H_2S and other sulfur compounds has been widely provided by a bacterium. The H_2S conversion efficiency of these methods shows promising results in some respects, but some problems still have been observed. These processes require high investment costs and equipment corrosion occurs during the process. Therefore, developing a new process and/or update the H_2S removal process is an important study area for scientists. Nowadays, the Fenton process is mainly preferred to remove and/or oxidize more organic/inorganic compounds in wastewater with generating powerful hydroxyl radicals (•OH) from that process [14, 15]. Due to several advantages such as strong oxidizing ability, simple process, and no secondary pollution, it has already started to apply wastewater treatment and also gas purification. The accepted possible reaction route of the Fenton process is following the formation of the hydroxyl radical. It was summarized in equation 1 [10, 14].

$$Fe^{2+} + H_2O_2 \longrightarrow Fe^{3+} + {\bullet}OH + OH^- \quad (1)$$

In this reaction, the ferrous ions (i.e.,Fe(II)) oxidized to ferric ion (i.e.,Fe(III)) and, the hydroxyl radical (i.e.,•OH) was produced. It is a strong oxidizer and, also the redox potential is 2.80 V. Several studies have been carried out regarding the removal of sulfur compounds from different kinds of waste sources with the Fenton reagent. For instance, the removal of

nitrogen monoxide (NO) from flue gas using the Fenton process has been studied [16]. A similar experimental setup was carried out [17] to remove SO_2 and NO from flue gas. According to the published articles, the possible reaction's mechanism between H_2S and •OH can be summarized in the following reactions:

$$H_2S + \bullet OH \rightarrow HS\bullet + H_2O \quad (2)$$
$$HS\bullet + \bullet OH \rightarrow S^{\circ}\downarrow + H_2O \quad (3)$$
$$HS^- + \bullet OH \rightarrow HSOH\bullet^- \quad (4)$$
$$HSOH\bullet^- + H_2O_2 \rightarrow H_2SO_3 + H_2 \quad (5)$$
$$H_2SO_3 + \bullet OH \rightarrow H_2SO_4 + \bullet H \quad (6)$$
$$H_2SO_3 + H_2O_2 \rightarrow H_2SO_4 + H_2O \quad (7)$$

Recently, amine-based solution has been studied to remove H_2S [2, 5, 18, 19] and also the Fenton process has been the most widely investigated by researchers. The results of the Fenton process encouraged the authors to investigate the Fenton reagent on H_2S gas. Furthermore, some studies have been extensively published in this field. The removal of H_2S gas was investigated [4], who examined the conversion of H_2S from generating coal mining area. Another interesting study was published [20], who studied the conversion of H_2S in the presence of UV radiation as a catalyst in order to remove of H_2S. However, the studies related to remove H_2S from the gas phase using the Fenton process are very scarce.

The goal of this study was to establish facile methods for producing elemental sulfur and to determine the reaction parameters for the Fenton process. The determination of the Fenton process parameters is significant for the conversion reaction. The precipitated solid characterization showed that the elemental sulfur was found as a significant compound in the conversion of H_2S by the Fenton process. These results presented that the Fenton process can be applied for pollution control, and sustainable products are quickly recovered from wastewater for a circular economy prospect. By reusing the products for different chemical processes, the concentration of sulfuric acid could be increased. It is possible to increase the sulfuric acid concentration to the industrial usage such as: accumulator industry, fertilizers, and plasterboard industry [1-4]. The Fenton process has been applied in the chemical process for a long time and will undoubtedly play a prominent role in the future. As demonstrated, the Fenton reagent can convert the H_2S efficiently.

2. Materials and methods

All experiments were carried out in a 250 mL three-neck borosilicate-tempered glass reactor and three washing bottle reactors (12 cm internal diameter; 45 cm length; Glass; spraying height is about 20 cm). There are two bottle reactors were used to convert H_2S to sulfur compounds and, the last one was used to the measure concentration of the remaining gas (i.e., rest of H_2S). The H_2S gas was purged with a carrier gas (N_2) into the reactor. The mixture of gas (H_2S+N_2) was continuously purged into the reactor via a plastic pipe from a compressed gas cylinder. A 0.1 L/min of stripping gas that contained H_2S was measured by using the flow meter. The schematic image of the experimental setup was described in Fig. 1.

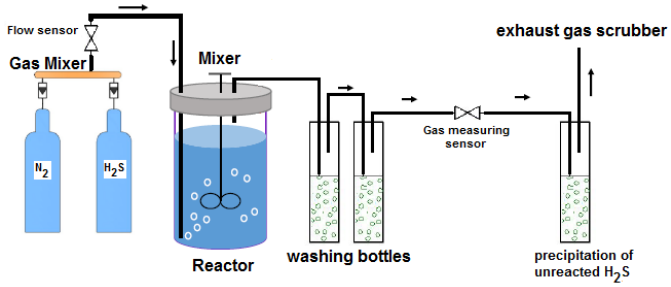

Figure 1. *Experimental process of the conversion of H_2S*

All chemicals were analytical grade, and also all experiments were carried out using deionized water unless otherwise stated. 400 mL of Fenton reagent (Fe^{2+}/H_2O_2) was prepared using H_2O_2 and $FeCl_2$ solution. The solution was divided into two washing bottles. The pH of the Fenton reagent solution was measured and, if necessary, set to the desired value by the HCl and the NaOH before adding the Fenton reagent into the washing bottle reactors. The temperature of the solutions was kept constant in the whole experiment. The mixture of gases (i.e., containing-H_2S and N_2) directly purged into the reactor and the solution was continuously stirred with a magnet to provide a gas-liquid reaction. The exhaust (i.e., unreacted gas) concentration of H_2S was measured by antimony potassium tartrate ($K_2Sb_2(C_4H_2O_6)_2$) solution. All experiment running time was kept for 60 min. The unreacted H_2S gas in the exhaust gas subsequently was precipitated as antimony tri sulfur (Sb_2S_3) for further purification. After completing the H_2S conversion process, the solution was filtrated and washed acetone to obtain dry powder. The weight of powder was recorded and then validated by XRD and SEM-EDX techniques which can reference the literature [9, 13]. Afterward, the possible ions (i.e., SO_3^{2-} and SO_4^{2-}) were determined by using ion chromatography (IC) (Perkin Elmer IC1000). The conversion of H_2S is calculated by the following Eq. (8):

$$H_2S \text{ conversion, } \% = [(C_{in} - C_{out})/C_{in}] \times 100 \quad (8)$$

Where; C_{in} is inital concentration of H_2S, ppm; C_{out} is H_2S concentration in exhaust gas, ppm.

3. Results and discussions

3.1. Effects of Fe^{2+} concentration on H_2S conversion

The effect of ferrous ion (Fe^{2+}) concentration on H_2S conversion was investigated. In this experimental study, 1000 ppm H_2S gas was continuously fed into the Fenton reactor containing 600 µL of H_2O_2 (30%) at 400 rpm for 60 min at 25°C. The H_2S conversion percentage and also distribution of

sulfur compound percentage results were demonstrated in Figure 2. Without Fenton reaction, the H_2S conversion percentage was recorded at 8.9% via H_2O_2. The direct oxidation of H_2S with H_2O_2 and •OH radical can be expressed by the following reactions [4]:

$$H_2S + H_2O_2 \rightarrow 2H_2O + S^\circ\downarrow \quad (9)$$

$$HS^\bullet + {}^\bullet OH \rightarrow S^\circ\downarrow + H_2O \quad (10)$$

H_2S conversion percentage consistently increased with increasing ferrous ion concentration in the range of 12.5–125 mM, as expected since the reaction was canalized to the right side with increasing ferrous ion concentration (see Eq.1). A similar experiment was carried out in the literature [21]. They found that ferrous ion has a positive effect on H_2S conversion. The conversion of H_2S percentage, however, was leveled off with further ferrous ion elevated. The results exhibited that the concentration of ferrous ion was increased while H_2S conversion percentage increased rapidly from around 30 to 80%.

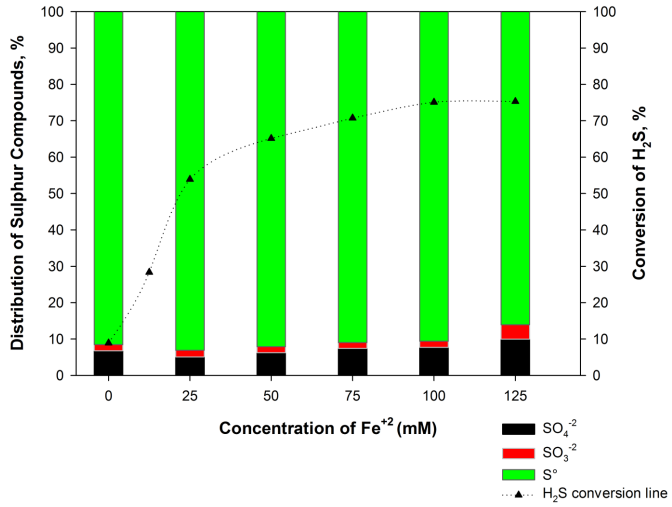

Figure 2. *Changes of H_2S conversion percentage versus Fe^{+2} ion concentration*

To understand the distribution of sulfur compounds (i.e., S°, SO_3^{2-}, SO_4^{2-}), they were determined using spectrometric methods, explained in the experimental section before. The results demonstrated that the small part of elemental sulfur could be directly oxidized by free H_2O_2. Interestingly, the sulfate ion (SO_4^{2-}) concentration was moderately increased when increasing Fe^{2+} concentration. When compared with the sulfite ion (SO_3^{2-}) concentration which was not regularly increased.

This result was supported via a chemical reaction between H_2O_2 and Fe^{2+}. Finally, the radical •OH can be produced in the solution. The possible reaction pathway is summarized in the introduction section (see Eq.1). According to this equation, the reaction was occurred between H_2O_2 and Fe^{2+} and also to produce •OH free radical. This reaction can be prompted to the right side with increasing of Fe^{2+} concentration. In this way, the yield of •OH radical can increase in solution and enhancing H_2S conversion percentage. However, more ferrous ion concentration consumes the radical •OH in the solution since it has a very high reaction rate given in Eq.11 [21].

$$Fe^{2+} + {}^\bullet OH \rightarrow Fe^{3+} + OH^- \qquad k = 3.0\times10^8\ M^{-1}s^{-1} \quad (11)$$

Due to this restriction, more Fe^{2+} ions cannot further provide an extensive conversion of the percentage of H_2S. The results showed that the Fenton process produced three sulfur species (S°, SO_3^{2-}, SO_4^{2-}) from the H_2S by oxidation potential of •OH radical and also H_2O_2 (see Eqs. 2-7). Based on the results, the conversion process includes two process stages: first producing •OH radicals to oxidize H_2S molecules, and second, determination of the type of sulfur compounds and recovery followed by S° conversion.

3.2. Effects of H_2O_2 concentration on H_2S conversion

The effects of H_2O_2 in the Fenton reactor on the conversion of H_2S were studied by varying the amount of H_2O_2 in the range of 0-1400 µL. In the experimental series, the Fenton reactor contained 100 mM Fe^{+2}, and other reaction parameters were kept constant (400 rpm, 60 min, 25°C). The effects of the amount of H_2O_2 on the conversion of H_2S and the distribution of sulfur compounds percentage were shown in Figure 3. The comparative experiments have shown that the use of the only Fe^{2+} was converted to 2.6% of H_2S. This result was expected since there are no free radical occurs in the solution. The results display that the increase of the H_2O_2 quantity from 0 to 800 µL, the H_2S conversion percentage was evaluated up to 80%. The H_2S conversion percentage was decreased from 80% to 55%, while their H_2O_2 quantity was increased from 800 µL to 1400 µL. This unexpected result can be supported by the self-consumption of •OH radical according to the following reaction [21]:

$$^\bullet OH + H_2O_2 \rightarrow H_2O + HO_2^\bullet \qquad k = 2.7\times10^7\ M^{-1}\ s^{-1} \quad (12)$$

As understood from the reaction rate, the possibility of the reaction has inhibited the conversion of H_2S, and also the numbers of unexpected productions were increased.

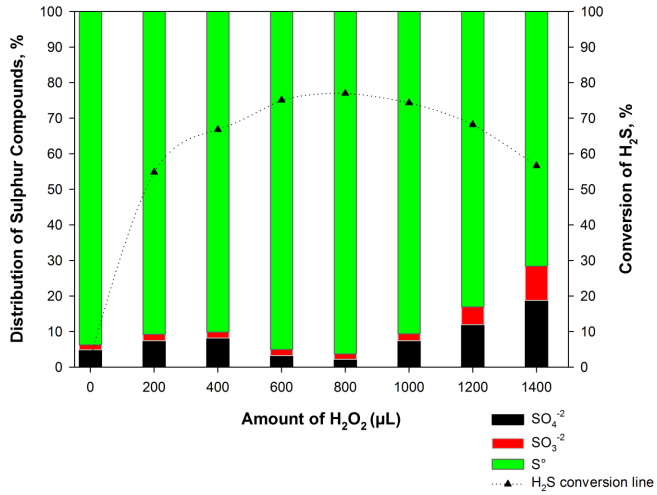

Figure 3. *Changes of H_2S conversion percentage versus H_2O_2 concentration*

The H_2S removal process can be carried out in two ways, •OH radicals play a major way in the removal of H_2S, and also the oxidation of H_2S by H_2O_2 can be defined as a minor way for the removal of H_2S.

In industrial applications, flue gas usually includes different kinds of pollutants such as SO_2, NOx, CO, CO_2, VOCs, etc.[1, 6] For this reason, the effects of combination (e.g., mixture of gases) of the industrial flue gas components on the H_2S removal mechanism should be defined and further studied in depth in future works.

3.3. *Effects of reaction time on H_2S conversion*

In this experimental series, the effect of reaction time on H_2S conversion was studied. 1000 ppm H_2S gas was fed into the Fenton reactor containing the mixture of 100 mM Fe^{+2} and 800 µL H_2O_2 solutions at 400 rpm and 25°C. Figure 4 displays the effects of reaction time on H_2S conversion percentage. Prolonging the reaction time to 600 min was investigated, expecting a higher conversion percentage. However, the conversion reaction was increased up to 90 min. At that time, the highest conversion percentage was recorded as around 80%. After that point, the extension of the reaction time and could not increase the conversion percentage of H_2S, but unwanted species (i.e., SO_3^{2-}, SO_4^{2-}) were increased in the reactor. This phenomenon may be expressed by equation 4-6. The SO_3^{2-} and SO_4^{2-} species in the solution were increased with further connection •OH radical with H_2S gas.

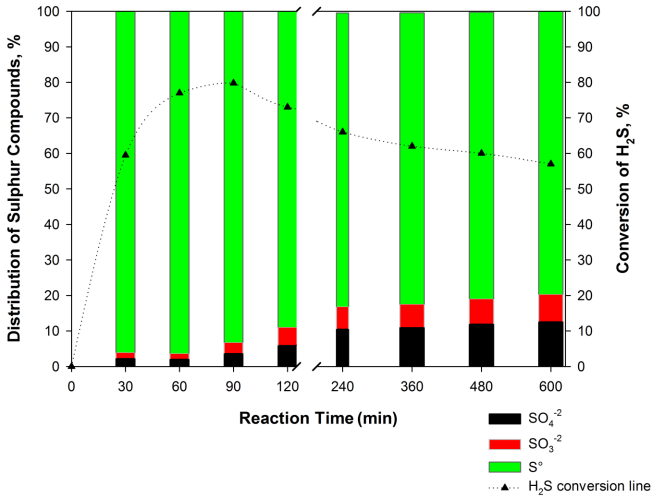

Figure 4. *Changes of H_2S conversion percentage versus reaction time*

After that point, the extension of the reaction time and could not increase the conversion percentage of H_2S, but unwanted species (i.e., SO_3^{2-}, SO_4^{2-}) were increased in the reactor. This phenomenon may be expressed by equation 4-6. The SO_3^{2-} and SO_4^{2-} species in the solution were increased with further connection •OH radical with H_2S gas.

3.4. *Effects of initial H_2S concentration on H_2S conversion*

The effect of the initial concentration of H_2S on conversion percentage was investigated. The experiments were carried out by varying the amount of H_2S gas in the range of 250-2000 ppm. The highest reaction parameters were selected from the previous experimental results (100 mM Fe^{+2} and 800 µL H_2O_2 solutions at 400 rpm, 90 min and 25°C) and they were kept constant during the experiments.

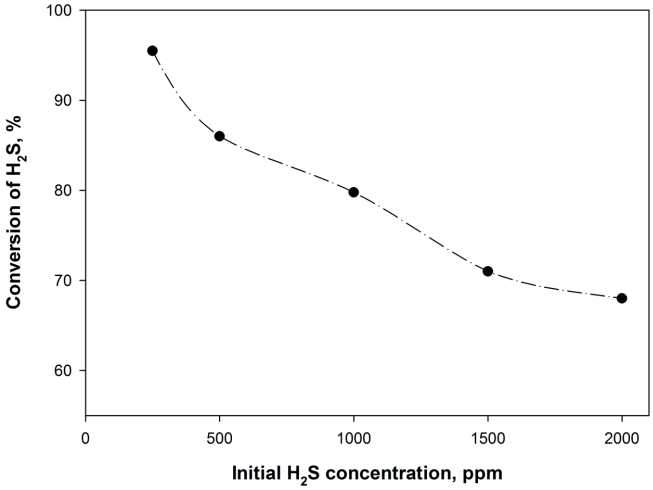

Figure 5. *Changes of H_2S conversion percentage versus reaction time*

According to Figure 5, the conversion percentage of H_2S decreased with increasing the amount of H_2S gas. This trend was the expected to result because the increase of the feeding

concentration of the H_2S decreased the interaction between the H_2S molecule and reactant. This result was supported [21], who found that the H_2S conversion percentage decreased as the initial amount of H_2S increased. This experimental were provided that the H_2S conversion percentage decreased while increasing the initial H_2S concentration.

3.5. Effects of liquid-gas ratio on H_2S conversion

Several experiments were carried out to understand the effect of liquid-gas ratio on H_2S conversion percentage. The obtained results were presented in Figure 6.

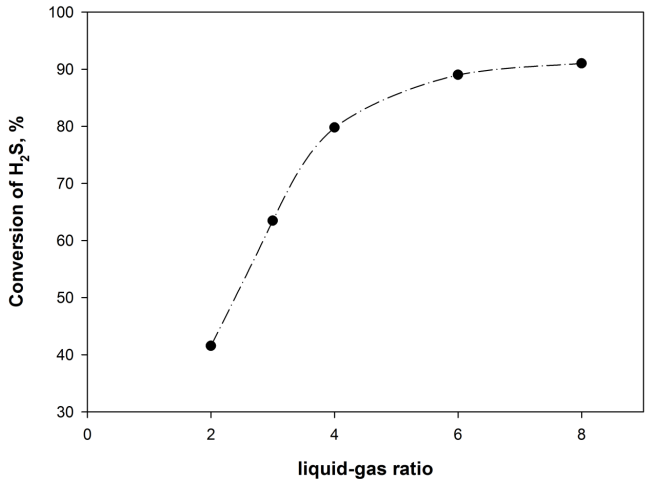

Figure 6. *Changes of H_2S conversion percentage versus reaction time*

It was demonstrated that the liquid-gas ratio evaluated from 2.0 to 10.0, H_2S conversion percentage significantly raised from around 40% to 90%. This trend can be expressed that the amount of the oxidants (H_2O_2 and •OH) abounded in the reactor. In addition, the conversion process was to be more effective due to the increase of the liquid-gas ratio. Thus, the high gas-liquid ratio improves the H_2S conversion percentage. This increasing trend in our work was found to be similar [20] As a result, it was evident that an increase in liquid-gas ratio shows a significant increase in H_2S conversion. However, since more liquid-gas ratio needs more investment, the most appropriate liquid-gas ratio should be determined by considering efficiency and energy costs.

3.6. Characterization of the reaction product

Following the H_2S conversion process, the reaction product, which was precipitated in the reactor, was characterized using X-ray diffraction (XRD) and Scanning Electron Microscopy (SEM) with Energy Dispersive X-ray Analysis (EDX). Before XRD and SEM-EDX analysis, the solid reaction product was filtered and washed with distilled water and subsequently acetone. Afterward, the powder was dried in a vacuum desiccator at 25°C overnight. The XRD results displayed in Figure 7 shows that the precipitated powder is elemental sulfur in the reactor.

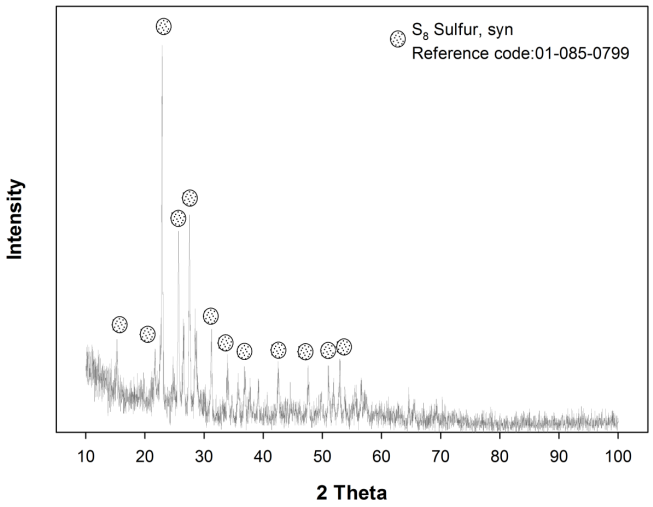

Figure 7. *Changes of H_2S conversion percentage versus reaction time*

To understand the morphological structure of the precipitated elemental sulfur powder was characterized by using SEM-EDX. Figure 8a discloses that the sulfur particles have clearly appeared. They have an orthorhombic structure, which is the most effective form of sulphur (alpha-Sulfur). It is the conventional form stable at room temperature and atmospheric pressure. The EDX peaks (see Figure 8b) show that the powder is characteristic of the elemental sulfur phase present.

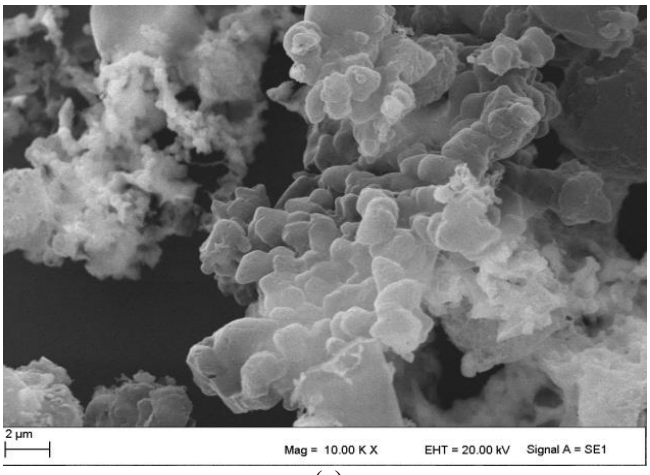

(a)

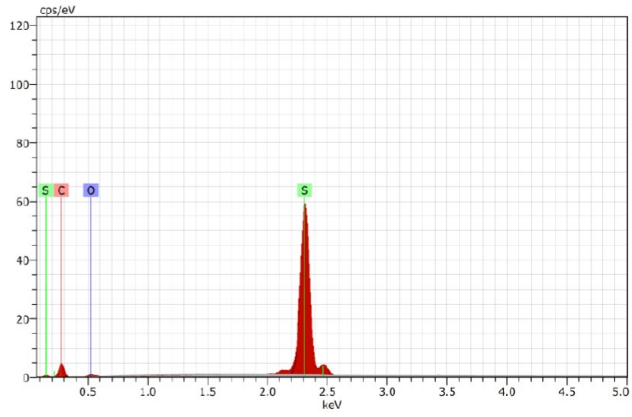

(b)

Figure 8. *Changes of H_2S conversion percentage versus reaction time*

The characterization result was compatible with the chemical reaction and related discussions. The precipitated elemental sulfur can be easily separated with filtration from the solution. The remaining sulfuric acid in the reactor can be concentrated by the evaporation processes or ammonium sulfate can be precipitated by adding ammonia in the reactor. Moreover, calcium sulfate can be produced by adding lime for plasterboard production, which is an essential building material. Hence, the designed process can provide zero waste liquid discharge.

4. Conclusions

This work covers the conversion behavior of the H_2S using Fenton regent and the determination of possible sulfur compounds in the reactor. It was found that the Fenton process facilitated the converting of S^{-2} to S° and controlled the occurring of other species significantly. Moreover, the number of ferrous ions (Fe^{+2}) and hydrogen peroxide (H_2O_2) were critical for the high conversion of H_2S in the Fenton process, with the optimal parameters of 100 mM Fe^{+2}, 800 µL H_2O_2 at 400 rpm, 90 min, and 25°C. Under these conditions, the conversion percentage of H_2S reached around 85%. Concurrently, sulfur species such as elemental sulfur (S°), sulfite ion (SO_3^{2-}); and sulfate ion (SO_4^{2-}) was found to 89%, 2%, and 9% in the reactor solution, respectively. These compounds can be further treated chemically to recover as new products. The possible conclusion results are summarized. The increase of ferrous concentration or peroxide quantity or liquid-gas ratio value can increase the conversion of H_2S percentage whereas more H_2O_2 no influenced on the conversion of H_2S. The evaluating the initial H_2S concentration observed adverse effect on H_2S conversion percentage. The reaction time has a positive effect on H_2S conversion percentage up to 90 min. The main pathway is accepted the oxidation of H_2S by radical •OH and the oxidation and hydrolysis of H_2S by H_2O_2 are the bypath. The main products of H_2S conversion are elemental sulfur and sulphuric acid. This study lays the groundwork for future research on the processability of industrial exhaust gas such as petroleum refineries, coal-fired power plants; other power plants (e.g. burning high-sulfur residual oil and/or petcoke).

Acknowledgments

The authors gratefully acknowledge the TUBITAK (217M284) for financial support

References

[1]. Liu Y, Shi S, Wang Y. "Removal of Pollutants from Gas Streams Using Fenton (-like)-based Oxidation Systems: A Review", J Hazard Mater, (2021), 125927.

[2]. Kailasa S.K, Koduru J.R, Vikrant K, Tsang Y.F, Singhal R.K, Hussain C.M, Kim K-H. "Recent progress on solution and materials chemistry for the removal of hydrogen sulfide from various gas plants", J Mol Liq, 297, (2020), 111886.

[3]. Rubright S.L.M, Pearce L.L, Peterson J. "Environmental toxicology of hydrogen sulfide. Nitric oxide: biology and chemistry", 71, (2017), 1-5.

[4]. Lin H, Wang Y-N, Wei W, Yu Y-J. "Treatment of H 2 S in mine water using Fenton reagent", J China Coal Soc, 37, (2012), 1760-1764.

[5]. Liu D, Wang Q, Wu J, Liu Y. "A review of sorbents for high-temperature hydrogen sulfide removal from hot coal gas", Environmental Chemistry Letters 17, (2019), 259-276.

[6]. Lin F, Wang Z, Zhang Z, He Y, Zhu Y, Shao J, Yuan D, Chen G, Cen K. "Flue gas treatment with ozone oxidation: An overview on NOx, organic pollutants, and mercury", Chem Eng J, 382, (2020), 123030.

[7]. Wang Y, Wang Z, Liu Y. "Oxidation absorption of gaseous H2S using Fenton-like advanced oxidation systems", Energy & Fuels 32, (2018), 11289-11295.

[8]. Liu Y, Wang Y. "Gaseous elemental mercury removal using VUV and heat coactivation of Oxone/H2O/O2 in a VUV-spraying reactor", Fuel 243, (2019), 352-361.

[9]. Wang H, Yuan B, Hao R, Zhao Y, Wang X. "A critical review on the method of simultaneous removal of multi-air-pollutant in flue gas", Chem Eng J 378, (2019),122155.

[10]. Pagella C, De Faveri D. "H2S gas treatment by iron bioprocess", Chem Eng Sci 55, (2000), 2185-2194.

[11]. Oyarzún P, Arancibia F, Canales C, Aroca GE. "Biofiltration of high concentration of hydrogen sulphide using Thiobacillus thioparus", Process Biochem 39, (2003), 165-170.

[12]. Deshpande A.S, Khomane R.B, Vaidya B.K, Joshi R.M, Harle A.S, Kulkarni B.D. "Sulfur nanoparticles synthesis and characterization from H2S gas, using novel biodegradable iron chelates in W/O microemulsion", Nanoscale Research Letters 3, (2008), 221-229.

[13]. Dumont E. "H2S removal from biogas using bioreactors: a review", International Journal of Energy and Environnement 6, (2015), 479-498.

[14]. Safarzadeh-Amiri A, Bolton JR, Cater SR. "The use of iron in advanced oxidation processes" Journal of Advanced Oxidation Technologies 1, (1996), 18-26.

[15]. Cetinkaya SG, Morcali M.H, Akarsu S, Ziba C.A, Dolaz M. "Comparison of classic Fenton with ultrasound Fenton processes on industrial textile wastewater", Sustainable Environment Research 28, (2018), 165-170.

[16]. Guo R-t, Pan W-g, Zhang X-b, Ren J-x, Jin Q, Xu H-j, Wu J. "Removal of NO by using Fenton reagent solution in a lab-scale bubbling reactor", Fuel 90, (2011), 3295-3298.

[17]. Liu Y, Zhang J, Sheng C, Zhang Y, Zhao L. "Simultaneous removal of NO and SO2 from coal-fired flue gas by UV/H2O2 advanced oxidation process", Chem Eng J 162, (2010), 1006-1011.

[18]. Ma Y, Jin X, Hu Y, Huang Q, Wang Z. "Recovery of Hydrogen and Sulfur by Electrolysis of Ionized H2S in an Amine-Containing Organic Electrolyte with Highly Temperature-Dependent Sulfur Solubility", Energy & Fuels 34, (2020), 7756-7762.

[19]. De Crisci AG, Moniri A, Xu Y. "Hydrogen from hydrogen sulfide: towards a more sustainable hydrogen economy", Int J Hydrogen Energy 44, (2019), 1299-1327.

[20]. Liu Y, Wang Y. "Removal of gaseous hydrogen sulfide by a photo-Fenton wet oxidation scrubbing system", Energy & Fuels 33, (2019), 10812-10819.

[21]. Wang Y, Wang Z, Pan J, Liu Y. "Removal of gaseous hydrogen sulfide using Fenton reagent in a spraying reactor", Fuel 239, (2019), 70-75..

MANAS Journal of Engineering
ISSN 1694-7398 | e-ISSN 1694-7398

Volume 9, Issue 2, (2021) Pages 160-168
https://doi.org/10.51354/mjen. 917837

Training of the feed-forward artificial neural networks using butterfly optimization algorithm

Büşra Irmak, Şaban Gülcü*

Necmettin Erbakan University, Faculty of Engineering, Turkey, sgulcu@erbakan.edu.tr, ORCID: 0000-0003-0972-7954, ORCID: 0000-0001-7714-8861

ABSTRACT

Artificial Neural Network (ANN) learns from inputs and outputs. The values of the weights and biases in ANN are updated according to inputs and outputs. Researchers have proposed algorithms to train Multi-Layer Perceptron (MLP). However, classical techniques often face problems in solving this optimization problem. They tend to need large amounts of computing time, large amounts of memory. More importantly, they get stuck within the local optimum and produce poor-quality solutions. To overcome these difficulties, meta-heuristic algorithms have been used to train MLP. In this article, the Butterfly Optimization Algorithm (BOA) which was designed by modeling the behaviors of butterflies was used for the first time to train the multi-layer perceptron. The developed algorithm was named BOA-MLP where the BOA algorithm optimized the values of the weights and biases in the MLP. The success of the BOA-MLP algorithm was tested on five data sets (iris, breast cancer, heart, balloon and xor) which are frequently used in the literature. In the experiments, the BOA-MLP algorithm was compared with the BAT-MLP, SMS-MLP and BP algorithms. The average and standard deviation of the mean squared error, the average classification accuracy, the sensitivity, the specificity, the precision and the F1-score were used as the performance metrics. According to the experimental results, it is seen that the BOA-MLP algorithm surpasses the BAT-MLP, SMS-MLP and BP algorithms on all data sets and shows superior success.

ARTICLE INFO

Research article

Received: 27.04.2021
Accepted: 14.06.2021

Keywords:
artificial neural networks,
butterfly optimization algorithm,
multi-layer perceptron,
optimization,
training of artificial neural networks

**Corresponding author*

1. Introduction

Artificial Neural Networks (ANNs) are one of the most important and biggest inventions in its field. It was developed by taking the behavior of the human brain as a role model. ANN is used in many areas such as classification, recognition, prediction and optimization. ANN developed by imitating the human brain has proven its success in the field of optimization as in many other fields.

Artificial Neural Networks include studies for computer learning. Today, digital devices and digital systems occupy an important place in our lives. Computers are used in almost every field. Computers have gained a feature that summarizes large amounts of data over time and can make comments about events using this data, while only calculating or performing data transfers in the past years. Today, computers can both make decisions about events and learn the relationship between events. It is seen that computers used today have both the ability to establish the pattern between events and to make interpretations and decisions about events. Computers have the ability to solve difficult problems that are not mathematically represented. Thanks to the superior learning ability of ANNs, they offer solutions to complex problems to solve with traditional methods. Again, thanks to the tribe of learning, it can generalize/predict situations that have not been encountered before using known examples. The most commonly used ANN method while performing these operations is the Multi-Layer Perceptron (MLP).

The ability of ANN to give correct results and to make successful classifications is provided by updating the bias and weight values in the most appropriate way. In the literature, researchers have proposed algorithms to train Multi-Layer Perceptron. However, classical techniques often face problems in solving optimization problems in the real world. They tend to need large amounts of computing time, large amounts of memory. More importantly, they get stuck within the local optimum and produce poor-quality solutions. To overcome these difficulties, meta-heuristic algorithms have been used to train ANNs [1].

The meta-heuristic algorithms designed by taking the biological movements of living things as role models, such as

hunting, reproduction and feeding, aim to find the optimum result by producing solutions to problems in a search space [2]. Many challenging problems have been optimized using meta-heuristic algorithms. Meta-heuristic algorithms have been developed by taking inspiration from their unique behaviors in order to continue the vital activities of living things in nature. For this reason, these algorithms are named Natural Optimization Algorithms [3].

Many meta-heuristic algorithms have been used in the literature for training ANN. Some of these are those: Mirjalili [4] used the recently proposed Gray Wolf Optimization (GWO) algorithm for multi-layer perceptron (MKP) training. Five classifications and eight standard data sets were used to test the proposed method. It was compared with the best-known meta-heuristics algorithms. In [5], harmony search algorithms applied for supervised training of feed-forward (FF) type ANNs, which are frequently used for classification problems. Five different types of fit search algorithms were examined, paying special attention to the self-adaptive global best-fit search (SGHS) algorithm. A structure suitable for data representation of ANNs has been adapted to the SGHS algorithm. The technique has been empirically tested and validated by training ANN on the six criteria classification problem and the real-world problem. In [6], a model based on the Artificial Bee Colony (ABC) algorithm was produced to estimate the safety factors of the retaining walls. The weight and bias values of the ANN have been optimized with the ABC algorithm in order to obtain a higher level of accuracy and performance estimation in safety factors. It has been determined that the network performance is strengthened with the produced model. Tang and Fong [7] used the Dynamic Group Optimization (DGO) algorithm, which is semi-transverse and semi-evolutionary, to train a feed-forward neural network. They named the model FSADGO. In the training neural network, the DGO plays an optimization role. It optimizes the parameters and the structure of the feed-forward neural networks. It tested with two real-world problems and compared with other training algorithms. Zhang and Suganthan [8] discussed the randomized training of ANN, which attracted great attention from researchers in areas such as machine learning, statistics, and computer vision. Ojha and Abraham [9] investigated the optimization of weights of artificial neural networks, network architecture, activation nodes, learning parameters, learning environment, etc. Hacibeyoglu and Ibrahim [10] proposed a new particle swarm optimization to train multi-layered, feed-forward neural networks. It was observed that the proposed algorithm searches the solution space more than once and gives better results than particle swarm optimization by testing on ten data sets. Recently, Gülcü [11] has developed the SMS-MLP algorithm to train ANN using the States of Matter Search algorithm. He used five classification problems in the experiments. The SMS-MLP algorithm was compared with the six algorithms. The experimental results showed that the SMS-MLP algorithm is more efficient than six algorithms.

In this study, the Butterfly Optimization Algorithm is employed to train ANN for the first time. The BOA based on the swarm intelligence was developed by Arora and Singh [12]. BOA is a meta-heuristic algorithm. It is an algorithm that is made by modeling the foraging behavior of butterflies. They also use it when migrating, escaping from a predator, or laying eggs somewhere. In this study, we aimed to optimize the bias and weight values. In the experimental study part, the BOA-MLP algorithm was run on the most important five data sets in the literature and compared with three different algorithms. As a result of the comparison, the success of the BOA-MLP algorithm has been demonstrated. The main reason for the success of the BOA-MLP algorithm is that the BOA-MLP algorithm is able to escape the local optimum.

2. Material and method

2.1. Artificial Neural Network

Artificial neural networks are an information processing technique developed by modeling the operation of the nervous system of the human brain. In other words, it is the digital platform of the synaptic connections established by the neurons in the human brain. Because of the success of ANN, ANN has been used in many different areas such as system modelling [13], prediction, pattern recognition, and optimization [14, 15].

The basic building blocks of the human brain and ANN are nerve cells. The human nerve cell consists of the core, body and two extensions. The shorter of these extensions are called dendrites and dendrites are branched into thousands of branches. Its task is to get login information. The single and long extension is called the axon and its task is to carry the output information to other nerve cells [16]. Artificial nerve cell has been developed by imitating the human nerve cell. The inputs entering the nerve cell are multiplied by the respective link weights to obtain the neuron's net input and then combined with the coupling function. The result is processed by the activation function, and thus the net output of the neuron is obtained. Fig. 1 shows an artificial nerve cell.

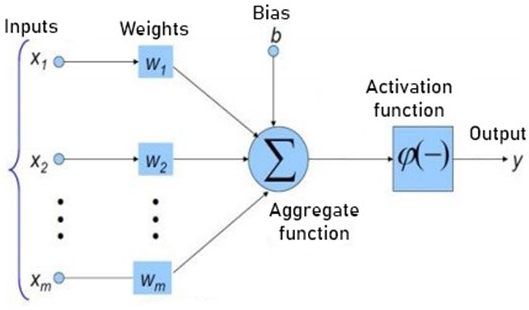

Figure 1. *Artificial Nerve Cell [17].*

ANNs are formed by the merging and grouping of artificial nerve cells. This merging consists of layers and as a result, ANN comes together from more than one interconnected layer. ANN consists of three layers as input layer, hidden layer and output layer. However, in some cases, the number of hidden layers may be more than one. In many ANN models, things go in order. That is, the hidden layer receives data from the previous input layer, processes the data and directs the results to the output layer. According to the type of ANNs, ANNS are divided into two groups as a feed-forward neural network and a feedback neural network. The feed-forward neural network is the network structure where data processing goes from input to output. A feedback neural network is the network structure where data processing can flow not only from input to output but also from output to input (backward).

The multi-layer perceptron is a feed-forward network structure with one or more hidden layers between the input layer and the output layer. In Fig. 2, the structure of the MLP with a single hidden layer is shown.

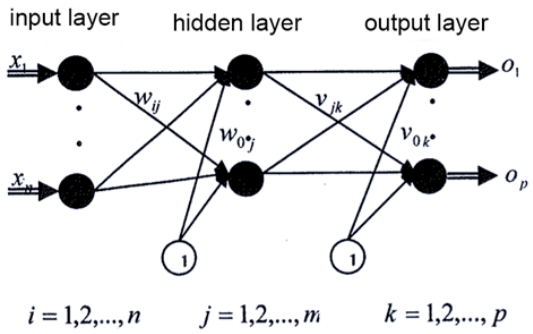

Figure 2. *MLP with a single hidden layer [18].*

An MLP consists of the following components: Artificial neural cell and layers, combine function, activation function, error function, learning algorithm.

The artificial nerve cell, consisting of inputs, concatenation and activation functions, was developed by imitation of the human nervous system. In an artificial nerve cell, input values (weights) are multiplied by node weights and sent to the merge function. The result returned from the merge function is sent to the activation function, so that the net output of the artificial nerve cell is obtained. Sigmoid, hyperbolic, ramp, identity and step functions are the most important activation functions. However, the most used one among these functions is the sigmoid function. The sigmoid function is shown in Equation (1).

$$Sigmoid(x) = \frac{1}{1 + e^{-x}} \quad (1)$$

The error function, which is one of the components of the MLP, is the objective function that finds the error in the ANN system. The most used error function is the Mean Square Error (MSE) whose formulation is given in Equation (6). Finally, the learning algorithm is the last component of the MLP. The learning algorithm mostly affects the performance of the ANN.

2.2. Butterfly Optimization Algorithm (BOA)

The Butterfly Optimization Algorithm (BOA) has been developed to solve challenging optimization problems. The main strategy of the BOA is to find nectar using the sense of smell. This strategy is generally as follows: Butterflies use their sense of smell to obtain the position of nectar, smell and analyze the air. The BOA algorithm takes this behavior as a role model to find the optimum value in the search space for a predefined problem. Considering scientific research, it has been observed that butterflies have a superior ability to reach the source of the scent. Butterflies are the BOA algorithm's search agents for optimization. A butterfly will produce an intensity of scent associated with its suitability.

The BOA algorithm has been developed considering the following three vital strategies:

1) All butterflies are expected to produce a scent that causes the butterflies to turn towards each other.
2) Each butterfly is expected to act randomly or move towards the superior butterfly emitting more scent.
3) The scent of a butterfly is determined or influenced by the value of its objective function.

We can explain these three stages in the BOA algorithm which is made by taking the behavior of butterflies as a role model.

1) Initialization Phase: Parameters are determined, an initial population is generated for the algorithm. When creating the starting population, the location of the butterflies is randomly assigned by calculating their odor values.
2) Iteration Stage: This stage is the part where the main processes are carried out and each butterfly tries to achieve the best result with parameters specific to the BOA algorithm. All butterflies in the search area are moved to new locations and new fitness values are calculated at each iteration.
3) Last stage: It is the part where the stopping criterion is fulfilled and the optimum result or the closest result is reached.

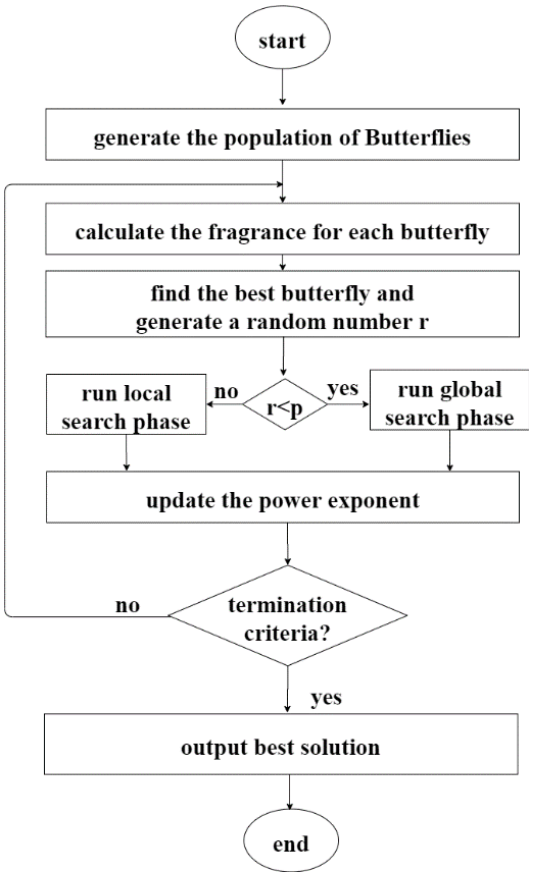

Figure 3. *The flowchart of the BOA algorithm.*

The BOA modality shown in Equation (2) is based on three basic concepts: sensory method (*c*), stimulus intensity (*I*) and power exponent (*a*). The sensory method refers to the raw input used by receptors to measure sensory energy form and process it in similar ways. The parameter *I*, which is the stimulus intensity, is limited to an exponential value. This is because, in previous studies by scientists, it was seen that as the stimulus gets stronger, the insects intensely go to the stimulus and this situation eventually becomes less sensitive. The parameter *a* is involved in correcting this situation. The parameter *a* is the power base depend on modality (smell in BOA). If *a* is equal to 1, it means there is no odor absorption. In other words, the rate of smell produced by a specified butterfly is perceived by other butterflies with the same capacity. This brings the butterfly closer to a single solution, usually the optimum. If *a* is equal to 0, it means that the scent emitted by the butterfly cannot be perceived by others. This allows searching locally.

$$f = c \times I^a \tag{2}$$

where *a* and *c* are random numbers in [0, 1], *f* is the perceived magnitude of the scent, and *I* is the stimulus intensity.

There are two important stages in the algorithm: local search and global search. The global search is shown in Equation (3).

$$X_i^{t+1} = X_i^t + (r^2 \times g^* - X_i^t) \times f_i \tag{3}$$

where g^* represents the best available solution among all the solutions in the current iteration. X_i^t and X_i^{t+1} are the positions of the butterfly i in the iterations t and $t+1$ respectively. r provides a randomness that takes value in the range [0, 1] and f_i represents the perceived smell of the butterfly.

Local search is shown in Equation (4). Here, unlike the global, the X_i^t butterfly does not go towards the global best (g), it exhibits a random walk in the search space.

$$X_i^{t+1} = X_i^t + \left(r^2 \times X_j^t - X_k^t\right) \times f_i \tag{4}$$

where X_j^t and X_k^t are the positions of the butterflies i and j which are the randomly selected neighbors of the butterfly i. r provides a randomness that takes value in the range [0, 1] and f_i represents the perceived smell of the butterfly.

Searching for food can happen both locally and globally. Thus, a switching probability *p* is used in the BOA algorithm to switch between the global search and the local search. The key value is the probability value that decides whether the butterflies will show the best movement or a random walk. The flowchart of the BOA algorithm is presented in Fig. 3.

2.3. Training MLP using BOA Algorithm (BOA-MLP)

ANN learns from inputs and outputs. For this, the values of the weights and biases in ANN are updated according to inputs and outputs [11]. The ability of ANN to give correct results and to make successful classifications is provided by updating the bias and weight values in the most appropriate way. In the literature, researchers have proposed algorithms to train Multi-Layer Perceptron (MLP). However, classical techniques often face problems in solving this optimization problem. They tend to need large amounts of computing time, large amounts of memory. More importantly, they get stuck within the local optimum and produce poor-quality solutions. To overcome these difficulties, meta-heuristic algorithms have been used to train MLP [1]. In this study, the hybrid BOA-MLP algorithm is proposed to optimize the values of the weights and biases. The BOA algorithm which is a meta-heuristic algorithm was employed to train MLP for the first time. The process of the optimization of the weights and biases is shown in Fig. 4.

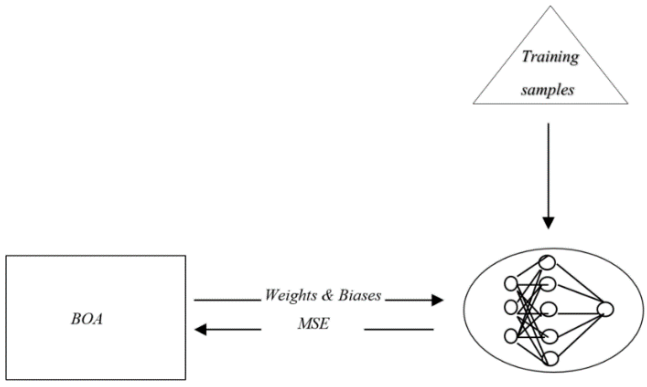

Figure 4. *The process of the optimization of the weights and biases in BOA-MLP.*

The first and most important element in training multilayer perceptron using meta-heuristic algorithms is the problem representation [19]. Meta-heuristic algorithms need a structure that shows the values of the weights and biases to solve the MLP training problem. In order to optimize the values of the weights and biases in the MLP, they must first be represented in the BOA-MLP algorithm. For this purpose, a representation vector consisting of weights and biases is used. This vector is shown in Equation (5) according to the MLP structure in Fig. 2.

$$Vector = \left(w_{i,j} \sqcup w_{j,k} \sqcup v_{0,j} \sqcup v_{0,k}\right) \quad (5)$$

where $w_{i,j}$ represents the values of weights between the input layer and the hidden layer, $w_{j,k}$ represents the values of weights between the hidden layer and the output layer. $v_{0,j}$ represents the values of biases between the input layer and hidden layer and $v_{0,k}$ represents the values of biases between the hidden layer and the output layer. The notation $\sqcup$ represents the concatenation of two sets.

At the beginning of the BOA-MLP algorithm, the population of butterflies is randomly generated. Each butterfly represents a different MLP, namely the representation vector in Equation (5). Then, the fragrance for each butterfly is calculated using the training dataset and the best butterfly in the population is found. Then the position (the values of the weights and biases in MLP) of each butterfly is updated using Equations (3) and (4). The power exponent is updated. This process continues until the termination criteria are met.

The purpose of training an MLP is to achieve the highest classification or prediction accuracy for both training and test samples. For this, Mean Square Error (MSE) is a common evaluation criterion [4]. MSE is also used as the objective function in the BOA-MLP algorithm. The formulation of MSE is given Equation (6).

$$MSE = \frac{1}{N}\sum_{i=1}^{N}\sum_{k=1}^{p} {e_k}^2 \quad (6)$$

where N and p are the number of samples in the dataset and the number of neurons in the output layer, respectively. e_k is the error of the kth neuron in the output layer.

3. Experimental results

To test the success of the BOA-MLP algorithm, five classification datasets with different levels of difficulty were selected: balloon, xor, iris, heart, and breast cancer. The datasets used were taken from the UCI resource pool which is used for machine learning and is available to everyone.

Table 1 shows the characteristics of the data sets. When we examine Table 1, it is seen that it is easy to solve the xor problem with 8 training and 8 test examples, 3 features and 2 classes. When we examine the balloon dataset, the difficulty is more than the difficulty of the xor dataset and less than the difficulty of the other datasets because the balloon dataset has 4 features, 20 training and 20 test samples and 2 classes. When we look at the iris dataset, it has 4 features, 150 training and 150 test samples and 3 classes. In the breast cancer data set, there are 2 classes and 9 characteristics. 599 samples are used in the training phase and 100 samples are used in the test phase. Finally, there are 22 features, 2 classes, 80 training and 187 test samples in the heart dataset.

This study does not focus on finding the optimal number of neurons in the hidden layer. In the literature, the number of neurons in the hidden layer is usually calculated by the formula $(2 \times n) + 1$ where n is the number of neurons in the input layer [4, 20]. Therefore in this study, the number of neurons in the hidden layer was calculated by the formula $(2 \times n) + 1$. Table 1 also shows the MLP structure and the dimension of a butterfly for each data set.

Table 1. *Properties of the classification datasets*

	Attribute number	Training	Test	Class number	MLP architecture	Vector size
Xor	3	8	8	2	3-7-1	36
Balloon	4	20	20	2	4-9-1	55
Iris	4	150	150	3	4-9-3	75
Breast Cancer	9	599	100	2	9-19-1	210
Heart	22	80	187	2	22-45-1	1081

The BOA-MLP algorithm was compared with the BAT-MLP algorithm based on the BAT algorithm [21], the SMS-MLP [11] algorithm and the Back Propagation (BP) algorithm. To fairly compare the algorithms, the experiments were run under the same situations for each algorithm. The initial values of the weights and biases were randomly selected between -10 and 10. The population size was 50 for the xor and balloon datasets, 200 for the other datasets. The maximum number of function evaluations was the same for each algorithm, 12500 for the xor and balloon datasets, 50000 for the other datasets. Each algorithm was run 30 times and the performances of the algorithms were evaluated by classification accuracy, sensitivity, specificity, precision, F1-score, the average (ave) and standard deviation (std) of the MSE results. The average (ave) and standard deviation (std) of the MSE results on training data are presented in Table 2 as ave±std. It is seen that the BOA-MLP algorithm gives better results than the other algorithms for all the datasets.

Table 3 presents the average classification accuracy on test data and average runtime of the algorithms. The BOA-MLP algorithm has better classification accuracy for all the datasets than the other algorithms. The BOA-MLP algorithm achieved 100% success on the xor and balloon datasets, 97.18% on the iris dataset, 99.37% on the breast cancer dataset and 74.46% on the heart dataset. Besides, the BOA-MLP algorithm is the slowest algorithm and the BP algorithm is the fastest algorithm. Table 4 presents the results of the sensitivity, specificity, precision and F1-score. According to Table 4, the performance of the BOA-MLP algorithm is very good for all the datasets.

Table 2. *The average and standard deviation of the MSE results on training data*

Dataset	BOA-MLP	BAT-MLP	SMS-MLP [11]	BP
Xor	**7.83E-03±9.62E-03**	1.27E-01±6.22E-02	1.33E-01±3.39E-02	1.41E-01±1.65E-01
Balloon	**2.79E-09±6.90E-09**	1.07E-02±2.83E-02	1.11E-02±1.31E-02	1.00E-01±1.51E-01
Iris	**4.74E-02±8.15E-03**	2.10E-01±1.38E-01	2.58E-01±5.12E-02	5.38E-02±1.30E-01
Breast Cancer	**1.78E-03±8.25E-05**	6.83E-03±7.92E-03	2.27E-02±4.33E-03	2.88E-02±1.21E-01
Heart	**1.15E-01±4.75E-03**	1.51E-01±3.21E-02	1.18E-01±3.13E-02	2.98E-01±1.32E-01

Table 3. *The average classification accuracy on test data and the average run time of the algorithms*

Dataset	Classification Accuracy (%)				Time (s)			
	BOA-MLP	BAT-MLP	SMS-MLP	BP	BOA-MLP	BAT-MLP	SMS-MLP	BP
Xor	**100.00**	85.00	83.75	84.17	9.2	4.7	5.5	**1.6**
Balloon	**100.00**	98.83	99.17	90.00	37.0	19.4	20.2	**1.7**
Iris	**97.18**	82.91	86.78	90.82	1408.6	775.2	881.6	**9.6**
Breast Cancer	**99.37**	96.13	85.67	93.03	5101.9	2607.3	2830.3	**29.5**
Heart	**74.46**	71.35	68.57	61.66	1479.0	937.0	892.4	**16.5**

Table 4. *The results of the sensitivity, specificity, precision and F_1-score*

Algorithm	Xor				Balloon			
	Sensitivity	Specificity	Precision	F_1-Score	Sensitivity	Specificity	Precision	F_1-Score
BOA-MLP	**100.00%**	**100.00%**	**100.00%**	**1.0000**	**100.00%**	**100.00%**	**100.00%**	**1.0000**
BAT-MLP	82.50%	87.50%	89.44%	0.8435	99.17%	98.61%	98.30%	0.9859
SMS-MLP	81.70%	86.70%	88.90%	0.8349	99.20%	99.20%	98.80%	0.9894
BP	84.17%	84.17%	85.94%	0.8221	75.00%	100.00%	86.67%	0.7838
	Iris				Breast Cancer			
	Sensitivity	Specificity	Precision	F_1-Score	Sensitivity	Specificity	Precision	F_1-Score
BOA-MLP	**97.38%**	**98.69%**	**97.42%**	**0.9738**	**99.05%**	**99.45%**	**98.02%**	**0.9850**
BAT-MLP	82.91%	91.46%	78.07%	0.7883	87.46%	98.44%	93.29%	0.8922
SMS-MLP	82.10%	91.10%	81.00%	0.8002	50.20%	95.10%	83.70%	0.5828
BP	90.82%	95.41%	88.43%	0.8899	85.87%	94.94%	81.16%	0.8255
	Heart							
	Sensitivity	Specificity	Precision	F_1-Score				
BOA-MLP	**74.71%**	71.56%	**96.79%**	**0.8422**				
BAT-MLP	71.32%	**71.78%**	96.73%	0.8180				
SMS-MLP	68.39%	70.67%	96.41%	0.7980				
BP	62.00%	57.78%	88.48%	0.6965				

Fig. 5 shows the boxplot charts of the BOA-MLP, BAT-MLP, SMS-MLP and BP algorithms on test data. It is a graphical representation of the distribution of results obtained by running the BOA-MLP, BAT-MLP, SMS-MLP and BP

algorithms on the xor, balloon, iris, breast cancer and heart datasets. Fig. 6 shows the convergence graphs of the algorithms. It is seen that the BOA-MLP algorithm has a better start in many datasets and converges faster than the other algorithms. According to Fig. 5 and Fig. 6, the BOA-MLP algorithm exhibits good performance.

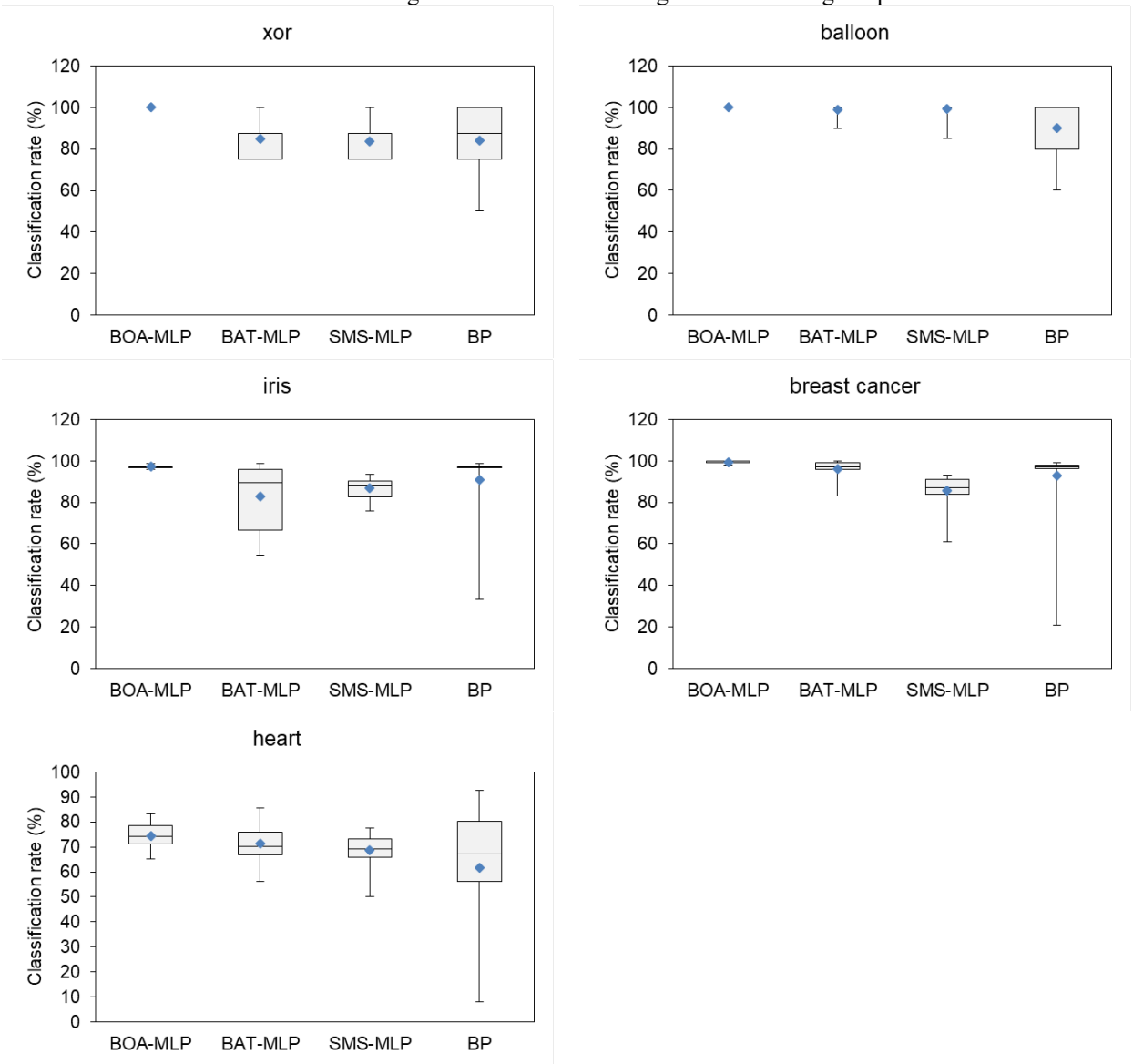

Figure 5. *The boxplot charts of the classification rate results on test data.*

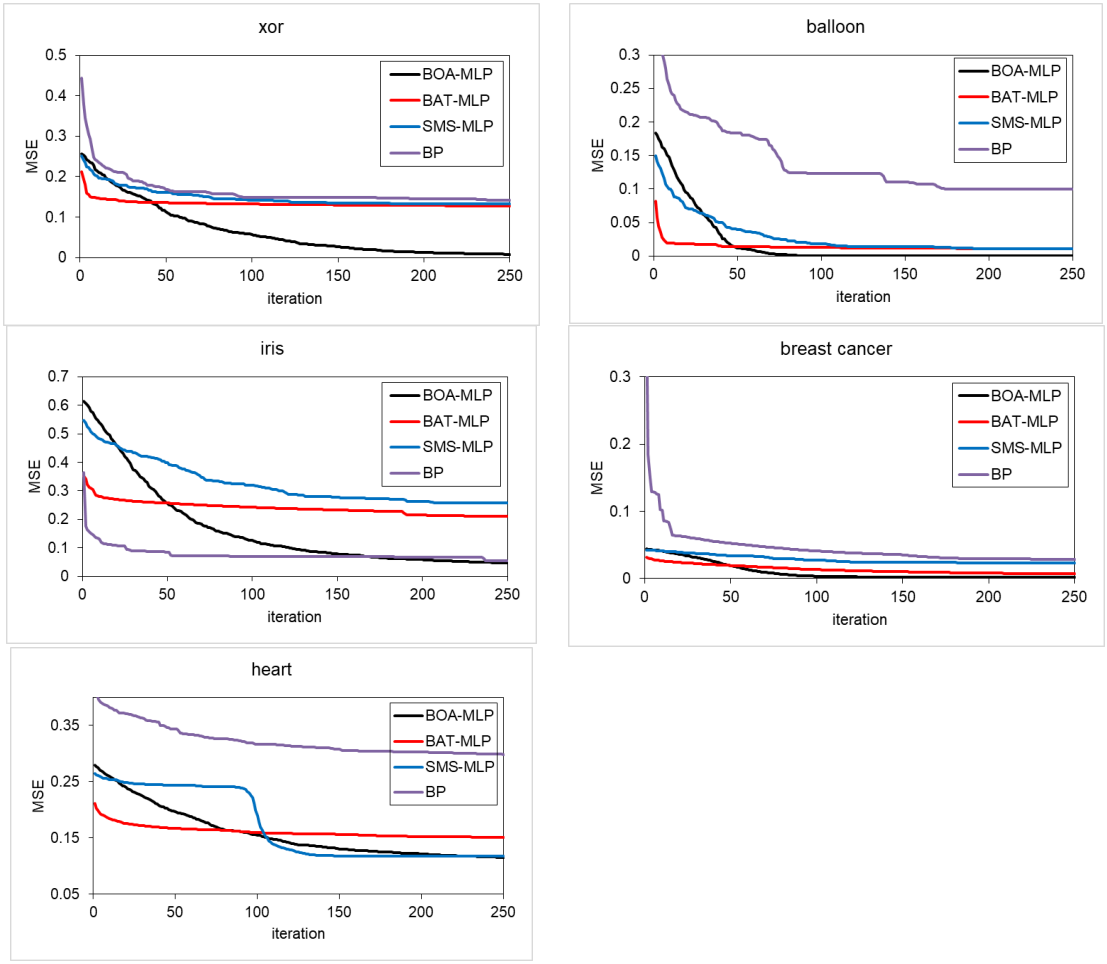

Figure 6. *The convergence graphs of the algorithms*.

4. CONCLUSION

Artificial neural networks (ANNs) are an information processing technique developed by modeling the operation of the nervous system of the human brain. In other words, it is the digital platform of the synaptic connections established by the neurons in the human brain. ANNs are formed by the merging and grouping of artificial nerve cells. This merging consists of layers and as a result, ANN comes together from more than one interconnected layer. ANN consists of three layers as input layer, hidden layer and output layer. However, in some cases, the number of hidden layers may be more than one. The multi-layer perceptron (MLP) is a feed-forward network structure with one or more hidden layers between the input layer and the output layer. MLP learns from inputs and outputs. The values of the weights and biases in MLP are updated according to inputs and outputs. Researchers have proposed algorithms to train MLP. However, classical techniques often face problems in solving this optimization problem. They tend to need large amounts of computing time, large amounts of memory. More importantly, they get stuck within the local optimum and produce poor-quality solutions. To overcome these difficulties, meta-heuristic algorithms have been used to train MLP. In this study, the Butterfly Optimization Algorithm (BOA) algorithm is used for the first time as the MLP trainer. Butterflies are the BOA algorithm's search agents for optimization. The greatest motivation in using the BOA algorithm is the superiority of its search strategy and the success of the escape ability from the local optima. The BOA algorithm is used to find the optimal values of weights and biases in MLP.

In the experiments, the proposed BOA-MLP algorithm was run on five classification data sets in the literature: iris, breast cancer, heart, xor and balloon. The datasets used were taken from the UCI resource pool used for machine learning available to everyone. The BOA-MLP algorithm was compared with the BAT-MLP algorithm, the SMS-MLP algorithm and the Back Propagation algorithm. To fairly compare the algorithms, the experiments were run under the same situations for each algorithm. Each algorithm was run 30 times and the performances of the algorithms were evaluated by classification accuracy, sensitivity, specificity, precision, F1-score, the average and standard deviation of the MSE results. The BOA-MLP algorithm has better classification

accuracy for all the datasets than the other algorithms. The BOA-MLP algorithm achieved 100% success on the xor and balloon datasets, 97.18% on the iris dataset, 99.37% on the breast cancer dataset and 74.46% on the heart dataset. According to the results of the sensitivity, specificity, precision and F1-score, the performance of the BOA-MLP algorithm is very good for all the data sets. Overall, the BOA-MLP algorithm gives better results than the other algorithms for all the datasets.

References

[1]. Jaddi N.S., Abdullah S., "Optimization of neural network using kidney-inspired algorithm with control of filtration rate and chaotic map for real-world rainfall forecasting." Engineering Applications of Artificial Intelligence, 67, (2018), 246-259.

[2]. Türkoğlu B., "Artificial algae algorithm on training artificial neural networks." 2019, Selcuk University Natural Science Institute.

[3]. Haupt R.L., Ellen Haupt S., Practical genetic algorithms. 2004.

[4]. Mirjalili S., "How effective is the Grey Wolf optimizer in training multi-layer perceptrons." Applied Intelligence, 43(1), (2015), 150-161.

[5]. Kulluk S., Ozbakir L., Baykasoglu A., "Training neural networks with harmony search algorithms for classification problems." Engineering Applications of Artificial Intelligence, 25(1), (2012), 11-19.

[6]. Ghaleini E.N., et al., "A combination of artificial bee colony and neural network for approximating the safety factor of retaining walls." Engineering with Computers, 35(2), (2019), 647-658.

[7]. Tang R., Fong S., Deb Ss, Vasilakos A.V., Millham R.C., "Dynamic group optimisation algorithm for training feed-forward neural networks." Neurocomputing, 314, (2018), 1-19.

[8]. Zhang L., Suganthan P.N., "A survey of randomized algorithms for training neural networks." Information Sciences, 364, (2016), 146-155.

[9]. Ojha V.K., Abraham A., Snášel V., "Metaheuristic design of feedforward neural networks: A review of two decades of research." Engineering Applications of Artificial Intelligence, 60, (2017), 97-116.

[10]. Hacibeyoglu M., Ibrahim M.H., "A novel multimean particle swarm optimization algorithm for nonlinear continuous optimization: application to feed-forward neural network training." Scientific Programming. 2018.

[11]. Gulcu Ş., "Training of the Artificial Neural Networks using States of Matter Search Algorithm." International Journal of Intelligent Systems and Applications in Engineering, 8(3), (2020), 131-136.

[12]. Arora S.,. Singh S, "Butterfly optimization algorithm: a novel approach for global optimization." Soft Computing, 23(3), (2019), 715-734.

[13]. Tümer A., Edebali S., Gülcü Ş., "Modeling of Removal of Chromium (VI) from Aqueous Solutions Using Artificial Neural Network." Iranian Journal of Chemistry and Chemical Engineering (IJCCE), 39(1), (2020), 163-175.

[14]. Madenci E., Gülcü Ş., "Optimization of flexure stiffness of FGM beams via artificial neural networks by mixed FEM." Structural Engineering and Mechanics, 75(5), (2020), 633-642.

[15]. Karaşahin A.T., Tümer A.E., "Real time traffic signal timing approach based on artificial neural network." MANAS Journal of Engineering, 8(1), (2020), 49-54.

[16]. Pandya A., Macy (1996) "Pattern Recognition with Neural Network in C++." CRC Press, Florida.

[17]. Keskenler M.F., Keskenler E.F., "From Past to Present Artificial Neural Networks and History" Takvim-i Vekayi, 5(2), (2017), 8-18.

[18]. Hamzaçebi C., "Yapay sinir ağları: tahmin amaçlı kullanımı MATLAB ve Neurosolutions uygulamalı." 2011: Ekin Basım Yayın Dağıtım.

[19]. Belew R.K., McInerney J., Schraudolph N.N., "Evolving Networks: Using the Genetic Algorithm." 1990.

[20]. Aljarah I., Faris H., Mirjalili S., "Optimizing connection weights in neural networks using the whale optimization algorithm." Soft Computing, 22(1), (2018), 1-15.

[21]. Yang X.-S., "A new metaheuristic bat-inspired algorithm," Nature inspired cooperative strategies for optimization (NICSO 2010)., Springer, (2010), 65-74.

MANAS Journal of Engineering
ISSN 1694-7398 | e-ISSN 1694-7398

Volume 9, Issue 2, (2021) Pages 169-183
https://doi.org/10.51354/mjen.954609

Sedimentological and mineralogical-petrographic characteristics of Miocene evaporitic deposits (SW Erzincan)

Pelin Güngör Yeşilova*, Şeyma Yavuz

Van Yüzüncü Yıl Üniversitesi, Mühendislik Fakültesi, Jeoloji Mühendisliği Bölümü, KAMPÜS, 65080, VAN
yesilovapelin@gmail.com, seymayavuz639@gmail.com, ORCID: 0000-0002-0748-6192

ABSTRACT

This study aimed to find the depositional environment and formation conditions of the gypsum-dominated Miocene succession alternated and intercalated with clastics and carbonates in the southwestern part of the Erzincan Basin. As a result of sedimentological, mineralogical-petrographic investigations, it was determined that the gypsum in this sequence was formed as primary and secondary. Primary lithofacies; nodular anhydrite, selenitic, discoidal, gypsum arenitic secondary lithofacies; It is divided into massive, laminated, banded, nodular, brecciated, satin-spar. The facies repetitions and folds, fractures, cracks and faulting in the sequence showed the effect of tectonism with the water level fluctuations in the basin. In addition, these investigations revealed sedimentary structures such as cross-bedding, ripple undulations, chicken-wire, enterolithic and bacterial-algal structures, parallel laminations in gypsum lithofacies. In addition to these, it was understood that gypsum lithofacies were exposed to diagenetic processes under the influence of a hot-humid and semi-arid climate, organic matter activity, meteoric/underground-water and hydrothermal solution factors, and were subjected to high temperature, pressure, salinity and pH conditions.

ARTICLE INFO

Research article

Received: 19.06.2021
Accepted: 16.10.2021

Keywords:
evaporite,
lagoon,
playa lake,
Miocene,
Erzincan

**Corresponding author*

1 Introduction

During the Paleocene-Eocene period, the branches of the Neotethys began to close to a great extent, the existence of this ocean in Eastern Anatolia ended with the continentalization process that lasted until the end of the Middle Miocene [1]. The increase of the Cretaceous seas or the Eocene transgression enabled these seas to accumulate in the Pontide and Anatolid belts. Following this, the Eastern Anatolian Region was affected by a north-south compressional regime with the collision of Arabian-Anatolian plates in the Middle-Late Miocene [2-4]. Therefore, this combination of events led to the formation of the basins formed in this region and to contain shallow marine-terrestrial sequences reaching kilometers thick [5-7]. Erzincan basin is one of these basins and was formed in the late closure phase of the northern branch of Neo-Tethys, which separated Pontides from Anatolides during the Late Cretaceous-Early Paleocene times [8]. The basin, which became largely land after this closure, was covered by shallow seas during the Early Miocene, but these seas could not be long-lived because the region gained a overthrusted structure and uplifted with north-south directional compression [8]. Intense evaporation periods occurred in the Late Eocene-Late Miocene time interval [7, 9-11]. Tertiary evaporite deposits were formed along the line where Eskişehir-Mihalıççık, Ankara-Beypazarı, Çankırı-Çorum, Sivas-Zara-Hafik, Erzincan, Refahiye-İliç, Erzurum, Tercan-Aşkale-Tekman, Iğdır-Tuzluca basins were located [12]. Volcanism products (volcanics/volcanoclastics) emerging from faults and cracks that developed due to compressional tectonism during the Middle-Late Miocene period are observed in an interbedded manner with evaporite deposits of mostly shallow-marine-terrestrial characteristics [13-16]. The study area, which is an intra-continental basin developed under the control of right lateral strike-slip fault zones and contains volcanoclastic units, is located in the southwest of the Erzincan basin and the North Anatolian Fault Zone, and in the northwest of İliç district and on the northeast edge of the Tauride-Anatoloid tectonic units [17] (Fig. 1). The gypsiferous units in the study area are distributed among Turgutlu, Küçükarmutlu, Doruksaray and Dostal Villages in the northwest of İliç district. The study area and its immediate surroundings have been studied stratigraphically, tectonically, sedimentologically, petrologically and hydrologically by some researchers [10, 18-28]. However, detailed

sedimentological, petrographic-mineralogical studies of gypsum-bearing units in the study area have not been conducted. Therefore, the purpose of this article is to contribute to regional geology by understanding the lithofacies distinctions, paleoenvironment, climate and storage conditions to be obtained by these studies.

The basis of the study area is the Upper Triassic-Upper Cretaceous allochthone Munzur limestone, which consists of shelf type neritic limestones [19]. Later this unit is followed by ophiolites consisting of Late Cretaceous serpentinite, peridotite, gabbro and dunite. It was emplaced on the Munzur limestones with a tectonic contact. Bayhan (1982) named these ophiolites Güneş ophiolite, while Özgül et al (1981) named these ophiolites as Uluyamaç ophiolite. This ophiolitic unit thrusts over the flysch unit in the Middle Eocene deep sea-shelf character in the field (Fig. 1). This unit is composed of ophiolite and recrystallized limestone blocks and the alternation of limestone and clastic units (sandstone, conglomerate, siltstone) containing partly tuff and breccia levels (Fig. 1). This unit has been named as Dedek, Kozluca and Bozbel formation by some researchers [10, 19, 30-32]. Above this flysch unit is the sequence intercalated and alternated with Miocene gypsum-weighted carbonates and clastics, which are the subject of our study, with an angular unconformity (Fig. 1). These evaporites are mostly primary and secondary gypsum and contain anhydrite in places. The clastics found together with the evaporites are predominantly sandstone, mudstone and claystone, while carbonates are limestone and dolomite [10, 33-35]. These units are laterally and vertically transitive with each other. Kurtman (1973) distinguished the lower parts of this sequence as Karacaören Formation and the upper parts as Hafik Formation. According to the fossils in the clastics belonging to these two formations, the age of the evaporitic sequence extends from Lower Miocene to Upper Miocene [32]. However, since there is no unconformity between the two formations and they have lateral and vertical transitions, this article has been investigated as a whole under the name of Miocene evaporites. This gypsiferous unit is bedded, faulted, fractured and occasionally folded. These folds originated from the Alpine orogeny that occurred at the end of the Miocene [10]. All these units are respectively covered by Pleistocene terrestrial clastics (conglomerate, sandstone, claystone and siltstone) and Quaternary alluviums [19] (Fig. 1). This Miocene sequence is sometimes observed as overthrusted by the Upper Cretaceous ophiolitic melange in the study area [19, 35-36].

2. Methodology

This study consists of research, field and laboratory studies. During the field study, measured stratigraphic sections were prepared for the areas where Miocene evaporites were observed well, and systematic sampling was performed for mineralogical-petrographic analysis. Accordingly, 30 of the samples collected from the field were prepared for thin section and made in Dokuz Eylül University Thin Section Laboratory. Since the water of crystallization disappears when samples containing gypsum is heated and bassanite is formed, the grinding of the samples was done using machine oil instead of water. Then, the epoxy used in thin section production was hardened at room temperature and this harden process was continued by heating in the drying oven. After the adhesion process was completed, thinning was made with abrasives varying between 400 and 800 microns and the photos of the sections presenting features were taken with a Leica model microscope. In addition, the Scanning Electron Microscope (SEM-EDS) analysis on 10 gypsum samples was carried out at the Scientific Research and Application Center of Van Yüzüncü Yıl University. The gypsum samples were coated with Au-Pd and examined by scanning the sample surface with an electron beam in the ZEISS Sigma 300 model SEM microscope and photographed with the SE2 detector.

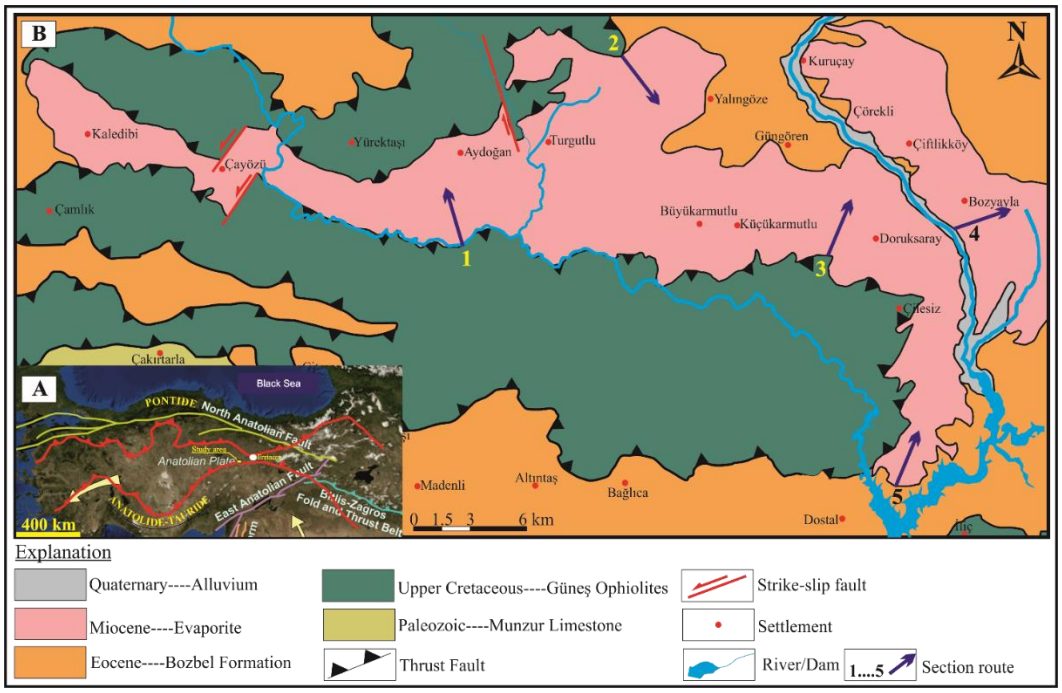

Figure 1. *(A) Location of the study area. (B) Geological map of the study area (1/25000).*

3. Results and discussion

3.1. Sedimentology

Existing sedimentological studies have been carried out on Miocene evaporitic units around Doruksaray and Dostal villages. These evaporitic units are mainly consist of primary (selenitic, gypsum arenite and discoidal gypsum rosette) and secondary gypsum lithofacies (such as masive, masive-bedded, massive laminated, nodular, nodular-banded, laminated and laminated-banded and satin-spar) with nodular anhydrite. In the study area, 5 measured stratigraphic sections were taken from the localities where evaporitic lithofacies are best observed, and as a result of their correlation, a general evaporitic sequence with a thickness of approximately 300 m was obtained (Fig. 2). Primary and secondary gypsums in this sequence are alternated with each other at some levels, and at some levels are intercalated, inerbanded and alternated with volcanoclastic (tuff and volcanic gravel), basalts, red, green and gray clastics (gravel, sand, clay and mudstone) and carbonated units (limestone and dolomite) (Fig. 2). Secondary gypsum derives mainly from hydration of primary anhydrite rocks or from dehydration-rehydration processes of primary gypsum. These secondary gypsum generally show alabastrine and porphyroblastic textures in the field. Alabastrine texture is milky white, homogeneous and fine-grained, while porphyroblastic-textured gypsum is more medium-coarse-grained and the grains are observed to float in alabastrine gypsum texture. These textures are easily distinguished with the naked eye in the field and sometimes appear together. Some sedimentary structures (such as enterolithic, undulated, folded, bedded, brecciated, cross-bedded, parallel laminated) are observed in all these gypsum-bearing sequence with the effect of regional tectonics, climate and strong diagenesis. In addition, there are faults, deformations and inter-banded of ferrous-mangane alterations in some areas.

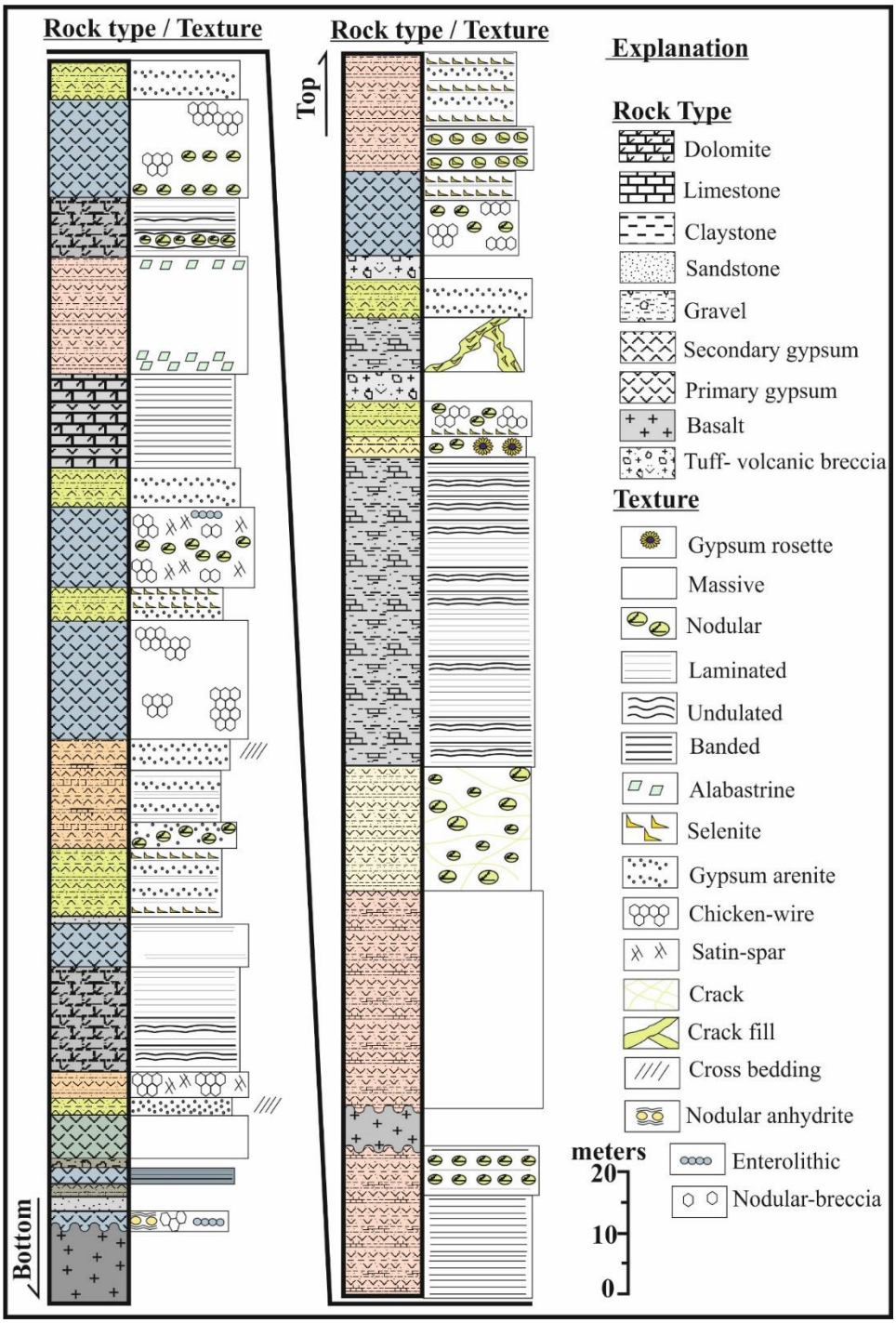

Figure 2. *Generalized measured stratigraphic section of the Miocene evaporites*.

The anhydrite nodules observed in the field were formed by the combination and growth of primary anhydrite lats in the unconsolidated red-brownish carbonated mud in the syn-sedimentary stage [37]. Carbonated mudstone is accumulated in subaqueous conditions during dilution of brine in an evaporite environment. These are then partially or completely transformed into secondary alabastrine and porphyroblastic gypsum at the end of early and/or late diagenetic processes. Nodular anhydrite is mostly formed in sabkha environment dominated by terrestrial conditions [38]. These anhydrites are separated from each other by a light brownish and carbonated mud matrix in the study area. They consist of a mosaic of white nodules and their diameters vary between 0.1-10 cm (Fig. 3A). These nodules exhibit some levels of chicken-wire internal structure. The splicing of nodular anhydrites with each other in the sabkha environment are formed the chicken-

wire cage structure [39] (Fig. 3B, C). Due to the continuous sedimentation, tectonic deformation, volume changes in rocks and excessive pressure, the nodules acquire a ductile fluid property and acquire a folded enterolithic-like structure in the study area [40].

The free-growed-twinninned selenitic gypsum are observed in different crystal types, colors and sizes in the study area. Crystal shapes and sizes of selenitic gypsum give information about the temperature, acidity and organic matter content of the environment. In addition, environmental salinity change rates and refreshing periods can also cause different types of selenite crystallization [41]. These gypsum are fine to medium coarse crystalline (1 micron-40 cm) and transparent, and cleavage and twinning levels can be distinguished by the naked eye (Fig. 3D, E). Selenitic gypsum precipitates directly from brine and grows freely upward from the sediment-brine interface (Fig. 3E). They are sometimes observed in the study area in the form of freely grown in gray colored or red carbonate-clayey mudstones or with clay-carbonate interband and sometimes as a crack fill in mudstone (Fig. 3E, F). Selenitic gypsum crystalline mudstones reflect dry-shallow lake environment conditions [42-43]. Fine to medium grained selenitic gypsum are sometimes cemented together with carbonate and gypsum matrix (Fig. 3G, H). The presence of longitudinally developed and clustered prismatic selenites (Fig. 3I) in the study area indicates that acidic conditions prevail in the sedimentation environment, while the presence of lenticular, dark brown-black colored selenite crystals (Fig. 3G, I, J) can be attributed to the organic matter [44]. The rosette-shaped crystal cluster of selenites (Fig. 3K) is formed by the combination of very high organic matter content and temperature factor in the environment [45]. Ground-water is effective for this type of gypsum, which reflects the lake-shore swamp environment [46-47]. Selenitic gypsum is sometimes bedded, laminated, folded and undulated, while those with medium grains are alternated with gypsum arenites (Fig. 3L). In addition, microfaults, anhydritization and carbonation bands are occasionally encountered among these (Fig. 3M). The gypsum arenite lithofacies, which is the size of clastic sand, which is formed by the separation of selenitic gypsum lithofacies by the effect of waves and re-working and deposition, is another a lithofacies in the study area (Fig. 3B). Among these, cross-bedding, ripple corrugations, laminations, and clastic and carbonate intercalations are common (Fig. 3L, M, N). This type of gypsum is mostly settled in the shallow water-shore side of the salt water body [48-49]. The primary discoidal gypsum rosettes observed in the sequence were developed by displacement in organic matter rich claystone and red colored mudstone [37-38, 50-51] (Fig. 3K). Later, these primary gypsum are diagenetically transformed into anhydrite and secondary gypsum, respectively (Fig. 3J). The observation of gypsum arenites together with the nodules in the sequence proves that some of these secondary gypsum originate from the primary gypsum origin (Fig. 3B). Separate concentric salt solutions are formed as a result of the addition of evaporitic ground-water into the cracks and a mud-flat rich in organic matter (humic acid) that rises to the surface during the drying phase of the environment. High concentrations of sulfate and calcium in ground-water lead to the replacement of these salt solutions in-situ and then crystallization of these solutions into a as discoidal gypsum rosettes [51, 54-55]. Humic acid is a type of acid produced by bacteria under reducing environment conditions. The fact that the crystal sizes in discoidal gypsum are approximately equal to each other (approximately 0.2-0.5 cm) shows that the salinity and temperature conditions at these levels of the sequence are not very variable (Fig. 3K). There are areas rich in red colored Fe-oxide in these parts. Selenitic gypsum in most levels of the sequence are alternated and intercalated with secondary gypsum (Fig. 3O). This alternation; It is important in terms of showing that gypsarenites transform into anhydrite with the effect of the salinity of the evaporating brine and then re-form secondary gypsum through rehydration.

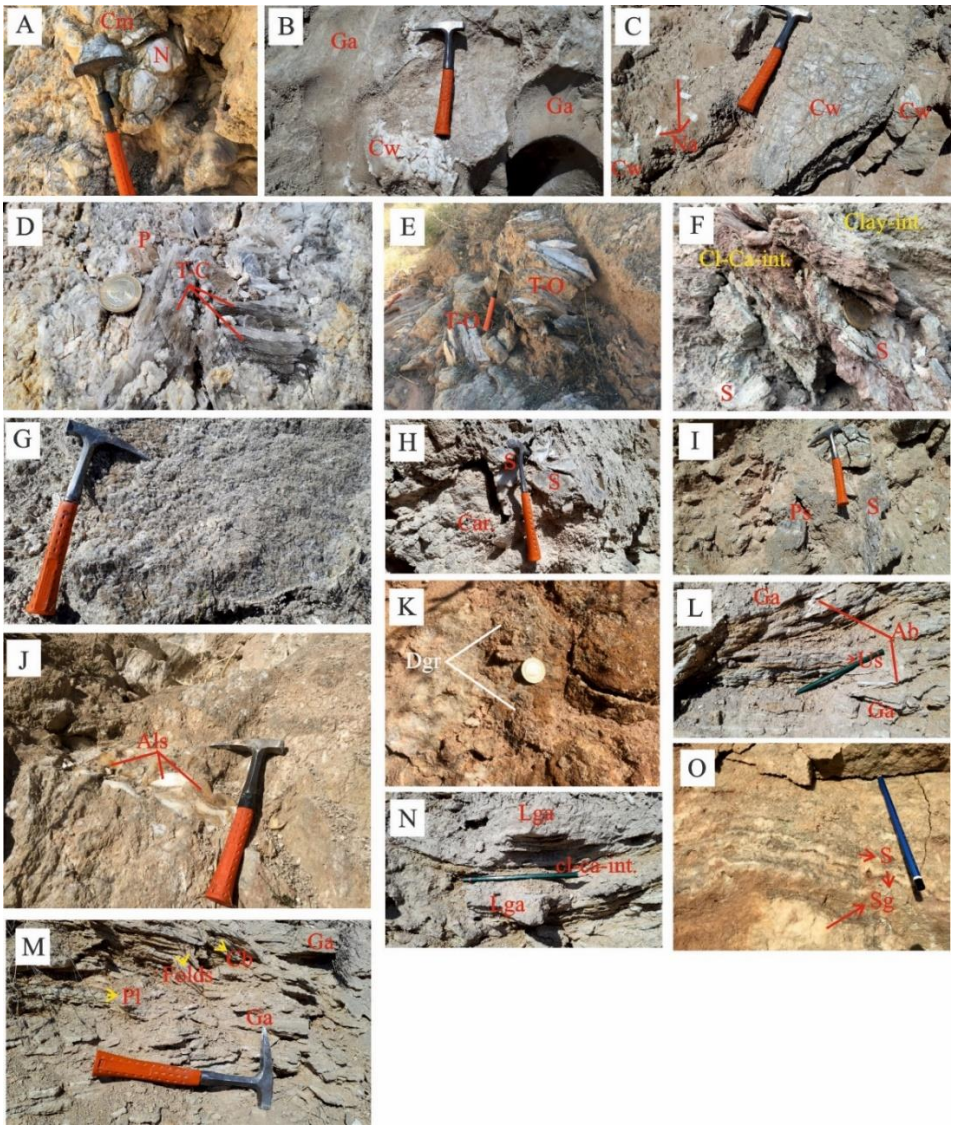

Figure 3. *Sedimentologic aspects of gypsum lithofacies. (A) Anhydrite nodules (N) within the carbonated mudstone (Cm). (B) Nodules showing chicken-wire interior structure in gypsum arenites (Ga). (C) Anhydrite nodules (Na) and chicken-wire structures (Cw) in selenites. (D) Twinned-cleavage (T-C) selenites and prismatic (P) selenites rich in organic matter. (E) Carbonated, coarse crystallized, organic matter containing (O) dark colored and twinned (T) selenites. (F) Selenite (S) with clay carbonate intercalations (Cl-Ca-int). (G) Fine to medium grained selenitic gypsum cemented together with a gypsum matrix. (H) Medium grained, prismatic selenitic gypsum (S) cemented together with a carbonate (Car) matrix. (I) Longitudinally developed and clustered (S) prismatic selenites (Ps). (J) Anhydritized (A), brownish and lenticular (l) selenite (s) level. (K) Discoidal gypsum rosettes (Dgr) within the red mudstone. (L) Undulated selenites (Us) alternated with gypsum arenites (Ga) and alabastrine gypsum (Ab). (M) Cross-bedded (Cb) and folded gypsum arenites (Ga). (N) Laminated gypsum arenite (Lga) with clay-carbonate intercalations (cl-ca-int.). (O) Undulated selenite (S) gypsum alternated with secondary gypsum (Sg) levels and nodules.*

Massive gypsum shows a rhythmic alternation with red mudstones and are sometimes observed as laminated and banded and sometimes bedded (Fig.4A, B).. The presence of lamina and bands in massive gypsum is important in terms of showing shallow water environments [37, 56]. Massive gypsum varied in thicknesses between 3-25 m in the sequence and transformed into white colored homogeneous alabastrine or porphyroblastic texture secondary gypsum in the late diagenetic phase (Fig. 4C). Mudstones are characterized by massive textured red claystone and siltstone (Fig. 4D). The alternation of these gypsum with red mudstones is probably evidence that the climate changes periodically to arid and semi-arid [9, 57]. This alternation shows that terrestrial sedimentation has developed and evaporation is interrupted from time to time due to the gradual decline of the sea [58]. However, in some outcrops these gypsiferous red mudstones transition to gray-green claystones. This transition is an indication that the playa lake can reach the sea [9, 59].

However, the fact that the massive gypsum is interlayered with grayish-green sandstones with a thickness of approximately 1 m at some levels in the sequence and cream-beige colored marl and limestone indicates that the depositional conditions are sometimes subaquaeous and deeper conditions [9, 60] (Fig. 4E). Massive layers show a chicken-wire texture with undulated and tepee structure type folds at most levels of the sequence (Fig. 4F). These structures are formed as a result of the effects of climate and diagenesis and show that these gypsum sometimes came out subaerial of water [39, 47, 55, 61]. In addition, the presence of chicken-wire texture in this gypsum and the alternation of these gypsum with red clastics indicates the transition from sea conditions (by fresh water inputs) to very shallow and highly salty environments separated by a barrier [9, 59]. Laminated, laminated-banded gypsiferous lithofacies contain clay-carbonate inter-bands and intercalations and some levels alternate with carbonates in the field (Fig. 4G, H). These structures are indicative of a shallow water environment such as a lagoon [62-63]. Laminas contain nodules of white gypsum that range in size from 5 to 20 cm (Fig. 4I). The reason of this; It is the decrease of the water level in a shallow water environment such as a lagoon, followed by the introduction of sulfate-rich groundwater and a partial dissolution in laminated gypsum and the salinity of the brine water increases as a result of evaporation. Hence, nodular gypsum precipitates instead of laminated gypsum [64]. Lamina thickness is 1 cm or less, and band thickness varies between 1 cm and 10 cm. There are undulations, parallel laminations, fructures and folds in these structures and these structures (Fig. 4I) reflect high energy shallow water conditions [65]. The nodular, nodular-banded, nodular-laminated and nodular-breccia gypsum lithofacies are usually found in sandy carbonate and mudstone. White nodules with a diameter of approximately 0.5 to 5 cm come together and exhibit a nodular banded or laminated appearance (Fig. 4J, K). These lithofacies are sometimes in the form of irregular nodules in the field, partially or completely separated from each other by mudstone and / or carbonate matrix. These are often observed within the massive and laminated gypsum layers, sometimes between gypsum arenite and selenite layers, and may show chicken-wire and enterolithic internal structures (Fig. 3O, 4L). The observation of these structures indicates that the temperature, pressure and salinity conditions are increasing. Nodular gypsum, which displacives within the carbonates, are both derived from the hydration of nodular anhydrites, and also derived from the anhydritization of selenitic gypsum in the early-late diagenetic phase and rehydration in the late diagenetic phase (Fig. 4L). These gypsum exhibit secondary alabastrine and porphyroblastic textures. Breccia-nodular gypsum lithofacies, on the other hand, is an eroded gypsum formed as a result of intense tectonism simultaneously with sedimentation, which became active in the last stage of evaporite deposition in the studied basin (Fig. 4M). All these nodular lithofacies denote sabkha or mud-flat environments [38, 50, 66]. Since tectonic activities affected the basin, brecciation occurred throughout the deposition. As a result of dissolution in carbonates and nodular and laminated gypsum, veins and fractures varying between 0.5 and 2 cm in thickness and mudstone cracks were filled with satin-spar gypsum. Satin-spar gypsum crystals are oriented and their long axes are perpendicular or semi-parallel to the vein walls and their widths vary between a few mm and cm (Fig. 4N). These gypsum are formed in mud flat-sabkha environments [38, 67].

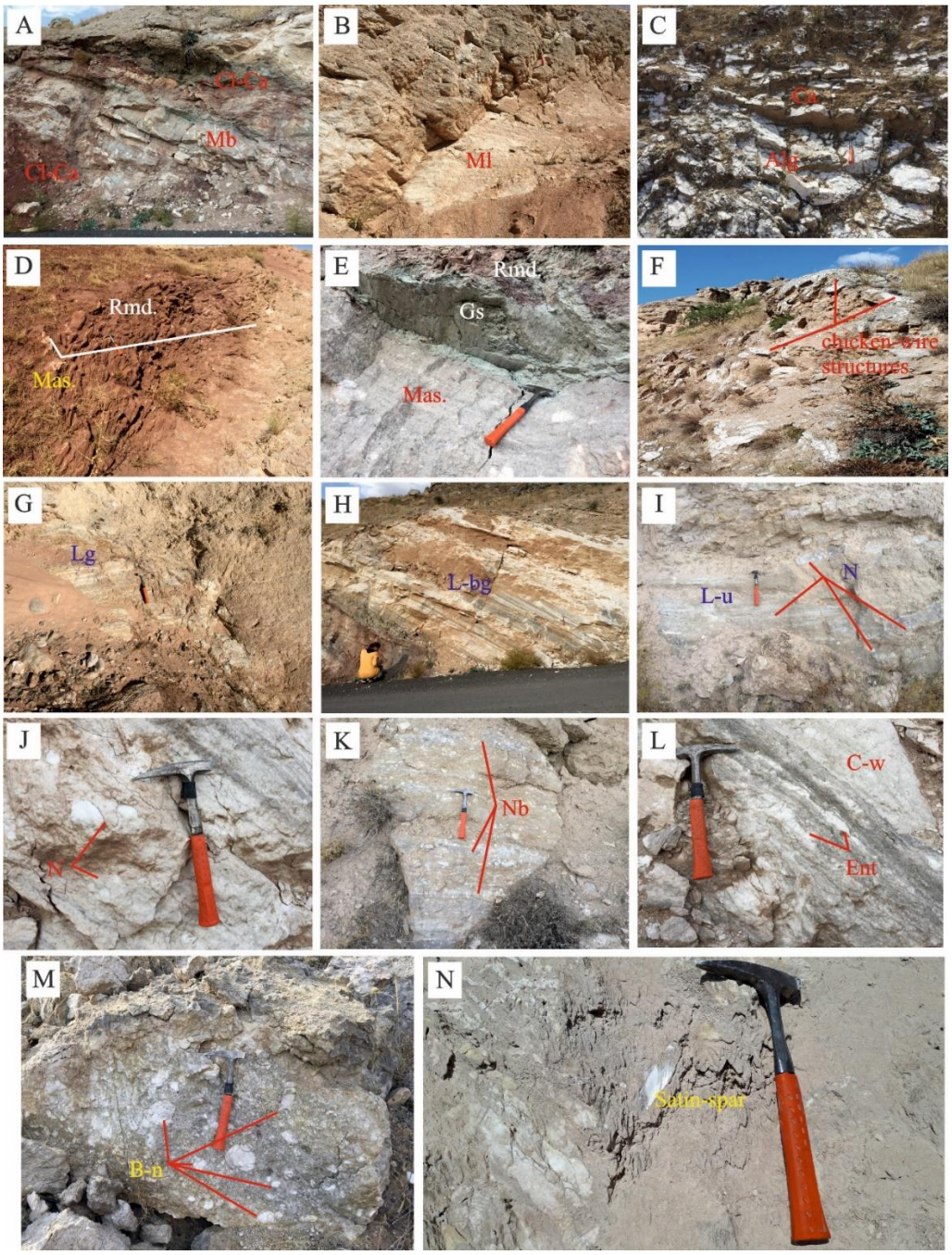

Figure 4. *Sedimentological aspects of secondary gypsum lithofacies. (A) Massive-bedded (Mb) gypsums alternated with clayey (Cl) and carbonated (Ca) units.(B) Massive-laminated gypsums (Ml). (C) Massive alabastrin secondary gypsum (Alg) alternated with carbonates (Ca). (D) Massive gypsums (Mas) within the red mudstones (Rmd). (E) The alternation of red mudstones (Rmd) and green sadstone (Gs) between massive (mas) gypsum levels. (F) Chicken-wire structures in the massive gypsums. (G) Laminated gypsums (Lg). (H) Laminated-banded gypsums (L-bg). (I) Nodular (N) structures within the laminated-undulated (L-u) gypsums. (J) Nodular (N) alabastrine secondary gypsum. (K) Nodular-banded (Nb) gypsums. (L) Chicken-wire (C-w) and enterolithic structures (Ent) in the nodular gypsum levels. (M) Brecciated-nodular (B-n) gypsums within the clayey carbonates. (N) Satin-spar gypsums within the grey mudstone cracks.*

a. Petrography

It is determined most secondary gypsum textures were alabastrine, porphyloblastic, sutured-bounded porphyroblastic, mosaic, microcrystalline, nodular, mosaic, nodular banded, brecciated and satin-spar textures with primary selenitic and arenitic gypsums in petrographic studies. Secondary gypsum textures are formed either directly from anhydrite or by dehydration (losing the water in its body)

of primary gypsum and then rehydration. Hydration channels are clearly observed in porphyroblastic gypsum. The greatest evidence of these events is the presence of anhydrite relicts in the form of euhedral, very coarse crystalline and sometimes euhedral prismatic crystals in porphyroblastic gypsum (especially in nodular gypsum) (Fig. 5A). The anhydrite relicts show 3rd order vibrant interference colors, their sizes are between 0.1 mm and 0.4 mm, the optical relief is medium (Fig. 5A). In addition, the presence of pseudomorphic secondary gypsum that preserves the crystal structure of tabular primary gypsum proves that some of these secondary are derived from primary gypsum (Fig. 5B). These two textures, which show the effect of dissolution and recrystallization processes in some sections, are observed in each other. Generally, alabastrine texture is formed by recrystallization of porphyroblastic textured gypsum. Porphyroblastic gypsum is medium-coarse grained (1-2 mm), with marked grain boundaries, showing first order interference colors, and cleavage marks have not disappeared yet, although they are in the advanced stage of diagenesis (Fig. 5C). Alabastrine texture is dominated by a lacy texture with lost grain boundaries and interlocking and inter-twined optical properties (Fig. 5D). If this texture consists of very fine grained gypsum crystals (approximately 1µm), it is called microcrystalline massive texture (Fig. 5E). This texture is formed by dissolution and recrystallization of gypsum crystals by the brine coming in the flooding period [68]. Chicken-wire texture is observed in thin section studies of these massive gypsum samples (Fig. 5F). Alabastrine texture development occurs under conditions where contact with water is excessive, and is observed in thin sections as replacing porphyroblastic gypsum [68] (Fig. 5C). Simple twinning is observed in both gypsum textures. Late diagenetic euhedral, semi-euhedral and anhedral calcite minerals in all secondary textures are observed in thin sections, replacing secondary gypsum with the effect of carbonate-rich surface waters (Fig. 5G). At the same time, black colored organic matter relicts and carbonation areas replacing with grains around the grains are observed in some of these types of porphyroblastic gypsum (Fig. 5H). The observation of sutured-bounded porphyroblastic secondary gypsum (Fig. 5A) in some thin sections indicates that they were formed before alabastrine gypsum [69]. Along with these, nodular gypsum framed with micritic mud and interlocking chicken-wire texture are frequently observed. The nodular-brecciated banded structures formed by the combination of brecciated or nodular gypsum are clearly observed (Fig. 5I). In addition, satin-spar gypsum perpendicular to the vein wall filling the cracks of secondary alabastrine porphyroblastic textured gypsum or micritic textured limestones are also encountered (Fig. 5J). These cracks were formed due to the increase in volume during conversion from gypsum to anhydrite or from anhydrite to gypsum.

In optical microscopic examinations, selenitic gypsums are fine-medium-grained, euhedral-subhedral prismatic, tabular forms, first order colors, unidirectional cleavage and twinning (Fig. 5K). These gypsum transformed into alabastrine and porphyroblastic textured gypsum in the advanced stages of diagenesis. The arenitic gypsum texture is composed of sand-sized gypsum formed by selenite recrystallization [70] (Fig. 5L). The spaces between the grains are filled with carbonate, clay cement and detritic material.

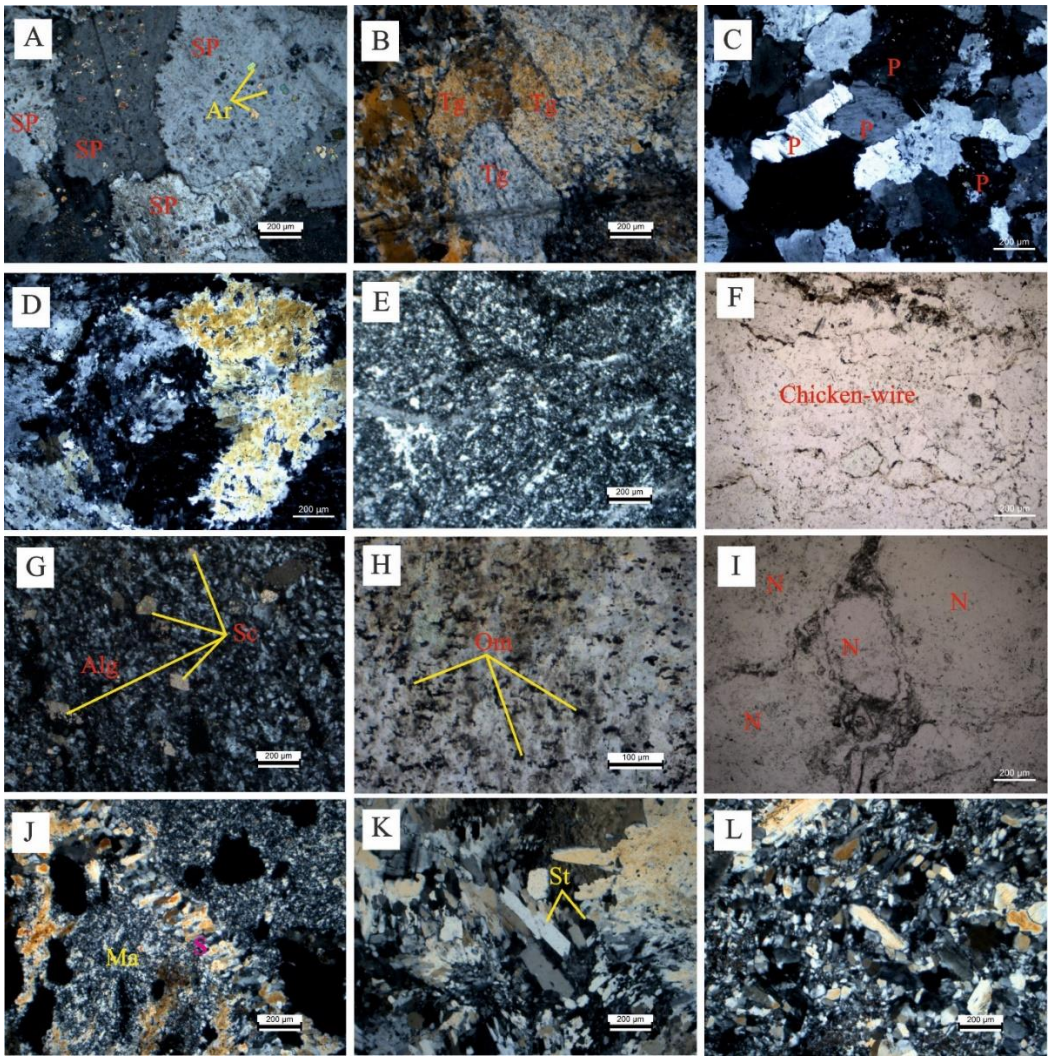

Figure 5. *Petrographic aspects of gypsum lithofacies. (A) Sutured-bounded porphyroblastic (SP) gypsum with anhydrite relicts (Ar) in them. (B) Pseudomorphic secondary gypsum formed as a result of dehydration-rehydration processes of tabular gypsum (Tg). (C) Porphyroblastic (P) gypsum with clear grain boundaries preserving cleavage marks. (D) Alabastrine textured secondary gypsums. (E) Microcrystalline tectured alabastrine gypsums. (F) Chicken-wire structures. (G) Euhedral and semi-euhedral secondary calcite (Sc) crystals replaced by alabastrine secondary gypsum (Alg). (H) Organic material (Om) relicts within the secondary gypsums. (I) Nodular (N)-brecciated structues. (J) Satin-spar (S) gypsums within the microalabastrine (Ma) secondary gypsum texture. (K) Simple twinned (St) selenites. (L) Arenitic gypsum texture.*

b. Mineralogy (Sem)

In order to determine properties such as micro-textural, crystal morphologies and relationships with other minerals in gypsum samples belonging to the study area, image examinations performed with Scanning Electron Microscopy (SEM) and quantitative analysis were performed by EDS studies. As a result of SEM studies, gypsum ($CaSO_4.2H_2O$), orthorhombic celestine ($SrSO_4$) and dolomite (Ca-Mg carbonate), calcite ($CaCO_3$) and some iron-rich minerals, clay and siliciclastic minerals (such as quartz, feldspar) were observed.

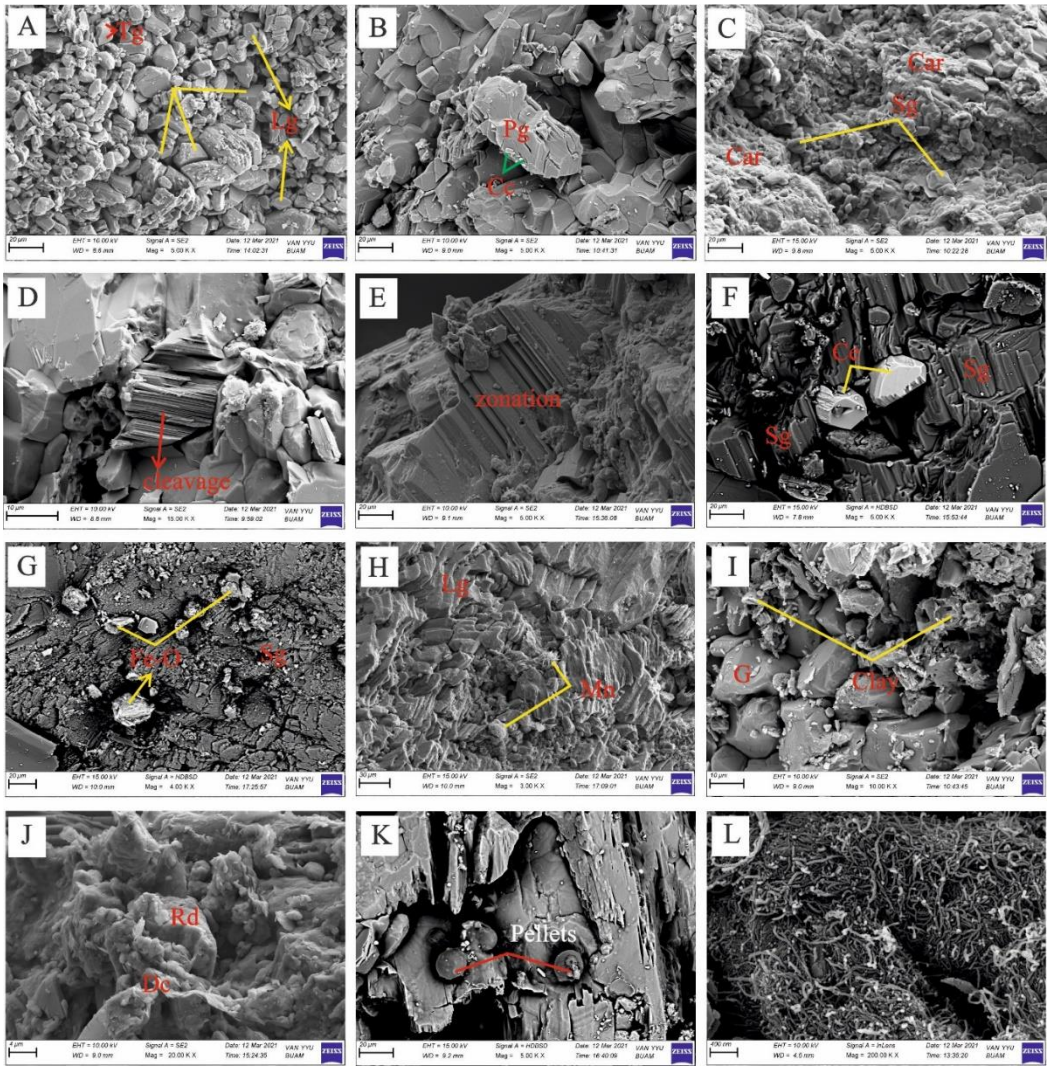

Figure 6. *SEM images of gypsum lithofacies. (A) Tabular (Tg) and lensoidal (Lg) primary gypsums. (B) Folds and ruptures in prismatic gypsum (Pg) with calcite cement (Cc). (C) Late diagenetic carbonation (Car) in secondary gypsum (Sg). (D) Cleavage in prismatic gypsum. (E) Zonation of gypsum. (F) Celestine minerals replaced with secondary gypsums. (G) Minerals rich in Fe-oxide in secondary gypsums (Sg). (H) Mangane (Mn) formations in laminated gypsum (Lg). (I) Plate-like clay formations with gypsum (G). (J) Detritic clay minerals secondary replaced with rhombohedral dolomit minerals. (K) Pellets in the gypsums. (L) Bacterial-algal structures.*

During the early diagenesis, dolomite mineral was observed, which replaced calcite. The Mg-rich liquids caused the formation of dolomite instead of calcite with surface alteration. Gypsum are generally prismatic, tabular and lenticular and contain fractures and folds due to deformations (Fig. 6A, B). The presence of these smooth surfaces in gypsum can be attributed to the high temperature, salinity and pH conditions [42]. In the late diagenetic phase, carbonation with the effect of carbonate-rich surface waters and also detrital clay minerals carried into the gypsum are common in gypsum (Fig. 6C). Cleavage marks are evident and there are calcite cements along the cleavage surfaces (Fig. 6D). Selenitic crystals follow each other in the form of transparent and zoned growth structures and are in the form of dark-light colored zones (Fig. 6E). There are carbonate inclusions along the growth surfaces. Inside the prismatic gypsum, the mineral of the celestine replacing the white gypsum was found (Fig. 6F). Diagenetic solutions rich in strontium (waters released during gypsum anhydrite transformation) or hydrothermal related waters mix with groundwater, allowing the reaction of Sr and Ca in the late diagenetic stage. Thus, the mineral of celestin rich in $SrSO_4$ is formed instead of gypsum [71-72]. At the same time, high amounts of iron-rich hematite or magnetite type Fe oxide minerals, very high amounts of manganese and Fe-rich Ca, Mg, Al silicate minerals (smectite, saponite type) were detected in these gypsum (Fig. 6G, H, I). These minerals are observed in a fine-grained plate-like form and have a grain size of ≤10μm (Fig. 6I). The presence of these clay minerals is important in terms of showing that the climate is humid-hot and dry and shallow water conditions [37, 73-74].

Apart from these, some metallic elements (Co, Cu, Ni, Zn, Zr) were detected in the EDS study. All these elements, including Mn and Fe elements, were probably transported into gypsum by hydrothermal solutions passing through the fractures and faults in the basin and created hydrothermal alteration zones observed in the study area [75]. High observation of Rb element in some samples in EDS study indicates that dolomite content increased in these gypsum samples [76] (Fig. 6J). These dolomites were replaced by detritic clay minerals in the late diagenetic phase (Fig. 6J). In some gypsum samples, pellets with a grain size of 10μm in general, equal size and with a smooth surface and spherical morphology were detected (Fig. 6K). Pellets are formed in environments with high organic material and bacteria content [77]. These are carbonate grains formed in subtropical environments [78]. In addition to these, bacterial-algal structures have been found (Fig. 6L). These structures generally show shallow water conditions and the region close to the coastline [79-80]. Laminated gypsum was found on SEM images, and lamination thicknesses vary between 1 and 2 μm. It has been observed that the lamination surfaces are quite smooth, but sometimes there are indentations and protrusions (Fig. 6H).

4. Conclusions

Lithofacies and sedimentary structures distinguished in the study area were decisive in terms of the deposition environment and formation conditions. Accordingly, while primary lithofacies such as gypsarenite and selenite were deposited at the margins of the basin (such as coastline-sabkha), discoidal gypsum rosettes and satin-spar gypsum were deposited in intra-continental areas such as mud flats-sabkha or playa, where reggressed of saline waters related to ground-fresh water intake. In addition, cross-bedding, ripple undulations, green clay interlayers (smectite, saponite) and red clast alternates within these showed a playa lake environment formed by temporary streams developed under arid-semi-arid and hot-humid climatic conditions. The laminated and banded lithofacies and parallel laminations, folds and bacterial-algal structures observed within the units mostly marked shallow sea-lagoon environments, while all of the chicken-wire, enterolithic and nodular lithofacies were deposited on the sabkha and salty mud flats. Massive gypsum deposited relatively deeper parts of the basin due to the uplift of the basin. Therefore, due to climatic-seasonal changes and tectonic effects, it is observed that the basin where gypsum-dominated lithofacies deposited deepened over time, then became shallow and gradually dried up completely. It is understood that facies change depending on these different conditions. According to all these facies changes, sedimentary structures, and the alternation and transition of these lithofacies with red and green clastic units and carbonate units, the basin is of a size reaching up to the lagoon-coastal sabka-playa lake which separated by a barrier from the shallow sea [37, 81]. In addition, it was determined that they were subjected to some diagenetic processes (volumetric shrinkage, recrystallization, dissolution and replacement, etc.) under the varying temperature, pressure, salinity and pH conditions, and as a result, they exhibit mineralogical, structural and textural changes as a result of sedimentological petrographic and mineralogical investigations of the evaporitic units.

The presence of dark colored (brown-black) and smaller gypsum crystals and pelloidal structures determined by sedimentological and mineralogical studies showed that organic / bacterial activity was intense and environmental conditions were more reducing and acidic. The high amounts of metallic elements (such as Fe, Zn, Ni, Co) in gypsum detected in the SEM-EDS study can be attributed to the fact that they may have been transported from the bedrock by washing with hydrothermal solutions in the post-deposition. In addition, the presence of volcanoclastic levels and celestine mineral in the gypsum in the sequence showed the effect of possible active hydrothermal solutions rising from the faults limiting the basin, depending on the activity of the volcanism and tectonic activity during the Middle-Late Miocene in the region. These solutions were formed intermediate bands with hydrothermal alteration, rich in iron-mangane determined in the SEM studies, between the evaporites.

Acknowledgements

This study was carried out within the scope of Yüzüncü Yıl University Scientific Research Projects project no " FYL-2019-8742". I would like to thank Çetin Yeşilova for their contribution in the preparation of the article and field studies.

References

[1]. Brinkmann, R., “Geology of Turkey”, Elsevier, Amsterdam, (1976), 158.

[2]. Açlan, M., Altun, Y., “Syn-collisional I-type Esenköy Pluton (Eastern Anatolia-Turkey): an indication for collision between Arabian and Eurasian plates”, J. African Ear. Sci., 142, (2018), 1–11.

[3]. Oyan, V., “Ar-Ar dating and petrogenesis of the Early Miocene Taşkapı-Mecitli (Erciş-Van) granitoid, Eastern Anatolia Collisional Zone, Turkey”, Journal of Asian Earth Sciences, 158, (2018), 210-226.

[4]. Şengör, A. M. C., Yılmaz, Y., “Tethyan evolution of Turkey: a plate tectonic approach” Tectonophysics, 75, (1981), 181–241.

[5]. Hall, R., “Ophiolite emplacement and the evolution of the Taurus Suture Zone, southeastern Turkey”, Bull. Geol. Soc. Am., 87, (1976), 1078-1088.

[6]. Kurtman, F., Akkuş, M. F., Gedik, A., "The geology and oil potential of the Muş-Van region", Miner. Res. Explor. Inst., 169, (1978), 124-133.

[7]. Koşun, E., Çiner, A., "Zara güneyi (Sivas havzası) karasal-sığ denizel Miyosen çökellerinin litostratigrafisi ve fasiyes özellikleri", MTA Dergisi, 125, (2002), 65-88.

[8]. Tüysüz, O., "Erzincan çevresinin jeolojisi ve tektonik evrimi", 2nd National Earthquake Engineering Conference, Union of Chambers of Turkish Engineers and Architects Chambers of Civil Engineers, (1993), 271–280.

[9]. Çiner, A., Koşun, E., "Hafik güneyindeki (Sivas Havzası) Oligo-Miyosen yaşlı çökellerin stratigrafisi ve sedimantolojisi" TPJD Bült., 8 (1966a), 16-34.

[10]. Kurtman, F., "Sivas-Hafik-Zara ve imranlı bölgesinin jeolojik ve tektonik yapısı" MTA Derg., 80 (1973), 1-32.

[11]. Tatar, Y., "Kuzey Anadolu Fay zonunun Erzincan-Refahiye arasındaki bölümü üzerinde tektonik incelemeler" Yerbilimleri Derg., 4 (1978), 201-236.

[12]. Poisson, A. M., Guezou, J. C., Öztürk, A., İnan, S., Temiz, H., Gürsoy, H., Kavak, K., Özden, S., "Tectonic setting and evolution of the Sivas Basin, Central Anatolia, Turkey", Int. Geol. Rev., 38 (1996), 838-853.

[13]. Koçyiğit, A., Özkan, S., Rojay, B., "Examples from the forearc basin remnants at the active margin of northern Neo-Tethys: development and emplacement ages of the Anatolian Nappes, Turkey", Metu Journal of Pure And Applied Sciences, 21 (1988), 183-210.

[14]. Yılmaz, A., "Çarpışma sonrası bir çanak örneği: Sivas Havzası, Türkiye", Türkiye 10. Petrol Kongresi ve Sergisi Bildirileri, (1994), 21-33.

[15]. Kavak, K.S., İnan, S., "Savcun ve Karacaören (Ulaş-Sivas) yörelerinde Sivas havzası güney kenarındaki tektonostratigrafik özellikleri", Yerbilimleri, 23 (2001), 113-127.

[16]. Rojay, B., Karaca, A., "Post-Miocene deformation in the south of the Galatean Volcanic Province, NW of Central Anatolia (Turkey)", Turkish Journal of Earth Sciences,17 (2008), 653–672.

[17]. Akpınar, Z., Gürsoy. H., Tatar, O., Büyüksaraç, A., Koçbulut, F., Piper, J. D., "Geophysical analysis of fault geometry and volcanic activity in the Erzincan Basin, Central Turkey: complex evolution of a mature pull-apart basin" Journal of Asian Earth Sciences, 116 (2016), 97–114.

[18]. Arpat, E., Şarolu, F., "Türkiye'deki bazı önemli genç tektonik olaylar", Bullet. Geol. Cong.18 (1975), 91–101.

[19]. Özgül, N. Ç., Turşucu, A., Özyardımcı, N., Şenol, M., Bingöl, İ., Uysal, Ş., "Munzur Dağlarının jeolojisi, MTA Derleme Rap., No. (1981), 6995.

[20]. Barka, A. A., "Some neotectoic features of the Erzincan basin", Earthq. Symp. Spec. Publs., (1984), 115-125.

[21]. Gökçen. S. L., Kelling, G., "Oligocene deposits of the Zara-Hafik region (Sivas, Central Turkey); evolution from storrn-infuenced shelf to evaporitic basin", Geol. Rundschau, 74 (1985), 139-153.

[22]. Yılmaz, A., "Yukarı Kelkit Çayı ile Munzur Dağları arasının temel jeoloji özellikleri ve yapısal evrimi" Türkiye Jeol. Kur. Bült., 28 (1985), 79-92.

[23]. Barka, A. A., Gülen, L., "New constraints on the age and total offset of the North Anatolian Fault Zone: implifications for tectonics of the Eastern Mediterranean Region", METU Journal of Pure Applied Science, 21 (1989), 39-63.

[24]. Norman, T. N., "On the structural evolution of the melange belt, north of Hafik (Sivas), Central Turkey", Türkiye 8. Petrol Kongresi Bildiriler kitabı, Ankara, (1990).

[25]. Koçyiğit, A., "Neotectonic structures and related landforms expressing the contractional and extensional strains along the North Anatolian Fault at the northwetern margin of the Erzincan basin, NE Turkey" Bull. Tech. Univ., 44 (1991), 455-473.

[26]. Aktimur, H. T., Sarıaslan, M., Keçer, M., Turşucu, A., Örçen, S., Yurdakul, M. E., Mutlu, G., Aktimur, S., 1988., Yıldırım, T., "Erzincan dolayının jeolojisi" MTA Rapor No. (1995), 9772.

[27]. Emre, Ö., Duman T. Y., Kondo, H., Olgun, Ş., Özalp, S., Elmacı, H., "1/250 000 ölçekli Türkiye diri fay haritası serisi, Erzincan (NJ 37-3) Paftası", MTA Rapor No. (2012), 44.

[28]. Atalay, Z., "Sivas'ın batı ve güneybatısındaki çökellerin stratigrafisi ve çökel ortamları, Sivas Baseni Oturumu", Cumhuriyet Univ. Müh. Fak., (1993), 6-8.

[29]. Bayhan, H., Baysal, O., "Güneş-Soğucak (Divriği-Sivas) yöresinni petrografik ve petrolojik incelenmesi", TJK Bülteni, 25 (1982), 1-13.

[30]. Tunç, M., Özçelik, O., Tutkun, Z., Gökçe, A., "Divriği-Yakuplu-İliç-Hamo (Sivas) yöresinin temel jeoloji özellikleri", Tr. J. Eng. And Envi. Scie., 15 (1993), 225-245.

[31]. Yılmaz, A., Sümengen, M., Terlemez, İ., Bilgiç, T., "1/100000 ölçekli Türkiye jeoloji haritaları serisi. Sivas-G23 paftası", MTA, (1989), Ankara.

[32]. Aktimur, H. T., Ateş, Ş., Atalay, Z., Tekirli, M. E., Yurdakul, M. E., "Munzur Dağları ile Çavuşdağı

arasının jeolojisi" MTA Derleme Rapor No. (1988), 8320.

[33]. Kurtman, F., "Munzurlarda Kemah ve Ovacık bölgelerine ait petrol istikşaf etüdü" MTA Petrol Şubesi Rap. No. (1961), 22.

[34]. Özdemir, C., İçen, C., "Erzincan İli İliç İlçesi ve civarı demir etütleri raporu", MTA Rapor No. (1971), 4461.

[35]. Aktimur, H. T., Tekirli, M. E., Yurdakul, M. E., "Sivas-Erzincan Tersiyer Havzasının jeolojisi" MTA Derg., 111, (1990), 25-36.

[36]. Temiz, H., "The role of thrust ramp reactivation in pull-apart mechanism of the Erzincan basin, North Anatolian Fault Zone, Turkey", Geodinam. Acta, 17, (2004), 219–228.

[37]. Schreiber, B. C., Freidman, G. M., Decima, A., Schreiber, E., "Depositional environments of Upper Miocene (Messinien) evaporite deposites of the Silician Basin", Sedimentology, 23, (1976), 729–760.

[38]. Shearman, D. J., "Origin of marine evaporites by diagenesis" Trans. Inst. Min. Metal., 75 (1966), 208-215.

[39]. Warren, J. K., Kendall, G. C. S. C., "Comparison of marine sabkhas (subareial) and saline (subaqueous) evaporites: Modern and ancient", Bull. Am. Assoc. Petrol. Geol., 69, (1985), 1013-1023.

[40]. Warren, J. K., "Evaporites: sediments, resources and hydrocarbons", (2006) Springer, Berlin.

[41]. Garrison, R. E., Schreiber, B. C., Bernoulli, D., Fabricius, F. H., Kidd, R. B., Melieres, F., "Sedimentary petrology and structures of Messinian evaporitic sediments in the Mediterranean Sea,", Ini. Rep. Deep Sea Drill. Pro., 42, (1978), 571-611.

[42]. Babel, M., "Models for evaporite, selenite and gypsum microbialite deposition in ancient saline basins", Acta Geologica Polonica, 54, (2004), 219–249.

[43]. Schreiber, B. C., Babel, M., Lugli, S., "Evaporites through Space and Time", Geological Society, London Special Publications, 285, (2007), 1-13.

[44]. Cody, R. D., "Lenticular gypsum: occurrences in nature, and experimental determinations of effects of soluble green plant material on its formation", J. Sed. Pet., 49, (1979), 1015–1028.

[45]. Cody, R. D., Cody, A. M., "Gypsum nucleation and crystal morphology in analog saline terrestrial environments", J. Sediment. Petrol., 58 (1988), 247–255.

[46]. Shearman, D. J., Orti, F., "Upper Miocene gypsum: San Miguel de Salinas, SE Spain", Soc. Geol. Ital., 16, (1976), 327–339.

[47]. Warren, J. K., "The hydrological setting, ocuurence and significance of gypsum in the late Quaternery salt lakes in South Australia", Sedimentology, 29, (1982), 609–637.

[48]. Manzi, V., Lugli, S., Ricci Lucchi, F., Roveri, M., "Deepwater clastic evaporites deposition in the Messinian Adriatic foredeep (northern Apennines, Italy): did the Mediterranean ever dry out?", Sedimentology, 52, (2005), 875-902.

[49]. Carrillo, E., Rosell, L., Ortí, F., "Multiepisodic evaporite sedimentation as an indicator of palaeogeographic evolution in foreland basins (Southeastern Pyrenean basin, Early–Middle Eocene)", Sedimentology, 61, (2014), 7.

[50]. Kinsman, D. J. J., "Models of formation, sedimentary associations and diagnositic features of shallow water and supratidal evaporites", Am, Assoc: Petr. Geol., 53, (1969), 830-840.

[51]. Caldwell, R. H., "Holocene gypsum deposits of the Bullara Sunkland, Carnarvon Basin, Western Australia", Thesis, Univ.Western Australia, (1976), 123.

[52]. Hardie, L. A., Smooth, J. P., Eugster, H. P., "Saline lakes and their deposits", Sedimentology, 2, (1978), 7-41.

[53]. El-Tabakh, M., Riccioni, R., Schreiber, B. C., "Evolution of Late Triassic rift basin evaporites (Passaic Formation); Newark Basin, eastern North America", Sedimentology, 44 (1997), 767–790.

[54]. Arakel, A. V., "Genesis and diagenesis of Holocene evaporitic sediments in Hurt and Leeman Lagoons, western Australia", J. Sedimen. Petrol., 50, (1980), 1305-1326.

[55]. Magee, J. W., "Late Quaternary Lacustrine, groundwater, aeolian pedogenic gypsum in the Prungle lakes, Southeastern Australia", Paleogeography, Paleoclimatology-Paleoecology, 84, (1991), 3–42.

[56]. Ogniben, L., "Inverse graded bedding in primary gypsum of chemical deposition", J. Sed. Petrology, 25, (1955), 273-281.

[57]. Arzaghi, I. S., Khosrow-Tehrani. K., Afghah, M., "Sedimentology and petrography of Paleocene–Eocene evaporites: The Sachun Formation, Zagros Basin", Carbonates Evaporites, 27, (2012), 43–53.

[58]. Çiner, A., Koşun, E., Deynoux, M., "Fluvial, evaporitic and shallow-marine facies architecture, depositional evolution and cyclicity in the Sivas Basin (Lower to Middle Miocene), Central Turkey", J. Asian Earth Sci., 21, (2002), 147-165.

[59]. Aref, M. A., Basyoni, M. H., Bachmann, G. H., "Microbial and physical sedimentary structures in modern evaporitic coastal environments of Saudi Arabia and Egypt", Facies 60, (2014), 371–388.

[60]. Hardie, L. A., "Evaporites: Marine or non-marine" Amer. Jour. Scien., 284, (1984),193–240.

[61]. Hardie, L. A., Lowenstein, T. K., Spencer, R. W., "The problem of distinguishing between primary and secondary features in evaporites", Salt Institute, 1, (1985), 11-39.

[62]. Reineck, H. E., Singh, I. B., "Depositional Sedimentary environments", Springer verlag, Berlin, (1975), 549.

[63]. Orti, F., Rosell, L., "Evaporite systems and diagenetic patterns in the Calatayud Basin (Miocene, central Spain)" Sedimentology, 47, (2000), 665–685.

[64]. Peryt, T. M., Ortí, F., Rosell, L., "Sulfate platform-basin transition of the lower Werra Anhydrite (Zechstein, Upper Permian), western Poland: facies and petrography", Journal of Sedimentary Petrology, 63, (1993), 646–658.

[65]. Kendall, A. C., "Evaporites. Facies Models-response to sea level change", Geological Association of Canada, St John's, (1992), 375–409.

[66]. Ortí, F., Salvany, J. M., "Coastal salina evaporites of the Triassic–Liassic boundary in the Iberian Peninsula: The Alacón borehole", Geologica Acta, 2, (2004), 291–304.

[67]. Orti, F., Salvany, M., "Continental evaporitic sedimentation in the Ebro Basin during the Miocene. Sedimentary Deposition in Rift and Foreland Basins in France and Spain (Paleogene and Lower Neogene)", Columbia University Press, New York, (1997), 420-430.

[68]. Holliday, D. W., "The petrology of secondary gypsum rocks", Journal of Sedimentary Petrology, 40, (1970), 734-744.

[69]. Abdioğlu, E., Arslan, M., Kadir, S., Temizel, İ., "Alteration minerology, lithochemistry and stable isotope geochemistry of the Murgul (Artvin, Ne Turkey) volcanic hosted massive sulfide deposit: implications to alteration age and ore forming fluids", Ore Geol. Rev., 66, (2015), 219–242.

[70]. Orti, F., Rosell, L., "Sulfatos evaporiticos de interés petrologico (In Spanish)", Edicions Universitad de Barcelona, Fundacio Folch, (1997).

[71]. Forjanes, P., Astilleros, J. M., Fernández-Díaz, L., "The Formation of barite and celestite through the replacement of gypsum", Minerals, 10, (2020), 189.

[72]. Kushnir, J., "The composition and origin of brines during the Messinian desiccation event in the Mediterrnnean basin as deduced from concentrations of ions coprccipitated with gypsum and anhydrite" Chern. Geol., 35, (1982), 333–350.

[73]. Lan, X. H., "Clay minerals as an index of paleoclimate. Geological Science and Technology Information", 9, (1990), 31 – 35.

[74]. Kovacs, G. T., Morgan, G., Levine, M., McCrann, J.,"The Australian community overwhelmingly approves IVF to treat subfertility, with increasing support over three decades", Obstetr Gynaecol, 52, (2012), 302– 304.

[75]. Temel, A., Gençoğlu, H., Bayhan, H., Öner, F., Ağrılı, H., "Meke Dere (Güzelyurt-Aksaray) kaolinit ocağının hidrotermal mineral oluşumları", VII. Ulusal Kil Sempozyumu, (1995), 76-87.

[76]. Scholle, P. A., Ulmer, D. S., Melim, L. A., "Late-stage calcites in the Permian Capitan Formation and its equivalents, Delaware Basin margin, west Texas and New Mexico: evidence for replacement of precursor evaporites", Sedimentology, 39, (1992), 207–234.

[77]. Pryor, W. A., "Biogenie sedimentation and alteration of argillaceous sediments in shallow marine environments", Geological Society of America Bulletin, 86, (1975), 1244-1254.

[78]. Deik, H., Reuning, L., Petrick, B., Takayanagi, H., "Hardened faecal pellets as a significant component in deep water, subtropical marine environments", A Jour. Inter. Assoc. Sedim., (2019), DOI: 10.1002/dep2.64

[79]. Tucker, R. M., "Giant polygons in the Triassic salt of Cheshire, England: a thermal contraction model for their origin", J. Sediment. Pet., 51, (1981), 779-786.

[80]. Playa, E., Orti, F., Rosell, L., "Marine to non-marine sediementation in the upper Miocene evaporites of the Eastern Betics, SE Spain: sedimentological and geochemical evidences". Sed. Geol., 133, (2000), 135–166.

[81]. Hardie, L. A., Eugster, H. P., "The depositional environment of marine evaporites: a case for shallow, clastic accumulation" Sedimentology, 16, (1971), 187–220.

MANAS Journal of Engineering
ISSN 1694-7398 | e-ISSN 1694-7398

Volume 9, Issue 2, (2021) Pages 184-191
https://doi.org/10.51354/mjen.926504

Optimization of multi effect evaporation systems using a metaheuristic hybrid algorithm

Orhun Uzdiyem[1*], Yavuz Özçelik[2]

Ege Üniversitesi Fen Bilimleri Enstitüsü, Erzene, 3, Ege Ünv. No:172, 35040 Bornova/İzmir
orhun.uzdiyem@gmail.com, ORCID: 0000-0002-4725-0045

ABSTRACT

A computer program, capable of carrying out the mathematical modelling and optimization of multi effect evaporation (MEE) systems is developed in the scope of this study. C# programming language is used in the development of the computer program. A Particle Swarm Optimization (PSO) based algorithm is developed and hybridized with a Levenberg-Marquardt (LM) based algorithm. A computer program interface is developed in .NET platform for the user to give inputs such as feed and product streams flowrate and concetration. The optimization results is represented through this interface. Concentrating the sodium hydroxide content in the wastewater of the mercerization process is selected as the sample case.

ARTICLE INFO

Research article

Received: 22.04.2021
Accepted: 20.10.2021

Keywords:
Equation oriented modelling
Metaheuristic hybrid optimization
Particle swarm optimization
Levnberq-Marquardt
Multi effect evaporation

*Corresponding author

Nomenclature

Symbols

L_i	Outlet liquid flowrate of effect 'i', kg/h
V_i	Outlet vapor flowrate of effect 'i', kg/h
x_i	Solute concentration in the outlet liquid stream of effect 'i', kg solute/kg solution
h_i	Outlet liquid stream enthalpy of effect 'i', kJ/kg
H_i	Outlet vapor stream enthalpy of effect 'i', kJ/kg
$H_{vap,i}$	Outlet vapor stream vaporization enthalpy of effect 'i', kJ/kg
T_i	Operation temperature of effect 'i', K
P_i	Operation pressure of effect 'i', kPa
A_i	Heat transfer area of effect 'i', m^2
U_i	Overall heat transfer coefficient of effect 'i', W/m^2K
F	Feed stream flowrate, kg/h
V_0	Live steam flowrate, kg/h

Dimensionless parameters

$v_{j,d}$	PSO velocity of variable 'd' of particle 'j'
$x_{j,d}$	Value of variable 'd' of particle 'j'
$c_{j,d}$	Best known cluster position of variable 'd' of particle 'j'
$p_{j,d}$	Best known position of variable 'd' of particle 'j'
g_d	Global best known position of variable 'd'
ω	PSO constant of velocity
Φ_c	PSO constant of cluster gap
Φ_p	PSO constant of particle gap
Φ_g	PSO constant of global gap
r_c	PSO randomized value of cluster gap
r_p	PSO randomized value of particle gap
r_g	PSO randomized value of global gap

1 Introduction

Evaporation is the process of concentrating an aqeuous solution by vaporizing the water content. In a MEE system, the solution is evaporated using saturated steam in the first effect and the vapour which is the outlet of each effect (V_i) is used as heating medium in the following effects. This design provides a huge steam economy.

There are several ways of feed sequences for MEE systems. The most widely used ones are forward feed and backward feed sequences. The live steam (V_0) is fed from the first effect in both of these options. Weak concentration -the feed stream- is fed from the first effect to flow parallel with the heating medium in the forward feed option while it is fed from the last effect to flow counter to the heating medium in the backward feed option.

The evaporation capacity of each effect depends on the evaporation capacity of the previous effect in forward feed sequence while it is dependent on the evaporation capacities of both the previous and next effects in backward feed sequence. An equation oriented approach is a better choice for simulation and design of MEE systems due to these

dependencies. Backward feed sequence and preheating has a positive effect on evaporation economy through an equation-oriented simulation model [1]. A MEE system with higher number of effects will have a better steam economy [2]. Falling film evaporator is a better choice due to the lower pressure loss [2]. But the falling film evaporators must be forced circulated, because it would be difficult to uniformly distribute the solution to all tubes.

By investigating both the operating cost and capital cost, optimum number of effects is found as three for an evaporation amount of 6750 kg/h [3]. A genetic based algorithm should be followed instead of Newton's method especially for higher number of effects [4]. Because very complex Jacobian matrixes can be encountered while dealing with higher number of effects. In the mathematical model, correlations can be used to calculate temperature dependent properties such as enthalpy and heat capacity for simplification [5]. These simplifications do not effect the selection of optimal feed sequence. The main condition of the optimization of an evaporation system is the product quality [6]. The product quality, in other words the concentration of the product must be determined before starting the modelling and all of the parameters are calculated as values that can catch the desired product concentration.

Developing models and simultaneous solution algorithm which comprises the complete complex structure of the multi effect evaporation systems is challenging and further research in this field will aim the energy saving weighted optimization [7].

2. Mathematical modelling

An evaporation system that is optimally designed, aims to concentrate the aqueous solution with an energy efficient way. Steam and electricity consumptions will be minimized by optimizing the operating parameters along with integer values such as the feed sequence and the number of effects. So, the mathematical model that is needed to optimize the system is a mixed integer nonlinear problem.

Figure 1 represents a single effect evaporation which is part of a MEE system. Equations 1 and 2 are derived from the total mass balance and solute component mass balance around each effect respectively. Eq. 3 is used as the energy balance equation of each effect.

$$V_i = L_{i\pm1} - L_i \quad (1)$$

$$x_i = F * x_f / L_i \quad (2)$$

$$L_{i\pm1}h_{i\pm1} + V_{i-1}H_{vap,i-1} - V_iH_i - L_ih_i = 0 \quad (3)$$

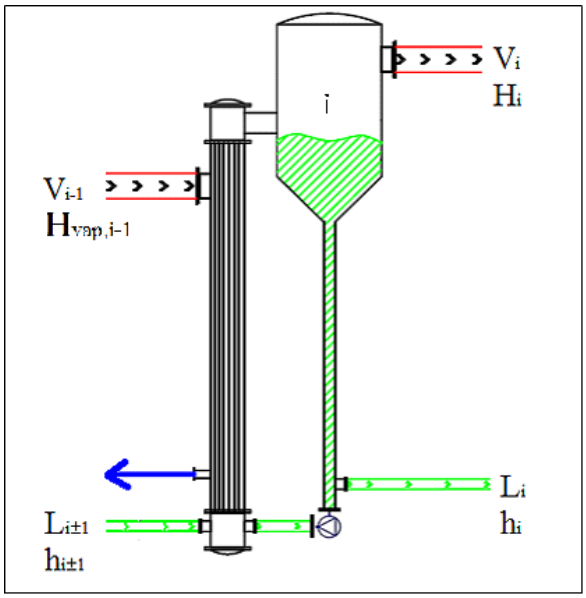

Figure 1. *Single effect evaporation*

Outlet vapor stream enthalpy (H_i) and outlet liquid stream enthalpy (h_i) can be calculated explicitly using operating temperature of each effect (T_i) which is dependent on two parameters. The first one is the operating pressure (P_i). The second one is the solute concentration (x_i) in the outlet liquid stream. The boiling point elevation (BPE) term represents the effect of the solute concentration on the boiling point of the solution and is calculated through a correlation of concentration particular to the solute type.

$$T_i = T_{sat,i} + BPE_i \quad (4)$$

Equations 5 and 6 are correlations derived from steam table data and are used to calculate saturation temperature and vaporization enthalpy [8]. The validity interval and the R-squared values of these equations are 10-1300 kPa and 0.995.

$$T_{sat,i} = 258.5 * P_i^{0.0803} \quad (5)$$

$$H_{vap,i} = 2 * 10^{-9} * P_i^4 - 4 * 10^{-6} * P_i^3 + 0.0033 * P_i^2 - 1.4124 * P_i + 2376.7 \quad (6)$$

Feed flowrate, feed concentration and product concentration are design variables because they are the design specifications. The remaining variables V_0, L_i and P_i are live steam consumption (LSC), outlet liquid flowrate and operating pressure of effect 'i' respectively. P_i is determined by the optimization algorithm while L_i remains as an unknown variable except for the last effect which makes one unknown variable for each effect. Since there are one energy balance equation for each effect –Eq. 3- the degrees of freedom is zero.

After the equation set is solved and all of the flowrates are determined, the evaporators are designed. Design of

evaporator is similar to a vertical shell and tube heat exchanger design. Heating medium is passed through the shell side while the concentration is passed through the tube side. The tube side fluid consists of the inlet liquid stream and the circulated portion of the outlet liquid stream ($L_{c,i}$). So, the flowrate of the tube side is the sum of the flowrates of these streams. $L_{c,i}$ is found by Eq. 7 where circulation rate (cr_i) of each effect is an optimization parameter. Higher cr values mean lower purchase cost of evaporators but higher pumping cost. Due to the high rate of circulation, the temperature of the tube side is assumed as consant at the outlet liquid temperature.

$$L_{c,i} = cr_i \times L_i \tag{7}$$

Along with optimization parameters tube length and tube diameter, tube side flowrate is used to calculate tube side heat transfer coefficient, which is used in iterative overall heat transfer coefficient calculation. The film coefficient of the condensing steam will be too high to limit the overall heat transfer coefficient. So, shell side heat transfer coefficient can be assumed to be 8000 W/m^2 - K at all cases. Thermal conductivity of stainless steel is taken as 1.6 W/m-K.

There are two main reasons for the operating pressure difference among effects. One of them is the pressure loss due to the friction. The larger heat loss is the conversion of kinetic energy during the flash evaporation at the entering of the separator tanks.

The pump power ($\mathcal{P}$) is calculated by Eq. 8 as kg.m^2/s^3 in other words as watts. The pump efficiency (η) is taken as 0.6. The mass flowrate ($\dot{V}$ of the pump must be in kg/s and the pressure difference (H_p) in mWH where 1 mWH is equal to 9.807 kPa.

$$\mathcal{P} = \dot{V} g H_p / \eta \tag{8}$$

While calculating the power of the circulation pump (CP) of effect 'i', $L_{c,i}$ is used as $\dot{V}$ and only the pressure loss due to the friction is used as H_p. While calculating the power of the feed pump (FP) or backward feed pump (BFP) of effect 'i', L_i is used as $\dot{V}$. As H_p the pressure difference between the outlet and inlet streams of the pump is converted to mWH and used in this wise.

Sum of the total purchase cost (TPC) and annual operating cost (AOC) is the value to be minimized as the objective of this study. TPC cosists of mainly the cost of evaporators (EvC) and the cost of pumps (PuC). Costs of condenser, vacuum pump, piping and instrumentation are neglected because these costs are assumed to be close for each option for the same design specifications and have no effect on finding the optimum variables. The cost of the seperator tanks are neglected because their prices would be negligibly small compared to the cost of evaporators.

$$TPC = EvC_T + PuC_T \tag{9}$$

The EvC is calculated using Hall method which is used for estimating the capital cost of stainless steel shell and tube heat exchangers [9].

$$EvC = 10000 + 324 \times A^{0.91} \tag{10}$$

Pump costs (PuC) is calculated through Eq. 12 where the purchase cost (PuC^0) of a carbon steel pump is calculated by Eq. 11 and the power of the pump ($\mathcal{P}$) is in kW (Turton et al., 2012). The material factor, F_M is taken as 3.25 and the bare module factor, F_P is taken as 3 for centrifugal stainless steel pumps [10].

$$log_{10} PuC^0 = 3.3892 + 0.0536 log_{10}(\mathcal{P}) + 0.1538[log_{10}(\mathcal{P})]^2 \tag{11}$$

$$PuC = PuC^0(1.89 + 1.35 F_M F_P) \tag{12}$$

AOC consists of the price of steam and electricity used. Steam cost (StC) is calculated as \$/h through live steam consumption and unit price of electricity (UP_{st}). The plant is assumed to work 24 hours a day and 300 days in a year. The required conversions from [\$/h] to [\$/year] are needs to b performed while solving Eq. 13.

$$AOC = StC + ElC \tag{13}$$

$$StC = V_0 \times UP_{st} \tag{14}$$

$$ElC = \left(\mathcal{P}_{FP} + \sum_{i=1}^{n} \mathcal{P}_{CP,i}\right) \times UP_{el} \tag{15}$$

$$ElC = \left(\mathcal{P}_{FP} + \sum_{i=1}^{n} \mathcal{P}_{BFP,i} + \sum_{i=1}^{n} \mathcal{P}_{CP,i}\right) \times UP_{el} \tag{16}$$

Equations 15 and 16 represent the method of calculating the electricity cost (ElC) as \$/h in the cases of forward feed and backward feed respectively. Unit price of electricity (UP_{el}) is the cost of 1 kWh electricity. In the case of backward feed, the outlet liquid stream of each effect is fed to the previous effect as the inlet liquid stream, which has a higher operating pressure. So there is need of a backward feed pump at each effect except the first effect. There is no such need in the case of forward feed.

3. Optimization algorithm

Particle swarm optimization (PSO) is a computational optimization method that aims to find the optimum point of a function. PSO algorithm is based on simulating the social behavior of a bird swarm that tries to find the area which contains better food [11]. The bird which finds the best food sings and calls the other members of the swarm to his surroundings. But each bird keeps the memory of the location where he found the best food resource until he finds a better food. Each bird in the swarm is named as 'particle'.

Coordinates and velocity vectors of each particle is randomly initialized. The coordinate's vectors of the particles are moved by the velocity vectors at each iteration. Each particle has a memory that keeps the best-known point of that particle. The global best-known point of all particles is also kept in the parent memory. The velocity is recalculated in each iteration. There are three values that effect the velocity vector. The first of them is the difference between the global best-known position and the particle's current position. The second one is the difference between the particle's best-known position and the particle's current position. The third one is the particle's previous velocity.

This algorithm allows the particles gather around the position that has a higher possibility to have optimum results. Also, local optimum points can be found by this algorithm. But that doesn't prevent the algorithm to find the global optimum. When a particle is trapped in a position and no longer moves, that point is marked as local optimum, the particle is taken out of the swarm and the algorithm continues with the remaining swarm. So, the particle which is trapped in the local optimum can no longer attract the swarm to the local optimum surroundings.

The main mathematical operations of the PSO are the velocity vector calculation and the movement of each particle by the velocity vector.

3.1. Hybridization of PSO with LM

A hybrid algorithm using PSO and a modified Levenberg-Marquardt (LM) method has been developed for this study. The modified LM method is a combination of Newton-Raphson and Gradient Descent methods reinforced by a homothopy parameter which keeps the results in physically meaningful area [12]. The variables that is determined by the PSO algorithm are sent to LM algorithm to solve the nonlinear equation set that is constructed using the energy balance equations. The LSC and flowrates between the effects are calculated as a result of the modified LM algorithm. By these values the evaporators are designed and the objective function result (Y) is calculated. Objective function is the combination of AOC and TPC by a coefficient called capital recovery factor (CRF).

$$Y = AOC + CRF * TPC \tag{17}$$

The main algorithm is represented in Figure 2. After the design specifications are taken from the user inputs and the initial swarm is created by randomization, the PSO algorithm is triggered. At each iteration of the PSO, alias at the beginning of each LM operation, all of the optimization parameters are checked if they satisfy the constraints. If they don't satisfy the constraints, the algorithm returns the value of -1 which means this particle must be destroyed. The procedure that is going to be followed when there is a particle that must be destroyed, is described in section 3.2.

3.2. Modification of PSO

To apply PSO method to constrained mixed integer programming, some modifications are needed. Most variables in our mathematical model are integer and have minimum and maximum boundaries. In fact, some of the boundaries are dependent on other variables. For example, the operating pressure of each effect must be high enough for the outlet vapor stream to heat the next effect. The necessary value is dependent on the operating pressure and outlet liquid stream concentration of the next effect. Another conflict is the dependency of most of the variables on the number of effects (NoE). When NoE of a particle increase during the optimization, the number of variables of that particle increases too. That makes the recently added variables unable to make their way, because neither previous velocity value for that particle nor the best-known position value exist for those variables.

These problems are solved by some modifications on the original PSO algorithm. The main modification is the cluster term. The particles which have the same NoE and feed sequence are the members of a cluster. The NoE of the particles are initialized to numbers between 2 and 6. As there are two feed sequences, there are 12 numbers of clusters at the beginning of the algorithm. If the NoE of any particle moves to a larger value than 6, a new cluster is created.

$$\begin{aligned} v_{j,d} = \omega v_{j,d} &+ \Phi_c r_c \left(c_{j,d} - x_{j,d}\right) \\ &+ \Phi_p r_p \left(p_{j,d} - x_{j,d}\right) \\ &+ \Phi_g r_g \left(g_d - x_{j,d}\right) \end{aligned} \tag{18}$$

The best-known position of the clusters is also kept like the global and particle best known positions and is included to the velocity calculation formula as seen in Eq. 18. If any particle is the best-known particle of its cluster, NoE and the feed sequence of that particle is not moved, in other words that particle is not allowed to move out of its cluster.

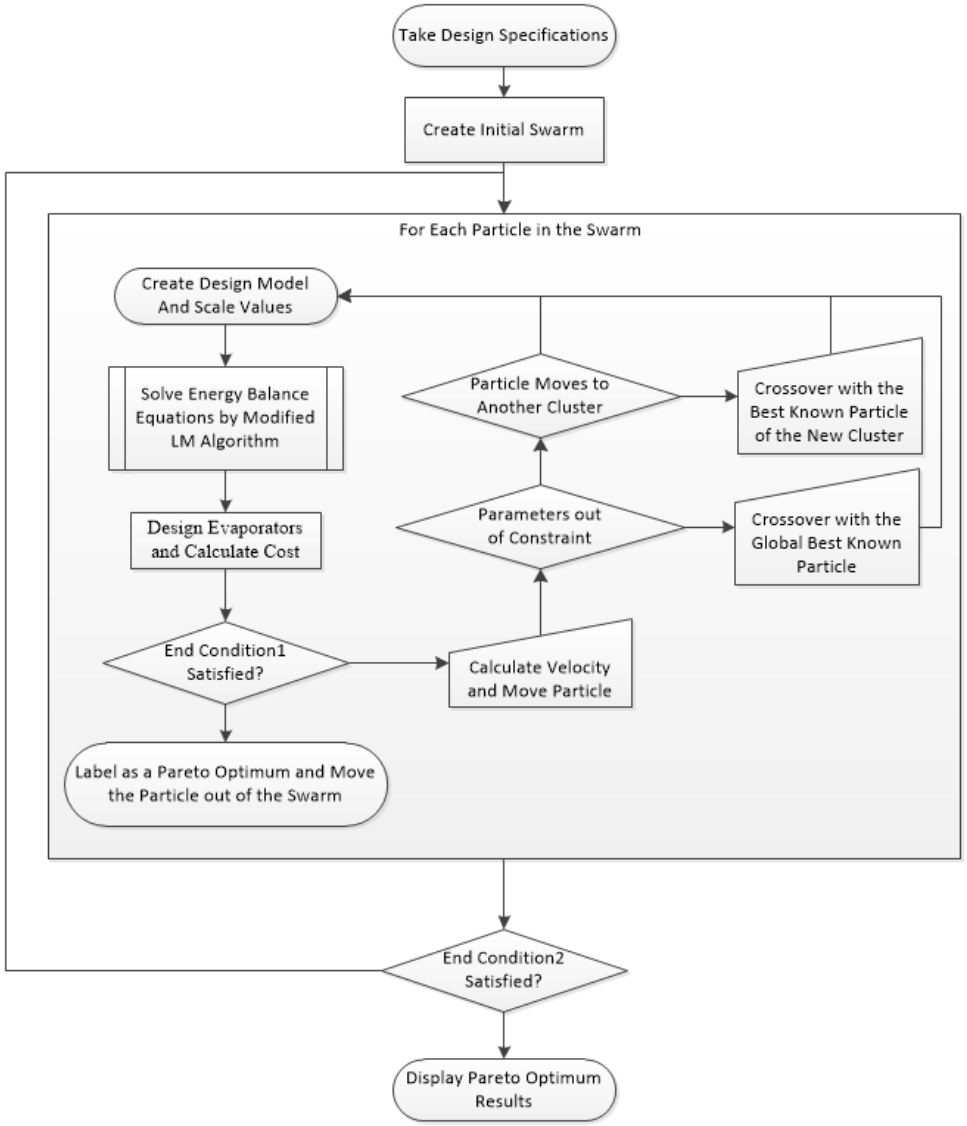

Figure 2. *Main Algorithm*

In some cases, the particle moves to an uncommon position. In those cases, uncommon operations are needed to be performed.

3.2.1. Out of Constraint Parameters

Whenever a particle moved out of constraints, that particle is destroyed. This operation is similar to the natural selection event. Out of constraint particles are destroyed because in the debug mode it is observed that these particles are tend to stay out of constraints. If natural selection occurs, new particles are needed to replace the destroyed ones. To create the new particle, the destroyed particle is crossed over by the global best-known particle before destruction. This crossover operation is a similar operation in the genetic algorithm [9]. But only one individual is created instead of two by using two random values as the crossover constants (ct). The ct_1 value is randomized between -1 and 1 as the first step. After this, ct_2 is randomized between -1 and $\min(1,|1.5-ct_1|)$ if ct_1 is positive. If ct_1 is negative, then ct_2 is randomized between $\max(-1,|ct_1-1.5|)$ and 1. By this approach, ct_1 and ct_2 are kept between -1 and 1, and their sum is kept between -1.5 and 1.5.

$$x_{offspring} = \frac{1+ct_1}{2}x_1 + \frac{1+ct_2}{2}x_2 \qquad (19)$$

3.2.2. Movement Out of the Cluster

If a particle moves out of the cluster which means NoE or feed sequence parameter of that particle is changed during the execution of the algorithm, that particle is destroyed similar to another natural selection event just as in the 'Out of Constraint

Parameters' case. Moving out of the cluster means getting into another cluster. Instead of moving just the same particle to its new cluster, a crossover operation is performed just as in the 'Out of Constraint Parameters' case. But this time the particle is crossed over with its new cluster's best-known position instead of the global best-known position.

3.3. Optimization Check

Before executing the algorithm on evaporation problem, PSO algorithm is run with a 2 variable optimization problem to observe the movement of the particles. The related problem is described in Eq. 20 and the movement of the particles is represented in Figure 3.

$$y = e^{-(x_1{}^2+x_2{}^2)} + 2e^{-[(x_1-1.7)^2+(x_2-1.7)^2]} \quad (20)$$

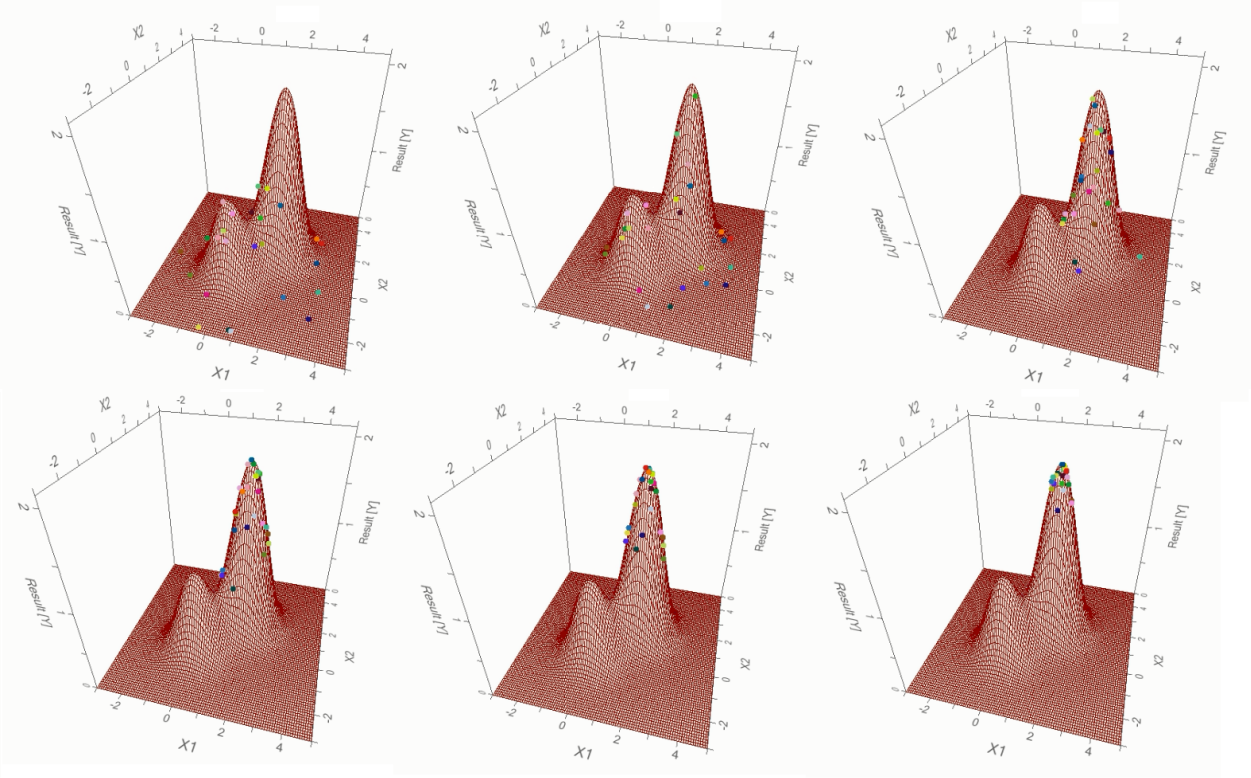

Figure 3. *Movement of PSO Particles*

As seen in Fig. 3, almost all of the particles are gathered around the optimum point at six iterations and the optimum point is found as x_1=x_2=1.7 and the optimum result is 2.

3.4. Development of the Computer Program and User Interfaces

A computer program including the mathematical models, nonlinear equation set solver, the hybrid optimization algorithm and other auxiliary methods was developed using C# programming language in .NET Framework 4.5 Environment using Microsoft Visual Studio. The pipe standards used in the calculation of overall heat transfer coefficient are kept at a related database.

The inputs form tabs are represented in Figures 4-6. As seen in Figure 5, user can select to enter some optimization parameters instead of the algorithm to optimize those parameters. The results form is represented in Figure 7.

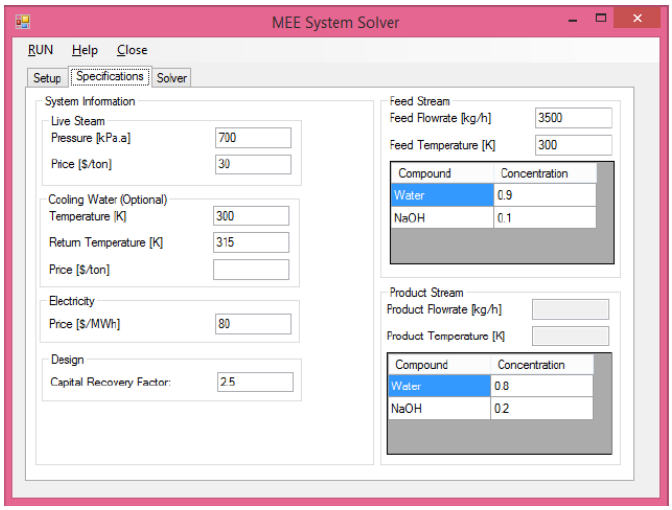

Figure 4. *Specifications tab*

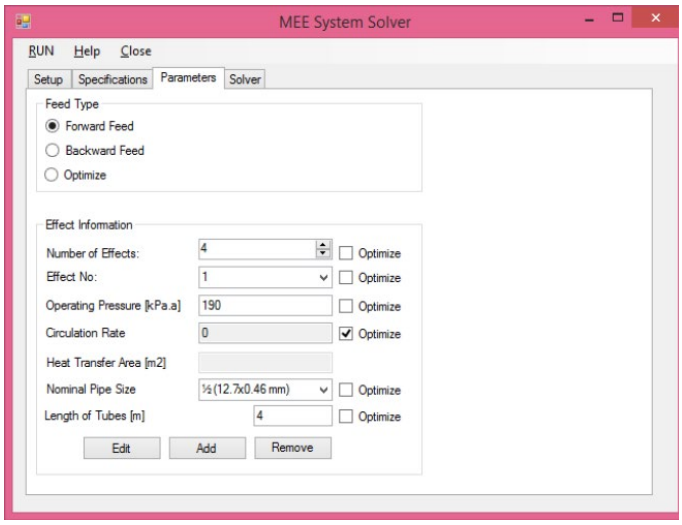

Figure 5. *Parameters tab*

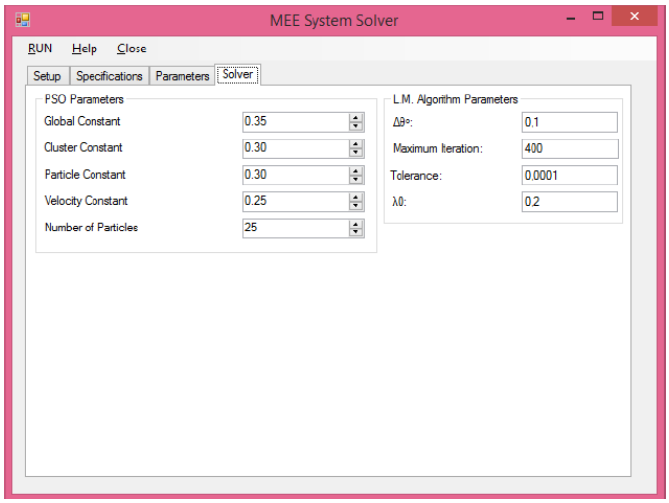

Figure 6. *Solver tab*

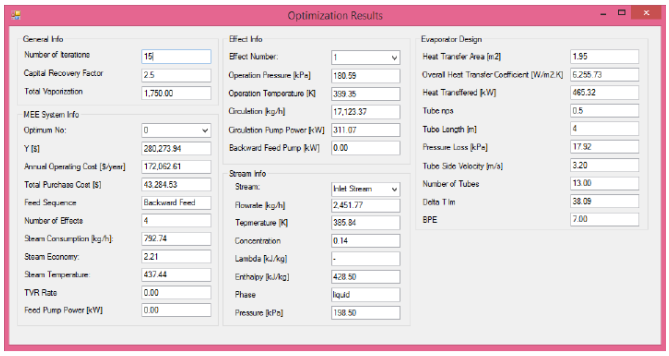

Figure 7. *Results form*

4. Case study and results

Concentrating a 8500 kg/h mercerization waste water having 10% NaOH to 30% is selected as the case study. Live steam pressure is selected as 700 kPa. Unit prices of steam and electricity are taken as 20 $/kg and 50 $/MWh respectively. The initial swarm of the optimization algorithm contains 5*NoE particles of each cluster. The Φ_g, Φ_c, Φ_p, and ω are taken as 0.35, 0.3, 0.3 and 0.25 respectively. Optimization algorithm is run with a CRF of 1 and best three pareto optimum results (PO) are taken into consideration. Problem is solved in 14 iterations. The total vaporization amount is calculated as 5667 kg/h and the live steam temperature is calculates as 437 K. the results are represented in tables.

Table 1. *Pareto optimum points*

	PO-1	PO-2	PO-3
Y [$]	410504	468547	480251
AOC [$/year]	350934	430289	430733
TPC [$]	59510	38269	49518
Feed Sequence	Backward	Backward	Forward
NoE	4	3	4
V_0	2428.7	2982.1	2981.5

Table 2. Detailed results of PO-1

	1st Effect	2nd Effect	3rd Effect	4th Effect
P [kPa]	336	230	130	10
T [K]	427.4	405.3	385.6	314.2
L_c [kg/h]	29707	43963	42243	67397
L [kg/h]	2833	5028	6945	7843
c	0.3	0.17	0.12	0.11
V [kg/h]	2194	1918	898	657

References

[1]. Kaya D., Ibrahim Sarac H., "Mathematical modeling of multiple-effect evaporators and energy economy", Energy, 32, (2007), 1536–1542. https://doi.org/10.1016/j.energy.2006.09.002

[2]. Shah D.J., Bhagchandani P.C.G., "Design , Modelling and Simulation of Multiple Effect Evaporators" 05, (2012), 1–5.

[3]. Ahmetović E., Suljkanović M., Kravanja Z., Maréchal F., Ibrić N., Kermani M., Bogataj M., Čuček L., "Simultaneous optimisation of multiple-effect evaporation systems and heat exchanger network." Chem. Eng. Trans. 61, (2017), 1399–1404. https://doi.org/10.3303/CET1761231

[4]. Verma O.P., Suryakant Manik G., "Solution of SNLAE model of backward feed multiple effect evaporator system using genetic algorithm approach." Int. J. Syst. Assur. Eng. Manag. 8, (2017), 63–78. https://doi.org/10.1007/s13198-016-0533-0

[5]. Khanam S., Mohanty B., "Development of a new model for multiple effect evaporator system." Comput. Chem. Eng. 35, (2011), 1983–1993. https://doi.org/10.1016/j.compchemeng.2010.11.001

[6]. Simpson R., Almonacid S., López D., Abakarov A., "Optimum design and operating conditions of multiple effect evaporators: Tomato paste." J. Food Eng. 89, (2008), 488–497. https://doi.org/10.1016/j.jfoodeng.2008.05.033

[7]. Ahmetović E., Ibrić N., Kravanja Z., Grossmann I.E., Maréchal F., Čuček L., Kermani M., "Simultaneous optimisation and heat integration of evaporation systems including mechanical vapour recompression and background process." Energy 158, (2018), 1160–1191. https://doi.org/10.1016/j.energy.2018.06.046

[8]. Felder R.M., Roussau R.W., "B.6 Properties of Saturated Steam: Pressure Table" in Elementary Principles of Chemical Processes, 3rd ed., New Jersey: John Wiley & Sons, 2005, 638-649.

[9]. Özçelik Y., "Exergetic optimization of shell and tube heat exchangers using a genetic based algorithm." Appl. Therm. Eng. 27, (2007), 1849–1856. https://doi.org/10.1016/j.applthermaleng.2007.01.007

[10]. Turton R., Bailie C.R., Whiting W.B., Shaeiwitz J.A., Bhattacharyya D., "A1. Purchases Equipment Cost" in Analysis, Synthesis and Design of Chemical Processes, 4th ed., New Jersey: Prentice Hall, 2012, 909-935.

[11]. Golbon-Haghighi M.H., Saeidi-Manesh H., Zhang G., Zhang Y., "Pattern synthesis for the cylindrical polarimetric phased array radar (CPPAR)." Prog. Electromagn. Res. M 66, (2018), 87–98. https://doi.org/10.2528/PIERM18011016

[12]. Özçelik Y., "Kimya mühendisliği sistemlerinin nonlineer analizi.", M.S. thesis, Chem. Eng. Dep., Ege Univ., İzm., Tur., 1990.

MANAS Journal of Engineering
ISSN 1694-7398 | e-ISSN 1694-7398

Volume 9, Issue 2, (2021) Pages 192-197
https://doi.org/10.51354/mjen. 929656

Fitting the Itô Stochastic differential equation to the COVID-19 data in Turkey

Sevda Özdemir Çalıkuşu[1*], Fevzi Erdoğan[2]

[1] Yuzuncu Yıl Unıversıty, Özalp Vocational School, Turkey, sevdaozdemir@yyu.edu.tr, ORCID: 0000-0002-0238-2677

[2] Van Yuzuncu Yil University, Faculty of Economics and Administrative Sciences, Turkey, ORCID: 0000-0003-3745-0198

ABSTRACT

In this study, COVID-19 data in Turkey is investigated by Stochastic Differential Equation Modeling (SDEM). Firstly, parameters of SDE which occur in mentioned epidemic problem are estimated by using the maximum likelihood procedure. Then, we have obtained reasonable Stochastic Differential Equation (SDE) based on the given COVID-19 data. Moreover, by applying Euler-Maruyama Approximation Method trajectories of SDE are achieved. The performances of trajectories are established by Chi-Square criteria. The results are acquired by using statistical software R-Studio.These results are also corroborated by graphical representation.

ARTICLE INFO

Research article

Received: 30.04.2021
Accepted: 20.10.2021

Keywords:
Itô stochastic differential equation, Euler-Maruyama approximation method, Maximum likelihood estimation method, COVID-19 data

*Corresponding author

1 Introduction

Coronavirus disease (COVID-19) is an infectious disease caused by a newly discovered coronavirus. Most people infected with the COVID-19 virus will experience mild to moderate respiratory illness and recover without requiring special treatment. Older people, and those with underlying medical problems like cardiovascular disease, diabetes, chronic respiratory disease, and cancer are more likely to develop serious illness [1]. The first case of COVID-19 in Turkey was reported on 11 March 2020, and the number of reported cases has increased day by day.

Stochastic differential equations model (SDEM) stochastic evolution as time evolves. These models have a variety of applications in many disciplines and emerge naturally in the study of many phenomena. Examples of these applications are physics, astronomy, mechanics, economics, mathematical finance, geology, genetic analysis, ecology, cognitive psychology, neurology, biology, biomedical sciences, epidemiology, political analysis and social processes, and many other fields of science and engineering [2]. And it is known that SDEMs are more realistic mathematical model than normal differential equation models of the situation [3]. Because stochastic differential equations, unlike normal differential equations, contain random effects called “white noise”.

In [4], Kostrista E. and Cibuku D. are looking for answers to some questions which are related with stochastic differential equations. These questions are ‘In what situations does the SDE arise?’, ‘What are its essential features?’, ‘What are the applications and the connections to the other fields?’ and ‘How does SDEs model the physical situation and white noise process which is the generalized mean-square derivative of the Wiener process or Brownian motion?’. In [5], Ince N. and Shamilov A. develop a new method to obtain approximate probability density function (pdf) of random variable of solution of stochastic differential equations (SDEs) by using generalized entropy optimization methods (GEOM). By starting given statistical data and Euler–Maruyama (EM) method approximating SDE are constructed several trajectories of SDEs. The constructed trajectories allow to obtain random variable according to the fixed time. In [6], Mahrouf M. et al. extend the well-known SIR compartmental model to deterministic and stochastic time-delayed models in order to predict the epidemiological trend of COVID-19 in Morocco and to assess the potential role of multiple

preventive measures and strategies imposed by Moroccan authorities. In [7], Bak J. Et al. propose a method to test for lack-of-fit of an estimated stochastic differential equation. The method is based on Monte Carlo simulation of trajectories between neighbour observations and, thus, it does not rely on the availability of explicit expressions of the conditional densities. Consequently, both non-linear models and models with state-dependent drift and diffusion can be handled. In [8], Rezaeyan R. and Farnoosh R. present an application of the continuous Kalman-Bucy filter for a RC circuit. The analytic solution of the resulting stochastic integral equations are found using the Ito formula. In [9], Ang examine the use of a simple stochastic differential equation in the modelling of an epidemic. Real data for the Singapore SARS outbreak are used for a detailed study. The model is solved numerically and implemented on matlab, with further analysis and refinement. This article is built around several matlab programs and serves to provide a practical and accessible introduction to numerical methods for a stochastic model for epidemics. In [10], Simha A. et al. model the region-wise trends of the evolution to COVID-19 infections using a stochastic SIR model. The SIR dynamics are expressed using Itô stochastic differential equations. In [11], Zhang et al. consider stochastic mathematical model for COVID-19. Firstly, the formulation of a stochastic susceptible–infected–recovered model is presented. Secondly, they devote with full strength our concentrated attention to sufficient conditions for extinction and persistence. Thirdly, they examine the threshold of the proposed stochastic COVID-19 model, when noise is small or large. Finally, they show the numerical simulations graphically using MATLAB.

Considering the studies mentioned above, the main features of the work finds an appropriate stochastic differential equation model for the given COVID-19 data. So in this research, we have examined by SDEM the COVID-19 data in Turkey between 11.03.2020 and 09.06.2020. In here, parameter values have been estimated from real data using the Maximum Likelihood procedure and approximate solutions of the established stochastic differential equation model have been obtained by using Euler-Maruyama method.

2. Stochastic calculus

2.1. Probability Theory

Stochastic differential equations provide a link between probability theory and the much older and more developed fields of ordinary and partial differential equations [4]. So, the terms of probability theory are significant in stochastic calculus. For instance, a stochastic integral is a random variable and the solution of a stochastic differential equation at any fixed time is a random variable [12]. Therefore, if anybody wants to learn about probability theory in detail, [3, 12-18] can be refered.

2.2. Itô Stochastic Differential Equation

Modeling physical systems by ordinary differential equations (ODEs) ignores stochastic effects. Addition of random elements into the differential equations leads to what is called stochastic differential equations (SDEs), and the term stochastic is called noise. A stochastic differential equation (SDE) is a differential equation in which one or more of the terms is a stochastic process, thus resulting in a solution which is itself a stochastic process [8].
A typical one dimensional Itô stochastic differential equation has the form

$$X(t,\omega) = X(0,\omega) + \int_0^t f\big(s, X(s,\omega)\big)\,ds + \int_0^t g\big(s, X(s,\omega)\big)dW(s,\omega) \tag{2.1}$$

and differential form

$$dX(t) = f(t,X) + g(t,X)dW(t) \tag{2.2}$$

for $0 \le t \le T$ with $X(0,\cdot) \in H_{RV}$, H_{RV} is the Hilbert space of random variables and $X(t,\omega)$ is a stochastic process not a deterministic function. $W(t,\omega) = W(t)$ is a Wiener process of Brownian motion and since it is nowhere differentiable. $W(t)$, $t \ge 0$ is a continuous stochastic process with stationary independent increments such that $W(0) = 0$, $\int_c^d dW(s) = W(d) - W(c) \sim N(0, d-c)$ for all $0 \le c \le d$. The function f is often called the drift coefficient of the stochastic differential equation while g is referred to as the diffusion coefficient [12].

3. Material and methods

3.1. Euler-Maruyama Method

An Ito stochastic differential equation on the interval [0,T] has the form

$$dX(t) = f(t, X(t);\ \theta)dt + g(t, X(t);\ \theta)dW(t) \tag{3.1}$$

is considered where $\theta \in \mathbb{R}^m$ is a vector of parameters that are unknown for $0 \le t \le T$ where $X(0) = X_0$, $X_0 \in H_{RV}$ and $W(t)$ is the Wiener process.
As the exact solution to a stochastic differential equation is generally difficult to obtain, it is useful to be able to approximate the solution. Euler-Maruyama method is a simple numerical method. When applied to (3.1), Euler's method has the form

$$X_{j+1,i}^{(m)}\left(t_{i-1}+(j+1)\frac{\Delta t}{K}\right)=X_{j,i}^{(m)}\left(t_{i-1}+j\frac{\Delta t}{K}\right)$$
$$+f\left(t_{i-1}+j\frac{\Delta t}{K},\ X_{j,i}^{(m)}\left(t_{i-1}+j\frac{\Delta t}{K}\right)\right)\frac{\Delta t}{K}+ \qquad (3.2)$$
$$+g\left(t_{i-1}+j\frac{\Delta t}{K},\ X_{j,i}^{(m)}\left(t_{i-1}+j\frac{\Delta t}{K}\right)\right)\sqrt{\frac{\Delta t}{K}}\,\eta_{j,i}^{(m)}$$

for $i=0,1,2,\dots,N-1$ and $j=0,1,2,\dots,K-1$ where $\Delta t=\frac{T}{N}$, $t_i=i\Delta t$, and $\Delta t_i=t_{i+1}-t_i=\frac{\Delta T}{K}$, $\eta_{j,i}^{(m)}\sim N(0,\Delta t)$, $\Delta W(t,w)=W(t_{i+1},w)-W(t_i,w)$, $\Delta W(t,w)\sim N(0,\Delta t_i)$, and m indicates a simulation number. This means that by changing number K, m times then m simulations realized, [14].
In this research, the extreme values of approximation trajectories $X_{j+1,i}^{(m)}$ by applying Euler-Maruyama Approximation Method are achieved.

3.2. Parameter Estimation for Stochastic Differential Equations

The problem is to find an estimate of the vector θ given these $N+1$ data points. Two estimation methods are a maximum likelihood estimation method and a nonparametric estimation method, [12].

In this study, we use the maximum likelihood estimation method to estimate parameters from the real data.

3.3. Maximum-Likelihood Estimation Method

Let $p(t_k,x_k|t_{k-1},x_{k-1};\boldsymbol{\theta})$ be the transition probability density of (t_k,x_k) starting from (t_{k-1},x_{k-1}) given the vector $\boldsymbol{\theta}$. Suppose that the density of the initial state is $p_0(x_0|\boldsymbol{\theta})$.
In maximum likelihood estimation of $\boldsymbol{\theta}$, the joint density

$$D(\boldsymbol{\theta})=p_0(x_0|\boldsymbol{\theta})\prod_{k=1}^{N}p(t_k,x_k|t_{k-1},x_{k-1};\boldsymbol{\theta})$$

is maximized over $\boldsymbol{\theta}\in\mathbb{R}^{\mathbf{m}}$ [12]. However, to avoid small numbers on a computer, it is more convenient to minimize the function $L(\boldsymbol{\theta})=-\ln\big(D(\boldsymbol{\theta})\big)$ which has the form

$$L(\boldsymbol{\theta})=-\ln\big(p_0(x_0|\boldsymbol{\theta})\big)-\sum_{k=1}^{N}\ln\big(p(t_k,x_k|t_{k-1},x_{k-1};\boldsymbol{\theta})\big).$$

4. A Stochastic Model for a COVID-19 outbreak

A simple stochastic model for a disease such as COVID-19 that spreads very quickly is given by the stochastic differential equation

$$dX(t)=\theta_1X(t)\big(n-X(t)\big)dt+\theta_2X(t)dW(t),\quad X(0)=X_0\,,\quad 0\le t\le T \qquad (3.3)$$

where $X(t)$ is the number of infected and susceptible individuals at time t (days), θ_1 and θ_2 are real constants, n is the total number of individuals in that community and $W(t)$ is a random variable representing a standard Wiener process. In here, it is obvious that drift represents the deterministic portion of the model, while diffusion represents the stochastic component [9].

In this study, we use equation (3.3) in the modeling of an infectious disease, using the outbreak of COVID-19 data in Turkey between 11.03.2020 and 09.06.2020.

4. An application

One of the important application areas of stochastic differential equations is population biology such as epidemic model. In this study, the COVID-19 data in Turkey between 11.03.2020 and 09.06.2020 are examined. This data set is accessed with the help of World Health Organization (WHO) shared the link via https://www.who.int/ [1], and the data set is shown in Table 1.

Table 1. *The COVID-19 data in Turkey between 11.03.2020 and 09.06.2020*

Day	Total number of confirmed cases	Day	Total number of confirmed cases	Day	Total number of confirmed cases	Day	Total number of confirmed cases
1	1	24	20921	47	110130	70	151615
2	1	25	23934	48	112261	71	152587
3	5	26	27069	49	114653	72	153548
4	5	27	30217	50	117589	73	154500
5	5	28	34109	51	120204	74	155686
6	47	29	38226	52	122392	75	156827
7	47	30	42282	53	124375	76	157814
8	191	31	47029	54	126045	77	158762
9	191	32	52167	55	127659	78	159797
10	670	33	56956	56	129491	79	160979
11	947	34	61049	57	131744	80	162120
12	1236	35	65111	58	133721	81	163103
13	1529	36	69392	59	135569	82	163942
14	1872	37	74193	60	137115	83	164769
15	2433	38	78546	61	138657	84	165555
16	3629	39	82329	62	139771	85	166422
17	5698	40	86306	63	141475	86	167410
18	7402	41	90980	64	143114	87	168340
19	9271	42	95591	65	144749	88	169218
20	10827	43	98674	66	146457	89	170132
21	13531	44	101790	67	148067	90	171121
22	15679	45	104912	68	149435	91	172114
23	18135	46	107773	69	150593		

We shall use following stages of investigation to solve our problem. Firstly, the parameters of SDE established for the COVID-19 data that mentioned above are estimated by using maximum likelihood estimation method. Then, we have obtained reasonable Stochastic Differential Equation (SDE) based on the given COVID-19 data. Moreover, by applying Euler-Maruyama Approximation Method trajectories of SDE are achieved and they are demonstrated in Figure 1.

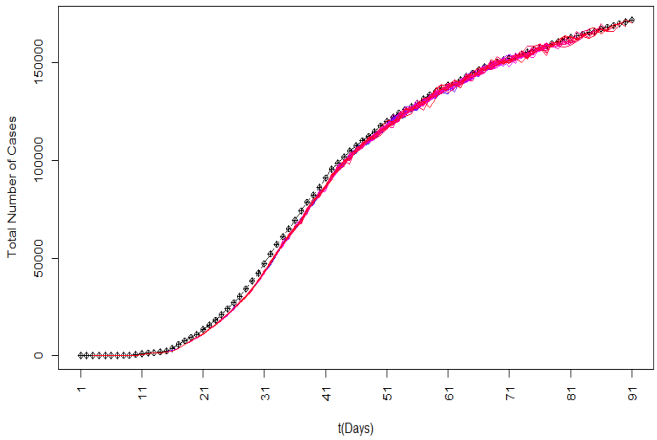

Figure 1. *The COVID-19 data in Turkey between 11.03.2020 and 09.06.2020 (black line) and approximate EM trajectories (colored lines) of the SDE*

Using the maximum likelihood estimation method, $\hat{\theta}_1 = 0.000004$ and $\hat{\theta}_2 = 0.98$ are obtained. If these estimated parameters are considered in the equation (3.3), dX(t) has the following form

$$dX(t) = 0.000004X(t)\big(172114 - X(t)\big)dt + 0.98X(t)dW(t), \quad X(0) = 1 \tag{3.4}$$

Hence, a reasonable stochastic differential equation based on COVID-19 data is achieved. Furthermore, the approximate EM values of the data set $\widehat{X}(t_i)$, $i = 1,2,\dots,91$ are obtained corresponding to the COVID-19 data in Turkey between 11.03.2020 and 09.06.2020. Approximate trajectories taken randomly according to $\widehat{X}(t_i)$ for $i = 91$ is given in Table 2.

The performances of SDE are established by Chi-Square criteria. The results are acquired by using statistical software R-Studio. These results are also corroborated by graphical representation in Figure 2.

Table 2. *The COVID-19 data in Turkey between 11.03.2020 and 09.06.2020 and the approximate $\hat{X}(t_{91})$ EM values of the data set*

Total number of confirmed cases	EM	Total number of confirmed cases	EM	Total number of confirmed cases	EM	Total number of confirmed cases	EM
1	1.0	20921	20979.3	110130	110413.4	151615	150807.5
1	1.0	23934	24225.2	112261	113325.3	152587	152389.3
5	5.1	27069	27249.7	114653	113652.6	153548	153784.1
5	5.0	30217	29969.5	117589	117343.4	154500	155002.8
5	5.0	34109	34189.8	120204	121549.8	155686	156362.2
47	46.8	38226	38414.4	122392	124744.7	156827	154897.3
47	47.3	42282	42731.3	124375	125322.3	157814	158103.2
191	193.6	47029	47344.9	126045	127087.2	158762	162560.7
191	193.0	52167	52638.2	127659	127618.1	159797	160550. 4
670	684.4	56956	56883.4	129491	131721.1	160979	164169.5
947	944.5	61049	61073.1	131744	131106.9	162120	162024.3
1236	1266.3	65111	66423.3	133721	134270.7	163103	163335.7
1529	1526.7	69392	70377.5	135569	135853.1	163942	164039.0
1872	1893.8	74193	74002.2	137115	133322.9	164769	163312.3
2433	2451.1	78546	80126.2	138657	137647.4	165555	162744.7
3629	3730.0	82329	84909.8	139771	138586.6	166422	167981.2
5698	5693.9	86306	87982.4	141475	139412.4	167410	166266.3
7402	7416.3	90980	91190.2	143114	144217.7	168340	166437.7
9271	92478.0	95591	95935.5	144749	147099.5	169218	169196.8
10827	10909.2	98674	100407.8	146457	147548.3	170132	171263.2
13531	13660.9	101790	101573.0	148067	146751.3	171121	170532.4
15679	15759.2	104912	106494.3	149435	149706.2	172114	172661.0
18135	18290.2	107773	107175.1	150593	149324.4		

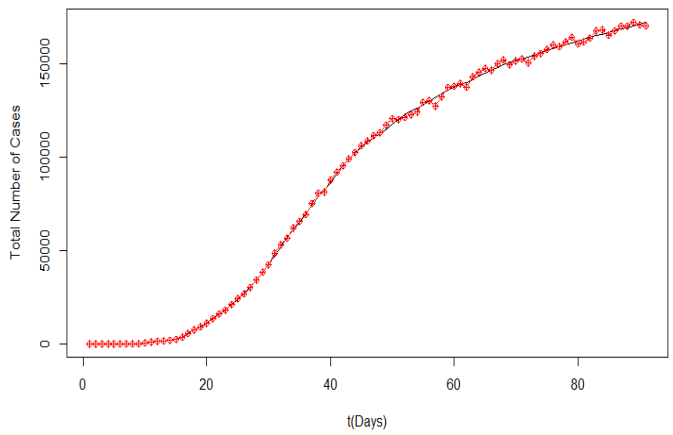

Figure 2. *The COVID-19 data in Turkey between 11.03.2020 and 09.06.2020 (black line) and its EM trajectory starting from $\hat{X}(t_{91})$ (red line)*

5. Conclusion

In this study COVID-19 data in Turkey between 11.03.2020 and 09.06.2020 is investigated by Stochastic Differential Equation Modeling (SDEM). Firstly, parameters of SDE established for the COVID-19 data that mentioned above are estimated estimated $\hat{\theta}_1 = 0.000004$ and $\hat{\theta}_2 = 0.98$ by using maximum likelihood estimation method. Then, we have obtained reasonable Stochastic Differential Equation (SDE) based on the given data. Moreover, by applying Euler-Maruyama Approximation Method trajectories of SDE are achieved. The acceptancy of equation (3.3) with parameters θ_1 and θ_2 to consider in our study for COVID-19 data in Turkey is provided with Chi-square value equal to 7735 of Goodness of fit test. The performances of trajectories according to $\hat{X}(t_{91})$ is established by Chi-Square criteria. The acceptancy of Chi-Square criteria for $\hat{X}(t_{91})$ is realized by values of $p_{value} = 0.2451$ and we do not reject the null hypothesis that given COVID-19 data is fit to last values of EM estimations. As a result, the SDEM we established fits well with COVID-19 data Turkey between 11.03.2020 and 09.06.2020.

References

[1]. World Health Organization (WHO). Coronavirus. Available from: https://www.who.int/health-topics/coronavirus#tab=tab_1 (Accessed: April 15, 2021).

[2]. Iacus S.M., Simulation and Inference for Stochastic Differential Equations with R Examples. USA: Springer, 2008.

[3]. Oksendal B., Stochastic Differential Equations an Introduction with Applications, 5th ed., Corrected Printing. New York: Springer-Verlag Heidelberg, 2003.

[4]. Kostrista E., Çibuku D., "Introduction to Stochastic Differential Equations", Journal of Natural Sciences and Mathematics of UT, 3, (2018), 5-6.

[5]. Ince N., Shamilov A., "An application of new method to obtain probability density function of solution of stochastic differential equations", Applied Mathematics and Nonlinear Sciences, 5.1 (2020), 337-348.

[6]. Mahrouf M. et al. "Modeling and forecasting of COVID-19 spreading by delayed stochastic differential equations", Axioms 10.1, (2021), 18.

[7]. Bak J., Nielsen A. and Madsen H., "Goodness of fit of stochastic differential equations", 21th Symposium I Anvendt Statistik, Copenhagen Business School, Copenhagen, Denmark. 1999.

[8]. Rezaeyan R., Farnoosh R., "Stochastic Differential Equations and Application of the Kalman-Bucy Filter in the Modeling of RC Circuit", Applied Mathematical Sciences, 4, (2010), 1119-1127.

[9]. Ang K. C., "A Simple Stochastic Model for an Epidemic-Numerical Experiments with MATLAB", The Electronic Journal of Mathematics and Technology, 1, (2007), 117-128.

[10]. Simha A., Prasad R.V., and Narayana A.,. "A simple stochastic sir model for covid 19 infection dynamics for karnataka: Learning from europe." arXiv preprint arXiv:2003.11920, (2020).

[11]. Zhang Z., et al. "Dynamics of COVID-19 mathematical model with stochastic perturbation." Advances in Difference Equations, 2020.1, (2020), 1-12.

[12]. Allen E., Modeling with Itô Stochastic Differential Equations. USA: Springer, 2007.

[13]. Shamilov A., Measurement Theory, Probability and Lebesgue Integral, Eskişehir: Anadolu University Publications, 2007.

[14]. Shamilov A., Differential Equations with Theory and Solved Problems, Turkey: Nobel Publishing House, 2012.

[15]. Shamilov A., Probability Theory with Conceptional Interpretations and Applications. Turkey: Nobel Publishing House, 2014.

[16]. Andersson H., Britton T., Stochastic Epidemic Models and Their Statistical Analysis. New York: Springer, 2000.

[17]. Allen L.J.S., An Introduction to Stochastic Processes with Applications to Biology. Upper Saddle River, New Jersey: Pearson Education Inc., 2003.

[18]. Higham D.J., "An Algorithmic Introduction to Numerical Simulation of Stochastic Differential Equations", SIAM Review, 43, (2001), 525-546.

MANAS Journal of Engineering
ISSN 1694-7398 | e-ISSN 1694-7398

Volume 9, Issue 2, (2021) Pages 198-205
https://doi.org/10.51354/mjen946652

On elementary soft compact topological spaces

İsmet Altıntaş[*1,2], Arzıgul İmankulova[1]

[1] Department of Applied Mathematics and Informatics, Kyrgyz Turkish Manas University, Bishkek, Kyrgyzstan, ismet.altintas@manas.edu.kg, ORCID: 0000-0002-9925-8954

[2] Department of Mathematics, Sakarya University, Sakarya, Turkey, ialtintas@sakarya.edu.tr, ORCID: 0000-0002-9925-8954

ABSTRACT

This paper is a work on elementary soft (ϵ-soft) compact spaces. We first define the cofinite ϵ-soft compact space and prove that the image of an ϵ-soft compact space under a soft continuous mapping is ϵ-soft compact space. We then examine the relationship between ϵ-soft compact space and classical compact space and give an illustrative example.

ARTICLE INFO

Research article

Received: 1.06.2021
Accepted: 20.06.2021

Keywords:
soft set,
soft element,
elementary operations,
ϵ-soft compactness

[*]*Corresponding author*

1 Introduction

In 1999, Molodtsov [1] introduced the concept of soft sets as a new mathematical tool for dealing with uncertainties. He showed several applications of this theory in solving many practical problems in economics, engineering, social science, medical science, etc. Interest in the soft sets and their applications has been continued to grow rapidly afterwards. Maji et al. [2, 3] studied soft set theory in detail and applied it to decision making problems. In the line of reduction and addition of parameters of soft sets, some works have been done by Chen et al. [4], Pei and Miao [5], Kong et al. [6], Zou and Xiao [7]. Shabir and Naz [8] introduced the notion of soft topological space. Many authors studied on soft topological spaces and considered the concept of soft point [9-15]. Then, Das and Samanta introduced notions of soft element, soft reel set and number [16] and soft complex set and number [19] over soft sets. Samanta et al. and several authors examined some mathematical structures such as soft metric, soft vector, soft norm, etc. by using the notion of soft element [18-20]. Also, works on fixed point theory have been ongoing over the soft sets, the soft metrics and soft cone metrics [21-26]. In recent years some authors studied on ϵ-soft topological spaces by using elementary operations on soft sets [27-31].

In this paper we study ϵ-soft compact spaces. ϵ-soft compact spaces and many of their properties are studied in [30, 31]. Here we proved the following features related to compactness:

1. Let $\mathcal{T}=\left\{\Phi, U_i \in S(\tilde{X}): U_i^{C} \in S(\tilde{X}), \bigcap U_i^{C} \in S(\tilde{X}), U_i^{\mathbb{C}} \text{ is finite}\right\} \subset S(\tilde{X})$ be a family of soft sets over X with parameter set A. Then $\left(\tilde{X}, \mathcal{T}, A\right)$ is an ϵ-soft compact topological space.

2. Let $\left(\tilde{X}, \mathcal{T}, A\right)$ and $\left(\tilde{Y}, \mathcal{T}^{*}, A\right)$ be two ϵ-soft topological spaces and $F \in S(\tilde{X})$ be an ϵ-soft compact set. If $f: SE\left(\tilde{X}\right) \to SE\left(\tilde{Y}\right)$ is a soft continuous mapping, then $SS\left(f(SE(F))\right) \in S(\tilde{Y})$ is ϵ-soft compact.

3. Let $\left(\tilde{X}, \mathcal{T}, A\right)$ be a ϵ-soft compact space. If $U \tilde{\cap} V \in S(\tilde{X})$ for every $U, V \in \mathcal{T}$, Then for every $\lambda \in A$;

i. $(X, \mathcal{T}_\lambda)$ is a compact space.

ii. For every ϵ-soft compact set $F \in S(\tilde{X})$, $F(\lambda) \subset X$ is a compact set.

Also, we give an example that explains the relationship between ϵ-soft compact space and classical compact space.

2 Preliminaries

Definition 2.1. [1] Let A be a set of parameters and E be an initial universe. Let $\mathcal{P}(E)$ denote the power set of E. A pair (F, A) is called a soft set over E, where F is a mapping given by $F: A \to \mathcal{P}(E)$. In other words, a soft set over E is a parametrized family of subsets of the universe E. For $\lambda \in A$, $F(\lambda)$ may be considered as the set of λ-approximate elements of the soft set (F, A) and denoted by *F* for short.

Definition 2.2. [2] Let *F* and *G* be two soft sets over a common universe E.

1. *F* is said to be null soft set, denoted by Φ, if for all $\lambda \in A$, $F(\lambda) = \varnothing$. *F* is said to an absolute soft set denoted by $\tilde{E}$, if for all $\lambda \in A$, $F(\lambda) = E$.
2. *F* is said to be a soft subset of *G* if for all $\lambda \in A$, $F(\lambda) \subseteq G(\lambda)$ and it is denoted by $F \tilde{\subseteq} G$. *F* is said to be a soft upper set of *G* if *G* is a soft subset of *F*. We denote it by $F \tilde{\supseteq} G$. *F* and *G* is said to be equal if *F* is a soft subset of *G* and *G* is a soft subset of *F*.
3. The intersection *H* of *F* and *G* over E is defined as $H(\lambda) = F(\lambda) \cap G(\lambda)$ for all $\lambda \in A$. We write $H = F \tilde{\cap} G$.
4. The union *H* of *F* and *G* over E is defined as $H(\lambda) = F(\lambda) \cup G(\lambda)$ for all $\lambda \in A$. We write $H = F \tilde{\cup} G$.
5. The product *H* of *F* and *G* over E is defined as $H(\lambda) = F(\lambda) \times G(\lambda)$ for all $\lambda \in A$. We write $H = F \tilde{\times} G$.
6. The difference (H, A) of (F, A) and *H* of *F* and *G* over E is defined as $H(\lambda) = F(\lambda) \setminus G(\lambda)$ for all $\lambda \in A$. We write $H = F \tilde{\setminus} G$.
7. The complement F^c of *F* is defined as $(F, A)^c = (F^c, A)$, where $F^c: A \to \mathcal{P}(E)$ is a mapping given by $F^c(\lambda) = X \setminus F(\lambda)$ for all $\lambda \in A$. Clearly, we have $\tilde{E}^c = \Phi$ and $\Phi^c = \tilde{E}$

Definition 2.3. [16, 19] Let A be a non-empty parameter set and E be a non-empty set. Then a function $\epsilon: A \to E$ is said to be a soft element of E. A soft element ϵ of E is said to belongs to a soft set *F* of E which is denoted by $\epsilon \tilde{\in} F$ if $\epsilon(\lambda) \in F(\lambda)$, $\forall \lambda \in A$. Thus for a soft set *F* of E with respect to the index set A, we have $F(\lambda) = \{\epsilon(\lambda) : \epsilon \tilde{\in} F\}$, $\lambda \in A$. In that case, ϵ is also said to be a soft element of the soft set *F*. Thus every singleton soft set (a soft set *F* of E for which $F(\lambda)$ is a singleton set, $\forall \lambda \in A$) can be identified with a soft element by simply identifying the singleton set with the element that it contains $\forall \lambda \in A$.

Throughout this paper, we consider the null soft set Φ and those soft sets *F* over E for which $F(\lambda) \neq \varnothing$, $\forall \lambda \in A$. We denote this collection by $S(\tilde{E})$. Thus for a soft set $F(\neq \Phi) \in S(\tilde{E})$, $F(\lambda) \neq \varnothing$ for all $\lambda \in A$. For any soft set $F \in S(\tilde{E})$, the collection of all soft elements of *F* is denoted by $SE(F)$. Also, we use the notation $\tilde{x}, \tilde{y}, \tilde{z}$ to denote soft elements of a soft set

Proposition 2.4. [19] The following statements about soft sets are satisfied.

1. For any soft sets $F, G \in S(\tilde{E})$, we have $F \tilde{\subset} G$ if and only if every soft element of *F* is also a soft elements of *G*.

2. Any collection of soft elements of a soft set can generate a soft subset of that soft set. The soft set constructed from a collection $\mathcal{B}$ of soft elements is denoted by $SS(\mathcal{B})$.
3. For any soft set $F \in S(\tilde{E})$, $SS(SE(F)) = F$; whereas for a collection $\mathcal{B}$ of soft elements, $SE(SS(\mathcal{B})) \supset \mathcal{B}$.

Remark 2.5. [19] $\tilde{x} \tilde{\in} F \tilde{\cup} G$ does not necessarily imply that either $\tilde{x} \tilde{\in} F$ or $\tilde{x} \tilde{\in} G$. Also, the intersection of two soft sets or complement of a soft set of $S(\tilde{E})$ is not necessarily a member of $S(\tilde{E})$

Definition 2.6. [19] Let $F, G \in S(\tilde{E})$ be two soft sets.

1. $F \Cup G$ denotes the e-union of *F* and *G*, that is defined by $F \Cup G = SS(\mathcal{B})$, where $\mathcal{B} = \{\tilde{x} \tilde{\in} \tilde{E} : \tilde{x} \tilde{\in} F \text{ or } \tilde{x} \tilde{\in} G\}$, ie, $F \Cup G = SS\left(SE(F) \cup SE(G)\right)$.
2. $F \Cap G$ denotes the e-intersection of *F* and *G*, that is defined by $F \Cap G = SS(\mathcal{B})$, where $\mathcal{B} = \{\tilde{x} \tilde{\in} \tilde{E} : \tilde{x} \tilde{\in} F \text{ and } \tilde{x} \tilde{\in} G\}$, ie, $F \Cap G = SS\left(SE(F) \cap SE(G)\right)$. If the two soft sets have no soft elements in common, then $F \Cap G = \Phi$.
3. $F^{\mathbb{C}}$ denotes the e-complement of *F*, that is defined by $F^{\mathbb{C}} = SS(\mathcal{B})$, where $\mathcal{B} = \{\tilde{x} \tilde{\in} \tilde{E} : \tilde{x} \tilde{\in} F^{C}\}$, ie, $F^{\mathbb{C}} = SS\left(SE(F^{\mathbb{C}})\right)$.

Remark 2.7. [19]. It can be easily verified that $F \Cup G$, $F \Cap G$, and $F^{\mathbb{C}}$ are members of $S(\tilde{E})$, if $F, G \in S(\tilde{E})$.

Definition 2. 8. [27, 28] Let $\mathcal{T} \subset S(\tilde{X})$ be a family of soft sets over *X* with parameter set *A*. $\mathcal{T}$ is a topology on $\tilde{X}$ according to the e-operations if it meets the following conditions.

1. $\Phi, \tilde{X} \in \mathcal{T}$,
2. If $\{U_i\}_{i \in I} \subset \mathcal{T}$, then $\Cup_{i \in I} U_i \in \mathcal{T}$,
3. If $\{U_i\}_{i=1}^{n} \subset \mathcal{T}$, then $\Cap_{i=1}^{n} U_i \in \mathcal{T}$.

This topology is called e-soft topology, and the triple $(\tilde{X}, \mathcal{T}, A)$ is called a ϵ-soft topological space. The members of $\mathcal{T}$ are called soft open sets.

Proposition 2.9. [28] Let $(\tilde{X}, \mathcal{T}, A)$ be a ϵ-soft topological space. If $U \tilde{\cap} V \in S(\tilde{X})$ for every $U, V \in \mathcal{T}$, then for every $\lambda \in A$, $\mathcal{T}_\lambda = \{U(\lambda) : U \in \mathcal{T}\}$ is a topology on *X*.

Definition 2.10. [28] Let $f : SE(\tilde{X}) \to SE(\tilde{Y})$ be a soft mapping. If for every $\lambda \in A$, $\tilde{x} \tilde{\in} \tilde{X}$ and $x \in X$, $\{f(\tilde{x})(\lambda) : \tilde{x}(\lambda) = x\}$ is a unit set, $f_\lambda : X \to Y$ given by $f_\lambda(\tilde{x}(\lambda)) = f(\tilde{x})(\lambda)$ is a mapping from *X* to *Y*. Then $f : SE(\tilde{X}) \to SE(\tilde{Y})$ is called a soft function.

Definition 2.11. [28] Let $(\tilde{X}, \mathcal{T}, A)$ and $(\tilde{Y}, \mathcal{T}^*, A)$ be two ϵ-soft topological spaces. A soft mapping $f : SE(\tilde{X}) \to SE(\tilde{Y})$ is called soft continuous at $\tilde{x} \tilde{\in} \tilde{X}$ if for any soft neighborhood N' of $f(\tilde{x})$ there exists N of $(\tilde{x})$

such that $f\left(SE(N)\right) \subset f\left(SE(N')\right)$. f is called soft continuous over $\left(\tilde{X}, \mathcal{T}, A\right)$, if it is soft continuous at every $\tilde{x} \tilde{\in} \tilde{X}$.

Theorem 2.12. [28] Let $\left(\tilde{X}, \mathcal{T}, A\right)$ and $\left(\tilde{Y}, \mathcal{T}^*, A\right)$ be two ϵ-soft topological spaces and $f : SE\left(\tilde{X}\right) \to SE\left(\tilde{Y}\right)$ be a soft mapping. f is soft continuous if and only if for every $U \in \mathcal{T}^*$, $SS\left(f^{-1}(SE(U))\right) \in \mathcal{T}$.

3. ϵ-soft compactness

Definition 3.1. [30] Let $\left(\tilde{X}, \mathcal{T}, A\right)$ be an ϵ-soft topological space, $F \in S(\tilde{X})$ and $\{U_i : i \in I\}$ be a family of soft open sets in $\left(\tilde{X}, \mathcal{T}, A\right)$.

i. $\{U_i : i \in I\}$ is called an ϵ-soft open cover of $\left(\tilde{X}, \mathcal{T}, A\right)$ if $\tilde{X} = \tilde{\bigcup}_{i \in I} U_i$

ii. $\{U_i : i \in I\}$ is called an ϵ-soft open cover of F if $F \tilde{\subseteq} \tilde{\bigcup}_{i \in I} U_i$.

The following definition is an adaptation of the definition for soft e-quasi compact space in [30].

Definition 3.2. Let $\left(\tilde{X}, \mathcal{T}, A\right)$ be a ϵ-soft topological space and $F \in S(\tilde{X})$.

i. $\left(\tilde{X}, \mathcal{T}, A\right)$ is called an ϵ-soft compact space if every ϵ-soft open cover of $\tilde{X}$ has a finite ϵ-soft open sub-cover.

ii. $F \in S(\tilde{X})$ is called an ϵ-soft compact set if every ϵ-soft open cover of F has a finite ϵ-soft open sub-cover.

Proposition 3.3. Let $\mathcal{T} = \left\{\Phi, U_i \in S(\tilde{X}) : U_i^{\,C} \in S(\tilde{X}), \bigcap U_i^{\,C} \in S(\tilde{X}), U_i^{\,\mathbb{C}} \text{ is finite}\right\} \subset S(\tilde{X})$ be a family of soft sets over X with parameter set A. Then $\left(\tilde{X}, \mathcal{T}, A\right)$ is an ϵ-soft compact topological space.

Proof. Let's first show that $\left(\tilde{X}, \mathcal{T}, A\right)$ is an ϵ-soft topological space. For this three axioms of Definition 2.8 must be provided.

1. Since $\tilde{X}^C = \Phi \in S(\tilde{X})$ and $\tilde{X}^{\mathbb{C}} = SS(SE(\tilde{X}^C)) = \Phi$ is finite, $\Phi, \tilde{X} \in \mathcal{T}$.

2. If $\{U_i\}_{i \in I} \subset \mathcal{T}$, Then $U_i^C \in S(\tilde{X})$ and $U_i^{\mathbb{C}}$ is finite . So $\tilde{\bigcup}_{i \in I} U_i^C \in S(\tilde{X})$ and $\tilde{\bigcup}_{i \in I} U_i^{\mathbb{C}}$ is finite. Thus $\tilde{\bigcup}_{i \in I} U_i \in \mathcal{T}$.

3. Let $U, V \in \mathcal{T}$. Then $U^C, V^C \in S(\tilde{X})$, $U^{\mathbb{C}}$ and $V^{\mathbb{C}}$ are finite and $U^C \tilde{\cap} V^C \in S(\tilde{X})$. Then $U^{\mathbb{C}} \tilde{\cap} V^{\mathbb{C}}$ is finite. So $U^{\mathbb{C}} \tilde{\cap} V^{\mathbb{C}} \in \mathcal{T}$.

Now let's show that $\left(\tilde{X}, \mathcal{T}, A\right)$ is ϵ-soft compact. Let $\{U_i : i \in I\}$ be an ϵ-soft open cover of $\left(\tilde{X}, \mathcal{T}, A\right)$. Let's take a soft open set U_j in the family $\{U_i : i \in I\}$. Then $U_j^C \in S(\tilde{X})$ and $U_j^{\mathbb{C}}$ is finite . Say $U_j^{\mathbb{C}} = \{\tilde{u}_1, \tilde{u}_2, ..., \tilde{u}_n\}$. Then, there are a finite number of the soft open sets $U_1, U_2, ..., U_n$ such that $u_1 \in U_1, u_2 \in U_2, ..., u_n \in U_n$. Thus, we obtain $\tilde{X} = U_j \tilde{\cup} U_j^{\mathbb{C}} = U_j \tilde{\cup} \left(\tilde{\bigcup}_{i=1}^{n} U_i\right)$. Hence, the space $\tilde{X}$ is ϵ-soft compact as it is covered by a finite number of soft open sets.

One of the most important properties of compact spaces is that compactness is a topological property. This is a result of the following theorem.

Theorem 3.4. Let $\left(\tilde{X},\mathcal{T},A\right)$ and $\left(\tilde{Y},\mathcal{T}^*,A\right)$ be two ϵ-soft topological spaces and $F\in S(\tilde{X})$ be an ϵ-soft compact set. If $f:SE\left(\tilde{X}\right)\to SE\left(\tilde{Y}\right)$ is a soft continuous mapping, then $SS\left(f(SE(F))\right)\in S(\tilde{Y})$ is ϵ-soft compact.

Proof. Let $\left\{U_i\in\mathcal{T}^*:i\in I\right\}$ be any ϵ-soft open cover of $K=SS\left(f(SE(F))\right)$. Then $K\tilde{\subseteq}\underset{i\in I}{\tilde{\cup}}U_i$. Since each U_i is soft open and f is soft continuous, for every $i\in I$,

$$SS\left(f^{-1}\left(SE(U_1)\right)\right)\in\mathcal{T},\ SS\left(f^{-1}\left(SE(U_2)\right)\right)\in\mathcal{T},\ldots$$

Also,

$$\begin{aligned}F\tilde{\subset}SS\left(f^{-1}\left(SE(K)\right)\right)&\tilde{\subseteq}SS\left(f^{-1}\left(SE(U_1)\right)\right)\tilde{\cup}SS\left(f^{-1}\left(SE(U_2)\right)\right)\tilde{\cup}\ldots\\&=\underset{i\in I}{\tilde{\cup}}SS\left(f^{-1}(SE(U_i))\right)=SS\left(\underset{i\in I}{\cup}f^{-1}(SE(U_i))\right)\\&=SS\left(f^{-1}\left(\underset{i\in I}{\cup}SE(U_i)\right)\right)=SS\left(f^{-1}\left(SE\left(\underset{i\in I}{\tilde{\cup}}U_i\right)\right)\right)\end{aligned}$$

Then $\left\{SS\left(f^{-1}\left(SE(U_i)\right)\right):i\in I\right\}$ is an ϵ-soft open cover of F. But F is ϵ-soft compact, so $\left\{SS\left(f^{-1}\left(SE(U_i)\right)\right):i\in I\right\}$ is an ϵ-soft open sub-cover, say

$$\begin{aligned}F\tilde{\subseteq}SS\left(f^{-1}\left(SE(U_{j1})\right)\right)&\tilde{\cup}SS\left(f^{-1}\left(SE(U_{j2})\right)\right)\tilde{\cup}\ldots\tilde{\cup}SS\left(f^{-1}\left(SE(U_{jm})\right)\right)\\&=\underset{i=1}{\overset{m}{\tilde{\cup}}}SS\left(f^{-1}(SE(U_{ji}))\right)=SS\left(f^{-1}\left(SE\left(\underset{i=1}{\overset{m}{\tilde{\cup}}}U_{ji}\right)\right)\right)\end{aligned}$$

Accordingly,

$$\begin{aligned}K=SS\left(f(SE(F))\right)&\tilde{\subseteq}SS\left(f\left(SE\left(\underset{i=1}{\overset{m}{\tilde{\cup}}}SS\left(f^{-1}(SE(U_{ji}))\right)\right)\right)\right)\\&=SS\left(f\left(SE\left(SS\left(\underset{i\in I}{\overset{m}{\cup}}f^{-1}(SE(U_{ji}))\right)\right)\right)\right)\\&=SS\left(f\left(SE\left(SS\left(f^{-1}\left(\underset{i\in I}{\overset{m}{\cup}}SE(U_{ji})\right)\right)\right)\right)\right)\\&=SS\left(SE\left(SS\left(\underset{i\in I}{\overset{m}{\cup}}SE(U_{ji})\right)\right)\right)\\&=SS\left(SE\left(\underset{i=1}{\overset{m}{\tilde{\cup}}}U_{ji}\right)\right)\\&=\underset{i=1}{\overset{m}{\tilde{\cup}}}U_{ji}\end{aligned}$$

Thus $K=SS\left(f(SE(F))\right)$ is ϵ-soft compact.

Corollary 3.5. Let $\left(\tilde{X},\mathcal{T},A\right)$ and $\left(\tilde{Y},\mathcal{T}^{*},A\right)$ are ϵ-soft topological spaces. If $\left(\tilde{X},\mathcal{T},A\right)$ is ϵ-soft compact and $f:SE\left(\tilde{X}\right)\to SE\left(\tilde{Y}\right)$ is a soft continuous and onto function, then $\left(\tilde{Y},\mathcal{T}^{*},A\right)$ is ϵ-soft compact.

The following theorem gives the relationship between ϵ-soft compactness and classical compactness.

Theorem 3.6. Let $\left(\tilde{X},\mathcal{T},A\right)$ be a ϵ-soft compact space. If $U\tilde{\cap}V\in S(\tilde{X})$ for every $U,V\in\mathcal{T}$, Then for every $\lambda\in A$;

i. $\left(X,\mathcal{T}_{\lambda}\right)$ is a compact space.

ii. For every ϵ-soft compact set $F\in S(\tilde{X})$, $F(\lambda)\subset X$ is a compact set.

Proof. *i.* By Proposition 2.10, for every $\lambda\in A$, $\mathcal{T}_{\lambda}=\left\{U(\lambda):U\in\mathcal{T}\right\}$ is a topology on *X*. So $\left(X,\mathcal{T}_{\lambda}\right)$ is a topological space. Since $\left(\tilde{X},\mathcal{T},A\right)$ is ϵ-soft compact space, every ϵ-soft open cover $\left\{U_i:i\in I\right\}$ of $\tilde{X}$ has a finite ϵ-soft open sub-cover $\left\{U_{ij}:j=1,2,...,m\right\}$. That is, $\tilde{X}=\tilde{\bigcup}_{i\in I}U_i$ implies $\tilde{X}=\tilde{\bigcup}_{j=1}^{m}U_{ij}$. Hence, form $\tilde{X}=\tilde{\bigcup}_{i\in I}U_i=SS\left(\bigcup_{i\in I}SE\left(U_i\right)\right)$ for every $\lambda\in A$, we have

$$X=\tilde{X}(\lambda)=SS\left(\bigcup_{i\in I}SE\left(U_i\right)\right)(\lambda)=\bigcup_{i\in I}U_i(\lambda)$$

and

$$X=\tilde{X}(\lambda)=\left(\tilde{\bigcup}_{j\in I}^{m}U_{ij}\right)(\lambda)=SS\left(\bigcup_{j=1}^{m}SE\left(U_{ij}\right)\right)(\lambda)=\bigcup_{j=1}^{m}U_{ij}(\lambda).$$

Thus $\left(X,\mathcal{T}_{\lambda}\right)$ is a compact space.

ii. Since *F* is ϵ-soft compact, every ϵ-soft open cover $\left\{U_i:i\in I\right\}$ of *F* has a finite ϵ-soft open sub-cover $\left\{U_{ij}:j=1,2,...,m\right\}$ such that $F\tilde{\subseteq}\tilde{\bigcup}_{i\in I}U_i$ implies $F\tilde{\subseteq}\tilde{\bigcup}_{j=1}^{m}U_{ij}$. Hence, $F\tilde{\subseteq}\tilde{\bigcup}_{i\in I}U_i=SS\left(\bigcup_{i\in I}SE\left(U_i\right)\right)$ implies, for every $\lambda\in A$,

$$F(\lambda)\tilde{\subseteq}SS\left(\bigcup_{i\in I}SE\left(U_i\right)\right)(\lambda)=SS\left(\bigcup_{i\in I}SE\left(U_i\right)(\lambda)\right)=\bigcup_{i\in I}U_i(\lambda).$$

Thus $F(\lambda)$ is compact.

Example 3.7. Let $A=\left\{\lambda,\mu\right\}$ be a parameters set and $X=\left\{x,y,z\right\}$ be a set. Then $\mathcal{T}=\left\{\Phi,\tilde{X},U_1,U_2,U_3\right\}$ is a ϵ-soft topology of $\tilde{X}$, where

$$U_1=\left\{\left(\lambda,\left\{x\right\}\right),\left(\mu,\left\{y\right\}\right)\right\}$$
$$U_2=\left\{\left(\lambda,\left\{x,y\right\}\right),\left(\mu,\left\{x,y\right\}\right)\right\}$$
$$U_3=\left\{\left(\lambda,\left\{x,z\right\}\right),\left(\mu,\left\{y,z\right\}\right)\right\}.$$

And $\tilde{X} = \{\tilde{x}_1, \tilde{x}_2, \tilde{x}_3, \tilde{x}_4, \tilde{x}_5, \tilde{x}_6, \tilde{x}_7, \tilde{x}_8, \tilde{x}_9\}$, where

$$\tilde{x}_1 = \{(\lambda, \{x\}), (\mu, \{x\})\}, \qquad \tilde{x}_6 = \{(\lambda, \{y\}), (\mu, \{z\})\},$$
$$\tilde{x}_2 = \{(\lambda, \{x\}), (\mu, \{y\})\}, \qquad \tilde{x}_7 = \{(\lambda, \{z\}), (\mu, \{x\})\},$$
$$\tilde{x}_3 = \{(\lambda, \{x\}), (\mu, \{z\})\}, \qquad \tilde{x}_8 = \{(\lambda, \{z\}), (\mu, \{y\})\},$$
$$\tilde{x}_4 = \{(\lambda, \{y\}), (\mu, \{x\})\}, \qquad \tilde{x}_9 = \{(\lambda, \{z\}), (\mu, \{z\})\}.$$
$$\tilde{x}_5 = \{(\lambda, \{y\}), (\mu, \{y\})\},$$

Since $\tilde{X}$ is finite, $(\tilde{X}, \mathcal{T}, A)$ is ϵ-soft compact. Also $(X, \mathcal{T}_\lambda)$ and $(X, \mathcal{T}_\mu)$ are topological spaces, where

$$\mathcal{T}_\lambda = \{\varnothing, X, \{x\}, \{x, y\}, \{x, z\}\},$$
$$\mathcal{T}_\mu = \{\varnothing, X, \{y\}, \{x, y\}, \{y, z\}\}.$$

Since X is finite, $(X, \mathcal{T}_\lambda)$ and $(X, \mathcal{T}_\mu)$ are the compact spaces.

4. Conclusion

In this paper, we define cofinite e-soft space as an example of e-soft compact space and prove that the image of an ϵ-soft compact (and an ϵ-soft compact set) space under a soft continuous mapping is ϵ-soft compact space (and is ϵ-soft compact). Also, we examine the relationship between ϵ-soft compact space and classical compact space. We think it will contribute to the studies in this context.

References

[1]. Molodtsov D., "Soft set theory-first results", Comput. Math. Appl., 37, (1999), 19-31.

[2]. Maji P.K., Biswas R., Roy A. R., "Soft set theory", Comput. Math. Appl., 45, (2003), 555-562.

[3]. Maji P.K., Roy A.R., Biswas R., "An application of soft sets in a decision making problem", Comput. Math. Appl., 44, (2002), 1077-1083.

[4]. Chen D., Tsang E.C.C., Yeung D.S., Wang X., "The parameterization reduction of soft sets and its applications", Comput. Math. Appl., 49, (2005), 757-763.

[5]. Pei D., Miao D., "From soft sets to information systems", 2005 IEEE International Conference on Granular Computing, vol. 2, IEEE, 2005, 617–621.

[6]. Kong Z., Jia W., Zhang G., Wang L., "Normal parameter reduction in soft set based on particle swarm optimization algorithm", Appl. Math. Model., 39, (2015), 4808-4820.

[7]. Zou Y., Xiao Z., "Data analysis approaches of soft sets under incomplete information", Knowledge-Based Systems, 21, (2008), 941-945.

[8]. Shabir M., Naz M., "On soft topological spaces", Comput. Math. Appl., 61, 7, (2011), 1786-1799.

[9]. Aygünoğlu A., Aygün H., "Some notes on soft topological spaces", Neural Computing and Applications, 21, (2012), 113-119.

[10]. Babitha K.V., John S. J., "Studies on soft topological spaces", J. Intell. Fuzzy Syst., 28, (2015), 1713-1722.

[11]. Çetkin V., Aygün H., "On convergence of soft nets", J. Mult.-Valued Logic Soft Comput., 26, (2016), 175-187.

[12]. Matejdes M., "Soft topological space and topology on the cartesian product", Hacet. J. Math. Stat., 45, (2016), 1091-1100.

[13]. Pazar Varol B., Aygün H., "Soft sets over power sets: Generalities and applications to topology", J. Intell. Fuzzy Syst, 29, (2015), 389–395.

[14]. Yang H.-L., Liao X., Li S.-G., "On soft continuous mappings and soft connectedness of soft topological spaces", Hacet. J. Math. Stat., 44, (2015), 385-398.

[15]. Zorlutuna İ., Akdağ M., Min W. K., Atmaca S., "Remarks on soft topological spaces", Ann. Fuzzy Math. Inform., 3, (2012), 171-185.

[16]. Das S., Samanta S. K., "Soft real sets, soft real numbers and their properties", J. Fuzzy Math., 20, (2012), 551-576.

[17]. Das S., Samanta S. K., "On soft complex sets and soft complex numbers", J. Fuzzy Math., 21, (2013), 195-216.

[18]. Das S., Majumdar P., Samanta S. K., "On soft linear spaces and soft normed linear spaces", Ann. Fuzzy Math. Inform., 9, (2015), 91-109.

[19]. Das S., Samanta S. K., "On soft metric spaces", J. Fuzzy Math., 21, (2013), 707-734.

[20]. Das S., Samanta S. K., "Soft linear operators in soft normed linear spaces", Ann. Fuzzy Math. Inform., 6, (2013), 295-314.

[21]. Abbas M., Murtaza G., Romaguera S., "On the fixed point theory of soft metric spaces", Fixed Point Theory Appl., (2016), 17.

[22]. Leyew B. T., Abbas M., "A soft version of the knaster–tarski fixed point theorem with applications", J. Fixed Point Theory Appl., (2017), 1-15.

[23]. Hosseinzadeh H., "Fixed point theorems on soft metric spaces", J. Fixed Point Theory Appl., (2016), 1-23.

[24]. Dağıstan Ş. et al., "An introduction to soft cone metric spaces and some fixed Point theorems", MANAS Journal of Engineering, 5 (3), (2017), 69-89.

[25]. Altintas I., Simsek D., Taskopru K., "Topology of soft cone metric spaces", : AIP Conference Proceedings 1880, 030006 (2017), 1-6 doi: 10.1063/1.5000605,

[26]. Altıntaş İ., Taşköprü K., "Compactness of soft cone metric space and fixed point theorems related to diametrically contractive mapping", Turkish Journal of Mathematics, 44, (2020), 2199 – 221.

[27]. Chiney M., Samanta S.K., "Soft topology redefined", J. Fuzzy Math., 27(2), (2019), 459-486.

[28]. Taşköprü K., Altıntaş İ., "A new approach for soft topology and soft function via soft element", Math Meth. Appl. Sci., (2021), 44, 7556–7570.

[29]. Altıntaş İ., Taşköprü K., Selvi B., "Countable and separable elementary soft topological space", Math Meth. Appl. Sci., (2021), 44, 7811–7819.

[30]. Bousselsal M., Saadi A., "Soft elementary compact in soft elementary topology", arXiv:1803.11448v2, Math GM, (2018).

[31]. Roy S., Chiney M., "On compactness and connectedness in redefined soft topological spaces", International Journal of Pure and Applied Mathematics, 120(5), (2019), 1505-1528.